# MODELING OCEAN ALKALINITY ENHANCEMENT IN SUBDUCTION REGIONS AND THE GLOBAL OCEAN

Dissertation zur Erlangung des akademischen Grades eines Doktors der Naturwissenschaften

DR. RER. NAT.
am Fachbereich 2 der Universität Bremen

TANVI NAGWEKAR

**Gutachter:**
Dr. Lester Kwiatkowski, Sorbonne Université, IPSL
Prof. Dr. Andreas Oschlies, GEOMAR

Bremen, March 2025
Datum des Kolloquiums: 24. April 2025

Universität
Bremen

ALFRED-WEGENER-INSTITUT
HELMHOLTZ-ZENTRUM FÜR POLAR-
UND MEERESFORSCHUNG

TANVI NAGWEKAR

# MODELING OCEAN ALKALINITY ENHANCEMENT IN SUBDUCTION REGIONS AND THE GLOBAL OCEAN

Tanvi Nagwekar: *Modeling Ocean Alkalinity Enhancement in Subduction Regions and the Global Ocean*, Bremen, March 2025

"For the globe as a whole, the ocean is the great regulator, the great stabilizer of temperature. It has been described as 'a savings bank for solar energy, receiving deposits in seasons of excessive insolation and paying them back in seasons of want.' Without the ocean, our world would be visited by an unthinkably harsh extremes of temperature...."

— *In The Sea Around Us* (1951) by Rachel Carson

# ABSTRACT

Anthropogenic $CO_2$ emissions have driven global warming since the Industrial Revolution, necessitating a phasing out of fossil fuels to limit warming to well below 2°C, preferably 1.5°C, as outlined in the Paris Agreement. However, emission reductions alone are unlikely to be sufficient to meet these targets, highlighting the need for large-scale carbon dioxide removal (CDR). While current CDR efforts primarily focus on land-based methods, challenges, such as land competition and biodiversity loss have led to growing interest in ocean-based approaches as a complementary solution. Ocean Alkalinity Enhancement (OAE) is one such ocean-based CDR method with high theoretical carbon sequestration potential that enhances $CO_2$ uptake by shifting carbonate equilibria in the surface ocean.

The ocean has absorbed ~25% of anthropogenic $CO_2$ since the Industrial Revolution and thus plays a crucial role in the global carbon cycle. Subduction regions in the Southern Ocean and North Atlantic are particularly important for anthropogenic carbon uptake as they transport carbon into the deep ocean, sequestering it for centuries to millennia. Building on this natural process, I hypothesize that deploying OAE in subduction regions will enhance deep ocean sequestration and OAE efficiency. To test this, OAE is simulated in subduction regions and globally using a low-resolution ocean circulation and biogeochemistry model (Publication I), a fully coupled emission-driven Earth System Model (ESM; Publication II), and a high-resolution ocean circulation and biogeochemistry model (Publication III).

This thesis identifies three key factors influencing simulated OAE efficiency: the amount of added alkalinity, climate feedbacks, and model resolution. Among these, alkalinity addition is the primary driver, which exhibits a strong linear relationship with oceanic $CO_2$ uptake and atmospheric $CO_2$ reduction after 60-70 years of OAE deployment, a relationship that is consistent across emission scenarios and aligns with previous literature. However, in contrast to this scaling observed after decades of alkalinity addition, the largest differences and highest uncertainties in OAE efficiency occur in the initial decade of deployment (2030s). During this period, OAE efficiency in subduction regions (0.60 in Publication I, 0.70 in Publication III) surpasses global OAE in ocean-only models (0.56 in Publication I, 0.57 in Publication III). In contrast, the ESM-based regional OAE simulation (Publication II) yields a lower efficiency of 0.38, with a ±55% uncertainty attributed to climate-feedback driven variability. As alkalinity perturbations disperse over time, regional differences diminish, reducing uncertainty and leading to a convergence of efficiency estimates between global and regional applications by the 2090s, with values of 0.85 (global and regional, Publication I), 0.72 (global and regional, Publication II), and 0.85-0.90 (global-regional; Publication III). The persistently lower efficiency in Publication II underscores the role of climate feedbacks as the second most influential factor in OAE efficiency. Model resolution has only a third-order impact. Notably, Publication III reports the highest regional OAE efficiency in the 2030s, potentially due to a combination of different dynamics in the high-resolution model and differences in the background state of carbonate chemistry across model setups, which further contributes to early-phase uncertainty.

Further, both high- and low-resolution ocean-only models demonstrate efficient deep-ocean carbon sequestration, with high-resolution global and regional simulations storing a relatively higher amount of carbon below 1 km throughout the simulation period than their low-resolution counterparts. Moreover, these models indicate that subduction regions transport nearly twice as much carbon to depths below 1 km as global OAE in their respective setups, although their smaller surface area leads to a lower total dissolved inorganic carbon (DIC) increase. In contrast, the regional OAE using the ESM model (Publication II) does not replicate such efficient deep transport, largely due to internal climate variability and feedbacks. The ocean-only simulations also reveal that subduction regions can be viable for OAE, but exhibit strong seasonal variability in excess carbon uptake, surface alkalinity, and DIC accumulation, driven by the seasonality of the mixed layer depth (MLD). A shallower summer MLD retains excess surface alkalinity, allowing $CO_2$-deficient waters to equilibrate with the atmosphere and enhance $CO_2$ uptake and DIC accumulation, while a deeper winter MLD increases mixing, leading to alkalinity loss and reduced $CO_2$ uptake. Therefore, to optimize OAE efficiency in regional deployments, future strategies must account for these seasonal dynamics.

Based on the findings of this thesis, model selection for OAE research should align with the specific goals: low-resolution models capture large-scale ocean processes, high-resolution models can be useful to resolve small-scale dynamics that are potentially important for deep ocean carbon sequestration, and ESMs incorporate Earth system feedbacks vital for assessing how CDR deployment can affect the climate trajectory with respect to climate targets. Most importantly, as all model setups in this study exhibit the highest uncertainty during the initial phase of OAE deployment, future modeling efforts should focus on understanding uncertainties in estimates of OAE efficiency in the early phases of regional applications, which are crucial for developing a robust MRV framework.

# ZUSAMMENFASSUNG

Die anthropogenen $CO_2$-Emissionen haben die globale Erwärmung seit der industriellen Revolution vorangetrieben und machen einen schrittweisen Ausstieg aus der Nutzung fossiler Brennstoffe erforderlich, um die Erwärmung auf deutlich unter 2°C, vorzugsweise 1,5°C, zu begrenzen, wie im Pariser Klima-Abkommen vorgesehen. Es ist jedoch unwahrscheinlich, dass Emissionssenkungen allein ausreichen, um diese Ziele zu erreichen, weshalb eine großskalige Kohlendioxidentnahme (CDR) notwendig sein wird. Während sich die derzeitigen CDR-Bemühungen in erster Linie auf landgestützte Methoden konzentrieren, haben Herausforderungen wie Landnutzungskonflikte und Biodiversitätsverlust zu einem wachsenden Interesse an meeresgestützten Ansätzen als ergänzende Lösung geführt. Ozeanische Alkalinitätserhöhung (OAE) ist eine solche ozeanbasierte CDR-Methode mit hohem theoretischem Kohlenstoffbindungspotenzial, die die $CO_2$-Aufnahme durch Verschiebung des Karbonatgleichgewichts im Oberflächenozean erhöht.

Der Ozean hat seit der industriellen Revolution etwa 25% des anthropogenen $CO_2$ aufgenommen und spielt somit eine entscheidende Rolle im globalen Kohlenstoffkreislauf. Subduktionsgebiete im Südlichen Ozean und im Nordatlantik sind für die anthropogene Kohlenstoffaufnahme besonders wichtig, da sie Kohlenstoff in die Tiefe transportieren und ihn dort für Jahrhunderte bis Jahrtausende speichern. Aufbauend auf diesem natürlichen Prozess stelle ich die Hypothese auf, dass der Einsatz von OAE in Subduktionsregionen die Kohlenstoffspeicherung im tiefen Ozean und die Effizienz von OAE erhöhen wird. Um dies zu testen, wird eine OAE-Anwendung in Subduktionsregionen sowie im globalen Ozean simuliert, und zwar mit einem Modell der Ozeanzirkulation und Biogeochemie mit niedriger Auflösung (Veröffentlichung I), einem vollständig gekoppelten emissionsgetriebenen Erdsystemmodell (Veröffentlichung II) und einem hoch aufgelösten Modell der Ozeanzirkulation und Biogeochemie (Veröffentlichung III).

In dieser Arbeit werden drei Schlüsselfaktoren identifiziert, die die OAE-Effizienz in Modellsimulationen beeinflussen: die Menge der hinzugefügten Alkalinität, Klima-Rückkopplungen und die Modellauflösung. Unter diesen Faktoren ist die Zugabe von Alkalinität der wichtigste Faktor, der eine starke lineare Beziehung mit der ozeanischen $CO_2$-Aufnahme und der atmosphärischen $CO_2$-Reduktion nach 60-70 Jahren OAE-Anwendung aufweist. Diese Beziehung ist über alle Emissionsszenarien hinweg konsistent und wird durch bisherige Literatur unterstützt. Im Gegensatz zu diesem linearen Zusammenhang, nach mehreren Jahrzehnten der Alkalinitätszugabe, treten die größten Unterschiede und die größte Unsicherheit bei der OAE-Effizienz jedoch im ersten Jahrzehnt des Einsatzes (2030er Jahre) auf. In diesem Zeitraum übertrifft die Effizienz der OAE in Subduktionsregionen die globale OAE in reinen Ozeanmodellen und erreicht Werte von 0,60 (Veröffentlichung I) und 0,70 (Veröffentlichung III). Im Gegensatz dazu ergibt die ESM-basierte regionale OAE-Simulation (Publikation II) eine niedrigere Effizienz von 0,38, mit einer Unsicherheit von ±55%, die auf klimabedingte Schwankungen zurückgeführt wird. Da sich die Alkalinitätssignale im Laufe der Zeit ausbreiten, nehmen die regionalen

Unterschiede ab, was die Unsicherheit verringert und bis 2090 zu einer Konvergenz der Effizienzschätzungen zwischen globalen und regionalen Anwendungen führt, mit Werten von 0,85 (global und regional, Veröffentlichung I), 0,72 (global und regional, Veröffentlichung II) und 0,85-0,90 (global-regional; Veröffentlichung III). Die anhaltend niedrigere Effizienz in Publikation II unterstreicht die Rolle der Klima-Rückkopplungen als zweitwichtigster Einflussfaktor für die OAE-Effizienz. Die Modellauflösung hat nur einen Einfluss dritter Ordnung. Tatsächlich wird in Publikation III die höchste regionale OAE-Effizienz in den 2030er Jahren festgestellt, was möglicherweise auf eine Kombination von unterschiedlicher Dynamik in der hochaufgelösten Konfiguration und Unterschiede im Hintergrundzustand der Karbonatchemie in den verschiedenen Modellkonfigurationen zurückzuführen ist und zu weiteren Unsicherheiten in der frühen Phase beiträgt.

Darüber hinaus zeigen sowohl hoch- als auch niedrigauflösende reine Ozeanmodelle eine effiziente Kohlenstoffspeicherung in der Tiefsee, wobei hochauflösende globale und regionale Simulationen während des gesamten Simulationszeitraums eine relativ größere Menge an Kohlenstoff unterhalb von 1 km speichern als ihre niedrigauflösenden Gegenstücke. Darüber hinaus zeigen diese Modelle, dass Subduktionsregionen fast doppelt so viel Kohlenstoff in Tiefen unterhalb von 1 km transportieren wie globale OAE in ihren jeweiligen Ansätzen, obwohl ihre kleinere Oberfläche zu einem geringeren Anstieg des gesamten gelösten anorganischen Kohlenstoffs (DIC) führt. Die regionalen OAE unter Verwendung des ESM-Modells (Publikation II) zeigen dagegen keinen derart effizienten Tiefentransport, was vor allem auf interne Klimavariabilität und Rückkopplungen zurückzuführen ist. Die reinen Ozean-Simulationen zeigen auch, dass Subduktionsregionen für OAE geeignet sein können, aber starke saisonale Schwankungen in der überschüssigen Kohlenstoffaufnahme, der Oberflächenalkalinität und der DIC-Akkumulation aufweisen, die durch die saisonale Abhängigkeit von der Tiefe der Mischungsschicht (MLD) bedingt sind. Eine geringere MLD im Sommer hält überschüssige Oberflächenalkalinität zurück und ermöglicht es CO2-armen Gewässern, mit der Atmosphäre ins Gleichgewicht zu kommen und die CO2-Aufnahme und DIC-Akkumulation zu verbessern, während eine tiefere MLD im Winter die Durchmischung erhöht, was zu Alkalinitätsverlusten und geringerer $CO_2$-Aufnahme führt. Um die OAE-Effizienz bei regionalen Einsätzen zu optimieren, müssen künftige Strategien daher diese jahreszeitlichen Dynamiken berücksichtigen.

Auf der Grundlage der Ergebnisse dieser Arbeit sollte die Modellauswahl auf die spezifischen Ziele der OAE-Forschungsprojekte abgestimmt werden: Biogeochemische Modelle mit geringer Auflösung erfassen großräumige ozeanische Prozesse, hochauflösende Modelle können nützlich sein, um kleinräumige Dynamiken zu erfassen, die potenziell für den Kohlenstofftransport in die Tiefe wichtig sein können, und Erdsystemmodelle umfassen Rückkopplungen des Erdsystems, die für das Verständnis der Auswirkungen des CDR-Einsatzes auf die Klimatrajektorie, besonders in Bezug auf die Klimaziele, entscheidend sind. Da alle Modellkonfigurationen in dieser Studie in der Anfangsphase der OAE-Anwendung die größten Unsicherheiten aufwiesen, sollten sich künftige Modellierungsstudien auf das Verständnis der Unsicherheiten der OAE-Effizienz in der frühen Phase von regionalen Anwendungen konzentrieren, die für die Entwicklung eines robusten MRV-Konzeptes entscheidend sind.

# ACKNOWLEDGEMENTS

It is the 4th of March 2025, just a day before I print my thesis. As I look back, these past few years of PhD have been the most challenging yet rewarding years of my life until now. And I am deeply grateful to everyone who has been part of this journey, supporting and motivating me until the very end.

The biggest thank you to Prof. Judith Hauck for her constant support and guidance and for being the amazing supervisor any PhD student could wish for. A very big thank you to Dr. Cara Nissen for all the valuable discussions throughout my PhD and specifically for supporting me even from a different timezone. I have learnt a lot from you. Thank you to the members of my thesis advisory committee: Prof. Maarten Boersma and Dr. Peter Köhler for your valuable inputs on my work. I would also like to thank Dr. Lester Kwiatkowski and Prof. Andreas Oschlies for agreeing to review my thesis.

A special thank you to my office mate Dr. Miriam Seifert and my former office mate Dr. Onur Karakus. Settling down in Bremerhaven during my first year here was only possible because of your help. It is/was really fun to share the office with you. Thank you to our entire Biogeochemical Modeling working group for many fun activities and very helpful scientific discussions: Christopher Danek, Özgür Gürses, Frauke Bunsen, Christoph Völker, Ying Ye, Laurent Oziel, Maya Dalby, Kathrin Wuttig and, Rony Peter. All the best to our new generation of PhD students: Sina Müller, Hannah Haines, Simone Le Chevère, and Ombeline Jouet. A big thank you to the entire Marine Biogeosciences section at AWI and specially to Bettina Singh for always helping me with my visa issues. Thank you to the graduate school POLMAR for being a great help to all the PhD students at AWI.

Then I would like to thank all my professors and friends from the Atmospheric Science Master program who motivated me to apply for this PhD position during the depressing covid years. The inspiring environment that you all had provided me during that time has proved to be very helpful over all these years.

Finally, a very heartfelt thanks to my family. To Aai and Baba, no words can express how grateful I am for the unwavering support and motivation you have given me throughout my life. You both mean a lot to me. To my brother Anuj for always being by my side. And last but not the least, a special thanks to you, Pranav, for being there during a crucial phase of this PhD and providing much-needed strength.

Writing even a page of this thesis would not have been possible without the support of all the people mentioned above. Eternally grateful!

CONTENTS

---

# 1

# PREFACE

## PREFACE

The Earth's climate has evolved over billions of years, with natural archives such as ice cores, tree rings, and sediment cores providing a window into its history. For instance, ice cores from polar regions that contain trapped air bubbles, reveal past atmospheric compositions and temperatures over 800,000 years (Lüthi et al., 2008; Petit et al., 1999). Similarly, sediment cores reveal chemical signatures that reflect ancient climate states, demonstrating the Earth's oscillation between glacial and interglacial phases over geological timescales. These changes are linked to shifts in radiative balance, the equilibrium between incoming solar radiation and outgoing longwave radiation reflected and re-emitted by the Earth's surface and atmosphere (Hartmann et al., 1986).

A variety of natural processes influence the Earth's radiative balance. Among the most prominent are the Milankovitch cycles, which describe predictable variations in Earth's orbital eccentricity, axial tilt, and precession (Berger, 1988; Lisiecki, 2010). These cycles alter the distribution and intensity of solar energy received by the planet, and thus drive long-term climate oscillations. Volcanic activity and, most critically, the composition of the Earth's atmosphere also modulate the radiative balance, amplifying or mitigating climatic changes over time (Mitchell, 1989).

The influence of atmospheric composition on radiative balance forms the basis of the greenhouse effect, first conceptualized by Fourier in 1827. Certain greenhouse gases (GHGs), including water vapor, carbon dioxide ($CO_2$), methane ($CH_4$), and nitrous oxide ($N_2O$), absorb and re-emit outgoing infrared radiation, trapping heat within the atmosphere (Mitchell, 1989). This natural effect maintains Earth's surface temperature at a life-supporting $+18°C$, compared to a frigid $-16°C$ in its absence (Pierrehumbert, 2011).

Among GHGs, water vapor is the most abundant and acts as a feedback amplifier. Its concentration increases with rising temperatures, enhancing its heat-trapping ability, but its short atmospheric residence time (8–10 days) limits its long-term impact (Held and Soden, 2000). By contrast, $CO_2$, although a minor atmospheric constituent (0.04% by volume), plays a pivotal role due to its efficiency in absorbing infrared radiation and its long residence time, ranging from decades to millennia. This unique combination allows $CO_2$ to act as a thermostat for the Earth's climate (Lacis et al., 2010). In 1897, Arrhenius quantified this relationship, predicting that a doubling of atmospheric $CO_2$ could lead to a 4°C temperature increase (Arrhenius and Holden, 1897) – a remarkably accurate projection aligned with current estimates of 3–4.5°C (Lee et al., 2021).

Since the Industrial Revolution, human activities, such as burning of fossil fuels, and land-use change for agriculture, industrialization and urbanization have significantly elevated atmospheric $CO_2$ levels, disrupting Earth's radiative balance and driving the global temperature increase. These changes have triggered severe impacts, including polar ice melting, rising sea levels, and an increase in extreme weather events (Intergovernmental Panel on Climate Change IPCC, 2023). To mitigate these effects, global efforts aim to limit temperature rise to well below 2°C, preferably 1.5°C, above preindustrial levels by the end of the 21st century (UNFCCC, 2015). Achieving this target demands not only phasing out fossil fuels usage to reduce anthropogenic emissions, but also active removal of $CO_2$ through human interventions (Ho et al., 2023). This imperative has spurred the development of Carbon Dioxide Removal (CDR) strategies, designed to artificially extract atmospheric $CO_2$ and store it in geological, terrestrial or ocean carbon reservoirs or in products (IPCC, 2018).

The ocean, covering 70% of Earth's surface, is an important natural carbon sink, absorbing 25–30% of anthropogenic emissions (Friedlingstein et al., 2024). Leveraging this capacity of the ocean, Ocean Alkalinity Enhancement (OAE) is a marine-based CDR approach that aims to enhance the ocean's capacity to sequester $CO_2$ by increasing its alkalinity (Kheshgi, 1995). The goal of OAE is to accelerate the natural weathering process through which the ocean takes up carbon on a geological timescale. This thesis examines the efficiency of OAE in the intermediate, deep and bottom water formation regions of the Southern Ocean and North Atlantic, which serve as critical bottlenecks that transfer carbon from the surface to the deep ocean and result in its sequestration away from the atmosphere on centennial to millennial timescales. By employing coarse- and high-resolution ocean-only models alongside a fully coupled emission-driven Earth System Model, this thesis evaluates the potential of OAE to sequester atmospheric $CO_2$ over the 21st century under high and low emission pathways.

# 2

# GENERAL INTRODUCTION

## GENERAL INTRODUCTION

## 2.1 GLOBAL CARBON CYCLE

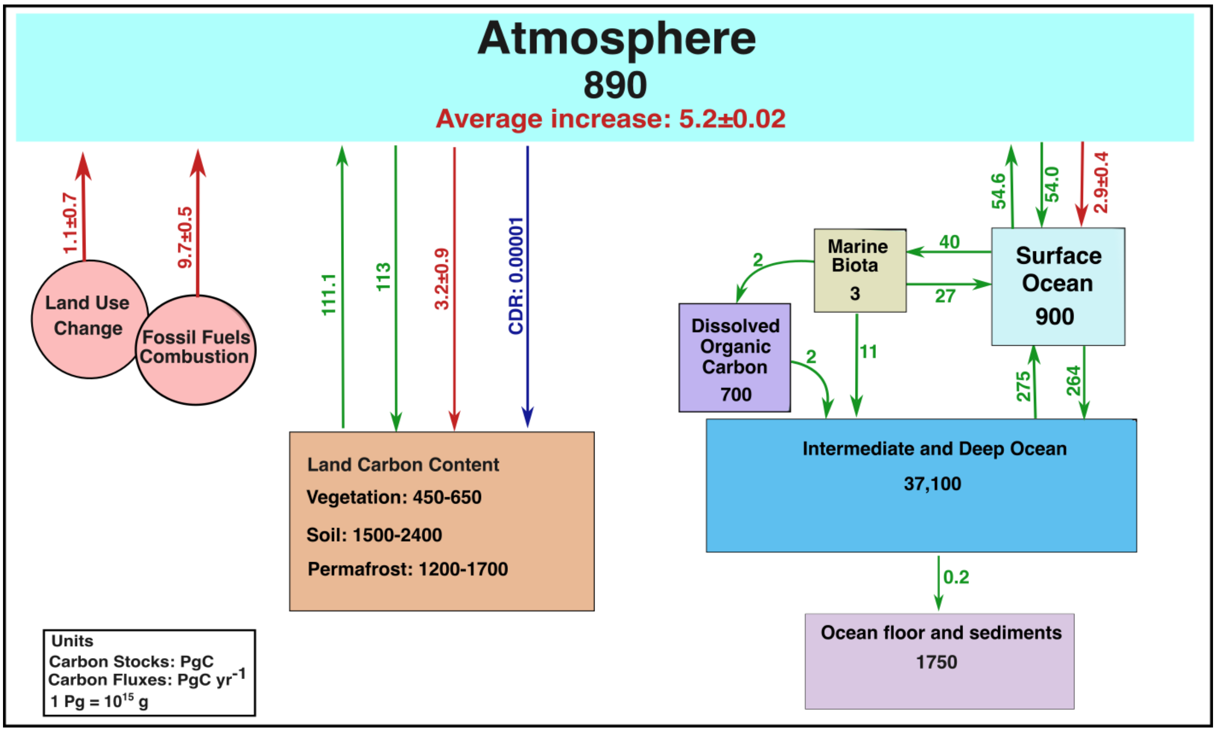

FIGURE 2.1: Schematic representation of carbon stocks and fluxes among major carbon reservoirs. Black numbers indicate carbon stocks within each reservoir, while green numbers and arrows represent natural carbon fluxes, based on Canadell et al. (2021). Anthropogenic carbon fluxes, averaged over the period 2014-2023, are shown using red arrows and numbers, uncertainty estimates are only given for the anthropogenic fluxes. The blue arrow and number denote carbon dioxide removal (CDR) for the year 2023. The anthropogenic fluxes as well as the CDR flux are based on Friedlingstein et al. (2024).

The atmosphere, land, and ocean carbon reservoirs are fundamental constituents of the Earth's carbon cycle. They undergo complex interactions via carbon exchanges that regulate global climate. These interactions happen over different timescales that exchange carbon through solubility of $CO_2$ in seawater, photosynthesis, respiration, chemical and mechanical weathering, and other geological processes (Falkowski et al., 2000; Archer, 2010; Figure 2.1). Understanding the carbon reservoirs and their interactions is critical to understand both natural climate regulation and the impacts of anthropogenic activities on the Earth's climate.

### 2.1.1 *Atmospheric Carbon*

The atmospheric carbon reservoir, primarily composed of $CO_2$ (∼870 PgC) with smaller contributions from $CH_4$ , $CO_2$ , and chlorofluorocarbons, plays a crucial role in regulating global temperatures (Canadell et al., 2021). It actively interacts with terrestrial, soil, and ocean carbon reservoirs and is highly sensitive to changes in the land and ocean carbon sources and sinks (Figure 2.1).

### 2.1.2 *Land Carbon*

The land carbon reservoir can be divided into land vegetation and soil carbon (Figure 2.1). Vegetation fixes carbon through photosynthesis, which converts $CO_2$ into organic matter. This carbon is released back to the atmosphere by heterotrophic and autotrophic respiration (Cao and Woodward, 1998; Post et al., 1982). Approximately 450-650 PgC is stored in the global vegetation biomass, with forest ecosystems representing 70% of all plant carbon (DeGryze et al., 2004; Saatchi et al., 2011; Bradshaw and Warkentin, 2015; Pan et al., 2011). Globally, the soil organic carbon pool constitutes approximately two thirds of the carbon in the terrestrial ecosystem. The soil carbon reservoir amounts to roughly 1500-1700 PgC but with considerable variation (Amundson, 2001; Guo and Gifford, 2002). The soil carbon pool is primarily dependent on the type of vegetation and its productivity at a particular site, and losses are dependent on heterotopic respiration which is modified by climatic conditions such as temperature and moisture (Jackson et al., 2017; Scharlemann et al., 2014). Since soil carbon is physically and chemically inert and not easily oxidized, it has a residence time of about few decades to centuries, making it an important carbon sink (Davidson and Janssens, 2006; Post et al., 1982). Wetlands, peatlands, and permafrost soils represent soil carbon reservoirs with high carbon densities and mean residence times approaching $\sim$1200 years (Davidson and Janssens, 2006).

Since the Industrial Revolution, land-use changes driven by agriculture, industrialization, and urbanization have significantly contributed to the release of carbon from vegetation and soils into the atmosphere (IPCC, 2019). Land-use change is recognized as the second largest source of anthropogenic $CO_2$ emissions, with recent estimates indicating an average release of approximately 1.1 PgC per year from 2014 to 2023 (Friedlingstein et al., 2024). While such activities have led to carbon loss, increased atmospheric $CO_2$ concentrations have simultaneously led to a $CO_2$ fertilization effect, promoting greater carbon uptake by vegetation (Adloff et al., 2018). This dynamic has led to the land carbon sink sequestering approximately 3.2 PgC annually over the past decade, accounting for about 30% of total anthropogenic $CO_2$ emissions (Friedlingstein et al., 2024). However, this uptake exhibits high interannual variability influenced by climatic and ecological factors (Bloom et al., 2016). Despite its current role as a crucial carbon sink, there is growing concern that the efficiency of land systems in sequestering carbon could decline rapidly under ongoing deforestation and biomass loss. Such a shift would have profound implications for climate mitigation efforts, emphasizing the need for sustainable land management and conservation strategies (Nabuurs et al., 2023).

### 2.1.3 *Ocean Carbon*

The ocean is the Earth's largest active carbon reservoir, which has absorbed about 25-30% of anthropogenic $CO_2$ emissions (Gruber et al., 2019; Iudicone et al., 2016; Khatiwala et al., 2009; Müller et al., 2023). This is caused by the ability of $CO_2$ to react with water and undergo the hydrolysis reaction to form carbonate and bicarbonate ions that are not directly exchangeable with the atmosphere (Zeebe and Wolf-Gladrow, 2001). The ocean reservoir is typically divided into the surface ocean and the deep ocean (Figure 2.1). The surface ocean, which extends to a depth of around 200 meters, contains approximately 900 PgC (Canadell et al., 2021). This carbon is actively cycled between the ocean surface and the atmosphere through gas exchange and is influenced by biological activities, including photosynthesis and respiration by marine organisms (Volk and Hoffert, 1985). Carbon introduced to the surface ocean through these processes is transported to the deep ocean through the overturning circulation and the sinking of organic and inorganic particles (Feely et al., 2001) (see section 2.2 for further details on ocean carbon pumps).

The deep ocean holds about 37,200 ± 200 PgC and this carbon is isolated from the atmosphere on the timescale of the ocean overturning circulation, i.e., up to 1000 years (Keppler et al., 2023). The significance of this deep ocean carbon storage is evident from the fact that the combined carbon content of the atmosphere, terrestrial biosphere, and surface ocean amounts to less than 10% of that stored in the ocean interior (Sigman and Boyle, 2000). On a glacial-interglacial timescale, the ocean has modulated atmospheric $CO_2$ concentrations through processes such as temperature-dependent $CO_2$ solubility, biological and carbonate pumps, and shifts in ocean circulation and stratification. Any changes in the atmospheric $CO_2$ concentrations are dampened by interaction with the ocean's huge $CO_2$ reservoir (Sigman and Boyle, 2000; Toggweiler, 1999). Thus, this carbon reservoir acts as a stabilizing mechanism for the Earth's climate.

## 2.2 PROCESSES IN THE OCEAN CARBON CYCLE

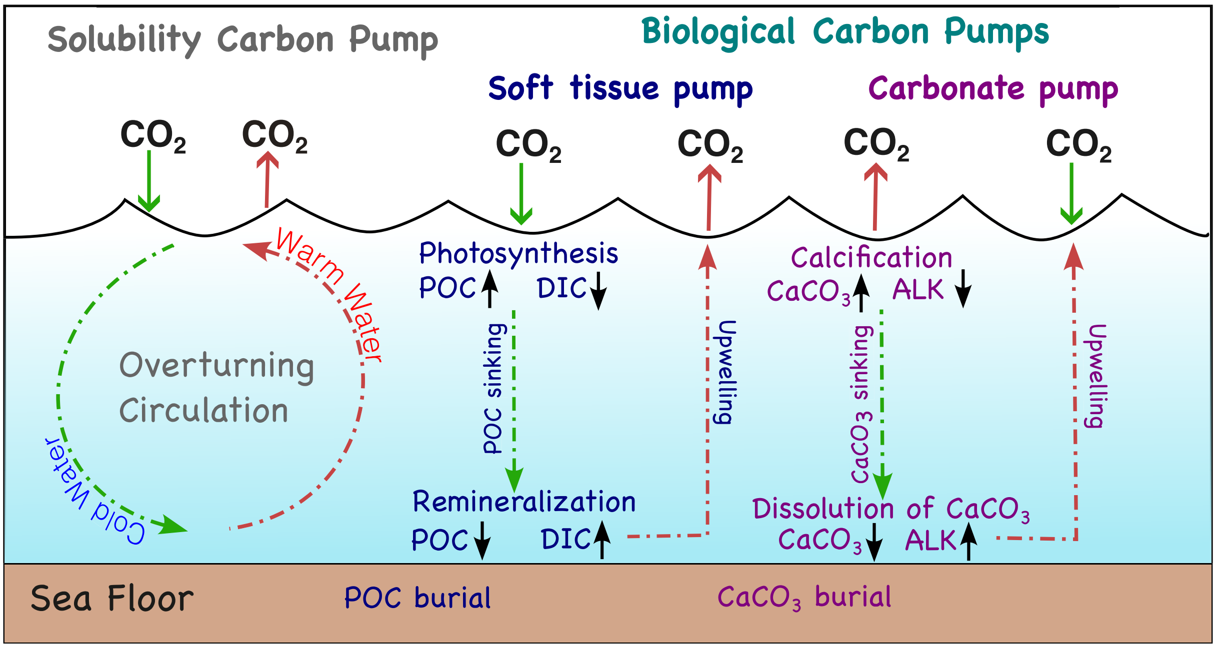

FIGURE 2.2: Schematic represents the solubility and biological carbon pumps through which carbon is cycled between the surface and the deep ocean. POC: particulate organic carbon; DIC: dissolved inorganic carbon; ALK: alkalinity; $CaCO_3$: calcium carbonate; $CO_2$: carbon dioxide.

The ocean carbon cycle is driven by three interconnected pumps: the solubility pump, the biological carbon pumps that consist of the soft tissue pump and the carbonate pump (Volk and Hoffert, 1985; Figure 2.2). The solubility pump facilitates the uptake of atmospheric $CO_2$

through gas exchange, driven by temperature-dependent solubility, and transports carbon to the deep ocean via the overturning circulation (Sarmiento, 2013). The soft tissue pump involves $CO_2$ fixation by phytoplankton during photosynthesis and its transformation into particulate organic carbon, of which a fraction sinks to the deep ocean and an even smaller fraction is typically sequestered at the sea floor (Boyd et al., 2019). The carbonate pump involves the formation of calcium carbonate ($CaCO_3$) by marine calcifying organisms with their sinking shells sequestering particulate inorganic carbon in sediments (Berelson et al., 2007). Together, these pumps regulate oceanic carbon storage and exchange with the atmosphere, playing a pivotal role in controlling Earth's climate (Volk and Hoffert, 1985; Figure 2.2).

### 2.2.1 *Solubility Carbon Pump*

Unlike most atmospheric gases, $CO_2$ interacts with seawater through both physical dissolution and chemical reaction, creating a complex exchange system between the ocean and atmosphere (Dickson and Millero, 1987). Initially, $CO_2$ dissolves into seawater in a process governed by Henry's law:

$$CO_{2(\mathrm{aq})} = K_{\mathrm{h}} \cdot pCO_{2(\mathrm{atm})} \tag{2.1}$$

Here, $CO_{2(aq)}$ is the concentration of $CO_2$ in seawater, $pCO_2$atm is partial pressure of $CO_2$ in the atmosphere, and $K_h$ is Henry's constant. The law thus states that as $CO_2$ solubility increases, the concentration of $CO_2$ in seawater increases for a given $pCO_2$ at the ocean surface (DeVries, 2022b). The solubility of $CO_2$ is temperature and salinity dependent. Temperature plays a dominant role, with cold polar waters exhibiting solubility more than twice that of warm equatorial waters (DeVries, 2022a; Khatiwala et al., 2019; Takahashi et al., 2002). The effect of salinity is comparatively minor due to its limited variation across the ocean (DeVries, 2022b).

The exchange of $CO_2$ between the atmosphere and ocean also depends on the gradient between atmospheric and surface ocean $pCO_2$. Uptake occurs when atmospheric $pCO_2$ is higher, while outgassing happens when the reverse is true (Sigman and Boyle, 2000). This exchange is further influenced by wind-driven turbulence, which enhances air-sea gas transfer and vertical mixing, allowing surface waters enriched in $CO_2$ to mix with deeper layers (Wanninkhof, 1992; Wanninkhof, 2014; Ho et al., 2006). These processes, in turn, also interact with sea surface temperature (SST), as wind-driven cooling alters $CO_2$ solubility, creating a feedback loop that impacts the overall air-sea $CO_2$ exchange (Takahashi et al., 2002; Wanninkhof et al., 2013).

Despite the physical dissolution process, the ocean's enormous carbon reservoir, estimated at approximately 37,200 ± 200 PgC, cannot be explained by solubility alone, which accounts for only ~550 PgC (Keppler et al., 2023; Emerson and Hedges, 2008). This discrepancy arises because dissolved $CO_2$ undergoes chemical reactions in seawater (Dickson and Millero, 1987). It forms carbonic acid ($H_2CO_3$), a weak and unstable acid that quickly dissociates into bicarbonate ($HCO_3{}^-$), carbonate ($CO_3{}^{2-}$), and hydrogen ($H^+$) ions:

$$CO_2 + H_2O \rightleftharpoons H_2CO_3 \rightleftharpoons HCO_3{}^- + H^+ \rightleftharpoons CO_3{}^{2-} + 2\,H^+ \tag{2.2}$$

This reaction system not only governs ocean $p$H, but also defines dissolved inorganic carbon (DIC) as the sum of dissolved $CO_2$, $HCO_3{}^-$, and $CO_3{}^{2-}$ ions (Zeebe and Wolf-Gladrow, 2001; Sarmiento, 2013). At an average oceanic $p$H of 8.1, about 90% of DIC exists as $HCO_3{}^-$, less than 10% as $CO_3{}^{2-}$, and roughly 1% as dissolved $CO_2$ (Zeebe and Wolf-Gladrow, 2001). Critically, only the dissolved $CO_2$ component can freely exchange with the atmosphere, while $HCO_3{}^-$ and $CO_3{}^{2-}$ ions do not, bestowing the oceans with its large carbon reservoir (Emerson and Hedges, 2008).

### 2.2.1.1 *Role of Alkalinity in the ocean carbon cycle*

Another important quantity that aids in regulating the ocean's ability to absorb and store carbon is the ocean alkalinity. Alkalinity is defined as the excess of bases over acids. It is also referred to as the buffering capacity of seawater as it neutralizes the carbonic acid formed when $CO_2$ is dissolved in the ocean (Wolf-Gladrow et al., 2007).

$$\begin{aligned}\text{Total Alkalinity} = {} & [HCO_3{}^-] + 2[CO_3{}^{2-}] + [B(OH)_4{}^-] + [OH^-] \\ & + [HPO_4{}^{2-}] + 2[PO_4{}^{3-}] + [H_3SiO_4{}^-] + [NH_3] + [HS^-] \\ & - [H^+]_F - [HSO_4{}^-] - [H_3PO_4]\end{aligned} \tag{2.3}$$

The primary input of alkalinity to the oceans is through the river inputs and small contribution from groundwater and hydrothermal fluxes (Middelburg et al., 2020). Accordingly, the total input of alkalinity amounts to about ~66 Tmol $yr^{-1}$, with an estimated residence time of around 120k years (Hartmann et al., 2014; Middelburg et al., 2020). The primary loss of alkalinity is through permanent burial of $CaCO_3$ (formed by marine organisms; see section 2.2.3) in the ocean sediments, which is estimated to be about ~60 Tmol $yr^{-1}$ (Middelburg et al., 2020).

As alkalinity is directly linked to the concentrations of carbonate, bicarbonate and borate ions in seawater, it plays a crucial role in regulating the carbonate equilibria in the ocean (Zeebe and Wolf-Gladrow, 2001; Equation 2.3). At a constant DIC, higher alkalinity indicates that the equilibria are shifted towards bicarbonate and carbonate ions, reducing the concentration of dissolved $CO_2$ and thus lowering $p$$CO_2$ at the ocean surface. This can lead to a higher influx of $CO_2$ from the atmosphere into the ocean (or reduced outgassing). Conversely, lower alkalinity results in a higher fraction of DIC as dissolved $CO_2$, increasing surface ocean $p$$CO_2$ and thus can reduce the oceanic $CO_2$ uptake (or increase outgassing, Wolf-Gladrow et al., 2007; Emerson and Hedges, 2008).

Alkalinity can also be understood as a buffer capacity, which is the ability to resist changes in $p$H when additional $CO_2$ dissolves in seawater (Middelburg et al., 2020; Jiang et al., 2019). In principle, oceanic $p$H should decrease when $CO_2$ reacts with seawater as it releases excess $H^+$ ions (Equation 2.2). However, the buffering capacity of the ocean neutralizes the excess $H^+$ ions by reaction with carbonate ions to form additional bicarbonate ions (Dickson, 1981). This process reduces the impact of anthropogenic $CO_2$ uptake on ocean $p$H. The strength of this buffering capacity can also be quantified by the Revelle factor that is defined as the ratio of the relative changes in oceanic $pCO_2$ to the relative changes in DIC (Egleston et al., 2010; Equation 2.4).

$$\text{Revelle Factor} = \frac{\partial \ln pCO_2}{\partial \ln DIC} \tag{2.4}$$

A high alkalinity is associated with a low Revelle factor, meaning that the ocean can absorb more atmospheric $CO_2$ per increase in the surface ocean $pCO_2$. In contrast, lower alkalinity results in a weaker buffer capacity, causing a more pronounced increase in $pCO_2$ and larger $p$H changes for the same amount of $CO_2$ uptake (Sarmiento, 2013). The Revelle factor is also dependent on the changes in partitioning of the carbonate species in DIC due to anthropogenic $CO_2$ uptake. As the oceans continue to take up anthropogenic carbon, the concentration of dissolved $CO_2$ increases (Zeebe and Wolf-Gladrow, 2001). As a result, the Revelle factor increases or the buffering capacity of the ocean decreases. This acts as a positive feedback that can limit the increase of the ocean $CO_2$ sink in the future (Wallace, 2001).

### 2.2.2 *Soft Tissue Pump*

The soft tissue pump plays a crucial role in the natural carbon cycle by converting dissolved $CO_2$ into organic carbon through photosynthesis by phytoplankton in the euphotic zone (Boyd et al., 2019; Jahnke, 1996; Passow and Carlson, 2012). This process not only creates a surface $pCO_2$ deficit that may drive $CO_2$ uptake from the atmosphere, but also forms the foundation of marine food webs by supplying energy and organic matter to higher trophic levels (Boyd et al., 2019). Remarkably, phytoplankton, which constitute just 0.2% of global primary producer biomass, contribute to nearly 50% of global net primary production (Falkowski et al., 1998).

Once produced, organic carbon undergoes transformation and redistribution within the ocean. Some of it becomes dissolved organic carbon or is respired back into $CO_2$, while a portion forms particulate organic carbon (POC; Marinov et al., 2008). POC aggregates into particles known as "marine snow," which sink into the deep ocean due to gravitational settling. The sinking speed varies from tens to hundreds of meters per day, with large aggregates like zooplankton fecal pellets reaching speeds of up to 1 km per day (Hayes et al., 2021). The sinking process transfers carbon to the ocean interior termed as export production (Dunne et al., 2007; Nowicki et al., 2022). Approximately 5–13 PgC $yr^{-1}$ sinks through top $\sim$100 m (Gehlen et al., 2006; Giering et al., 2020; Henson et al., 2011), of which about 5–6 PgC $yr^{-1}$ is remineralized at intermediate depths (Feely et al., 2004; Palevsky and Doney, 2018), and only 0.02–0.2 PgC $yr^{-1}$ is sequestered in marine sediments for geological timescales (Boyd and Trull, 2007; Carter et al., 2021; Siegel et al., 2023). The rest is recycled within the euphotic zone through microbial degradation, where organic carbon is converted back into inorganic forms available for reuse (Cartapanis et al., 2018; Guidi et al., 2015).

The soft tissue pump accounts for 70% of the dissolved inorganic carbon (DIC) gradient between the surface and deep ocean, vastly outweighing the contributions of the solubility and carbonate pumps (10% and 20%, respectively; DeVries, 2022b). During the last glacial maximum, when atmospheric $CO_2$ levels were as low as 180–200 ppm, the soft tissue pump was particularly efficient, driven by enhanced nutrient availability, iron inputs, and altered circulation patterns, which contributed to lowering of atmospheric $CO_2$ levels (Morée et al., 2021; Sigman et al., 2010; Brovkin et al., 2007; Lambert et al., 2015; Martin, 1990). Furthermore, without its carbon sequestration capabilities, preindustrial $CO_2$ levels might have been $\sim$200 ppm higher than observed (Maier-Reimer et al., 1996), underscoring its importance across glacial, interglacial, and preindustrial periods in shaping Earth's climate system.

### 2.2.3 *Carbonate Pump*

The carbonate pump, also termed as the hard tissue component of the biological carbon pump, is driven by the formation, sinking, and dissolution of calcium carbonate ($CaCO_3$). It facilitates the sequestration of particulate inorganic carbon (PIC) and is regulated by calcifying organisms such as coccolithophores and calcifying zooplankton (pteropods and foraminifera) that produce $CaCO_3$ shells (Buitenhuis et al., 2019; Knecht et al., 2023; Ridgwell and Zeebe, 2005). During calcification, bicarbonate and calcium ions are consumed, shifting carbonate equilibria toward dissolved $CO_2$. This process increases surface ocean $pCO_2$ and may reduce $CO_2$ uptake or strengthen $CO_2$ outgassing depending on the $pCO_2$ gradient between the ocean surface and atmosphere. This is because the process reduces alkalinity and DIC in a ration of 2:1, which increases $pCO_2$ and thus it is also termed as the "carbonate counter pump" (Feely et al., 2004; Morse and He, 1993).

The precipitation and dissolution of $CaCO_3$ are governed by the saturation state ($\Omega$), determined by the ratio of calcium and carbonate ion concentrations to the solubility constant, which varies with temperature, salinity, and pressure. When $\Omega > 1$, seawater is supersaturated, favoring thermodynamic $CaCO_3$ precipitation; when $\Omega < 1$, dissolution dominates. As sinking $CaCO_3$ particles experience increased pressure and decreased $\Omega$, dissolution intensifies, particularly below the saturation horizon ($\Omega = 1$), where rapid dissolution occurs (Sarmiento, 2013; Zeebe and Wolf-Gladrow, 2001; Zeebe and Westbroek, 2003).

However, most $CaCO_3$ dissolution (60–80%) occurs within the upper 500-1000 m of the ocean, where $\Omega$ is generally $>1$ (Jansen et al., 2002; Milliman et al., 1999). This suggests that dissolution in this depth range is not primarily driven by undersaturation but by other processes, such as dissolution within zooplankton guts or other microenvironments, indicating that factors beyond temperature, salinity, and pressure also play a role (Jansen and Wolf-Gladrow, 2002). Annually, about 0.4 PgC is transported to the deep ocean via $CaCO_3$ sinking, but only a quarter reaches the sediments, where it is buried and sequestered for millions of years (Berelson et al., 2007). This burial is balanced by chemical rock weathering, which replenishes oceanic calcium and carbonate ions while drawing down atmospheric $CO_2$. Consequently, although the carbonate pump can act as a short-term $CO_2$ source, it functions as a net carbon sink for atmospheric $CO_2$ over geological timescales (Feely et al., 2004).

The burial process is dynamically regulated by the calcite compensation feedback, a mechanism ensuring equilibrium between precipitation, dissolution, and burial of $CaCO_3$ in response to shifts in ocean carbonate chemistry and atmospheric $CO_2$ (Cartapanis et al., 2018). This feedback governs the depth of the saturation horizon—and is fundamental to the long-term operation of the carbonate pump and geological carbon sequestration (Ridgwell and Zeebe, 2005). This interplay highlights the pivotal role of alkalinity in sustaining carbon storage over geological timescales.

***Alkalinity: Calcite Compensation Feedback***

The calcite compensation feedback regulates the ocean carbonate chemistry by dynamically modulating the ${CO_3}^{2-}$ concentration, alkalinity, and the depth of the $CaCO_3$ saturation horizon (Broecker, 2008; Elderfield, 2002). Alkalinity plays a central role in this feedback mechanism by governing the saturation horizon so that loss and gain of alkalinity are balanced (Berner and Berner, 2012). For instance, when atmospheric $CO_2$ rises, increased terrestrial weathering, driven by warming, introduces alkalinity to the ocean (White et al., 1999). This enhances $CO_2$ uptake, and shifts the carbonate equilibrium (Emerson and Hedges, 2008). Consequently *p*H is reduced, causing the saturation horizon to shoal. As undersaturated conditions extend vertically in the ocean, $CaCO_3$ sediments dissolve releasing alkalinity that further supports $CO_2$ uptake and reduces atmospheric $CO_2$ levels (Boudreau et al., 2018; Boudreau et al., 2010). The reduced atmospheric $CO_2$ concentration leads to reduced dissolution of $CO_2$ into the ocean. Over time the *p*H is restored due to increased alkalinity and eventually it deepens the saturation horizon (Feely et al., 2004; Zeebe and Westbroek, 2003). This leads to an increase in $CaCO_3$ burial, consumption of alkalinity, and extends the areas where $CaCO_3$ can precipitate which in turn limits oceanic $CO_2$ uptake, again allowing $CO_2$ to accumulate in the atmosphere (Boudreau et al., 2018). As atmospheric $CO_2$ rebounds, warming resumes, accelerating weathering and replenishing ocean alkalinity, restarting the cycle. This feedback results in a dynamic but balanced exchange of carbon between the atmosphere and ocean, crucial for long-term climate stability (Ridgwell and Zeebe, 2005; Ridgwell et al., 2007).

## 2.3 NATURAL CARBON CYCLE: A GEOLOGICAL PERSPECTIVE

Over geological timescales, the carbon cycle is governed by interconnected feedbacks that regulate atmospheric $CO_2$ concentrations. Volcanic outgassing, driven by tectonic activity, serves as the primary source of atmospheric $CO_2$, releasing carbon from the Earth's mantle and lithosphere (Berner, 1990; Sundquist, 1985). In contrast, silicate weathering acts as a major sink, sequestering $CO_2$ on million-year timescales. This dynamic equilibrium, maintained at approximately 0.3 PgC $yr^{-1}$ due to rock weathering and 0.1 PgC $yr^{-1}$ due to volcanic activity, has historically stabilized Earth's carbon balance (Walker et al., 1981). The process begins when atmospheric $CO_2$ dissolved in water react with silicate minerals to produce bicarbonate and silicic acid (Gaillardet et al., 1999; Urey and Korff, 1952). These ions are transported to the oceans via rivers, enhancing alkalinity and promoting marine carbon uptake. In the ocean, bicarbonate ions contribute to the formation of calcium carbonate ($CaCO_3$) minerals by marine organisms, which eventually settle on the seafloor. Over time, these deposits are subducted and transformed into sedimentary rocks, storing carbon until volcanic eruptions release it back into the atmosphere, completing the geological carbon loop (Cusack and Freer, 2008; Keith et al., 1964). This cycle operates as a negative feedback mechanism: elevated temperatures accelerate weathering, enhancing $CO_2$ removal and cooling the planet, while cooler temperatures slow weathering, allowing $CO_2$ accumulation and warming (Walker et al., 1981; West et al., 2005). Although this feedback stabilizes global temperatures over geological timescales, it cannot mitigate the rapid $CO_2$ increases associated with anthropogenic emissions due to its slow pace (Archer et al., 1997).

## 2.4 THE ANTHROPOGENIC PERTURBATION

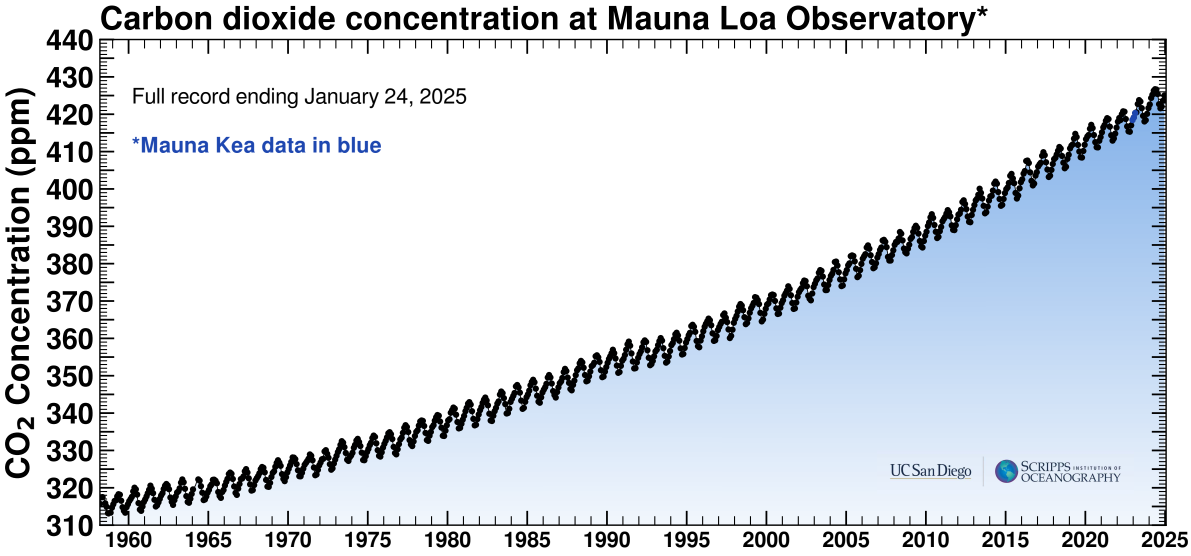

FIGURE 2.3: The Keeling Curve representing the increase in the atmospheric $CO_2$ concentration [ppm] since 1958. Source: `https://keelingcurve.ucsd.edu/`. Last accessed 24/01/25.

Pre-industrial atmospheric $CO_2$ levels remained stable at ~280 ppm, reflecting a balance in natural carbon fluxes (Prentice et al., 2001). This equilibrium began to shift during the Industrial Revolution (1750–1850) majorly due to land use change and increasing reliance on fossil fuels for energy. By 1850, $CO_2$ concentrations had risen modestly to 285 ppm (Rubino et al., 2024). As fossil fuel combustion intensified and deforestation expanded for agriculture and urban development, emissions accelerated, raising $CO_2$ levels to about 315 ppm by 1958 (Figure 2.3; Keeling et al., 2005). The post-1950s period witnessed exponential population growth and an increasing dependence on fossil fuels, driving $CO_2$ emissions to unprecedented levels, with annual growth rates exceeding 2 ppm after the 2000s (Figure 2.3). By 2023, annual emissions reached $\sim$11.1 PgC $yr^{-1}$, with atmospheric concentrations climbing to 419.3 ppm and further to 422.5 ppm in 2024, a 52% increase from pre-industrial levels (Figure 2.3; Friedlingstein et al., 2024). The IPCC warns that unchecked emissions could lead to 3-4.5°C warming above pre-industrial levels by 2100, exacerbating extreme weather events such as hurricanes, heatwaves, droughts, floods, and wildfires. These disruptions threaten ecosystems, economies, and human livelihoods, emphasizing the critical need for effective global climate mitigation strategies (Pörtner et al., 2022).

### 2.4.1 *Anthropogenic Perturbations to the Ocean Carbon Cycle*

The anthropogenic increase in atmospheric $CO_2$ causes the ocean to act as a carbon sink with the absorbtion of 25–30% of global $CO_2$ emissions, which mitigates climate change (Friedlingstein et al., 2024). Approximately 30% of this carbon resides in the upper 200 meters, while 50% is stored above 400 meters (Sabine et al., 2004; Gruber et al., 2019). The transport to deeper layers constitutes a smaller but critical fraction, with 20% of anthropogenic $CO_2$ sequestered below 1000 meters, where it is effectively isolated from the atmosphere for centuries to millennia (Gruber et al., 2019; Khatiwala et al., 2009).

### 2.4.2 *Transfer of Anthropogenic $CO_2$ into the Ocean Interior*

Carbon transport to the deep ocean is driven by physical processes in key regions like the Southern Ocean and North Atlantic, where densification occurs through heat loss, evaporation, and brine rejection during sea-ice formation (Sabine et al., 2004). These processes enable surface waters enriched with anthropogenic $CO_2$ to sink along constant density surfaces, transporting carbon into the ocean interior.

The Southern Ocean accounts for 40% of global ocean anthropogenic carbon uptake via the solubility carbon pump (Khatiwala et al., 2009). Intermediate and mode waters, such as the Antarctic Intermediate Water (AAIW) and Subantarctic Mode Water (SAMW), play a pivotal role in downward transport of anthropogenic carbon thus functioning as a bottleneck. AAIW originates from upwelled Circumpolar Deep Water, while SAMW forms through subduction north of the Subantarctic Front (Hartin et al., 2011). The formation regions of these water masses are characterized by high wind speeds and with continuous replenishment by Circumpolar Deep Water, which has low anthropogenic $CO_2$ content. This enables efficient uptake of anthropogenic $CO_2$ and its subsequent transport to intermediate depth through suppression of the natural $CO_2$ outgassing (Hauck et al., 2023). Together, AAIW and SAMW contribute substantially to the ocean's anthropogenic carbon inventory, with combined concentrations exceeding 50–60 $\mu$mol kg$^{-1}$ (Sloyan et al., 2010; Pardo et al., 2014). Deep and bottom water formation regions, such as the Weddell and Ross Seas, also contribute to anthropogenic $CO_2$ uptake, with the formation of Antarctic Bottom Water (AABW). This water mass stores about 6–12% of anthropogenic $CO_2$ into the abyssal ocean (Pardo et al., 2014). Anthropogenic $CO_2$ concentrations in the Ross Sea increased by 19-25 $\mu$mol kg$^{-1}$ over 2003 to 2014 (Ingrosso et al., 2022; Shadwick et al., 2014). In the Weddell Sea, reported values ranged from 8 to 11 $\mu$mol kg$^{-1}$ in the surface layer, 5 to 8 $\mu$mol kg$^{-1}$ along the shelf, and as low as 1.5 to 2 $\mu$mol kg$^{-1}$ in deeper layers over the period 1992 to 2008 (Hauck et al., 2010). Despite relatively low anthropogenic $CO_2$ concentrations in AABW compared to the intermediate layers, its vast volume, long residence time and widespread distribution across the global ocean basins underscore its importance for carbon storage over millennia (Gruber et al., 2019; Orsi et al., 1999).

In the North Atlantic, the formation of North Atlantic Deep Water (NADW) accounts for approximately 23% of global ocean anthropogenic $CO_2$ storage (Sabine et al., 2004). NADW comprises upper, middle, and lower layers formed primarily through surface heat loss (Dickson and Brown, 1994; Smethie and Fine, 2001). Upper NADW is formed from Labrador Sea Water and Mediterranean Water, while middle NADW originates from Denmark Strait Overflow Water and Greenland Sea Deep Water (Talley and McCartney, 1982; Jeansson et al., 2017). Lower NADW forms through mixing with AABW in the abyssal basin (McCartney et al., 1991). These water masses transported an estimated $\sim 74\ \mu\text{mol kg}^{-1}$ of anthropogenic $CO_2$ southward across the Atlantic between 1981 and 2006 (Pérez et al., 2010). Together, the subduction regions in the Southern Ocean and the North Atlantic act as bottlenecks for carbon storage, exposing deep waters to the surface only on millennial timescales via the overturning circulation, thus playing a crucial role in Earth's climate regulation.

Global warming, driven by rising atmospheric $CO_2$, disrupts these processes. Reduced seawater density due to warming and freshwater inputs from melting ice caps weaken deep-water formation, particularly NADW and AABW, with projections indicating significant declines by the end of the $21^{st}$ century under different emission trajectories (Rahmstorf et al., 2015; Nissen et al., 2022). A weakening overturning circulation reduces the downward transport of surface waters enriched with anthropogenic $CO_2$, diminishing the ocean's capacity to sequester carbon over centennial to millennial timescale (Caesar et al., 2018; Nissen et al., 2022).

### 2.4.3 *Ocean Acidification*

Ocean acidification, a direct consequence of ocean uptake of anthropogenic $CO_2$, has lowered surface $p$H by $\sim$0.1 units since the Industrial Revolution, corresponding to a 30% increase in hydrogen ion concentration (Hoegh-Guldberg et al., 2014). This reduction in $p$H disrupts the carbonate pump by decreasing carbonate ion availability, which impairs calcifying organisms and accelerates the dissolution of carbonate sediments (Caldeira and Wickett, 2005; Orr et al., 2005). Such disruptions jeopardize marine ecosystems and biodiversity, particularly in regions where aragonite and calcite saturation thresholds are being approached or exceeded (Nissen et al., 2024). Furthermore, the irreversible nature of deep ocean acidification on centennial timescales underscores the critical need for reductions in anthropogenic $CO_2$ emissions to mitigate these impacts (Gruber, 2011).

## 2.5 AGREEMENTS TO MITIGATE CLIMATE CHANGE

Climate change, with its far-reaching hazards, has evolved from a scientific concern to a pressing global political and economic challenge (IPCC, 2023). Thus, addressing climate change requires coordinated international efforts under the United Nations Framework Convention on Climate Change (UNFCCC). Two key treaties in this framework are the Kyoto Protocol, adopted in 1997, and the Paris Agreement from 2015 that both aimed to mitigate climate change through commitments of signing countries to reduce GHG emissions (UNFCCC, 2015; UNFCCC, 1998).

The Kyoto Protocol set legally binding targets for developed countries to reduce greenhouse gas emissions by at least 5.2% below 1990 levels during 2008-2012. While some nations, such as those in the European Union and Russia, achieved their targets, others, including Canada, Japan, and Australia, did not. Despite its limitations, the Kyoto Protocol laid the groundwork for future agreements by formalizing commitments to differentiated responsibilities (UNFCCC, 1998).

Adopted in 2015, the Paris Agreement (UNFCCC, 2015) represents a unified global effort to mitigate climate change, by aiming to limit the rise in global temperatures to "well below" 2°C and striving to keep it below 1.5°C above the preindustrial levels by the end of the 21$^{st}$ century. Accordingly, the agreement states that the GHG emissions should peak by 2025 at the latest followed by a 43% decline by 2030. Accounting for this, the agreement obliges all participating countries to submit Nationally Determined Contributions (NDCs) every five years, reflecting their commitments to reduce emissions and enhance climate resilience. Additionally, a global stocktake is conducted every five years to assess collective progress, prompting countries to revise and strengthen their NDCs accordingly. As of 2024, 197 countries have signed the Paris Agreement, and 194 have ratified it. While it has fostered a global commitment to combat climate change, significant gaps remain between current NDCs and the pathways required to limit warming to 1.5°C, necessitating enhanced ambition and action across all sectors (UNFCCC, 2015).

## 2.6 CARBON DIOXIDE REMOVAL (CDR) METHODS

To limit global warming to 2°C—preferably 1.5°C—above pre-industrial levels by the end of the 21$^{st}$ century, immediate and deep emission reduction is indispensable. Alongside these efforts, IPCC scenarios emphasize that large-scale CDR is crucial for stabilizing global temperatures. CDR plays a key role in pathways aimed at limiting warming to 2°C (>67%) or lower, regardless of whether emissions reach near-zero, net-zero, or net-negative levels (Figure 2.4; Babiker et al., 2022). However, it is essential to recognize that CDR is not a substitute for deep emissions reductions. Instead, it serves as a complementary tool in ambitious mitigation strategies. The primary purpose of CDR is to (i) further reduce net $CO_2$ or GHG emissions in the near term, (ii) offset residual emissions from hard-to-transition sectors like industry, aviation, and agriculture to facilitate mid-century net-zero goals, and (iii) enable and sustain net-negative emissions over the long term by removing more $CO_2$ than is emitted annually (Babiker et al., 2022).

The required scale of CDR depends on factors such as peak temperature reached and the pace of emissions reduction (Smith et al., 2024). Estimates suggest that, from 2025, the remaining carbon budget for limiting global warming to 1.5°C and 2°C is approximately 65 and 305 PgC, respectively, with a 50% probability. At the current emission rate, these budgets would be exhausted in about 6 and 27 years, respectively. (Friedlingstein et al., 2024). To stay within this budget, global emissions must decrease by 9.28 PgC annually by 2050, necessitating both rapid emission reductions and increased CDR deployment, particularly between 2030 and 2050 (Gidden et al., 2024). Current CDR processes removed $\sim$0.5 PgC yr$^{-1}$ over 2013-2022, but to meet the 1.5°C target, an additional removal of 0.27-0.79 PgC yr$^{-1}$ is required by 2030, and

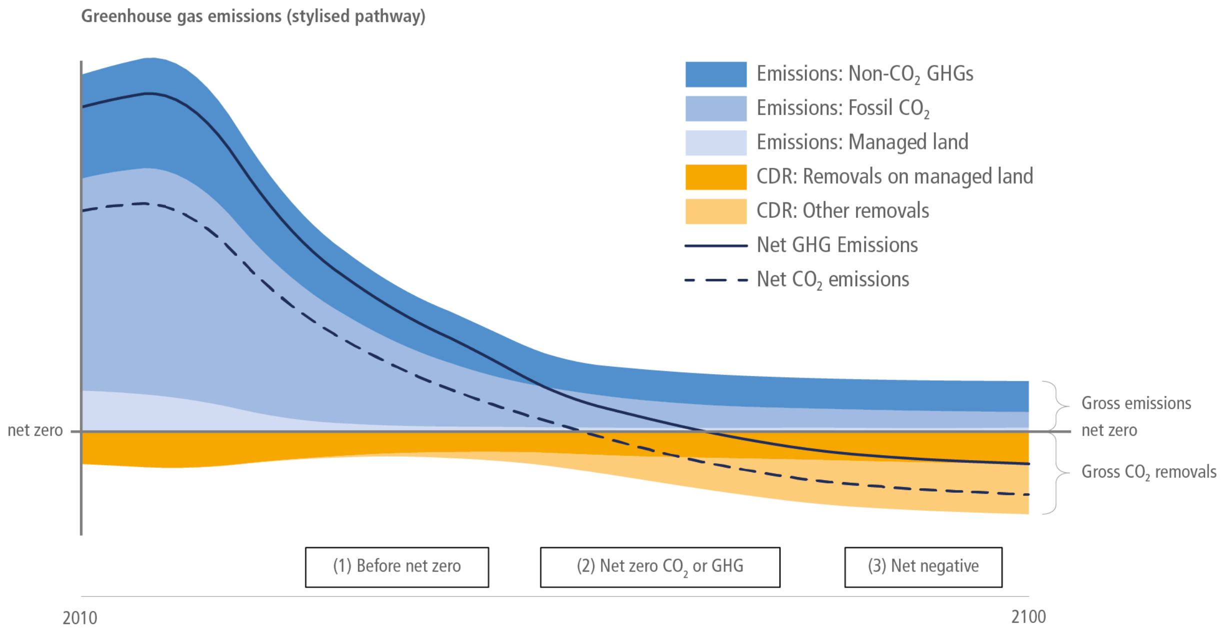

FIGURE 2.4: Representation of carbon dioxide removal (CDR) in a stylized pathway of ambitious climate mitigation. Dark orange indicates $CO_2$ removals from land management, while light orange represents removals from other CDR approaches, including ocean-based methods. Net-zero $CO_2$ is reached before net-zero greenhouse gas (GHG) emissions, and the CDR required to achieve net-zero $CO_2$ is substantially lower than that needed for net-zero GHG. Ocean alkalinity enhancement, if included, falls under "other removals" (light orange). Source: Babiker et al. (2022)

an additional 0.63-2.02 PgC $yr^{-1}$ by 2050 relative to the levels in 2020 (Pongratz et al., 2024; Lamb et al., 2024). However, the NDCs currently fall short, with a proposed additional CDR of 0.014-0.15 PgC $yr^{-1}$ by 2030, underscoring a CDR gap between existing commitments and the levels required under Paris Agreement-consistent scenarios (Lamb et al., 2024).

Currently, the global CDR effort is dominated by conventional methods, with Afforestation and Reforestation (AR) contributing 99.9% of the total (Pongratz et al., 2024; Friedlingstein et al., 2024). Other land-based approaches such as bioenergy with carbon capture and storage (BECCS), direct air capture and storage (DACCS), biochar application, soil carbon sequestration, and enhanced weathering also play a critical role in IPCC climate mitigation scenarios (Minx et al., 2018; Fuss et al., 2018). Meanwhile, novel ocean-based CDR methods, including blue carbon management, artificial upwelling, ocean fertilization, and ocean alkalinity enhancement (OAE), are gaining attention as complementary strategies and are being explored for their carbon sequestration potential, scalability, and possible negative impacts (Babiker et al., 2022; Ho and Bopp, 2024). Given the magnitude of the climate challenge, no single CDR approach is sufficient to meet the required carbon removal targets. A strategically tailored portfolio of CDR methods, optimized for specific geographic and temporal contexts, is essential for maximizing the effectiveness of carbon removal and long-term atmospheric $CO_2$ reduction (Riahi et al., 2022; Hoegh-Guldberg et al., 2018). Governance frameworks for research are advancing to systematically integrate these methods into policies on climate, land use, agriculture, biodiversity, energy, and industry (Schenuit et al., 2024). Along with these, efforts are taken to establish monitoring, reporting, and verification (MRV) protocols for each CDR method as a prerequisite for their implementation (Schulte et al., 2024).

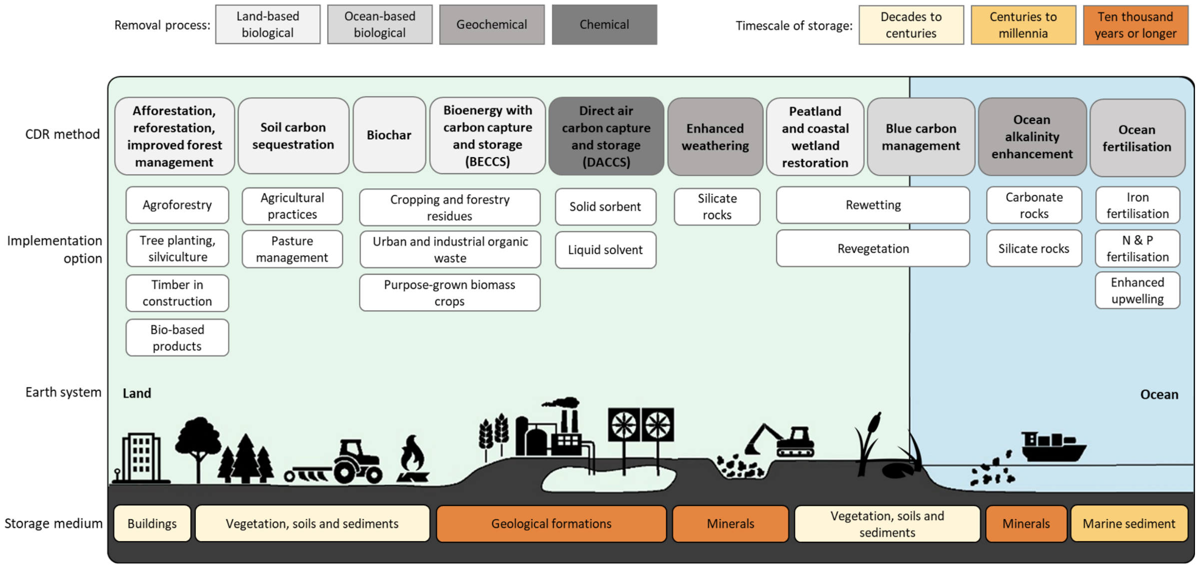

FIGURE 2.5: Representation of various land and ocean-based carbon dioxide removal (CDR) methods indicating their respective implementation option, removal process, $CO_2$ storage medium, and $CO_2$ storage durability. Source: Babiker et al. (2022)

### 2.6.1 *Land-based CDR methods*

Land-based CDR methods offer several approaches for mitigating climate change (Figure 2.5), but all face substantial limitations (Fuss et al., 2018). BECCS, widely used in integrated assessment models, combines bioenergy production with $CO_2$ capture and storage but is hindered by uncertainties in biomass supply, competition for land and water, risks of $CO_2$ leakage, uncertainties associated with geological storage, and groundwater contamination during storage (Creutzig et al., 2015; Holloway and Burnard, 2009; Smith et al., 2016; Smith et al., 2014). Afforestation and Reforestation sequester $CO_2$ through forest growth/re-growth, but require sustained management and are vulnerable to fires, droughts, and pests, reducing permanence of carbon storage (Jackson et al., 2008; Thomas et al., 2010; Locatelli et al., 2015). DACCS effectively removes $CO_2$ from ambient air, but faces high energy requirements for sorbent regeneration and $CO_2$ compression, along with concerns about waste, geological storage, and significant land and resource needs (Coninck and Benson, 2014; Barkakaty et al., 2017; Sanz-Pérez et al., 2016). Biochar enhances soil fertility and stores carbon, though questions about the permanence of storage and its impact on soil microbial communities remain (Lehmann and Joseph, 2015; Sohi et al., 2010; Joseph et al., 2021). Soil carbon sequestration deals with different land management techniques and offers temporary potential, as soil carbon stocks tend to stabilize after decades, with risks of re-emission if management practices are not maintained (Fuss et al., 2018; Lal, 2004). Enhanced land weathering accelerates $CO_2$ removal by applying finely ground silicate or carbonate rocks to soils, providing additional benefits like nutrient release (Moosdorf et al., 2014; Köhler et al., 2010; Schuiling and Krijgsman, 2006), but faces limitations due to high energy costs for material processing, potential heavy metal release, and material demands that may exceed global production capacities (Beerling et al., 2020; Hartmann et al., 2013).

Over recent decades, CDR efforts have predominantly focused on land-based methods. While these methods demonstrate some potential, significant challenges arise from land-use competition and socio-political constraints, complicating their large-scale implementation. Moreover, it remains uncertain whether the combined potential of these methods will suffice to meet net-zero targets by mid-century, as highlighted in the Land Gap Report (Dooley et al., 2023). Studies indicate that no land-based method is currently ready for extensive, long-term deployment (Dooley et al., 2023; Fuss et al., 2018; Minx et al., 2018). Consequently, the ocean-based CDR methods have gained attention in recent years.

### 2.6.2 *Ocean-based CDR methods*

Ocean based CDR involves removing $CO_2$ from the atmosphere and storing it directly in the ocean or retaining it in the marine environment where it would otherwise naturally return to the atmosphere (Figure 2.5; Oschlies et al., 2023). These approaches aim to enhance natural processes or introduce new mechanisms for carbon uptake, leveraging the extensive surface area and dynamic biogeochemical systems of the ocean. Methods include amplifying biological productivity, altering surface ocean carbonate chemistry, or restoring marine ecosystems (Gattuso et al., 2018; Oschlies et al., 2010a; Hartmann et al., 2013). Despite the considerable theoretical potential of ocean-based CDR strategies, significant uncertainties in MRV remain due to the dynamic and vast nature of marine environments (Ho et al., 2023). Additionally, ethical concerns, ecological trade-offs, and regulatory gaps pose challenges to large-scale deployment, underscoring the need for further research and responsible exploration (Lamb et al., 2024; Babiker et al., 2022).

The rationale for ocean-based CDR lies in its potential to sequester vast amounts of carbon on centennial to millennial timescales, thereby mitigating atmospheric $CO_2$ accumulation. However, not all ocean-based methods offer the same durability or effectiveness, and each faces specific limitations. For instance, blue carbon management focuses on conserving and restoring coastal ecosystems, such as mangroves, saltmarshes, and seagrass meadows, which can sequester carbon up to ten times faster than terrestrial forests (Donato et al., 2011; Duarte et al., 2005; Filbee-Dexter and Wernberg, 2020; Krause-Jensen and Duarte, 2016). Despite covering less than 0.2% of the seafloor, these ecosystems account for over half of marine sediment carbon storage (Duarte et al., 2013; Mcleod et al., 2011). While conservation helps preserve existing carbon stocks, it does not lead to additional carbon removal. Restoration, on the other hand, can enhance carbon sequestration and qualify as CDR, though its long-term potential is uncertain due to the susceptibility of these ecosystems to climate change (Gattuso et al., 2021; Johannessen and Christian, 2023).

Artificial upwelling has been proposed to increase biological productivity by pumping nutrient-rich deep waters to the surface (Jürchott et al., 2023; Lovelock and Rapley, 2007). While theoretically capable of enhancing atmospheric $CO_2$ drawdown, it presents significant risks, such as $CO_2$ outgassing from upwelled waters, ocean deoxygenation, and the release of potent greenhouse gases like methane and nitrous oxide (Dutreuil et al., 2009; Yool et al., 2009; Keller et al., 2014; Oschlies et al., 2010b).

Ocean fertilization also aims to enhance carbon uptake by stimulating biological productivity through phytoplankton blooms, achieved by depositing nutrients like iron in nutrient-deficient regions (Blain et al., 2007; Hauck et al., 2016; Minx et al., 2018). While the iron-limited Southern Ocean has shown potential for this method (Smetacek et al., 2012), it faces critical challenges. These include limited long-term carbon retention, oxygen depletion at depth, nutrient robbing that may exacerbate tropical ocean productivity declines, and potential ecosystem disruptions (Güssow et al., 2010; Oschlies et al., 2010a; Tagliabue et al., 2023).

Among various marine CDR methods, Ocean Alkalinity Enhancement (OAE), which aims to enhance carbon uptake by modifying marine carbonate chemistry, demonstrates the highest potential for carbon uptake and its durable sequestration. Despite its promise, it also faces challenges such as secondary mineral precipitation and uncertain biological impacts, which necessitate further investigation (Gattuso et al., 2018; National Academies of Sciences, Engineering, and Medicine et al., 2021). As the most promising approach among ocean-based CDR strategies (Gattuso et al., 2021), OAE will be discussed in detail in the following section.

### 2.6.3 *Monitoring, Reporting, and Verification (MRV) for CDR*

Effective MRV of CDR involves quantifying $CO_2$ removal, ensuring systematic tracking, and securing third-party verification to promote transparency, accountability, and comparability (Schulte et al., 2024). MRV is vital for assessing the effectiveness of CDR methods in climate mitigation and integrating them into NDCs under the Paris Agreement. MRV also strengthens voluntary carbon markets by standardizing carbon credit quantification, thereby building stakeholder trust (Ho et al., 2023). Beyond carbon accounting, MRV frameworks are expanding to evaluate broader environmental impacts such as biodiversity, water, soil, and air quality, and social benefits like job creation (Schulte et al., 2024). Despite its importance, substantial challenges persist, including difficulties in accounting for carbon removal amid spatial and temporal variability of the major carbon sinks, risks of carbon reversal due to natural disturbances or technological failures, and the need to establish reliable baselines (Fuss et al., 2024). High costs, inconsistent global standards, and transparency gaps further complicate MRV implementation. Addressing these issues through technological innovation and harmonized international standards is crucial for realizing the full potential of MRV in supporting robust CDR strategies (Fuss et al., 2024).

## 2.7 OCEAN ALKALINITY ENHANCEMENT (OAE)

Ocean alkalinity enhancement is an abiotic geochemical CDR method that entails manipulating marine carbonate chemistry to enhance carbon uptake and sequestration (Kheshgi, 1995). In principle, this method accelerates the natural chemical weathering reaction that leads to oceanic $CO_2$ storage on a geological timescale (Caldeira and Rau, 2000). The increase in ocean alkalinity results in repartitioning of the dissolved carbonate species with a shift of equilibrium towards bicarbonate and carbonate ion concentrations and reduction in the concentration of dissolved $CO_2$ and in turn surface ocean $pCO_2$ (Middelburg et al., 2020; Zeebe and Wolf-Gladrow, 2001). This chemical shift can either result in increased net ingassing of $CO_2$ from the atmosphere or reduced outgassing of $CO_2$ from the ocean depending on the $pCO_2$ disequilibrium at the ocean-atmosphere interface (Hartmann et al., 2013; Renforth and Henderson, 2017).

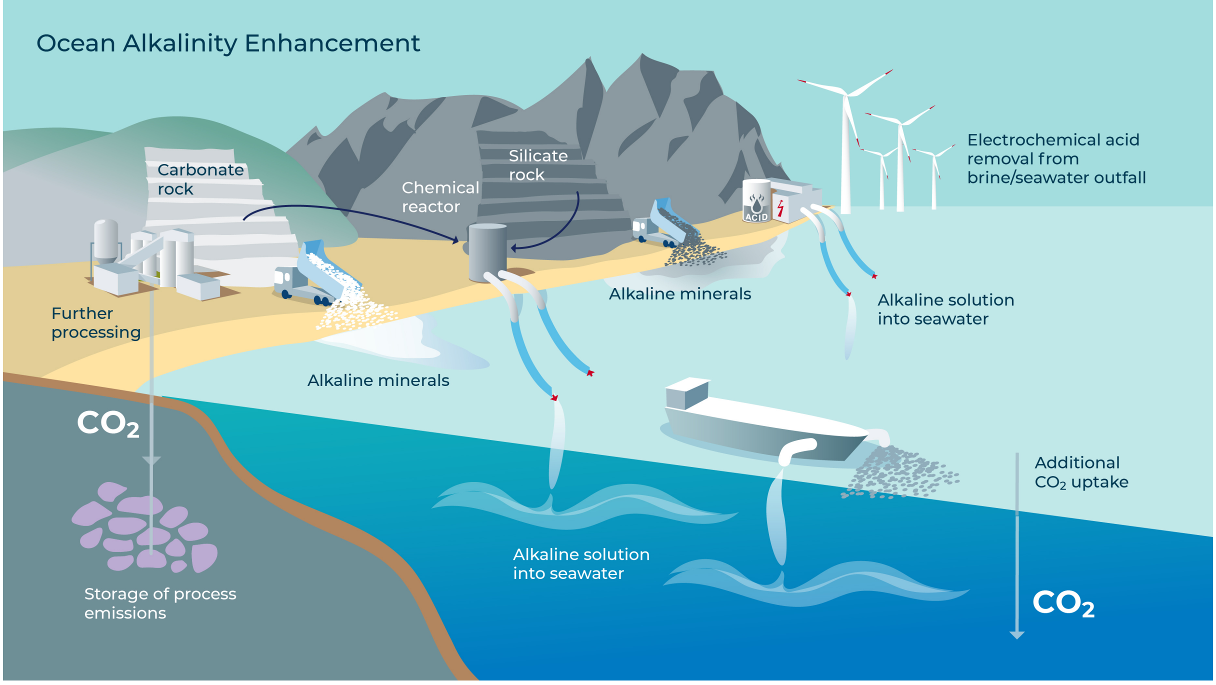

FIGURE 2.6: Representation of various ways through which ocean alkalinity enhancement can be realized. Source: Oschlies et al. (2023); Artwork: Rita Erven CDRmare/GEOMAR

### 2.7.1 *Methods for Artificial Enhancement of Alkalinity*

1. ***Alkaline Rock Powder***

   This method involves spreading of fine powder of Mg- and Ca-rich silicate rocks, such as basalt, olivine, peridotite, or carbonate rocks like limestone and dolomite in the coastal ocean or open ocean (Renforth and Henderson, 2017; Hauck et al., 2016; Hartmann et al., 2013). The release of alkalinity from these materials is primarily governed by their dissolution kinetics, which depend on both the mineral type and particle size. Fine particles (1-10 $\mu$m) are ideal for complete and rapid dissolution of silicate minerals in the surface ocean (Feng et al., 2017; Köhler et al., 2013). Smaller particles increase the surface area and enhance the reaction rates, which ensures maximum dissolution and release of alkalinity in the surface layer, reducing the loss of undissolved particles to the deep ocean. However, the energy-intensive grinding process to achieve small sizes is shown to offset the OAE efficiency by 30% (Köhler et al., 2013). In coastal regions, coarser particles ($<100$ $\mu$m) can be deployed, leveraging natural processes like wave action and tidal forces to break down the particles and accelerate dissolution (Eisaman et al., 2023). On the other hand, carbonate minerals, such as lime ($CaO$) or slaked lime ($Ca(OH)_2$), dissolve more rapidly than silicates, offering faster alkalinity release. However, the calcination process required to produce these materials from limestone is energy-intensive, further lowering the OAE efficiency. To address these limitations, alternative material like ikaite, a hydrated $CaCO_3$ mineral, is being investigated. Producing ikaite has a lower energy requirement than calcination, while it also offers comparable alkalinity release as other carbonates and silicates (Eisaman et al., 2023).

The scalability of OAE is closely tied to the global availability and transportation of these minerals to sites of deployment. Limestone, with an annual production of $\sim$0.41 Gt $yr^{-1}$ in 2017, is sufficient to support large-scale OAE deployment, unlike olivine (7.0-7.8 Mt $yr^{-1}$), magnesite (11-29 Mt $yr^{-1}$), and brucite (0.5-1.5 Mt $yr^{-1}$), which have much lower production rates and cannot meet the required scale for offsetting 1 PgC annually (Caserini et al., 2022). Substantial upscaling of mining operations would be necessary for these minerals to meet the demands for large-scale OAE that can induce further anthropogenic emissions lowering the OAE potential (Caserini et al., 2022).

2. ***Electrolysis and Electrodialysis***

   Aqueous salt solutions, such as seawater and brines (e.g., desalination wastes and geological fluids), serve as an abundant source of alkalinity. Electrochemical processing of these solutions generates aqueous NaOH or other hydroxides, which can be used for near-instant OAE and $CO_2$ drawdown (Eisaman et al., 2023; Ringham et al., 2024). Alkalinity can be produced by following two methods using electrochemical processes: Electrolysis and Electrodialysis. Electrolysis produces high concentration NaOH (26 wt%) along with significant quantities of $H_2$ and $Cl_2$. Electrodialysis produces low-concentration NaOH (4 wt%) along with HCl and negligible amounts of $H_2$ and $O_2$ that are vented (Eisaman et al., 2023). An advantage of using aqueous hydroxides (NaOH) over solid rock powders for OAE is that the rate at which alkalinity increases in the ocean equals the rate at which alkalinity is actually deposited to the ocean. Further, seawater and desalination brines are virtually unlimited resources for electrochemical processes, offering a sustainable supply for hydroxide production.

   However, both methods are energy-intensive, requiring electricity from renewable sources to minimize its carbon footprint (Lannoy et al., 2018). Additionally, managing chemical byproducts necessitates stringent safety measures to prevent environmental contamination (Eisaman et al., 2012). Scaling this method also demands substantial investments in production, storage, and distribution infrastructure, further introducing constraints in large-scale deployment (Eisaman et al., 2023; Lannoy et al., 2018).

### 2.7.2 *Limitations associated with OAE*

1. ***Biological Impacts of OAE***

   The biological and ecological impacts of OAE are intricately linked to the type of feedstock used and the background conditions in the regions of deployment (Bach et al., 2019).

Mineral-based OAE, particularly using olivine, poses significant risks due to the release of trace metals, such as Nickel (Ni), Chromium (Cr), Copper (Cu), and Cadmium (Cd), which can have toxic effects on marine organisms (Bach et al., 2019; Hartmann et al., 2013). Iron released alongside olivine, though initially bio-unavailable due to low solubility (Montserrat et al., 2017), could become bioavailable at large deposition scales ($\sim$3 Pg $\mathrm{yr}^{-1}$), potentially inducing iron fertilization and associated $CO_2$ uptake (Hauck et al., 2016; Nagwekar et al., 2024). However, this scale of deployment may also disrupt marine ecosystems, including benthic communities through the sinking of undissolved olivine grains (Feng et al., 2017; Eisaman et al., 2023). In contrast, feedstocks such as limestone derivatives and synthetic metal oxides (MgO and CaO) have lower toxic metal release and generally exhibit lower ecological risks (Fakhraee et al., 2023). Nonetheless, they are not without challenges, as abiotic mineral precipitation can remove essential nutrients and alkalinity from seawater (Gately et al., 2023).

Experimental studies have revealed nuanced biological responses to OAE. In situ and microcosm experiments indicate species-specific and region-dependent effects. For instance, microbial communities in the North Atlantic Subtropical Gyre exhibited negligible biological responses to extreme alkalinity additions ( 2000 $\mu$mol $\mathrm{kg}^{-1}$), although localized reductions in net primary production and shifts toward smaller particle size classes were observed suggesting that OAE might impact community compositions and/or aggregation/disaggregation processes (Subhas et al., 2022). Similarly, phytoplankton exhibited a species-specific but generally low sensitivity to a wide range of Ni addition (Guo et al., 2022), while diatom communities exhibited reduced silicic acid drawdown and biogenic silica buildup under added alkalinity (500 $\mu$mol $\mathrm{kg}^{-1}$; Ferderer et al., 2022). Gately et al. (2023) demostrated that certain phytoplankton functional groups showed neutral growth rate under moderate ($\sim$700 $\mu$mol $\mathrm{kg}^{-1}$) and high ($\sim$2700 $\mu$mol $\mathrm{kg}^{-1}$) alkalinity addition rates. However, in the high alkalinity addition case, they also observed abiotic mineral precipitation which removed inorganic nutrients (iron, silicate, and phosphate) along with alkalinity from the seawater solution. Broader assessments suggest that calcifiers may benefit from $CaCO_3$ derivatives through beneficial changes in carbonate chemistry, while silicate feedstocks could promote silicifiers and nitrogen-fixers, potentially increasing ocean productivity (Bach et al., 2019). Overall, these studies indicate that OAE-induced ecosystem perturbations are moderate, with no evidence of drastic changes observed thus far. Nevertheless, further research is required to assess long-term impacts, including potential shifts in community composition and functioning, proliferation of harmful species, disruption of trophic transfer, and alterations in elemental cycling to better evaluate potential of OAE as a climate mitigation strategy (Riebesell et al., 2023).

2. ***Secondary Mineral Precipitation***
Irrespective of the method for alkalinity addition, OAE increases the concentration of ${CO_3}^{2-}$ ions in the surface ocean. This results in an increase of the saturation states of various $CaCO_3$ morphotypes such as calcite and aragonite (Bach et al., 2019). The saturation state ($\Omega$) determines the safe limit for alkalinity deposition in the ocean, with an average $\Omega$ of 5 identified as the critical threshold beyond which secondary

$CaCO_3$ precipitation can occur (Renforth and Henderson, 2017; Moras et al., 2022). Such secondary precipitation should be avoided as it reduces the $CO_2$ uptake capacity of the ocean by consuming alkalinity (Hartmann et al., 2023). It can also eventually lead to runaway $CaCO_3$ precipitation, where more alkalinity is removed from the ocean surface than the amount added during OAE (Schulz et al., 2023; Suitner et al., 2024). The $CO_2$ uptake potential can be reduced by a factor of 8 due to such events (Fuhr et al., 2022; Moras et al., 2022). Owing to latitudinal variations in the saturation state, a 5-times higher alkalinity can be added in the high latitude ocean in comparison to low latitudes (Schulz et al., 2023). Additionally, the precipitation of $CaCO_3$ increases $CO_{2(aq)}$ concentrations (see section 2.2.3), raising surface ocean $pCO_2$. This, along with disturbances in the $CaCO_3$ cycling, such as changes in the calcification rate of marine organisms or alterations in the dissolution of $CaCO_3$ in the water column and sediments, may cause $CO_2$ leakage. Consequently, if the $pCO_2$ gradient shifts to favour $CO_2$ transfer from the ocean to the atmosphere, it could counteract the intended $CO_2$ drawdown of OAE (Hartmann et al., 2023).

The risk of secondary precipitation is particularly high when alkalinity is increased, but atmospheric $CO_2$ has not yet dissolved in the ocean to establish a new equilibrium. This results in elevated $\Omega$ and if the equilibration of atmospheric $CO_2$ takes longer than expected, then the risk of precipitation and subsequent loss of added alkalinity rises. However, this can be avoided by equilibrating seawater with respect to atmospheric $CO_2$ during alkalinity addition (Bach et al., 2019; Schulz et al., 2023). This would result in $\Omega$ being much lower for the same amount of alkalinity addition. Further, dilution of added alkalinity with unperturbed seawater has also shown to reduce or stop secondary precipitation due to reduction of $\Omega$ (Moras et al., 2022).

### 2.7.3 *Carbon Sequestration Durability of OAE*

In the context of OAE, durability denotes the temporal stability of sequestered carbon in the ocean post deployment. The principal advantage of OAE lies in its potential for high durability, whereby carbon is stored as DIC, predominantly in the form of bicarbonate and carbonate ions (Renforth and Henderson, 2017). These ionic species do not directly exchange with the atmosphere and remain within the oceanic system over timescales dictated by alkalinity cycling, often exceeding 1000 years (Middelburg et al., 2020). Owing to this, carbon sequestration in the surface ocean is considered chemically resilient, obviating the necessity for prioritizing deep ocean storage as a prerequisite for effective OAE (Ho et al., 2023).

Nonetheless, surface ocean carbon retention is potentially vulnerable to $CO_2$ outgassing due to the dynamic nature of the surface ocean, which continuously interacts with the atmosphere. This interaction creates the risk of $CO_2$ re-equilibration and efflux, particularly in response to temperature changes or shifts in carbonate equilibrium (Hartmann et al., 2023). Additionally, biological productivity contributes to this vulnerability. While dissolved $CO_2$ is initially assimilated by phytoplankton during photosynthesis, subsequent remineralization in the surface layer releases $CO_2$ back into the seawater, a fraction of which may re-equilibrate with the atmosphere and result in outgassing (Siegel et al., 2023). In contrast, if sequestered carbon is transferred to the deep ocean (>1000 m), it becomes incorporated into a more isolated deep ocean carbon reservoir. It has limited atmospheric interaction occurring only over multi-decadal to centennial timescale and over millennial timescale if the injected carbon reaches the abyss (Siegel et al., 2021). Such sequestration in the deep ocean could potentially enhance the long-term durability of carbon storage, offering a comparatively higher stability than the surface ocean retention.

### 2.7.4 *Modeling Studies for OAE*

Numerical ocean models, though inherently simplified representations of complex natural processes, are essential for OAE research due to their capacity to simulate large-scale ocean dynamics that are not captured by direct observations. By representing the spatial and temporal variability of added alkalinity, air-sea $CO_2$ exchange, and ecosystem responses under various scenarios, models facilitate the quantification of carbon uptake efficiency, assessment of potential ecological impacts, and development of robust MRV frameworks (Fennel et al., 2023; Ho et al., 2023). Furthermore, models allow for the testing of hypothetical deployment strategies and the exploration of uncertainties, offering crucial insights that inform both experimental design and large-scale implementation strategies for OAE (Fennel et al., 2022).

A variety of modeling approaches are used to address the diverse spatial and temporal scales associated with OAE. Regional models are used to understand effects of alkalinity injections on coastal biogeochemistry, air-sea $CO_2$ exchange, and ecosystem responses on spatial scales ranging from 4 to 10 kilometers (Butenschön et al., 2021; Mongin et al., 2021; Wang et al., 2023). These models are particularly valuable for planning field experiments and providing insights for observational designs. They also help to understand and assess the site-specific impacts of OAE (Fennel et al., 2023). Global models, by contrast, focus on the redistribution of alkalinity and carbon dynamics across entire ocean basins, providing insights into how OAE-induced changes propagate through large-scale ocean circulation and affect long-term carbon sequestration (Hauck et al., 2016; Ilyina et al., 2013; Keller et al., 2014; Köhler et al., 2013; Lenton et al., 2018).

1. ***Ocean-only Models***
   Ocean-only global models are a cornerstone of OAE research, as they allow for a focused examination of oceanic processes while accounting for large-scale alkalinity and carbon redistribution. These models can project how alkalinity-enhanced waters are transported and how they interact with biogeochemical cycles over multi-decadal to century long timescale (Burt et al., 2021; Hauck et al., 2016; He and Tyka, 2023). An early global study by Köhler et al. (2013) demonstrated that dissolving 3 Pg of olivine annually in surface waters over a decade (2000-2010) could sequester approximately 0.28 PgC per Pg of olivine. This work was extended by Hauck et al. (2016) in a century-scale simulation, where the same rate of olivine addition led to a sequestration of 0.57 PgC per Pg of olivine over 2090-2099. Both studies considered the effect of nutrient fertilization (iron and silicic acid; Hauck et al. (2016), but only silicic acid in Köhler et al. (2013)), and

concluded that iron fertilization contributed about 37% and silicic acid about 6-8% to the additional $CO_2$ uptake.

To enable consistent comparison across various modeling studies, Renforth and Henderson (2017) introduced a standardized OAE efficiency metric "$\eta CO_2$". This is defined as the ratio of depth-integrated changes in DIC to depth-integrated changes in alkalinity due to OAE. It accounts for these changes since the start of OAE simulation and can thus be termed as a long-term efficiency metric. It isolates the impact of OAE on the ocean carbonate chemistry and is agnostic to the alkaline feedstock used, supporting the cross comparison between studies.

Burt et al. (2021) investigated the regional response to OAE by simulating OAE in hydrodynamic biomes for 75 years and found that the Southern Ocean exhibited the highest efficiency ($\eta CO_2$) of 0.89, while the subpolar North Atlantic showed the lowest efficiency of 0.7 due to rapid alkalinity loss caused by strong vertical mixing. Similarly, Butenschön et al. (2021) reported a low efficiency of 0.5 for simulating OAE along ship tracks in the Mediterranean Sea for 50 years. This low efficiency was again due to loss of added alkalinity to the deep ocean. Meanwhile, He and Tyka (2023) explored a different and possibly more realistic approach of a month-long pulsed alkalinity addition in global coastal regions and reported efficiencies between 0.65 and 0.80 after a decade of deployment. This study also reported that the subduction regions in the North Atlantic regions are the least efficient for OAE due to the limited residence time of $CO_2$-deficit water masses at the surface ocean. Similar arguments about the subduction regions not being suitable for OAE and reporting efficiency as low as 0.2 were made by other studies which examined pulsed addition of alkalinity (Zhou et al., 2025; Yankovsky et al., 2024).

Thus, overall, these ocean-only model studies have collectively provided first information about the deployment strategies i.e., global, regional or along ship tracks. They have used either continuous or pulsed addition of alkalinity over varied timescales and have assessed nutrient impact on carbon uptake if olivine is used as an alkaline mineral. Despite these achievements, ocean-only models have inherent limitations. Since they assume prescribed atmospheric $CO_2$ concentration, they lack dynamic feedbacks between ocean, atmosphere, and terrestrial ecosystems. This absence leads to an overestimation of $CO_2$ uptake and OAE efficiency ($\eta CO_2$). As a result, the efficiencies reported by these models were recently termed as "capture efficiency" (Schwinger et al., 2024). Nonetheless, their results remain vital as a foundation for more complex simulations using fully coupled earth system models (Fennel et al., 2023).

2. ***Earth System Models***
A unique strength of Earth System Models, lies in their ability to represent atmospheric $CO_2$ as a dynamic variable, unlike ocean-only models, enabling them to simulate the full feedback loop between atmospheric, oceanic, and terrestrial carbon reservoirs (Fennel et al., 2023; Schwinger et al., 2024). Due to these feedbacks, the carbon uptake and OAE efficiencies reported using an ESM are lower than those reported by the ocean-only models, and this is referred to as "Earth System efficiency" (Schwinger et al., 2024). Until

now only Palmiéri and Yool (2024) and Schwinger et al. (2024) have reported $\eta CO_2$ using an ESM. Palmiéri and Yool (2024) conducted simulations of global coastal OAE with alkalinity addition rates between 0.036 and 0.073 Pmol yr$^{-1}$ and found $\eta CO_2$ ranging from 0.75 to 0.78, whereas, Schwinger et al. (2024) simulated global OAE deployment with alkalinity addition rate of 0.135 Pmol yr$^{-1}$ and reported $\eta CO_2$ of 0.69.

However, several studies have reported reductions in atmospheric $CO_2$ concentrations and surface air temperature (SAT) as a result of OAE deployment using varying amounts of alkalinity addition. Palmiéri and Yool (2024) observed a reduction of 5 to 11 ppm by 2100 for their coastal OAE scenarios. Keller et al. (2014) and Lenton et al. (2018) conducted global-scale OAE simulations with higher alkalinity addition rates of 0.25 Pmol yr$^{-1}$ over 80 years and reported atmospheric $CO_2$ reductions of $\sim$78–80 ppm by the end of the century. Additionally, Lenton et al. (2018) examined regional OAE across large latitudinal bands and found no significant regional sensitivity, as the atmospheric $CO_2$ reduction remained consistent at $\sim$80 ppm, similar to the global deployment. González and Ilyina (2016) and Sonntag et al. (2018) investigated more extreme cases with continuously high alkalinity addition ($\sim$1.4 Pmol yr$^{-1}$ over 80 years), resulting in an atmospheric $CO_2$ reduction of $\sim$450 ppm.

Temperature responses to OAE have been relatively modest across studies employing low to moderate alkalinity addition. Palmiéri and Yool (2024) reported SAT reductions ranging from 0.0°C to 0.2°C, whereas Keller et al. (2014) and Lenton et al. (2018), reported decreases between 0.20°C and 0.26°C. Only, González and Ilyina (2016) and Sonntag et al. (2018) observed a more pronounced SAT reduction of 1.5°C under high alkalinity addition ($\sim$1.4 Pmol yr$^{-1}$). These larger temperature decrease are however, related to extreme alkalinity additions, which is considered as infeasible due to availability of minerals and more importantly the associated risk of negative impacts of marine ecosystem (Caserini et al., 2022; González and Ilyina, 2016). Furthermore, Jeltsch-Thömmes et al. (2024) noted that the temperature response to OAE is delayed by more than a decade following the reduction in atmospheric $CO_2$. This lag implies that extending simulations beyond 2100 could reveal greater temperature reductions under moderate OAE scenarios, though the short-term impact on SAT remains relatively small for 70–80 year simulations.

Beyond atmospheric $CO_2$ and temperature changes, ESMs offer critical insights into the behavior of carbon sinks during and after OAE deployment. While the ocean carbon sink increases throughout OAE deployment, all studies consistently report a weakening of the terrestrial carbon sink over time. Furthermore, ESMs allow to investigate complex scenarios, including interactions between OAE and other CDR technologies, and to evaluate cumulative impacts on Earth system stability (Keller et al., 2018). These findings highlight that ESMs are indispensable for comprehensively evaluating the long-term impacts of OAE.

A critical yet unexplored approach for simulating OAE involves high-resolution modeling. Near-field or turbulence-scale models, spanning micrometer to kilometre scales, can offer distinct advantages by directly representing how turbulent eddies disperse added alkalinity in the critical early phase of OAE (Fennel et al., 2023). This high-resolution can resolve how different feedstock materials dissolve, aggregate, or precipitate, and how the resulting high-alkalinity waters mix with ambient seawater (Fornari et al., 2016; Mensa et al., 2015; Smith et al., 2018; Taylor et al., 2020). This local-scale insight is essential for designing efficient deployment strategies, as it can identify the conditions under which excessive precipitation might occur, assess the risk of localized pH spikes, and project how rapidly alkalized plumes can dilute (Fennel et al., 2023). If combined with observations, these models can be useful to give estimates about safe limits for alkalinity addition in order to reduce potential negative impacts on localized marine ecosystems and thus help optimize monitoring and verification efforts. However, such models are computationally expensive which restricts their applicability to localized domains (few meters) and short simulation periods, but their results can provide an important test bed to be used to develop parametrizations required in low-resolution models (Fennel et al., 2023).

Local- to regional-scale models extend from these near-field zones to broader domains, spanning from tens of meters to hundreds of kilometres. They incorporate realistic bathymetry, coastlines, broader circulation, and coupled biogeochemical components (Fennel et al., 2022; Mongin et al., 2016), thus can project how alkalinity-enriched waters disperse and drive additional air-sea $CO_2$ flux over longer timescales and larger domains. Incorporation of boundary conditions, riverine inputs, and sediment interactions can ensure robust estimates of carbon uptake efficiency, aid in environmental impact assessment, and can support field experimental design for OAE. This integration across scales, from turbulence-resolving near-field models to larger regional frameworks, can allow us to weigh both benefits and risks of OAE deployment at more comprehensive scales, ultimately supporting strategic field experiments, robust site selection, and sustainable large-scale implementation (Fennel et al., 2023).

### 2.7.5 *MRV for OAE*

MRV is essential for evaluating the effectiveness of OAE as a CDR strategy. Three key metrics guide MRV: additionality, leakage, and durability (Schulte et al., 2024). Additionality measures the $CO_2$ removed due to OAE relative to the baseline before the perturbation was deployed (Bach, 2024). Leakage accounts for potential $CO_2$ re-release caused by processes such as perturbations of the $CaCO_3$ cycle (Moras et al., 2022; Schulz et al., 2023). Durability refers to the expected storage lifetime of the sequestered $CO_2$, which in the case of OAE exceeds 1,000 years, as carbon is stored in the form DIC within the ocean (Middelburg et al., 2020; Ho et al., 2023).

Due to the turbulent and dynamic nature of the ocean, direct observational methods alone are insufficient for reliably quantifying the $CO_2$ removal achieved by OAE (Ho et al., 2023). The time required for the $CO_2$-deficit waters to equilibrate with the atmosphere adds another layer of complexity. This equilibration typically occurs over a period of six months (Sarmiento, 2013), although it is highly variable on a regional scale (Jones et al., 2014). Another challenge lies in the oceanic physical processes that influence the fate of alkalinity-enhanced water masses. These waters can be advected horizontally away from the injection sites or entrained vertically into deeper layers, leading to dilution or loss of alkalinity before it can equilibrate with the atmosphere (He and Tyka, 2023; Ho et al., 2023). Together with natural variability in ocean carbonate chemistry, these factors make the detection of OAE signals complex. Additionally, the absence of commercially available autonomous sensors for key parameters, such as total alkalinity and DIC, limits the ability to conduct real-time monitoring at scale. Consequently, numerical models play a vital role in complementing field observations by simulating processes such as alkalinity transport and air-sea $CO_2$ fluxes (Keller et al., 2014; Köhler et al., 2013; Lenton et al., 2018). However, models used for OAE have not yet incorporated key processes such as mineral dissolution kinetics, secondary precipitation, and biological response to OAE, making further development and validation essential (Fennel et al., 2023). Future MRV systems must combine high-resolution field measurements, improved sensor technology, and advanced modeling approaches to address current limitations. By refining these components, MRV will provide a rigorous framework for assessing effectiveness of OAE as a scalable CDR strategy (Ho et al., 2023; Fennel et al., 2023).

## 2.8 AIMS AND SCOPE OF THE THESIS

This thesis investigates the effects of Ocean Alkalinity Enhancement (OAE) when deployed in subduction regions of the Southern Ocean (SO), Northwest Atlantic (NWA), and Norwegian-Barents Sea (NBS). These regions are targeted because they serve as critical conduits, enabling carbon transfer from the surface ocean to its interior, where it can potentially be sequestered for centennial to millennial timescales. Consequently, they act as a bottleneck for anthropogenic carbon uptake and subsequent long-term carbon storage. The study thus compares these regional deployments with the global OAE approach to assess the impact on carbon uptake and deep ocean sequestration under low (SSP1-2.6) and high (SSP3-7.0) emission scenarios. To achieve these objectives and assess methodological uncertainties, three model setups were employed: the biogeochemical ocean-only model FESOM2.1-REcoM3, in coarse- and high-resolution setups, and the fully coupled emission-driven Earth System Model (ESM) AWI-ESM1-REcoM. The following research questions were addressed using these setups:

- How do the subduction regions, individually and collectively, perform in terms of carbon uptake and OAE efficiency compared to global OAE, and what are the uncertainty estimates?
- Can subduction regions increase deep ocean carbon sequestration due to OAE, and what are the associated uncertainty estimates?
- How do the global and regional OAE deployments affect land and ocean carbon sinks, atmospheric $CO_2$ concentration, and surface air temperature?

Publication I focuses on assessing the impact of OAE simulated in the subduction regions combined together and individually as compared to global OAE under SSP1-2.6 and SSP3-7.0 emission scenarios. To achieve this, OAE was simulated using the relatively coarse-resolution biogeochemical model FESOM2.1-REcoM3. It considers both alkalinity addition alone and a combined approach of alkalinity addition with nutrient fertilization. The alkalinity-only experiments are agnostic to the alkaline material used, while the combined approach (alkalinity+nutrients) evaluates the effects of iron and silicic acid fertilization to assess the impact if olivine were used as the feedstock for OAE. The publication investigates how these two OAE approaches affect carbon uptake, OAE efficiencies, and deep ocean carbon storage in the subduction regions compared to global OAE and explores the dependency of outcomes on the emission scenarios used. The simulations with nutrient fertilization assess the impact of OAE on changes in the net primary productivity and calcification rates. In addition, the research also investigates the seasonal variations in OAE induced carbon uptake and storage as well as its drivers, thus informing about optimal deployment strategies.

Publication II advances the research by simulating OAE globally and in subduction regions using the fully coupled emission-driven Earth system model AWI-ESM1-REcoM under the SSP3-7.0 emission scenario. This study focuses on the impacts of climate feedbacks on various parameters, including ocean carbon uptake, deep ocean carbon sequestration, OAE efficiency, atmospheric $CO_2$ reduction, surface air temperature, and changes in the land carbon sinks. Ensemble simulations for both global and regional OAE deployments were conducted, and uncertainty estimates were provided for each of these parameters.

Publication III, revolves around discerning the model resolution impact on OAE deployed in global oceans and subduction regions. Here a high-resolution (5-10 km in the subduction regions of interest) ocean-only model FESOM2.1-REcoM3 is used and simulations are carried out under SSP3-7.0 emission scenario. The resolution effect was assessed by comparing simulations from this setup with those from Publication I, which uses the same model but in a coarse-resolution (20-50 km).

Chapter 6 presents a synthesis of the key findings from Publications I-III, placing them in the context of existing literature on the subject. The chapter concludes with a discussion on future research directions for modeling OAE and potential considerations for the MRV framework.

## 2.9 LIST OF PUBLICATIONS

| | |
|---|---|
| **Publication I** | T. Nagwekar, C. Nissen, and J. Hauck (2024): Ocean Alkalinity Enhancement in Deep Water Formation Regions under Low and High Emission Pathways. *Earth's Future*, 12, e2023EF004213. `https://doi.org/10.1029/2023EF004213`.<br>I modified the model code to implement alkalinity enhancement and carried out all simulations in collaboration with the co-authors. I performed the data analysis and documented the final results with input from the co-authors. I have written the manuscript and worked on the revisions and feedback provided by the co-authors. |
| **Publication II** | T. Nagwekar, C. Danek, M. Seifert, and J. Hauck (2024): Alkalinity Enhancement in Subduction Regions: Efficiency, Earth System Feedbacks, and Deep Ocean Carbon Sequestration. *In review at Environmental Research Letters*.<br>I modified the model code to implement alkalinity enhancement and carried out all simulations in collaboration with the co-authors. I performed the data analysis and produced the final results with input from the co-authors. I have written the manuscript and worked on the revisions and feedback provided by the co-authors. |
| **Publication III** | T. Nagwekar, C. Danek, C. Nissen, M. Seifert, and J. Hauck (2025): *"Effect of Model Resolution on Ocean Alkalinity Enhancement in the Subduction Regions and the Global Ocean". In preparation*.<br>The same model code was utilized here as in Publication I, but on a high-resolution mesh. I carried out all simulations and performed the data analysis and derived the final results with input from the co-authors. I have written the manuscript and worked on the revisions and feedback provided by the co-authors. |

# 3

# PUBLICATION I

## OCEAN ALKALINITY ENHANCEMENT IN DEEP WATER FORMATION REGIONS UNDER LOW AND HIGH EMISSION PATHWAYS

Earth's Future

RESEARCH ARTICLE
10.1029/2023EF004213

# Ocean Alkalinity Enhancement in Deep Water Formation Regions Under Low and High Emission Pathways

**Tanvi Nagwekar**[1], **Cara Nissen**[2], **and Judith Hauck**[1]

[1]Alfred Wegener Institute for Polar and Marine Research, Bremerhaven, Germany, [2]Department of Atmospheric and Oceanic Sciences and Institute of Arctic and Alpine Research, University of Colorado, Boulder, CO, USA

**Key Points:**

- Southern Ocean and Northwest Atlantic Ocean Alkalinity Enhancement efficiencies are akin to the global ocean and larger than in the Norwegian-Barents Sea region
- The subduction regions can store a fraction of excess carbon in the deep ocean that is nearly two times higher than in the global ocean
- Seasonal mixed layer depth variations govern excess surface alkalinity concentrations and thus the excess carbon uptake and storage

**Supporting Information:**

Supporting Information may be found in the online version of this article.

**Correspondence to:**

T. Nagwekar,
tanvi.nagwekar@awi.de

**Citation:**

Nagwekar, T., Nissen, C., & Hauck, J. (2024). Ocean alkalinity enhancement in deep water formation regions under low and high emission pathways. *Earth's Future*, *12*, e2023EF004213. https://doi.org/10.1029/2023EF004213

Received 1 NOV 2023
Accepted 27 AUG 2024

## Abstract

Ocean Alkalinity Enhancement (OAE) is an ocean-based Carbon Dioxide Removal (CDR) method to mitigate climate change. Studies to characterize regional differences in OAE efficiencies and biogeochemical effects are still sparse. As subduction regions play a pivotal role for anthropogenic carbon uptake and centennial storage, we here evaluate OAE efficiencies in the subduction regions of the Southern Ocean, the Northwest Atlantic, and the Norwegian-Barents Sea region. Using the ocean biogeochemistry model FESOM2.1-REcoM3, we simulate continuous OAE globally and in the subduction regions under high (SSP3-7.0) and low (SSP1-2.6) emission scenarios. The OAE efficiency calculated by two different metrics is higher (by 8%–30%) for SSP3-7.0 than for SSP1-2.6 due to a lower buffer factor in a high-$CO_2$ world. All subduction regions show a CDR potential (0.23–0.31; PgC $CO_2$ uptake per Pg alkaline material) consistent with global OAE for both emission scenarios. Calculating the efficiency as the ratio of excess dissolved inorganic carbon (DIC) to excess alkalinity shows that the Southern Ocean and the Northwest Atlantic are as efficient as the global ocean (0.79–0.85), while the Norwegian-Barents Sea region has a lower efficiency (0.65–0.75). The subduction regions store a fraction of excess carbon below 1 km that is 1.9 times higher than the global ocean. The excess surface alkalinity and thus $CO_2$ uptake and storage follow the mixed-layer depth seasonality, with the majority of the excess $CO_2$ flux occurring in summer at shallow mixed layer depths. This study therefore highlights that subduction regions can be efficient for OAE if optimal deployment strategies are developed.

## Plain Language Summary

Increasing atmospheric $CO_2$ concentrations demand urgent reductions in the anthropogenic greenhouse gas emissions to limit the increase in global air temperatures to ≤2°C relative to preindustrial conditions. To compensate for/counteract the small fraction of unavoidable emissions, it will also be necessary to implement a portfolio of carbon dioxide removal (CDR) methods. In this study, we focus on the ocean-based CDR method Ocean Alkalinity Enhancement (OAE), which enhances oceanic carbon uptake and can thus aid in atmospheric $CO_2$ reduction. Oceanic subduction regions are key for anthropogenic carbon uptake and its centennial storage. Therefore, we simulate OAE in the deep and bottom water formation regions of the Southern Ocean, Northwest Atlantic and the Norwegian-Barents Sea region to assess their carbon uptake and storage efficiency compared to the global ocean. We find that the subduction regions exhibit equivalent carbon uptake efficiency to the global ocean, and are nearly two times more effective in deep ocean carbon storage with respect to OAE. Seasonal mixed layer depth variability, however, influences the resulting surface alkalinity concentrations and thus $CO_2$ uptake and DIC accumulation. Therefore, our study emphasizes that the subduction regions can be efficient for OAE when appropriate deployment strategies are developed.

## 1. Introduction

The Paris Agreement 2015 states that the average global surface temperature increase relative to preindustrial conditions should be limited to well below 2°C and preferably to 1.5°C by the end of the 21st century (UNFCCC, 2015). To reach this goal, the future emission pathways outlined by the Intergovernmental Panel on Climate Change (IPCC) emphasize the crucial role of emissions reductions. However, to attain a trajectory of net negative $CO_2$ emissions during the second half of the 21st century, deployment of Carbon Dioxide Removal (CDR) approaches are likely unavoidable (Riahi et al., 2022). Consequently, various CDR methods are actively assessed (Gattuso et al., 2021). Studies focusing on land-based CDR approaches highlight conflicts around land use, carbon storage durability, and risk of ecosystem disruption (Fuss et al., 2018). The documented potential impacts on marine ecosystem due to application of certain ocean-based CDR method are not profound and are mostly region specific (Hernández-Hernández et al., 2018). Hence, there is a growing interest to investigate various marine CDR methods to increase the oceanic carbon uptake and assess the possibility of any side effects it can have on the ecosystem.

Historically, the ocean has played a pivotal role in regulating atmospheric $CO_2$ concentration by taking up almost a third of anthropogenic $CO_2$ emitted since the preindustrial times (Friedlingstein et al., 2022). The subduction regions in the ocean play a prominent role by transporting the carbon taken up at the air-sea interface to the deep ocean where it is stored for decades to many centuries (Gruber et al., 2009). Due to the role of the ocean in the global carbon cycle, various ocean-based CDR methods like ocean fertilization, ocean alkalinization, restoring and increasing coastal vegetation, and marine carbon capture and storage are studied, of which Ocean Alkalinity Enhancement (OAE) shows promising results in terms of carbon storage potential and applicability (Gattuso et al., 2021). On a geological timescale, the natural drawdown of carbon by the oceans occurs through the silicate weathering process, which, however, is two orders of magnitude too slow to compensate for the current emission rates (Archer, 2005). Hence, the motivation behind OAE is to artificially accelerate the oceanic $CO_2$ uptake by elevating alkalinity through the dissolution of alkaline minerals like basalt, lime, olivine, calcium carbonate, or hydroxide (Caserini et al., 2022; Hartmann et al., 2013; Ilyina et al., 2013).

While it is of interest to study alkalinity addition in ocean biogeochemistry models that are agnostic to the specific alkaline material added for first order estimates of efficiency (Ilyina et al., 2013; Köhler et al., 2013), some early studies also discussed (Köhler et al., 2013) or simulated (Feng et al., 2017) the dissolution kinetics of the mineral olivine ($(\mathrm{Mg, Fe})_2\mathrm{SiO}_4$) despite limited experimental data. Olivine contains iron and silicic acid, thus its application in the surface ocean has a nutrient fertilization effect in addition to the alkalinity enhancement. Olivine dissolves in the sea water according to the following chemical reaction:

$$(\mathrm{Mg, Fe})_2\mathrm{SiO}_4 + 4\,\mathrm{CO}_2 + 4\,\mathrm{H}_2\mathrm{O} \longrightarrow 2\,(\mathrm{Mg, Fe})^{2+} + 4\,\mathrm{HCO}_3{}^{-} + \mathrm{H}_4\mathrm{SiO}_4 \qquad (1)$$

Olivine has a molar weight of 147 g $\mathrm{mol}^{-1}$, and a Mg:Fe molar ratio of 9:1 is typically found in nature (De Hoog et al., 2010; Hauck et al., 2016). Accordingly, the dissolution of one mol of olivine consumes 4 mol of $CO_2$ and releases 4 mol of bicarbonate ($HCO_3{}^-$**;** alkalinity), 1 mol of silicic acid ($H_4SiO_4$) and 0.2 mol of iron (Equation 1). The bicarbonate effect reduces sea surface partial pressure of $CO_2$ ($pCO_2$), and thus leads to an excess flux of $CO_2$ from the atmosphere into the ocean (Kheshgi, 1995). The addition of iron and silicic acid during olivine dissolution leads to nutrient fertilization that stimulates phytoplankton productivity and further enhances carbon uptake. The relative contribution to $CO_2$ uptake by iron is 37% and silicic acid is 6%–8% (Hauck et al., 2016; Köhler et al., 2013). Iron is a limiting micronutrient for phytoplankton growth, especially in the High Nutrient Low Chlorophyll (HNLC) areas, like the Southern Ocean, equatorial Pacific, and subpolar North Pacific (De Baar et al., 1995; Smetacek et al., 2012). Hence, iron fertilization on its own is considered a marine CDR method (Aumont & Bopp, 2006; Raven & Falkowski, 1999; Zeebe & Archer, 2005).

Previous modeling studies assess OAE through various alkalinity sources, carrying out simulations using models of varying complexity at a global and regional scale (Burt et al., 2021; Hauck et al., 2016; Ilyina et al., 2013; Köhler, 2020; Lenton et al., 2018). The CDR efficiency from alkalinity enhancement was found to scale with the amount of alkaline material added, whereas nutrient effects from alkaline materials will saturate once nutrients reach levels that do not limit phytoplankton productivity anymore (Hauck et al., 2016; Köhler et al., 2013). Carbon storage through OAE has a durability of several tens to hundreds or thousand years (Köhler, 2020; Middelburg et al., 2020). The ocean $CO_2$ uptake per unit of alkalinity added increases with increasing atmospheric $CO_2$ concentration, owing to the reduced buffer capacity in a high $CO_2$-world (Hauck et al., 2016; Keller et al., 2014) and maximum efficiency is achieved during peak $CO_2$ emissions (Köhler, 2020). Although often referred to as a remedy against ocean acidification, the increase in pH remains small (0.06) by the end of the 21st century in a high-emissions scenario, for OAE done with uniform deposition of 10 Pg $Ca(OH)_2$ per year (Keller et al., 2014). This is because the initial increase in pH is compensated by the increase in $CO_2$ uptake after equilibration with the atmosphere (Hauck et al., 2016; Hinrichs et al., 2023). Only when a substantial reduction in atmospheric $CO_2$ is obtained by OAE (only measurable in model simulations when conducted in emission-driven mode), further ocean acidification is reduced (González & Ilyina, 2016; Köhler, 2020). The pH increase correlates with atmospheric $CO_2$ reduction across a range of CDR methods (Keller et al., 2014).

Comparing OAE in large latitudinal bands versus a global application under low and high emission scenarios revealed that OAE efficiency has limited regional sensitivity (Lenton et al., 2018). Further, climate targets are easier to reach when OAE is applied in a low emission scneario, that is, accompanied by strong emission reduction (Lenton et al., 2018). In contrast, Burt et al. (2021) carried out OAE in large scale hydrodynamic biomes and found that regional OAE application has the potential for higher carbon uptake and OAE efficiency than global OAE. In particular, the Southern Ocean exhibited the highest $CO_2$ uptake efficiency, while the North Atlantic showed the lowest efficiency (Burt et al., 2021). Until now, the regional simulations of OAE were primarily focused on large tropical, subtropical or coastal depositions. Recently, some local OAE studies were also conducted, for example, for the Bering Sea (Wang et al., 2023) or the Mediterranean Sea (Butenschön et al., 2021). Other studies suggested that for a pulsed alkalinity addition, areas with long surface water residence time have the highest efficiency and deep water formation regions have a low efficiency due to the loss of alkalinity to the deep ocean (Bach et al., 2023; He & Tyka, 2023). However, an in-depth analysis of the efficacy of OAE in the deep and bottom water formation regions in the Southern Ocean and North Atlantic where carbon is transferred to abyssal ocean depths and sequestered for centennial timescale is so far missing.

Deep and bottom water formation regions are pivotal for oceanic anthropogenic carbon uptake, acting as the critical conduit for transferring carbon from the surface layer to the ocean's interior, which is the bottle-neck for ocean anthropogenic carbon uptake (Gruber et al., 2019). In general, the magnitude of anthropogenic carbon taken up by these subducting water masses depend on the rate of subduction as well as the water mass characteristics in terms of salinity and temperature (Gruber et al., 2009; Sabine et al., 2004; Walin, 1982). In the North Atlantic, the formation and downward spreading of Labrador Sea Water and North Atlantic Deep Water (NADW) result in the deepest penetration of anthropogenic carbon that reaches abyssal depths and contained ~7 PgC associated with NADW in 1994 (Sabine et al., 2004). The Antarctic Intermediate Water (AAIW) formed between 45 and 55°S contained 20 PgC in the year 1994 as a result of high wind speeds, which enhance the gas exchange, even though this water mass had very low initial anthropogenic $CO_2$ content due to upwelling of old waters in the vicinity (Khatiwala et al., 2009; Sabine et al., 2004). Of the three major water masses for anthropogenic carbon uptake, Antarctic Bottom Water (AABW) carries the lowest amount of anthropogenic $CO_2$, according to the current understanding, mainly due to limited contact of the water mass with the surface and physical barrier for $CO_2$ uptake due to the presence of sea ice (Sabine et al., 2004), although uncertainties are large due to scarcity of observations. However, the AABW formation region is where the carbon taken up is locked away from the atmosphere for the longest time period. Hence, overall, these subduction regions play a crucial role in oceanic anthropogenic carbon uptake and sequestration.

Recent studies suggest that subduction regions may not be optimal for OAE due to the short time for air-sea $CO_2$ equilibration before alkalinity is lost to the deep ocean (Bach et al., 2023; He & Tyka, 2023; Jones et al., 2014). However, our understanding of the efficiency of these regions to transfer the additional carbon taken up through OAE to the deeper ocean depths remains incomplete. In this study, we quantify the effectiveness of the deep and bottom water formation regions in the Southern Ocean, Northwest Atlantic (collective term for subduction regions in the Labrador Sea, Irminger Sea, Iceland Sea and shelf regions of Davis Strait), and the Norwegian-Barents Sea region in response to OAE in the 21st century under low and high emission scenarios. In addition to the effect of alkalinity addition, which is agnostic to the specific alkaline material added, we also diagnose the effect of nutrient fertilization that would go along with addition of the mineral olivine.

## 2. Methods

### 2.1. Model Description

We use the global ocean general circulation model FESOM2.1 (Danilov et al., 2017; Koldunov et al., 2019; Scholz et al., 2022) coupled to the ocean biogeochemistry model Regulated Ecosystem Model version 3 (REcoM3; Gürses et al., 2023). REcoM3 has 28 prognostic tracers in its standard set-up and simulates the marine carbonate system and air-sea $CO_2$ exchange using the mocsy routines (Orr & Epitalon, 2015). It comprises two phytoplankton classes (silicifying diatoms and small phytoplankton with an implicit representation of calcifiers), three zooplankton groups (microzooplankton, mesozooplankton, polar macrozooplankton; Karakuş et al., 2021) and resolves the cycling of the macronutrients dissolved inorganic nitrogen (DIN) and silicic acid (DSi) and the trace metal dissolved iron (DFe). The variable stoichiometry of REcoM3, that is, variable C:N:Chl:Si for diatoms and C:N:Chl:$CaCO_3$ for small phytoplankton, can, to some extent, represent the physiological response of phytoplankton to changing environmental conditions (light, nutrient availability; Schartau et al., 2007).

### 2.2. Experimental Setup

For this study, we use the so-called CORE mesh with 126,858 surface nodes. It has a resolution of ∼20 km along the Antarctic coast, in the equatorial region and north of 50°N, and a coarser resolution of ∼75 km in the regions with less dynamical variability, for example, in the subtropical ocean basins. In the vertical, it has 47 unevenly spaced z-levels, where layer thickness varies from 5 m at the surface to 250 m in the deep ocean. The timestep used for the simulations is 15 minutes.

As in Gürses et al. (2023), a 189 years long pre-spinup was conducted using a preindustrial atmospheric mixing ratio ($xCO_2$) of 278 ppm until the air-sea $CO_2$ flux reached a quasi-equilibrium state. The spinup used for our model simulations is the continuation of this pre-spinup with increasing atmospheric $CO_2$ and is conducted from 1800 to 1949. These spin-up simulations are forced by the repeating annual cycle of the year 1961 of atmospheric climate data from the JRA-55 reanalysis (Tsujino et al., 2018). Surface alkalinity restoring is switched off in the spin-up simulations and model experiments, in contrast to Gürses et al. (2023).

Following the spin-up, we perform simulations using FESOM2.1-REcoM3 from 1950 to 2100. At the ocean surface, we force the historical and future scenario simulations with the output from the AWI Climate Model (AWI-CM), precisely from its contribution to the “Coupled Model Intercomparison Project Phase 6 (CMIP6)” (Semmler et al., 2020). As in Nissen et al. (2022), the model simulations are forced with 3-hourly atmospheric momentum fluxes, freshwater fluxes, radiation and daily output of terrestrial freshwater runoff from the first ensemble member of the historical simulation until 2014 and of the SSP1-2.6 or SSP3-7.0 from 2015 until 2100 (Semmler et al., 2020).

We use the atmospheric $xCO_2$ from Meinshausen et al. (2017) in the historical simulation from 1950 to 2014, and the atmospheric $xCO_2$ from O’Neill et al. (2016) in the future projections from 2015 to 2100 under the SSP1-2.6 (low-emission) and SSP3-7.0 (high-emission) scenarios. The SSP1-2.6 scenario assumes a gradual reduction in emissions throughout the 21st century, leading to an atmospheric $xCO_2$ mixing ratio of 445.6 ppm by the end of the century. This scenario aligns with efforts to limit global warming to well below 2°C above preindustrial levels, and already includes some CDR. In contrast, the SSP3-7.0 scenario assumes a continuous increase in emissions, resulting in an atmospheric $CO_2$ mixing ratio of 867.2 ppm by the end of the 21st century. This scenario reflects inadequate climate policies and corresponds to a projected global warming of approximately 3–5°C above preindustrial levels by the end of the century (O’Neill et al., 2016).

### 2.3. Identifying Deep and Bottom Water Formation Regions

We use the Water Mass Transformation (WMT) framework to locate the subduction regions in the Southern Ocean (south of 40°S), Northwest Atlantic (50°N–75°N; 70°W–17°W), and the Norwegian-Barents Sea region (62°N–77°N; 60°E−10°W) using the historical simulation over the time period from 1950 to 2014. First introduced by Walin (1982), the framework enables the quantification of the magnitude at which the water in a given density class becomes denser or lighter as a result of diabatic processes such as surface fluxes, diapycnal mixing fluxes in the ocean interior, and the rate of change in the lateral transport and mixing (Abernathey et al., 2016; Nissen et al., 2022). Thus, the transformation rate represents an effective net volume flux across isopycnal surfaces, as water masses must subduct or upwell within a specified density range to ensure mass continuity when the volume flux at the ocean surface is not constant (Abernathey et al., 2016; Pellichero et al., 2018; Walin, 1982).

We relate monthly surface buoyancy fluxes, that is, heat fluxes and freshwater fluxes decomposed into contributions from evaporation minus precipitation (E-P) and sea-ice melting and formation, to the surface density distribution to derive WMT rates. As the density coordinate, we use the potential density referenced to 2,000 dbar ($\rho_2$; Nissen et al., 2022). Results are reported as the density anomaly, that is, $\sigma_2 = \rho_2 - 1{,}000\ \mathrm{kg\ m^{-3}}$. As in Nissen et al. (2022), we divide the surface density field $\rho$ into bins of width 0.025 kg $\mathrm{m^{-3}}$. The heat flux ($Q_{net}$) and freshwater flux ($F_{net}$) transform the water masses at the atmosphere-ocean and ice-ocean interface at a WMT rate (Sv), following

$$WMT(\rho_k, t) = -\frac{1}{\rho_{k+1} - \rho_k} \iint_A \frac{\alpha Q_{net}}{\rho_0 C_p}\, dA + \frac{1}{\rho_{k+1} + \rho_k} \iint_A \frac{\beta S F_{net}}{\rho_0}\, dA. \tag{2}$$

Here, A is the outcrop area between two consecutive density bins $k$ and $k+1$, $\rho_0$ is the reference density (35 kg $m^{-3}$) and $S$ is surface salinity. The coefficients $\alpha$, $C_p$ (3994 J $kg^{-1}$ $K^{-1}$), and $\beta$ are the thermal expansion coefficient, heat capacity, and haline contraction, respectively. The values for $\alpha$, $\beta$ and S were calculated as monthly means over the analysis period (1950–2014). $F_{net}$ is decomposed into freshwater fluxes between atmosphere and ocean ($F_{\mathrm{atm}\rightarrow\mathrm{ocean}}$, evaporation minus precipitation) and between sea ice and ocean ($F_{\mathrm{seaice}\rightarrow\mathrm{ocean}}$, sea-ice formation or melting):

$$F_{net} = F_{\mathrm{atm}\rightarrow\mathrm{ocean}} + F_{\mathrm{seaice}\rightarrow\mathrm{ocean}} \tag{3}$$

Water Mass Formation (WMF) rates are derived from the transformation rates in the chosen regions. The WMF rate is the derivative of the WMT rate with respect to density, and as such, a positive WMF rate represents convergence (downwelling) and a negative WMF rate denotes divergence (upwelling) in the given density bins (Abernathey et al., 2016; Pellichero et al., 2018). Following Abernathey et al. (2016) and Pellichero et al. (2018), the WMF rates are calculated by integrating over density bins of width 0.1 kg $m^{-3}$ for the subduction regions in the Southern Ocean, Northwest Atlantic and the Norwegian-Barents Sea region.

The WMF analysis provides us with density thresholds, which facilitate the localization of the deep and bottom water formation regions in the Southern Ocean, the Northwest Atlantic and the Norwegian-Barents Sea region (Figure 2). The resulting regional olivine deposition mask is shown in Figure 2, with the individual subduction regions shown in red in the individual panels for the Southern Ocean, the Northwest Atlantic and the Norwegian-Barents Sea region. While this analysis framework identifies more regions as contributing to deep and bottom water formation than typically documented in observation-based studies (e.g., coastal regions in Davis Strait), the main formation regions and its processes are adequately captured, as discussed in more detail below.

In the Southern Ocean, subduction/downwelling occurs predominantly due to sea-ice formation in the density bins >37.0 kg $m^{-3}$ (red-shaded regions in Figures 1a and 1b). This range of densities represent the Weddell and Ross Sea, that is, the regions where the formation of Antarctic Bottom Water (AABW) takes place. The AABW formation is characterized by intense cooling and sea-ice formation resulting in dense water masses which eventually sink and spread through abyss of the global ocean (Nissen et al., 2022; Orsi et al., 1999). In the Southern Ocean between 45 and 60°S, Antarctic Intermediate and Subantarctic Mode Water (AAIW and SAMW) masses can be found, whose characteristics are set by the freshwater component of the surface buoyancy fluxes (Cerovečki & Mazloff, 2016; Hartin et al., 2011; Pellichero et al., 2018; Talley, 2008). In agreement with these studies, our model experiment suggests the E-P component of the freshwater flux lead to subduction in the density bins between 35.5 and 36.1 kg $m^{-3}$ (Figures 1a and 1b) which represent the AAIW and SAMW formation region in the Subantarctic (Figure 2a). Buoyancy-induced upwelling in the Southern Ocean occurs between 36.1 and 37 kg $m^{-3}$ (blue-shaded regions in Figures 1a and 1b).

In the North Atlantic, the formation of NADW mainly occurs due to heat loss (Dickson & Brown, 1994; Våge et al., 2009). The Labrador Sea Water formed as a result of deep winter-time convection in the Labrador and the Irminger Sea is entrained by the dense overflow across the Greenland-Scotland ridge and thus contributes to NADW (Jeansson et al., 2023; Våge et al., 2009). The Iceland Sea features a comparatively shallower convection leading to the formation of Iceland Intermediate Waters which also is a component of the NADW (Jeansson et al., 2017). In agreement with observation-based studies, our model also suggests heat to be the main driver for subduction in the Northwest Atlantic in the density bins <35.1 and >36.1 kg $m^{-3}$ (Figures 1c and 1d). Heat loss also governs the subduction occurring in the Norwegian-Barents Sea region at higher densities, that is, in the density bins >36.8 kg $m^{-3}$ (Figures 1e and 1f). Here the intermediate waters formed in the Norwegian Sea resulting from the contribution of Greenland and Iceland intermediate waters eventually contribute to the formation of NADW (Jeansson et al., 2017). Despite the fact that the Barents Sea is a comparatively shallow basin, the formation of Barents Sea Deep water and its lateral deep injection into the Nansen Basin (~1.2 km into the ocean) suggests that the Barents Sea has the potential to contribute to deep-ocean carbon storage in the Arctic (Rogge et al., 2023).

We note that the WMT framework that we use to locate the subduction regions provides only the subduction rates of the water masses in the given regions and density classes. It does not provide any explicit information on how deep a water mass can sink in the ocean, as this further depends on the vertical density structure and the entrainment of lighter water masses. Hence, depending on the model setup, the locations of these regions can

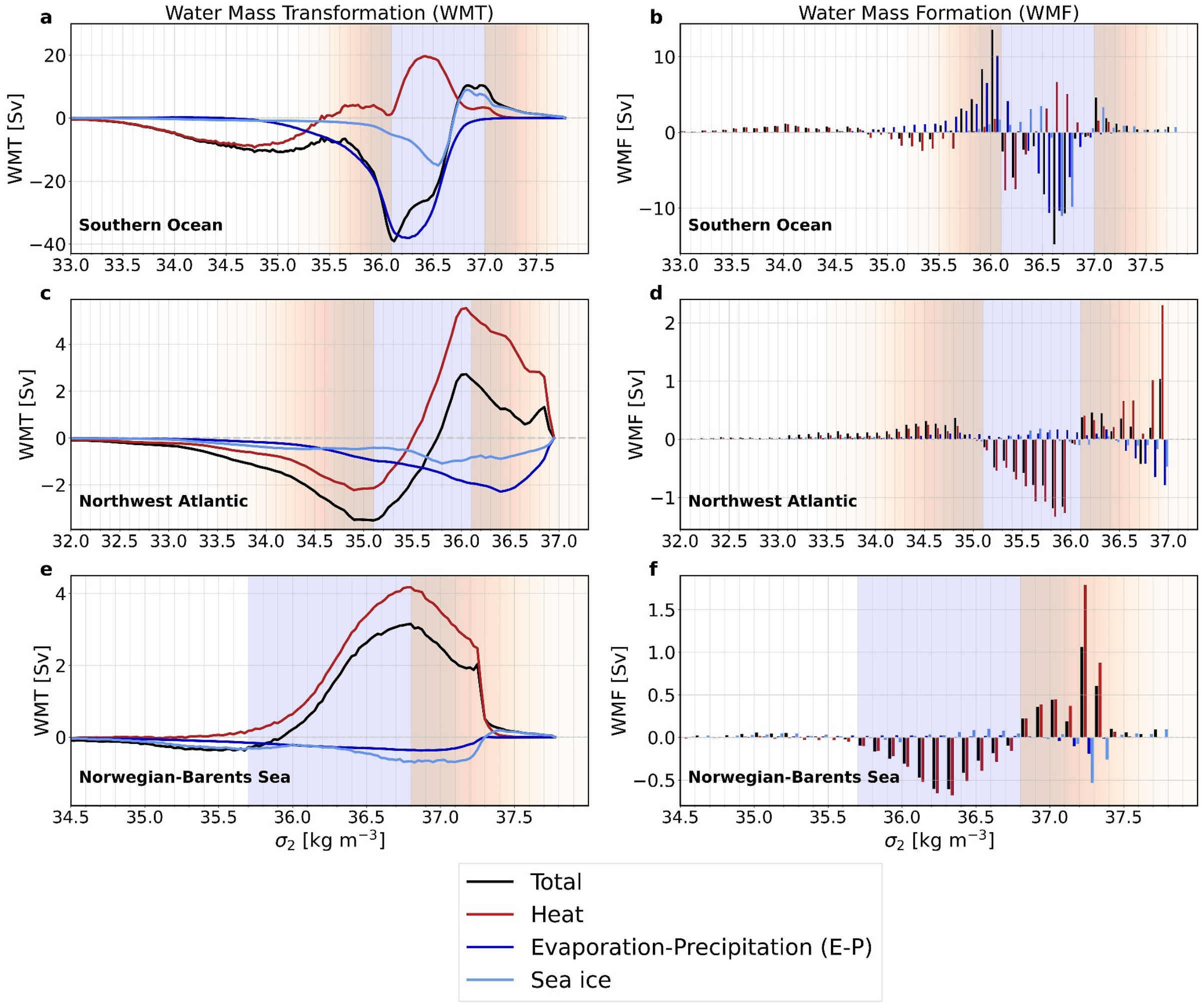

**Figure 1.** Water mass transformation (WMT, left) and Water mass formation (WMF, right) rates for the subduction regions. (a, c, and e) The annual mean surface WMT rates (Sv) integrated over 0.025 kg m$^{-3}$ density bins in panel (a) the Southern Ocean, (c) the Northwest Atlantic, and (e) the Norwegian-Barents Sea region as a function of the potential density anomaly $\rho_2$ (kg m$^{-3}$) due to the total buoyancy flux (black), heat flux (red), evaporation minus precipitation (E-P; dark blue), and the sea-ice induced freshwater flux (light blue). The shading marks the density ranges of downwelling (red) and upwelling (blue). (b, d, and f) The annual mean surface WMF rates (Sv) for the different subduction regions are integrated over 0.1 kg m$^{-3}$ density bins. The total WMF (black bars) results from the contribution of the heat flux (red bars) and the two components of the freshwater flux, that is, E-P (dark blue bars) and sea ice (light blue bars). Positive values represent subduction/downwelling (red shaded regions) and negative values represent upwelling (blue shaded regions).

differ from the real-world geographical locations of deep-water formation. In the context of OAE, we do not only consider subduction that leads to the formation of NADW in the North Atlantic and Antarctic Bottom Water in the Southern Ocean, but also the subduction that contributes to formation of subsurface water masses at intermediate depths. Despite the significant differences in physical conditions among these subduction regions (Dickson & Brown, 1994; Jeansson et al., 2017; Nissen et al., 2022; Orsi et al., 1999; Våge et al., 2009), we aggregate the results of OAE not only across all the sub-regions (Southern Ocean +Northwest Atlantic +Norwegian-Barents Sea region), but also across the sub regions with different dynamics within the Southern Ocean, Northwest Atlantic and the Norwegian-Barents Sea region. We do this to assess the collective potential for carbon uptake and storage in the Southern Ocean as well as the North Atlantic. In the remainder of the manuscript, we acknowledge that this precludes the attribution of OAE impacts to specific sub-regions. Hence, the experimental set-up

AGU ADVANCING EARTH AND SPACE SCIENCES

Earth's Future

10.1029/2023EF004213

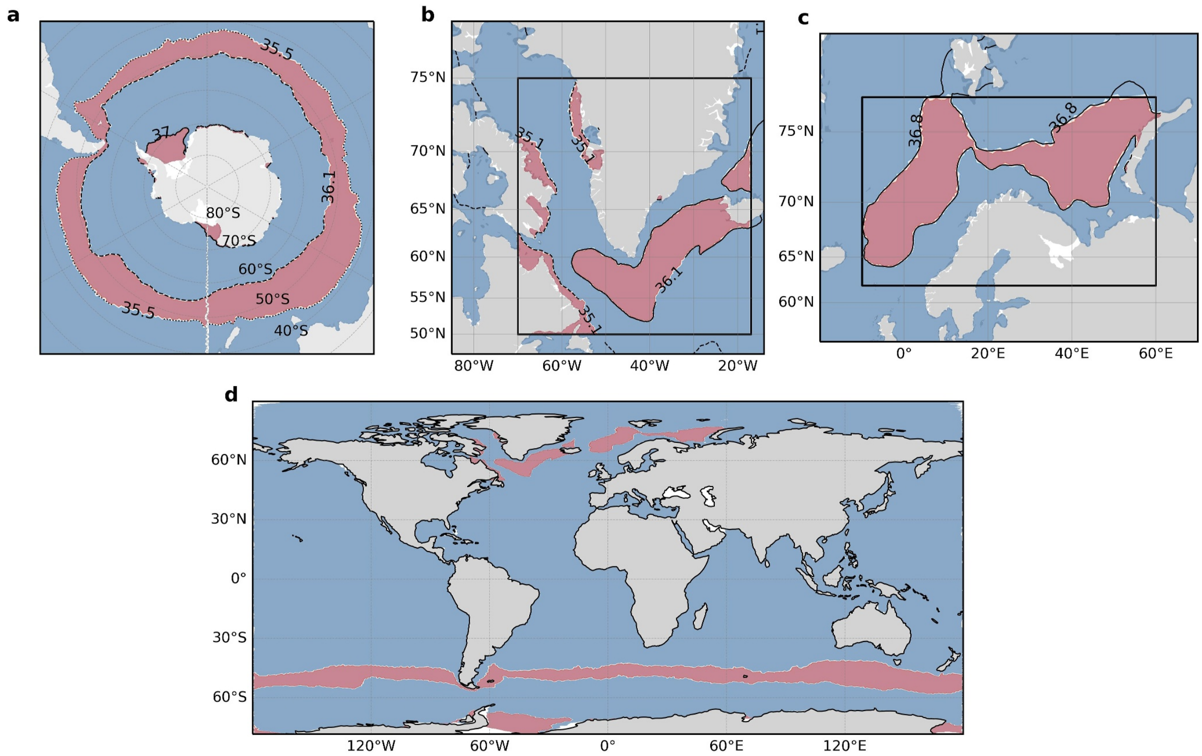

**Figure 2.** The regional mask for olivine deposition, obtained by using the isopycnal outcrops for deep and bottom water formation areas from the water mass formation analysis. (a) Southern Ocean. (b) Northwest Atlantic. (c) Norwegian-Barents Sea region. (d) All subduction regions combined. Red regions represent the olivine deposition areas for regional experiments (see Table 1). The black boxes for the Northwest Atlantic and the Norwegian-Barents Sea region denote the areas considered for the water mass transformation analysis. For the Southern Ocean, we consider the area south of 40°S.

described in the following section is to be understood in the context of the WMT framework applied to our model fields.

### 2.4. Ocean Alkalinity Enhancement Model Experiments

Following the historical simulation over 1950–2014, we conduct two simulations without olivine addition (CTRL) from 2015 to 2100 under the low-emission and the high-emission scenario. We further simulate eight OAE experiments over the period 2030–2100 under both emission scenarios, resulting in a total of 16 OAE experiments (Table 1). These experiments differ in the combinations of alkalinity and nutrient addition and region of application. We branch the OAE experiments from the scenario simulations (CTRL) in 2030 and simulate additions at a constant rate until the end of 2100. For the global simulation, we base the amount of alkalinity addition on the assumption of depositing 3 Pg $yr^{-1}$ of olivine following (Hauck et al., 2016; Köhler et al., 2013). For all experiments, the added olivine is scaled with the modeled sea-ice cover, which is scenario dependent. As a result, the effective amount of olivine entering the ocean surface is slightly lower than 3 Pg $yr^{-1}$ in the global case (same hold for the regional experiments, see Table 1). Thus, following Equation 1, a deposition of 2.89 Pg Olivine $yr^{-1}$ results in 78.80 Tmol $yr^{-1}$ alkalinity enhancement in the global experiments under the SSP3-7.0 scenario, as well as 3.94 Tmol $yr^{-1}$ $Fe^{2+}$ and 19.70 Tmol $yr^{-1}$ Si input in the simulations that account for nutrient addition. Similarly, under the SSP1-2.6 emission scenario, addition of 2.86 Pg Olivine $yr^{-1}$ results in 77.60 Tmol $yr^{-1}$ alkalinity enhancement, 3.88 Tmol $yr^{-1}$ $Fe^{2+}$ and 19.40 Tmol $yr^{-1}$ Si input. Table 1 gives the information about the amount of alkalinity and nutrients deposited for the individual subduction regions. The deposited material is assumed to be in liquid form or to be completely and instantaneously dissolved in the surface ocean. For the regional application, the same amount per area as in the global deposition is applied (8.2 g $m^{-2}$ $yr^{-1}$ olivine; before scaling with sea-ice cover, which leads to 0.21 mol $m^{-2}$ $yr^{-1}$ alkalinity), resulting in a lower total

**Table 1**
*Overview of Model Experiments to Assess Ocean Alkalinity Enhancement for the Period 2030–2100*

| Experiments | Olivine deposited (Pg $yr^{-1}$) | Effective olivine (Pg $yr^{-1}$) |  | Alkalinity (Tmol $yr^{-1}$) |  | $Fe^{2+}$(Tmol $yr^{-1}$) |  | Silicic acid (Tmol $yr^{-1}$) |  | Regions |
|---|---|---|---|---|---|---|---|---|---|---|
|  |  | SSP3-7.0 | SSP1-2.6 | SSP3-7.0 | SSP1-2.6 | SSP3-7.0 | SSP1-2.6 | SSP3-7.0 | SSP1-2.6 |  |
| CTRL | – | – | – | – | – | – | – | – | – | Global |
| GLO-ALK | 3 | 2.89 | 2.86 | 78.80 | 77.60 | – | – | – | – | Global |
| GLO-ALK-NUT | 3 | 2.89 | 2.86 | 78.80 | 77.60 | 3.94 | 3.88 | 19.70 | 19.40 | Global |
| SUB-ALK | 0.22 | 0.21 | 0.21 | 5.72 | 5.72 | – | – | – | – | Subduction regions combined |
| SUB-ALK-NUT | 0.22 | 0.21 | 0.21 | 5.72 | 5.72 | 0.29 | 0.29 | 1.43 | 1.43 | Subduction regions combined |
| SO-ALK | 0.20 | 0.19 | 0.19 | 5.20 | 5.20 | – | – | – | – | Southern Ocean |
| SO-ALK-NUT | 0.20 | 0.19 | 0.19 | 5.20 | 5.20 | 0.26 | 0.26 | 1.30 | 1.30 | Southern Ocean |
| NWA-ALK | 0.014 | 0.013 | 0.012 | 0.35 | 0.33 | – | – | – | – | Northwest Atlantic |
| NBS-ALK | 0.010 | 0.0099 | 0.0098 | 0.27 | 0.26 | – | – | – | – | Norwegian-Barents Sea region |

*Note.* All simulations are conducted for the SSP1-2.6 and SSP3-7.0 scenarios, resulting in 18 model experiments. The following regions are considered: global (GLO), subduction regions combined (SUB), Southern Ocean (SO), Northwest Atlantic (NWA) and Norwegian-Barents Sea region (NBS). While the model is agnostic to the choice of alkaline material with regards to alkalinity addition, the silicic acid and iron content is derived with the assumption of olivine addition. Region-ALK represents simulations with only alkalinity addition and Region-ALK-NUT represents simulations with alkalinity +nutrients (Fe, Si) addition. Effective olivine is the amount of olivine which is deposited at the ocean surface after accounting for the modeled sea-ice cover.

deposition of alkalinity and nutrients (Table 1). Applying it to regions in which high-density water masses are subducted based on an assessment of surface buoyancy fluxes (Section 2.3), this results in a regional alkalinity addition of 5.20 Tmol $yr^{-1}$ (SSP3-7.0 and SSP1-2.6) in the Southern Ocean (Figure 2a), 0.35 Tmol $yr^{-1}$ (SSP3-7.0) and 0.33 Tmol $yr^{-1}$ (SSP1-2.6) in the Northwest Atlantic (Figure 2b), and 0.27 Tmol $yr^{-1}$ (SSP3-7.0) and 0.26 Tmol $yr^{-1}$ (SSP1-2.6) in the Norwegian-Barents Sea region (Figure 2c). We carry out the simulations for the subduction regions individually and combined, in order to differentiate between the efficiency and contribution to carbon uptake of each region independently. When the regions are combined together, the resulting mask (Figure 2d) deposits 5.72 Tmol $yr^{-1}$ alkalinity uniformly.

We perform OAE experiments with alkalinity addition but without nutrient addition for all five regions, globally: GLO, combined subduction regions: SUB, Southern Ocean: SO, Northwest Atlantic: NWA, Norwegian-Barents Sea region: NBS. In addition, we conduct simulations with combined alkalinity and nutrient addition for the global ocean, the area combining all subduction regions and the subduction region in the Southern Ocean. As ~97% of the nutrient fertilization effect in the experiment combining all subduction regions occurs in the SO, we refrain from simulating the impact of nutrient addition separately for the NWA and NBS regions.

### 2.5. Computation of OAE Efficiency Metrics

As a first metric of efficiency, we use the excess air-sea $CO_2$ flux divided by the amount of alkaline material applied after scaling it with the sea-ice cover. This efficiency metric is referred to as CDR potential and has the unit PgC per Pg olivine (Hauck et al., 2016; Köhler et al., 2013). This metric may be considered as a short-term efficiency as it is calculated based on air-sea $CO_2$ flux in the considered period. It is calculated as the difference in the air-sea $CO_2$ flux between the OAE and the CTRL simulation ($\Delta CO_2$ flux), which is then divided by the effective amount of olivine added to the surface ocean that is, accounting for the percentage of the simulated ice-free area at each time-step (15 minutes) in the calculation. We calculate the CDR potential from globally integrated values for the effect of alkalinity addition as well as the combined effect of alkalinity and nutrient addition.

As a second metric, we use the ratio of volume-integrated changes in ocean dissolved inorganic carbon (DIC) to volume-integrated alkalinity (Burt et al., 2021; Renforth & Henderson, 2017). This metric is known as $\eta CO_2$ ($\Delta DIC/\Delta Alk$, unitless) and is agnostic to the alkaline material used and mode of application of OAE. It is thus highly comparable between different studies of OAE. The volume-integrated $\Delta DIC$ and $\Delta Alk$ quantify the total accumulation of DIC and alkalinity since the beginning of the alkalinity enhancement, and $\eta CO_2$ can thus be considered as a long-term efficiency metric. Specifically, $\eta CO_2$ is computed as the difference in volume-integrated DIC between the OAE and the CTRL simulations divided by the difference in volume-integrated alkalinity between the OAE and the CTRL simulations. Thus, the effect of sea ice on alkalinity addition is accounted for. This metric ($\eta CO_2$) targets carbonate chemistry specifics, hence, it cannot be applied to quantify the nutrient effect. As for the CDR potential, we calculate $\eta CO_2$ from globally integrated values.

## 3. Results

### 3.1. $CO_2$ Flux and OAE Efficiencies

Without perturbing the oceans (CTRL), the oceanic $CO_2$ uptake reaches 4.52 and 0.34 PgC $yr^{-1}$ over the last decade of the century in the SSP3-7.0 and SSP1-2.6 scenarios, respectively. OAE results in additional carbon uptake under both emission scenarios, and air-sea $CO_2$ flux scales to first order with the amount of alkalinity added. In general, the excess $CO_2$ uptake is higher in SSP3-7.0 than in SSP1-2.6, when only alkalinity addition is simulated globally and in the subduction regions (Figures 3a and 3b). For example, the global $CO_2$ uptake (GLO-ALK) increases by 0.9 PgC $yr^{-1}$ for SSP3-7.0 and by 0.8 PgC $yr^{-1}$ for SSP1-2.6 (Table 2). The SUB-ALK and SO-ALK experiments that cover 7.5% and 6.6% of the global surface ocean area, exhibit very similar excess $CO_2$ uptake of 0.05–0.07 PgC $yr^{-1}$ (SSP3-7.0) and 0.05–0.06 PgC $yr^{-1}$ (SSP1-2.6). The NWA-ALK and NBS-ALK that cover only 0.45% and 0.33% of global surface ocean area have the lowest excess $CO_2$ uptake (~0.003 PgC $yr^{-1}$). In the simulations with nutrient addition, biological productivity is enhanced, thus leading to a higher carbon uptake than in the 'only alkalinity' simulations. The global simulations (GLO-ALK-NUT) under both emission scenarios have equal increase in the $CO_2$ uptake (1.24 PgC $yr^{-1}$) which is a factor of 1.4 higher than in GLO-ALK. The excess $CO_2$ uptake in SUB-ALK-NUT and SO-ALK-NUT again are comparable in magnitude. Interestingly, the sensitivity to emission scenarios is reversed for the nutrient effect, as the excess $CO_2$ uptake is marginally higher in the SSP1-2.6 than in the SSP3-7.0 scenario (Figures 3a and 3b).

The CDR potential, defined as the excess air-sea $CO_2$ flux per unit of olivine deposited in the sea surface after scaling with the sea-ice cover ($\Delta CO_2$ flux (PgC) per Pg olivine; Köhler et al. (2013)) differs substantially between the simulations with only alkalinity and with alkalinity +nutrient addition (Figures 3c and 3d). Simulating only alkalinity addition, globally or in the subduction regions, the CDR potential is marginally higher in SSP3-7.0 than in SSP1-2.6, as expected from the higher $CO_2$ uptake. Regional differences in the CDR potential are small with the CDR potential ranging from 0.23 to 0.27 PgC per Pg olivine for SSP1-2.6 and from 0.29 to 0.31 PgC per Pg olivine for SSP3-7.0 for the global oceans and the subduction regions (Figures 3c and 3d, Table 2).

With the addition of nutrients, the CDR potential in SSP1-2.6 is slightly higher than in SSP3-7.0 in the subduction regions (SUB-ALK-NUT and SO-ALK-NUT), while no sensitivity to emission scenario is discernible in the global application case (Figures 3c and 3d; Table 2). The nutrient effect differs strongly between regions. As expected, the SO-ALK-NUT has the highest CDR potential of 1.06 PgC per Pg olivine for SSP1-2.6 and 1.00 PgC per Pg olivine for SSP3-7.0, that is ~2.3–2.5 times that of their respective global simulations (Figure 3d and Table 2). This is predominantly due to the iron fertilization occurring in the Southern Ocean between 40°–50°S, where 73% of the total CDR potential can be explained by the nutrient effect. In contrast, for GLO-ALK-NUT, alkalinity accounts for 61% and nutrient fertilization for 39% of the total CDR potential.

As with the CDR potential, $\eta CO_2$ (long-term efficiency $\Delta DIC/\Delta Alk$) is higher under the SSP3-7.0 than SSP1-2.6 scenario for the global and the subduction regions experiments (Table 2). The GLO-ALK, SUB-ALK, SO-ALK and NWA-ALK experiments exhibit indistinguishable $\eta CO_2$ values of 0.84–0.85 (SSP3-7.0) and 0.79–0.80 (SSP1-2.6). Of the subduction regions, the lowest $\eta CO_2$ levels (0.65–0.75) occur in the Norwegian-Barents Sea region (NBS-ALK) (Figures 3e and 3f). Thus, both efficiency metrics point to an insensitivity of OAE to deployment region, with the exception of $\eta CO_2$ in the Norwegian-Barents Sea region.

Substantial differences are observed between the spatial patterns of $CO_2$ flux increase for OAE experiments with and without nutrient addition relative to the CTRL simulations (Figure 4). The excess $CO_2$ flux is confined to the regions of alkalinity addition, with a nearly uniform distribution throughout the OAE deployment areas (Figures 4a and 4b). In the simulations with nutrient addition, the Southern Ocean exhibits the highest increase in carbon uptake due to elevated iron fertilization (Figures 4c and 4d; Hauck et al. (2016)). However, while higher carbon uptake in GLO-ALK-NUT is observed nearly everywhere south of 40°S, enhanced $CO_2$ uptake in SUB-

AGU ADVANCING EARTH AND SPACE SCIENCES

Earth's Future

10.1029/2023EF004213

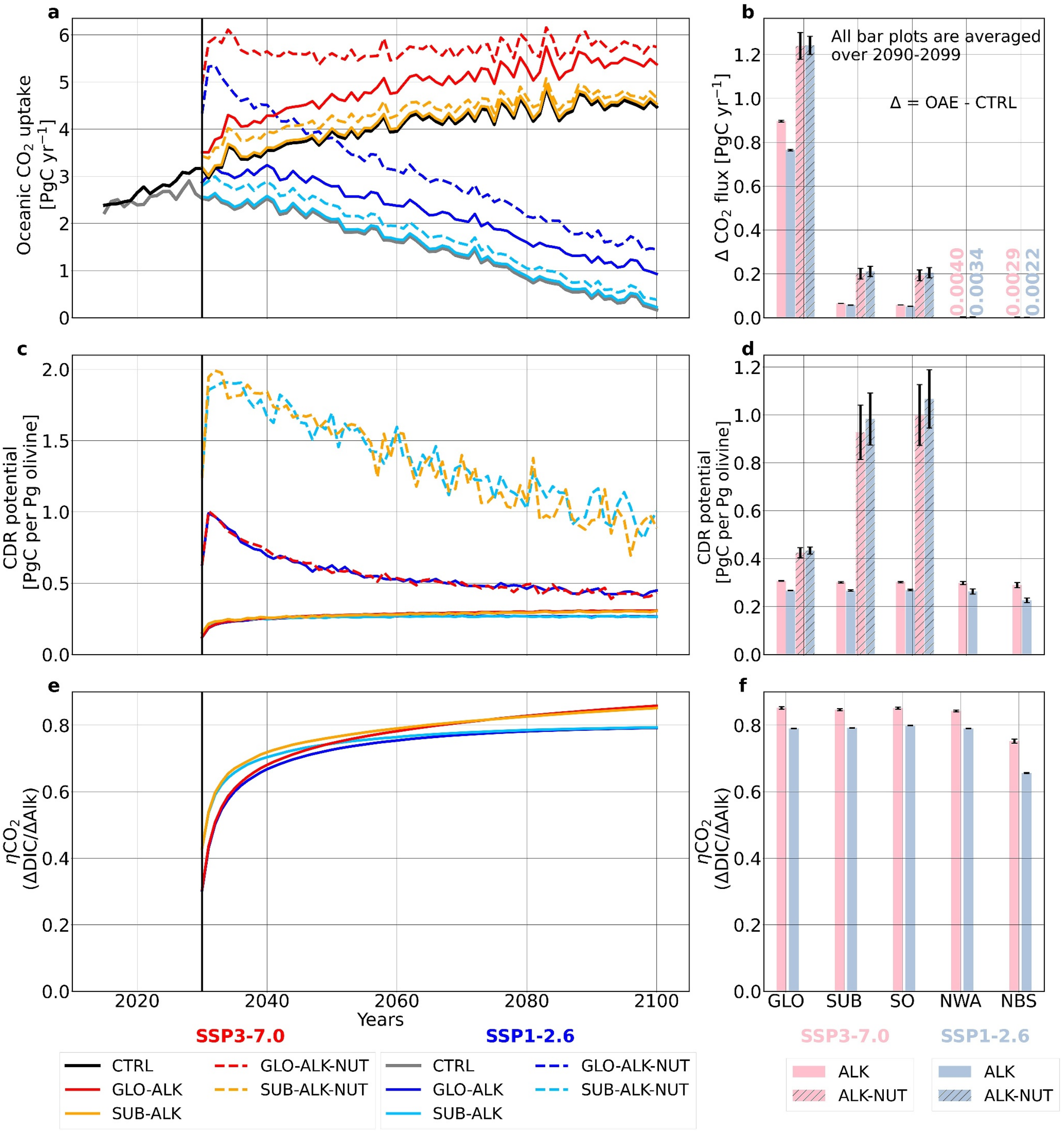

**Figure 3.** Response of ocean $CO_2$ uptake to ocean alkalinity enhancement (OAE) (Left column) Timeseries for (a) Oceanic $CO_2$ uptake (PgC $yr^{-1}$), positive values indicate a flux into the ocean, (c) Short term Carbon Dioxide Removal (CDR) potential (PgC $CO_2$ flux per Pg olivine) and (e) Long term OAE efficiency ($\eta CO_2$ (unitless); $\Delta DIC/\Delta Alk$ integrated over the entire water column), under SSP1-2.6 (blue colors) and SSP3-7.0 (red colors). OAE experiments with only alkalinity addition are shown by solid lines and the experiments with alkalinity and nutrient addition by dashed lines. (Right column) Bar plots representing the average over 2090–2099 of (b) $\Delta CO_2$ flux, (d) CDR potential and (f) $\eta CO_2$ under SSP1-2.6 (light blue bars) and SSP3-7.0 (pink bars). Solid bars show simulations with only alkalinity addition, while hatched bars denote combined alkalinity and nutrient addition. Error bars show the standard deviation over the 2090–2099 period for the respective time series. See Table 1 for details on the model experiments.

**Table 2**

*Excess Oceanic* $CO_2$ *Uptake (*$\Delta CO_2$ *Flux), Dissolved Inorganic Carbon (ΔDIC) in the Top 1 km and >1 km, Surface Alkalinity (ΔAlk), Diatom and Small Phytoplankton Net Primary Production (ΔNPPd and ΔNPPn) and Calcification Due To Ocean Alkalinity Enhancement With Respect to the CTRL Simulations*

| | | ΔDIC (PgC) | | | | | | | | |
|---|---|---|---|---|---|---|---|---|---|---|
| Experiments | $\Delta CO_2$ flux (PgC yr$^{-1}$) | Top 1 (km) | >1 (km) | ΔDIC >1 km (%) | Surface ΔAlk (mmol m$^{-3}$) | ΔNPPd (PgC yr$^{-1}$) | ΔNPPn (PgC yr$^{-1}$) | ΔCalc (PgC yr$^{-1}$) | CDR pot (PgC per Pg olivine) | $\eta CO_2$ ΔDIC ΔAlk |
| SSP3-7.0 | | | | | | | | | | |
| GLO-ALK | 0.9 | 50.95 | 1.73 | 3.3 | 35.62 | – | – | – | 0.31 | 0.85 |
| SUB-ALK | 0.07 | 3.70 | 0.25 | 6.3 | 3.75 | – | – | – | 0.30 | 0.85 |
| SO-ALK | 0.05 | 3.40 | 0.15 | 4.2 | 3.76 | – | – | – | 0.30 | 0.85 |
| NWA-ALK | 0.004 | 0.20 | 0.06 | 23.1 | 3.25 | – | – | – | 0.30 | 0.84 |
| NBS-ALK | 0.003 | 0.12 | 0.05 | 29.4 | 2.41 | – | – | – | 0.29 | 0.75 |
| GLO-ALK-NUT | 1.24 | 69.51 | 32.43 | 31.8 | 26.84 | 3.53 | 5.91 | 0.13 | 0.43 | – |
| SUB-ALK-NUT | 0.20 | 11.10 | 7.12 | 39.0 | 4.94 | 0.70 | 0.44 | 0.01 | 0.93 | – |
| SO-ALK-NUT | 0.19 | 10.74 | 7.00 | 39.5 | 5.06 | 0.68 | 0.44 | 0.01 | 1.00 | – |
| SSP1-2.6 | | | | | | | | | | |
| GLO-ALK | 0.8 | 46.54 | 2.11 | 4.3 | 33.28 | – | – | – | 0.27 | 0.79 |
| SUB-ALK | 0.06 | 3.41 | 0.30 | 8.1 | 3.62 | – | – | – | 0.27 | 0.79 |
| SO-ALK | 0.05 | 3.15 | 0.20 | 5.9 | 3.67 | – | – | – | 0.27 | 0.80 |
| NWA-ALK | 0.003 | 0.17 | 0.06 | 26.1 | 2.91 | – | – | – | 0.26 | 0.79 |
| NBS-ALK | 0.002 | 0.10 | 0.05 | 33.3 | 2.09 | – | – | – | 0.23 | 0.65 |
| GLO-ALK-NUT | 1.24 | 67.31 | 33.90 | 33.5 | 24.70 | 4.32 | 6.60 | 0.15 | 0.43 | – |
| SUB-ALK-NUT | 0.21 | 11.10 | 7.44 | 40.1 | 4.85 | 0.67 | 0.36 | 0.01 | 0.98 | – |
| SO-ALK-NUT | 0.20 | 10.82 | 7.31 | 40.3 | 5.02 | 0.66 | 0.37 | 0.01 | 1.06 | – |

*Note.* Short-term Carbon Dioxide Removal (CDR) potential is calculated as increase in $CO_2$ flux per alkaline material added (PgC per Pg olivine) and $\eta CO_2$ is the volume-integrated excess DIC over volume-integrated excess alkalinity (see Section 2.5). Efficiency metrics are calculated over the global ocean and all numbers are averaged over 2090–2099.

ALK-NUT is confined to the regions of alkalinity enhancement in the Southern Ocean, with some partly compensating reduction of carbon uptake between 60°-70°S.

### 3.2. Carbon Transferred to the Deep Ocean in the Form of Dissolved Inorganic Carbon (DIC)

To estimate the carbon storage potential of the subduction regions relative to the global ocean, we evaluate the enhancement in deep-ocean carbon inventory. Simulating OAE with or without nutrient addition substantially influences the amount of carbon transferred to the deep ocean (Figure 5). For GLO-ALK, the DIC inventory increases by 50.95 PgC in the top 1 km and by 1.73 PgC below 1 km compared to the CTRL under the SSP3-7.0 scenario (Figure 5a). Owing to the smaller surface area for alkalinity addition in SUB-ALK, the DIC storage increases by a lower amount, namely 3.70 PgC in top 1 km and by 0.25 PgC below 1 km (Figure 5b). Thus, 3.3% of the total ΔDIC storage in GLO-ALK occurs below 1 km, whereas the proportion rises to 6.3% for SUB-ALK. Hence, we conclude that the carbon transferred to the deep ocean is nearly twice as high for OAE in the subduction regions than in the global case (Figures 5a and 5b). In the Northwest Atlantic and Norwegian-Barents Sea region, ~25%–30% of the total carbon taken up reached below 1 km, thus making them the most effective regions for deep ocean carbon storage (Table 2).

In simulations with nutrient addition, carbon storage within the top 1 km rises by 26% for GLO-ALK-NUT and 66% for SUB-ALK-NUT compared to the respective experiments without nutrients. Due to the efficient downward transport of the biological carbon pump, carbon storage below the 1 km threshold increases by 94% in GLO-ALK-NUT and 96.5% in SUB-ALK-NUT (Figures 5c and 5d; Table 2). In the GLO-ALK-NUT experiment, the deepest carbon penetration to about ~5 km occurs in the Southern Ocean, primarily due to stimulation of

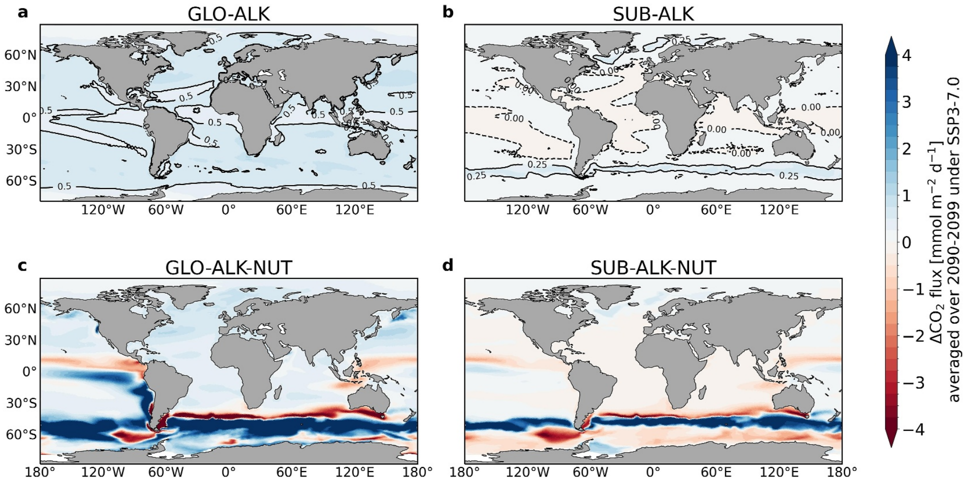

**Figure 4.** Spatial patterns of the difference in the $CO_2$ flux with respect to the CTRL run ($\Delta CO_2$ flux), averaged over 2090–2099 for the SSP3-7.0 scenario for four experiments: (a) GLO-ALK, (b) SUB-ALK, (c) GLO-ALK-NUT, (d) SUB-ALK-NUT. Positive values (blue color) represent enhanced $CO_2$ uptake and negative values (red color) represent reduced $CO_2$ uptake compared to the CTRL simulation. See Figure S1 in Supporting Information S1 for the SSP1-2.6 scenario.

biological activity in response to nutrient fertilization (Figure 5c). Of the total increase in DIC storage relative to the CTRL, 31.8% occurs below 1 km in the GLO-ALK-NUT, while for SUB-ALK-NUT the proportion is 39%. In the SUB-ALK-NUT experiment, of the three considered subduction regions, the Southern Ocean is the dominant contributor to the carbon transfer to a depth of ~2 km (Figure 5d). Similar conclusions can be drawn for the SSP1-2.6 scenario, where the increase in DIC storage compared to CTRL in the top 1 km has lower values globally and regionally than in the SSP3-7.0 scenario. However, more carbon is stored below 1 km (Table 2) under SSP1-2.6 than under SSP3-7.0 scenario. This can be attributed to the more stratified ocean in the higher emission scenario than in the lower emission scenario (Gattuso et al., 2015).

### 3.3. Net Primary Production (NPP)

Addition of nutrients leads to an increase in total Net Primary Production (NPPt) in the global and subduction region OAE experiments under both emission scenarios (Figure 6). For the GLO-ALK-NUT experiment, the increase in NPPt relative to CTRL simulation (ΔNPPt), amounts to 10.9 PgC yr$^{-1}$ (SSP1-2.6) and 9.4 PgC yr$^{-1}$ (SSP3-7.0) averaged over 2090–2099. As expected due to the smaller surface ocean area, the increase in NPPt for SUB-ALK-NUT is smaller, namely 1.0 and 1.1 PgC yr$^{-1}$ in the two emission scenarios (Figure 6a). Small phytoplankton, with an implicit representation of calcification, dominate the NPPt increase with a relative contribution of 67.4% in the global experiment. In contrast, diatoms dominate the NPPt increase in the subduction region experiments with a 63.6% contribution (Figure 6b).

The spatial distribution of changes in primary productivity shows that the increase in NPPt for GLO-ALK-NUT occurs largely in the southern subtropical Pacific and the Southern Ocean (Figure 7a). The southern subtropical Pacific basin shows the largest increase in NPPn compared to other basins (Figure 7e), whereas ΔNPPd increases most in the Southern Ocean, and to a smaller extent in the equatorial Pacific, which we relate to weakened iron limitation (Figure 7c). In the SUB-ALK-NUT experiment, the increase in NPP occurs mostly in the Southern Ocean regions of alkalinity enhancement and in the equatorial upwelling region, while the subduction regions in the Northwest Atlantic and the Norwegian-Barents Sea region show no response to nutrient addition (Figure 7b). Small phytoplankton and diatom NPP exhibit similar spatial patterns, except for the signal in the equatorial Pacific basin, caused by small phytoplankton NPP (NPPn) (Figures 7d–7f).

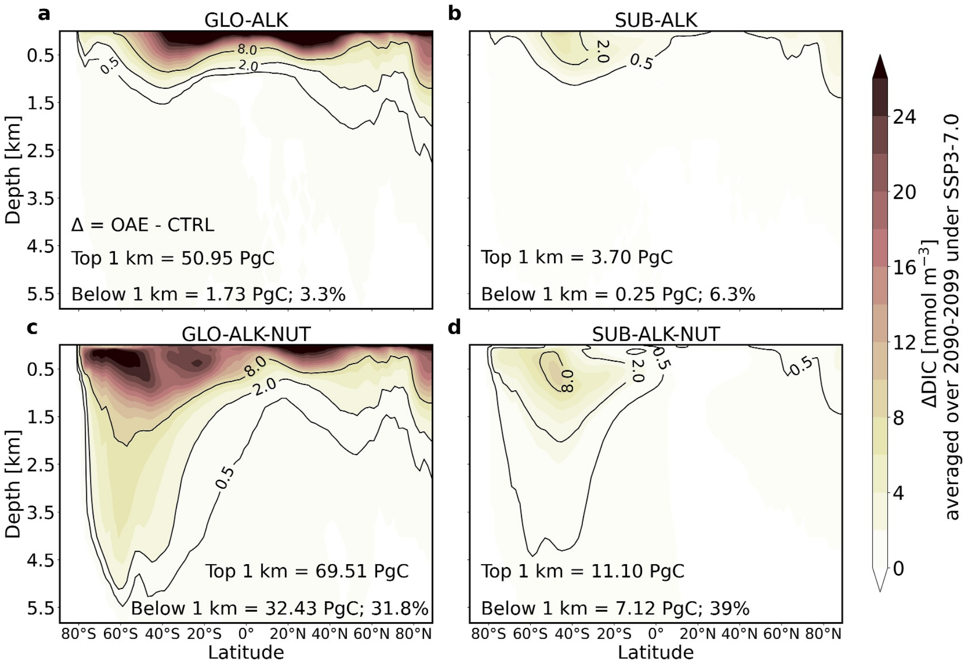

**Figure 5.** Zonal mean of the increase in dissolved inorganic carbon concentrations in the ocean alkalinity enhancement experiments with respect to the CTRL run (ΔDIC), averaged over 2090–2099 for SSP3-7.0 scenario for four experiments: (a) GLO-ALK, (b) SUB-ALK, (c) GLO-ALK-NUT and (d) SUB-ALK-NUT. See Figure S2 in Supporting Information S1 for the SSP1-2.6 scenario.

### 3.4. Surface Alkalinity and Calcification

The increase in surface alkalinity compared to the CTRL simulation scales largely with the amount of alkaline material added and thus with the areas of application, with a second-order difference between the emission scenarios. In SUB-ALK, the excess surface alkalinity per area is lower than in GLO-ALK, despite equal amounts of alkalinity being added per area. This decrease can be attributed to dilution and the loss of alkalinity to deeper ocean layers within the subduction regions (Figures 9a and 9b). Surface alkalinity also shows pronounced differences for OAE with or without nutrient addition (Figure 8). For GLO-ALK, surface alkalinity increases by

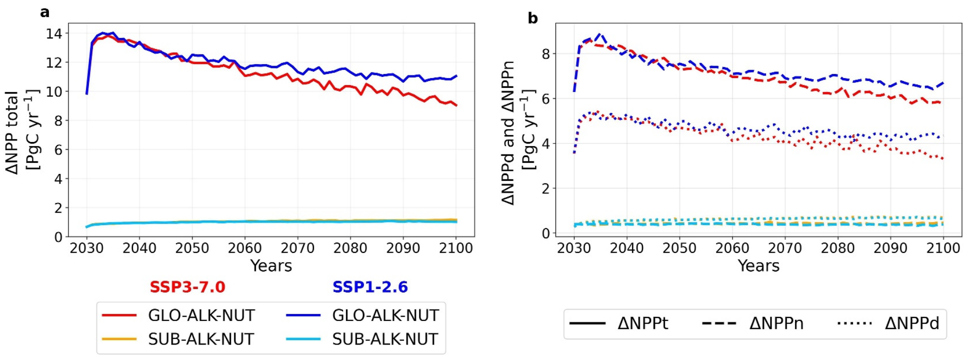

**Figure 6.** (a) Timeseries for excess total net primary production (NPPt) relative to the CTRL simulations (ΔNPPt; solid lines) in the ocean alkalinity enhancement experiments in PgC yr$^{-1}$ for GLO-ALK-NUT and SUB-ALK-NUT under the SSP3-7.0 (red colors) and SSP1-2.6 (blue colors) scenarios. (b) Excess small phytoplankton NPP (ΔNPPn; dashed lines) and diatom NPP (ΔNPPd; dotted lines) for GLO-ALK-NUT and SUB-ALK-NUT.

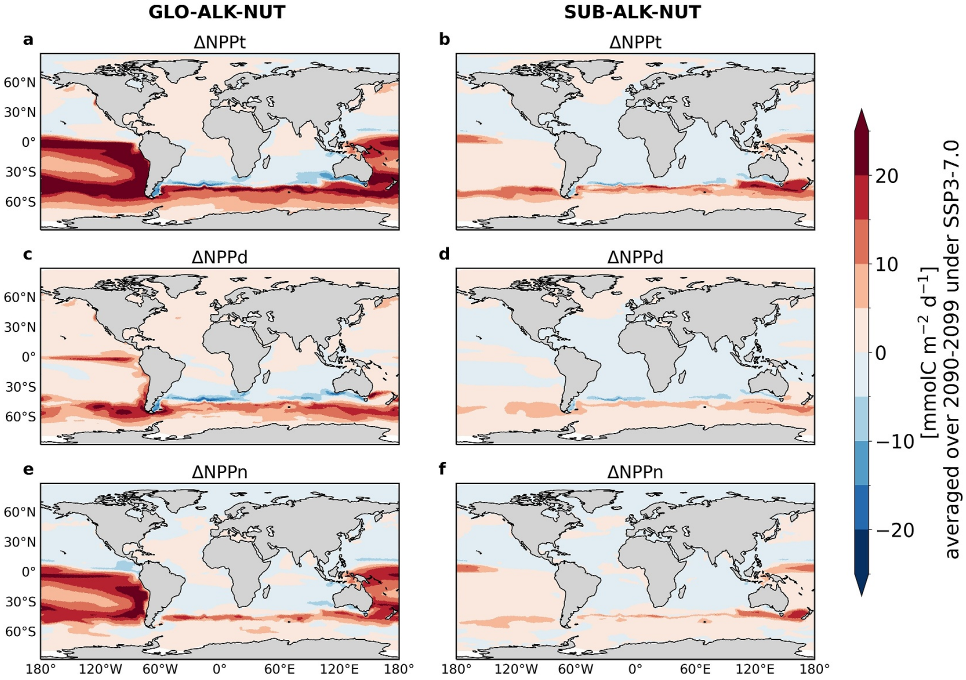

**Figure 7.** Spatial distribution of the excess total net primary production (ΔNPPt), diatom NPP (ΔNPPd), and small phytoplankton NPP (ΔNPPn) in the ocean alkalinity enhancement experiments relative to the CTRL simulation, averaged over 2090–2099 for the SSP3-7.0 scenario (a, c, and e) ΔNPPt, ΔNPPd, and ΔNPPn for GLO-ALK-NUT (b, d, and f) ΔNPPt, ΔNPPd, and ΔNPPn for SUB-ALK-NUT. See Figure S3 in Supporting Information S1 for the SSP1-2.6 scenario.

35.62 mmol $m^{-3}$ (SSP3-7.0) and 33.28 mmol $m^{-3}$ (SSP1-2.6) (Table 2). We relate these differences to distinct mixed layer and circulation between the emission scenarios. The alkalinity increase is dampened by concomitant nutrient addition and amounts to 26.84 mmol $m^{-3}$ (SSP3-7.0) and 24.70 mmol $m^{-3}$ (SSP1-2.6) in GLO-ALK-NUT. The 34% higher surface alkalinity in GLO-ALK than in GLO-ALK-NUT can be explained by the disproportional stimulation of small phytoplankton productivity in GLO-ALK-NUT (Figure 6b). As a result, the calcification rate is ~23% higher in GLO-ALK-NUT than in GLO-ALK, which reduces the surface alkalinity (Figure 8; Figure 9e; Table 2).

In contrast, the excess surface alkalinity in the 2090s in the subduction region experiments is 24%–25% lower in SUB-ALK than in SUB-ALK-NUT (both emission scenarios, Figure 8; Table 2). Again, this is related to the ratio of NPPd to NPPn increase, with a stronger contribution of diatoms to the total change in NPP in the subduction region experiments (Figure 9d). This results in a positive feedback for surface alkalinity due to a higher productivity from diatoms because nitrogen assimilation of both phytoplankton groups generates alkalinity (Figure 6b). While calcification from an increase in small phytoplankton productivity would overcompensate this alkalinity generation, this is not the case for diatoms. Thus, the resulting calcification is not sufficient to reduce surface alkalinity in SUB-ALK-NUT to levels lower than in SUB-ALK, in contrast to the global experiments (Figure 9f). The Southern Ocean features a higher increase in surface alkalinity compared to other subduction regions, under both alkalinity-only and alkalinity +nutrients simulations (Table 2). As the same amount of alkalinity per surface area was added in all regions, this has to be a result of dilution by advection and mixing that is stronger in the northern hemisphere subduction regions.

### 3.5. Seasonality of Olivine Deposition

Ocean alkalinity enhancement leads to a response in surface alkalinity, $CO_2$ uptake, NPP, and DIC accumulation that varies seasonally (Figure 10). We calculate the seasonality in these parameters as the average over the regions of alkalinity addition only (Figures 2a–2c). As a consequence of alkalinity deposition being scaled with sea-ice

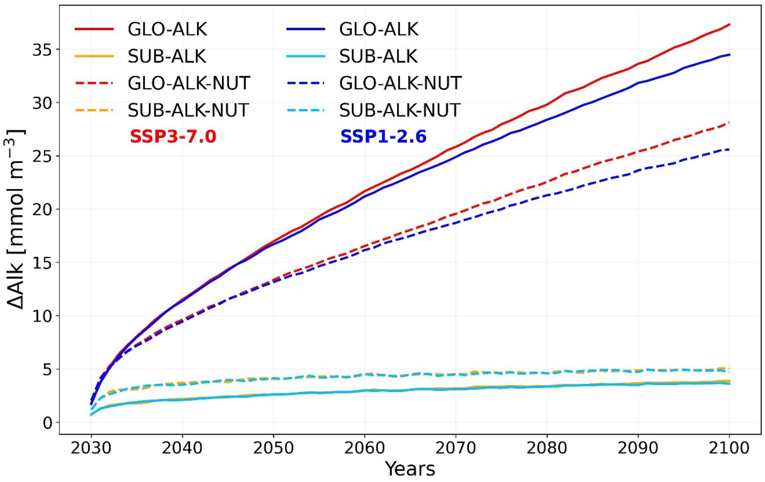

**Figure 8.** Timeseries of excess surface alkalinity in the ocean alkalinity enhancement experiments relative to the CTRL simulation under the SSP3-7.0 (red colors) and SSP1-2.6 (blue colors) emission scenarios. The experiments shown are GLO-ALK and SUB-ALK (solid lines), GLO-ALK-NUT and SUB-ALK-NUT (dashed lines).

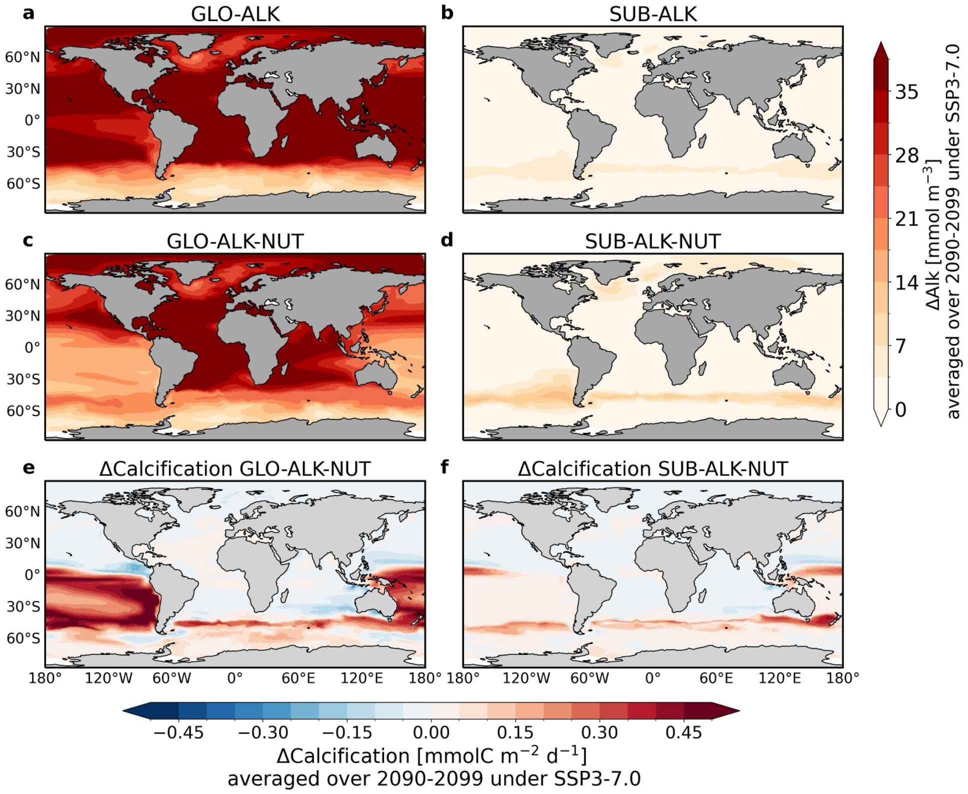

**Figure 9.** Spatial patterns of excess surface alkalinity and calcification in ocean alkalinity enhancement experiments relative to CTRL averaged over the years 2090–2099 under the SSP3-7.0 scenario. ΔAlk is shown for the experiments (a) GLO-ALK, (b) SUB-ALK, (c) GLO-ALK-NUT, (d) SUB-ALK-NUT and ΔCalcification for (e) GLO-ALK-NUT and (f) SUB-ALK-NUT. See Figure S4 in Supporting Information S1 for SSP1-2.6 scenario.

cover, olivine addition is at its minimum when sea-ice cover peaks in the Southern Ocean winter (July-September; Figures 10a–10c). For the Norwegian-Barents Sea region, olivine addition is almost constant throughout the year except during March-April when it is lower as the sea-ice cover increases (Figures 11a–11d). Irrespective of the seasonal variations in the alkalinity addition, the excess surface alkalinity is in phase with the seasonal changes in the Mixed Layer Depth (MLD) in both hemispheres. We quantify MLD in our model by identifying the depth at which the potential density of the water column exceeds the sea surface potential density by 0.03 kg $m^{-3}$. As the MLD begins to shoal in the summer months (December-April: Southern Ocean, and June-October: North Atlantic), the surface alkalinity increases more strongly relative to CTRL due to reduced mixing thus a low loss of excess alkalinity to the deep ocean (Figures 10b, 10e, and 10f; Figures 11b and 11e). In contrast, in the winter months, the deeper MLD leads to a lower ΔAlk concentration for both hemispheres (Figures 10b, 10e, and 10f; Figures 11b and 11e). As high excess surface alkalinity results in high excess $CO_2$ uptake, the dominant driver of CDR efficiency is MLD and its seasonal variations. We note that the simulated winter MLD in the Northwest Atlantic and specifically in the Labrador Sea is <150 m in our model, which is lower than observation-based estimates (1,000–1,550 m; Lavender et al. (2002); Lorbacher et al. (2006); Figures S7 and S8 in Supporting Information S1). This model bias is possibly due to a combination of biases in the simulated distributions of temperature and salinity in the ocean (and thus stratification) and biases in the atmospheric fields used to force our ocean-only simulations (Semmler et al., 2020). Thus, the simulated shallow MLD due to this bias in the Northwest Atlantic regions implies that our model might underestimate the excess carbon uptake and storage capacity from OAE in this region.

Evidently, the increase in the $CO_2$ flux relative to CTRL ($\Delta CO_2$ flux) follows the seasonal variation of the increase in surface alkalinity (ΔAlk) and thus MLD in the Southern Ocean as well as in the North Atlantic (Figures 10b and 10e–10h; Figures 11b, 11c, and 11e). For the SO-ALK simulation, the highest $\Delta CO_2$ flux occurs in the months of February to May with a few months lag after the MLD minimum, while the minimum is found during August to December period, again with a few months lag after the MLD maximum (Figures 10e and 10g). When including the nutrient effect (SO-ALK-NUT), $\Delta CO_2$ flux is higher than in SO-ALK due to the excess phytoplankton production (Figure 10d). Here, the maximum additional uptake occurs during December to February and the minimum during July to September (Figure 10h). Hence, when the nutrients are included, the seasonality in excess carbon uptake relative to CTRL is shifted from April in SO-ALK to December as this is when primary production peaks in SO-ALK-NUT. In the North Atlantic, the maximum $\Delta CO_2$ flux occurs between August and October after MLD had been at its minimum for about 3 months. The minimum $\Delta CO_2$ flux is found between March and May for the NBS-ALK and NWA-ALK experiments (Figures 11e and 11c for Norwegian-Barents Sea region, see Figures S7 and S8 in Supporting Information S1 for the seasonality in the Northwest Atlantic).

In order to assess the seasonal cycle of excess DIC accumulation compared to the CTRL simulation (ΔDIC), we calculate the difference in ΔDIC between the consecutive months for the period December 2089 to December 2099. Afterward, the ΔDIC accumulation is averaged over the 10 year period as for the other metrics. The seasonality in ΔDIC accumulation is strongly influenced by the seasonality in the $\Delta CO_2$ flux for the simulations in the Southern Ocean (Figures 10g–10j) and the North Atlantic (Figures 11c and 11f). The top 0.5 km layer strongly follows the variations of the $\Delta CO_2$ flux, while the intermediate (0.5–1 km) and the bottom (>1 km) layer have only a weak seasonal cycle for all the simulations. High surface ΔDIC accumulation is observed between January and April for the Southern Ocean and between August to October in the North Atlantic regions. The deepening of the mixed layer over the winter months results in negative ΔDIC accumulation, where the $CO_2$ uptake happening at the surface ocean in the particular region is not sufficient to increase the DIC concentration in the water column. The lateral transport of the water masses leads to advection of DIC outside the regions of consideration, thereby reducing the DIC to levels below those in the CTRL simulation (Figures 10i and 10j; Figure 11f). For the NBS-ALK experiment, the signal below 0.5 km can be assumed to mainly stem from the Norwegian Sea as the Barents Sea is shallower than 400 m (Figure 11f), but we note that the latter has also been shown to contribute to deep-ocean carbon transfer through lateral transport (Rogge et al., 2023). In the case of SO-ALK-NUT, the negative ΔDIC accumulation is larger due to enhanced respiration and remineralization in response to the nutrient fertilization (Figure 10j).

AGU ADVANCING EARTH AND SPACE SCIENCES

Earth's Future

10.1029/2023EF004213

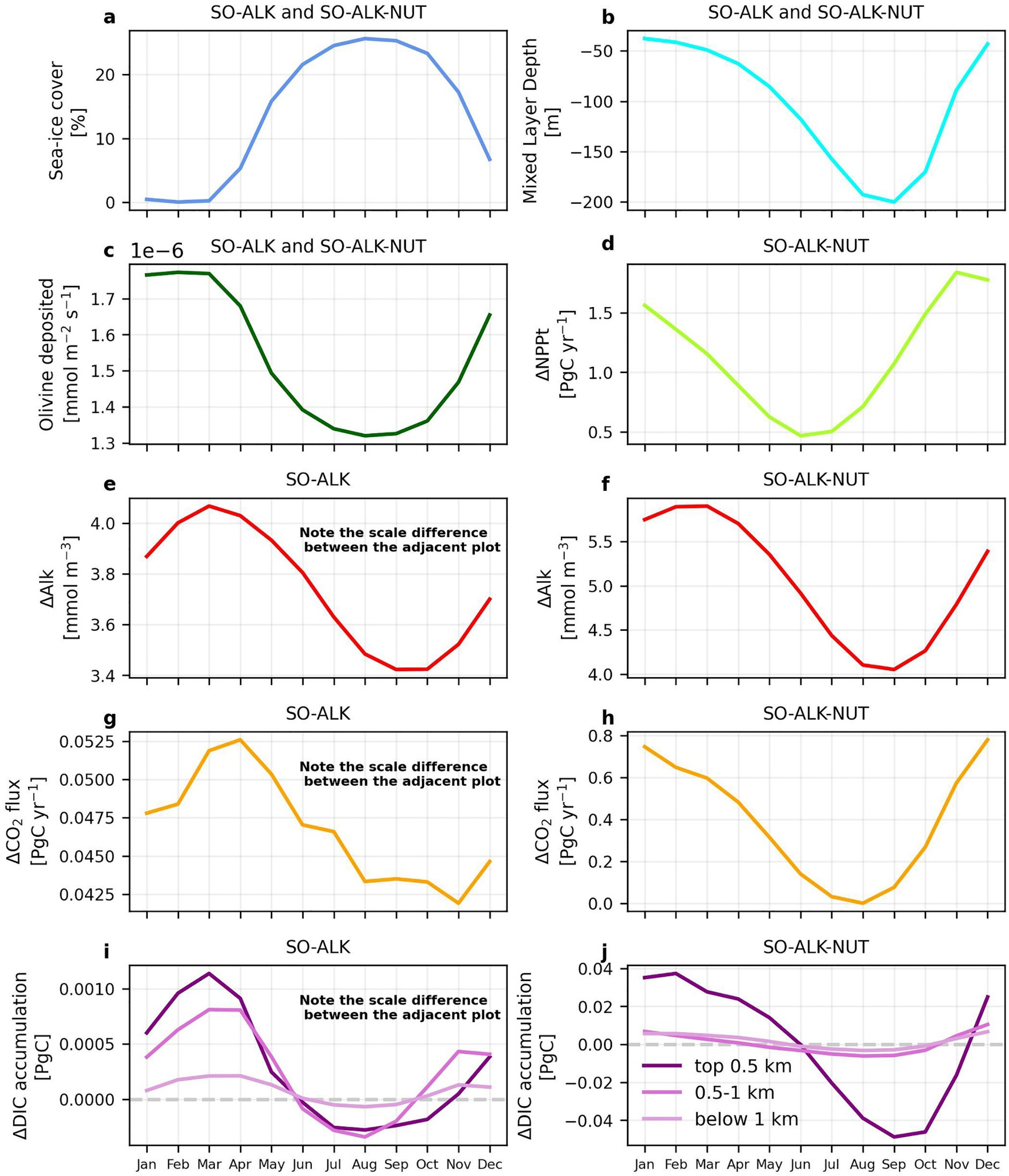

**Figure 10.** Seasonality for olivine deposition and biogeochemical responses in the ocean alkalinity enhancement experiments relative to CTRL in the Southern Ocean. The SO-ALK and SO-ALK-NUT simulations are shown and numbers are averaged over 2090–2099 under the SSP3-7.0 scenario. (a, b, and c) Sea-ice cover (%), Mixed Layer Depth (MLD; m) Olivine deposition (mmol m$^{-2}$ s$^{-1}$) for SUB-ALK and SUB-ALK-NUT. (d) Excess Total Net Primary Production ΔNPPt (PgC yr$^{-1}$) for SUB-ALK-NUT (e, f) Surface ΔAlk; (mmol m$^{-3}$); (g, h) ΔCO$_2$ flux (PgC yr$^{-1}$; positive: enhanced uptake, negative: reduced uptake) and (i, j) ΔDIC accumulation (PgC; positive: increase in dissolved inorganic carbon (DIC) accumulation; negative: loss of DIC due to vertical and lateral transport) in top 0.5 km (dark purple), 0.5–1 km (orchid), below 1 km (light purple). See Figure S5 in Supporting Information S1 for a corresponding figure for the emission scenario SSP1-2.6.

## 4. Discussion

The aim of this study was to assess the $CO_2$ uptake and storage efficiency of regional OAE in the deep and bottom water formation regions in the Southern Ocean, the Northwest Atlantic and the Norwegian-Barents Sea region under both the SSP3-7.0 and SSP1-2.6 emission scenarios. In contrast to previous reports by He and Tyka (2023); Bach et al. (2023), the OAE efficiency in the subduction regions under both SSP1-2.6 and SSP3-7.0 scenarios is comparable in our model experiments to that in the global ocean when calculated based on the final decade of air-sea $CO_2$ fluxes (CDR potential: 0.23–0.31 PgC per Pg olivine; Table 2). When calculating the efficiency based on decades-long cumulative carbon storage ($\eta CO_2$; depth-integrated $\Delta$DIC/$\Delta$Alk), only the Norwegian-Barents Sea region stands out with a lower efficiency (0.65–0.75; Table 2), whereas both the Southern Ocean and the Northwest Atlantic subduction regions still exhibit efficiencies comparable to the global ocean (0.79–0.85; Table 2). The Norwegian-Barents Sea region exhibits a lower efficiency due to its initially lower increase in DIC accumulation compared to the control simulation from 2030 to 2040. The lower $\Delta$DIC accumulation over this period could be due to prolonged equilibration time for gas-exchange or stronger vertical transport in this basin. Either way, this lower efficiency from 2030 to 2040 ultimately affects the averaged $\eta CO_2$ efficiency over 2090–2099 in the Norwegian-Barents Sea region.

The global OAE efficiency numbers reported in this paper are comparable to previous studies. Assessing the OAE efficiency for global OAE simulations with similar alkalinity addition as in our global simulation, Köhler et al. (2013) report an efficiency of 0.25 PgC per Pg olivine for the present-day (2000–2010). This is comparable to our global CDR potential (0.27 PgC per Pg olivine) under the SSP1-2.6 scenario (Table 2). This close agreement is rooted in the fact that the atmospheric $CO_2$ concentration over the period 2000–2010 is close to that in the low emission scenario SSP1-2.6. For the simulation under the SSP3-7.0 scenario, our model experiments yield a slightly higher CDR potential of 0.31 PgC per Pg of olivine. This outcome is close to the results of Hauck et al. (2016), who reported an efficiency of 0.33 PgC per Pg of olivine for a future high-emission scenario (RCP8.5) when deploying the same amount of olivine as in our simulations (Table 2). These findings confirm the small but existent scenario dependency that we will discuss below. In the context of the long-term efficiency ($\eta CO_2$), Burt et al. (2021) reported a global efficiency of 0.79 over the last decade of their simulation under constant atmospheric $CO_2$ of 280 ppm when depositing 0.25 Pmol $yr^{-1}$ of alkalinity over 75 years. This agrees well with our $\eta CO_2$ for global OAE under the SSP1-2.6 scenario (0.79; Table 2).

The CDR potential for OAE based on air-sea $CO_2$ flux in the subduction regions yields values comparable to that for global OAE under both emission scenarios. This highlights that the surface efficiency of OAE is insensitive to the region of application. This agrees with Köhler et al. (2013), who found the potential for global OAE and for OAE along commercial ship tracks to be comparable. Studying broad latitudinal bands, Lenton et al. (2018) also concluded that OAE exhibits little sensitivity to the region of application. In contrast, the efficiency metric based on cumulative $\Delta$DIC storage ($\eta CO_2$) shows the highest efficiency in the Southern Ocean (0.85) and the lowest in the North Atlantic subduction regions, particularly the Norwegian-Barents Sea region (0.73). This agrees with Burt et al. (2021) who report a regional sensitivity of the response to OAE. The authors showcase the Southern Ocean to be the most efficient (0.89) and the subpolar North Atlantic to be the least efficient (0.7), which they attribute to the rapid loss of added alkalinity to the deep ocean.

Even though the surface CDR potential displays very low regional sensitivity in our study, the deep ocean carbon storage (below 1 km) relative to the added alkalinity in the subduction regions is nearly twice as large as compared to the global oceans (Figures 5a and 5b), acknowledging a smaller absolute magnitude in the former related to the smaller area of application (Table 2). Notably, the Northwest Atlantic and the Norwegian-Barents Sea region transfer a higher fraction (25%–30%) of the additional carbon taken up to depths below 1 km than both the global oceans and the Southern Ocean (see NWA-ALK and NBS-ALK experiments). Importantly, our results are in contrast to the findings by He and Tyka (2023); Bach et al. (2023), who suggested that deep and bottom water formation regions are not suitable for OAE due to their limited residence time at the ocean surface. While we find a reduced efficiency for the Norwegian-Barents Sea region, this cannot be confirmed for the Northwest Atlantic and the Southern Ocean. A key difference between the studies is that we simulated continuous alkalinity addition whereas He and Tyka (2023); Bach et al. (2023) assumed a pulsed deployment for a month. It remains to be tested whether the continuous addition of alkalinity may compensate for the limited residence time, thus resulting in a higher surface alkalinity and a higher OAE efficiency in the subduction regions. Siegel et al. (2021) highlighted that the carbon discharged in the deep ocean below 500 m will lead to sequestration times over decades to

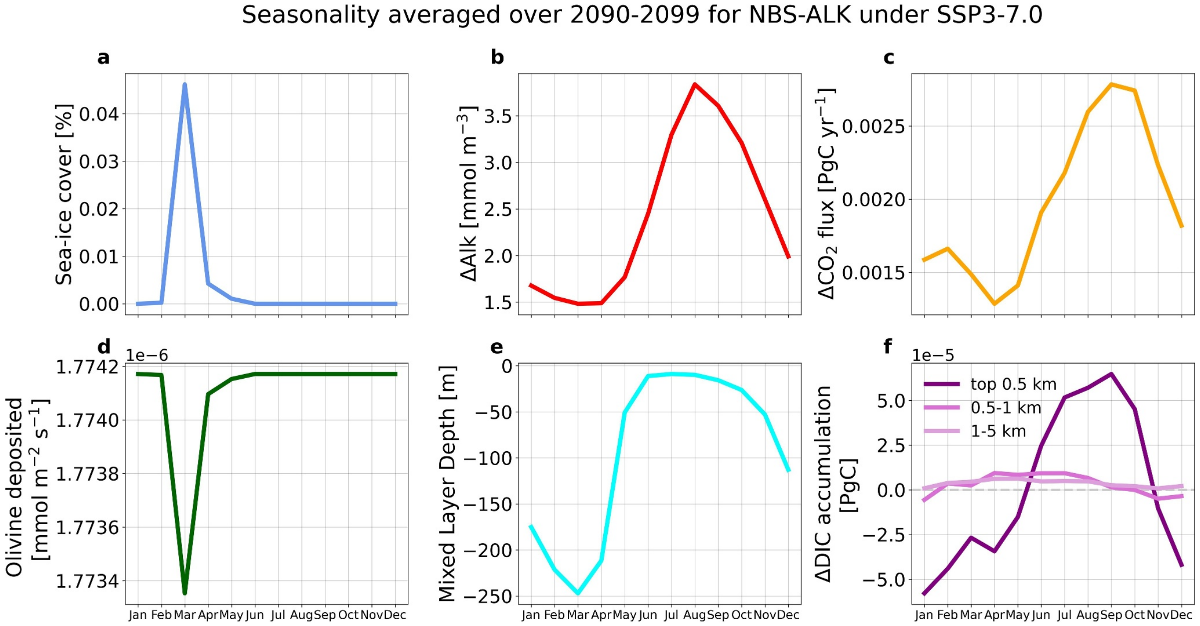

**Figure 11.** Seasonality for olivine deposition and biogeochemical responses in the ocean alkalinity enhancement experiments relative to CTRL in the Norwegian-Barents Sea region. The NBS-ALK simulation is shown and numbers are averaged over 2090–2099 under the SSP3-7.0 scenario. (a) Sea-ice cover (%), (b) Surface ΔAlk (mmol $m^{-3}$), (c) $\Delta CO_2$ flux (PgC $yr^{-1}$; positive: enhanced uptake, negative: reduced uptake), (d) Olivine deposited (mmol $m^{-2}$ $s^{-1}$) (e) Mixed Layer Depth (MLD; m), and (f) ΔDIC accumulation (PgC; positive: increase in dissolved inorganic carbon (DIC) accumulation; negative: Loss of DIC due to vertical and lateral transport) in top 0.5 km (dark purple), 0.5–1 km (orchid), below 1 km (light purple). See Figure S6 in Supporting Information S1 for the results of the NBS-ALK experiment under the SSP1-2.6 emission scenario and Figures S7 and S8 in Supporting Information S1 for the Northwest Atlantic (NWA-ALK) experiment under the SSP3-7.0 and SSP1-2.6 emission scenarios, respectively.

centuries, thus increasing the durability of OAE efficiency. This supports our hypothesis to simulate OAE in the subduction regions, which would facilitate long-term carbon storage away from the atmosphere.

The sensitivity of the CDR potential to the addition of nutrients (iron and silicic acid) along with alkalinity varies regionally. Iron availability limits primary productivity and the associated carbon uptake (Blain et al., 2007). Specifically the Southern Ocean displays a low ambient concentration of iron which acts as a limiting micronutrient for phytoplankton growth (Aumont & Bopp, 2006; Oschlies et al., 2010; Smetacek et al., 2012). Therefore, carrying out OAE along with nutrient addition leads to an increased drawdown of carbon through enhanced productivity. Our results thus agree with the studies by Oschlies et al. (2010); Hauck et al. (2016) which also highlight that the Southern Ocean is the most efficient region in terms of carbon uptake efficiency due to nutrient fertilization with silicic acid and iron. The CDR potential for global olivine deposition including the nutrient effects was previously reported to be 0.57 PgC per Pg olivine using the same biogeochemical model as ours but with a different physical ocean model (Hauck et al., 2016). This is slightly higher than our global CDR potential (0.43 PgC per Pg olivine; Table 2). This difference in CDR potential between our study and that of Hauck et al. (2016) can be traced back to the differing ratios of small phytoplankton to diatom productivity. In their study, the ratio stands at 0.65 compared to our 1.53, due to a higher increase in diatom productivity on their end. This led to a heightened NPP of 17.8 PgC $yr^{-1}$ in their study, as opposed to our 10.92 PgC $yr^{-1}$. This distinction likely stems from difference in the background state of the simulated ecosystem.

The scenario dependency of both metrics is generally weak, but the OAE efficiencies with only alkalinity addition are slightly higher in the high-emission scenario. While the absolute $CO_2$ flux is higher under SSP3-7.0 due to the higher atmospheric $CO_2$ concentration, any additional $CO_2$ flux following OAE is more closely linked to the state of ocean carbonate chemistry than background $CO_2$ concentrations. Thus, the lower buffer capacity under SSP3-7.0 leads to a higher additional carbon uptake and in turn higher OAE efficiencies than under SSP1-2.6 (Figures 3a and 3b; Gattuso et al. (2015); Keller et al. (2014); Hauck et al. (2016)). Using an

Earth System Model, Lenton et al. (2018) reported that the low emission scenario is more efficient in terms of atmospheric $CO_2$ drawdown than the high emission scenario. This apparent contradiction with our results can be understood by considering their different definition of 'efficiency'. Defining OAE efficiency as the amount of OAE needed to achieve a given atmospheric temperature and $CO_2$ concentration target, it is unsurprising that a lower emission scenario is more effective than a high emission scenario in Lenton et al. (2018). Yet, we note that using their definition, the absolute reduction in atmospheric $CO_2$ concentration for a fixed OAE is comparable in Lenton et al. (2018) for both scenarios, reconciling their results with ours. In our results, we also find a scenario dependence of the fraction of carbon stored below 1 km. Under the SSP3-7.0 scenario, a lower fraction of total carbon taken up is stored below 1 km than under the SSP1-2.6 scenario (Table 2). This is due to a stronger stratification in the higher-emission scenario and thus a less efficient carbon transfer to the deeper oceans. This holds true for simulations with and without nutrient addition in the global and the subduction regions (Table 2).

The results presented here assume the complete and instantaneous dissolution of olivine as in Köhler et al. (2013); Hauck et al. (2016). Thus, our results give a theoretical upper limit of the OAE potential for global and subduction regions. However, in reality, the dissolution of olivine and in turn the OAE efficiency are influenced by the grain size, MLD and sea surface temperature (SST) (Köhler et al., 2013). Fine grain sizes of ~1 $\mu$m lead to a high residence time in the mixed layer, resulting in high OAE efficiency, whereas the efficiency decreases substantially as the grain size increases and most of the material is lost to the deep ocean undissolved (Feng et al., 2017; Köhler et al., 2013). But, the necessity of grinding the material to a very fine size is expensive in terms of energy consumption which offsets the OAE efficiency by about 30% and also poses a practical challenge in terms of mining and transportation (Caserini et al., 2022; Köhler et al., 2013; Renforth et al., 2013). One of the risks of using olivine for OAE is that, it is accompanied by addition of heavy trace metals, for example, nickel which can negatively impact the ecosystem (Hartmann et al., 2013). For instance, nickel addition leads to significant reduction in the growth rate of some phytoplanktons, for example, diatom (Guo et al., 2022; Xin et al., 2023). Thus, it is critical to assess the choice of alkaline material used for OAE considering the side effects it may have on the marine ecosystem. Similarly, sinking particulate olivine grains may have undesired effects on the benthic ecosystem through optical and mechanical stress (Feng et al., 2017). If alkalinity is excessively enhanced above a certain threshold, increased secondary $CaCO_3$ precipitation is possible (Hartmann et al., 2013; Middelburg et al., 2020). Increased $CaCO_3$ precipitation will counteract the purpose of OAE by consuming the added alkalinity and thus dampening the carbon uptake efficiency. Therefore, to avoid secondary $CaCO_3$ precipitation, it is necessary to examine the safe limits for alkalinity enhancement (Hartmann et al., 2013). Laboratory experiments for OAE using CaO and $Ca(OH)_2$ in the natural sea water collected 200–300 m offshore at New South Wales Australia were conducted by Moras et al. (2022). They found that increment of 500 $\mu$mol kg$^{-1}$ of total alkalinity drastically reduced OAE efficiency due to increased $CaCO_3$ precipitation, while for an increase of 250 $\mu$mol kg$^{-1}$ no $CaCO_3$ precipitation was observed, implying it to be a safe limit for OAE (Moras et al., 2022). In our simulations with uniform addition of only alkalinity, the excess surface alkalinity in SUB-ALK (3.75 mmol m$^{-3}$) is much smaller than in GLO-ALK (35.62 mmol m$^{-3}$) at comparable efficiency. This lower excess surface alkalinity in the SUB-ALK simulation is due to dilution of added alkalinity resulting from the lateral and vertical spreading, which in turn may also reduce the risk of secondary precipitation.

The temperature dependence of alkalinity addition through olivine deposition highlight that the favourable regions for maximum dissolution are between 40°N and 40°S. Additionally, the deep water formation regions in the North Atlantic, characterised by deep MLD, allow olivine to remain at the ocean surface longer, facilitating maximum dissolution. As a result, these areas are also deemed favorable for OAE (Köhler et al., 2013). However, our results suggest that the shallow MLD in summer for both hemispheres is favourable for higher OAE efficiency when dissolved alkaline material is added. This is because the added alkalinity is not lost to the deep oceans due to reduced mixing and thus results in higher $CO_2$ uptake and OAE efficiency. Hence, it is crucial to critically investigate the intricacies of the regions, acknowledging the distinct dynamics exhibited by various sub-regions encompassed within our regional masks for OAE. Furthermore, careful consideration of modes of application is essential to optimize OAE efficiency and mitigate negative impacts it can have on the marine ecosystems.

## 5. Conclusion

Simulating OAE in the subduction regions of the Southern Ocean, the Northwest Atlantic and the Norwegian-Barents Sea region revealed that these regions are as efficient as the global ocean for OAE, with the Norwegian-Barents Sea region showing a comparatively lower efficiency. It is crucial to note that we address the theoretical upper limit of OAE efficiencies, assuming instantaneous effects of added alkalinity on oceanic carbon uptake, which may not hold in practical scenarios. The time period required for added alkalinity to shift the equilibrium at the ocean surface is not accounted for and can thus introduce uncertainties in the OAE efficiencies. In terms of practical OAE implementation, coastal deployments are deemed more realistic owing to the current legal restrictions on open-ocean deployments. Acknowledging the logistical challenge associated with mining and transportation of the alkaline mineral used for OAE, it is more likely that OAE is in the form of pulsed alkalinity addition rather than the uniform continuous additions as simulated in our study. Seasonal variations in MLD influence the increase in surface alkalinity, which in turn affects carbon uptake and storage. The shallow mixed layer depths during summer are associated with higher surface alkalinity, carbon uptake and storage in both hemispheres. Hence, this accentuates the importance of identifying optimal times of the year to maximize the efficiency of OAE deployment. Although not tested in this study, the choice of alkaline mineral used for OAE would also influence the efficiency and have varying ecological impacts, depending on the mineral used. In summary, this study underscores that the subduction regions can be efficient for carbon uptake and storage due to OAE, if OAE is optimized and strategic deployment scenarios are developed.

## Data Availability Statement

The data set required to reproduce the findings of this study is available in Nagwekar et al. (2024b). The Fortran source code of FESOM2.1-REcoM3 can be obtained via github (https://github.com/tanvinagwekar/fesom2/tree/OAE_Experiments) or via Zenodo (Nagwekar et al., 2024a). Analysis was performed using the open-source software Python.

**Acknowledgments**

This study was funded by the Federal Ministry of Education and Research of Germany (BMBF) in the framework of RETAKE-B, one of the six research consortia of the German Marine Research Alliance (DAM) research mission “Marine carbon sinks in decarbonization pathways” (CDRmare), Grant 03F0895B. JH was funded by the Initiative and Networking Fund of the Helmholtz Association (Helmholtz Young Investigator Group Marine Carbon and Ecosystem Feedbacks in the Earth System, MarESys; Grant VH-NG-1301). Open Access funding enabled and organized by Projekt DEAL.

## References

Abernathey, R. P., Cerovecki, I., Holland, P. R., Newsom, E., Mazloff, M., & Talley, L. D. (2016). Water-mass transformation by sea ice in the upper branch of the Southern Ocean overturning. *Nature Geoscience*, *9*(8), 596–601. https://doi.org/10.1038/ngeo2749

Archer, D. (2005). Fate of fossil fuel CO$_2$ in geologic time. *Journal of Geophysical Research*, *110*(C9). https://doi.org/10.1029/2004JC002625

Aumont, O., & Bopp, L. (2006). Globalizing results from ocean in situ iron fertilization studies: Globalizing iron fertilization. *Global Biogeochemical Cycles*, *20*(2). https://doi.org/10.1029/2005GB002591

Bach, L. T., Ho, D. T., Boyd, P. W., & Tyka, M. D. (2023). Toward a consensus framework to evaluate air-sea CO$_2$ equilibration for marine CO$_2$ removal. *Limnology and Oceanography Letters*, *8*(5), 685–691. https://doi.org/10.1002/lol2.10330

Blain, S., Quéguiner, B., Armand, L., Belviso, S., Bombled, B., Bopp, L., et al. (2007). Effect of natural iron fertilization on carbon sequestration in the Southern Ocean. *Nature*, *446*(7139), 1070–1074. https://doi.org/10.1038/nature05700

Burt, D. J., Fröb, F., & Ilyina, T. (2021). The sensitivity of the marine carbonate system to regional Ocean Alkalinity enhancement. *Frontiers in Climate*, *3*. https://doi.org/10.3389/fclim.2021.624075

Butenschön, M., Lovato, T., Masina, S., Caserini, S., & Grosso, M. (2021). Alkalinization scenarios in the Mediterranean Sea for efficient removal of atmospheric CO$_2$ and the mitigation of Ocean Acidification. *Frontiers in Climate*, *3*. https://doi.org/10.3389/fclim.2021.614537

Caserini, S., Storni, N., & Grosso, M. (2022). The availability of limestone and other raw materials for Ocean Alkalinity enhancement. *Global Biogeochemical Cycles*, *36*(5). https://doi.org/10.1029/2021GB007246

Cerovečki, I., & Mazloff, M. R. (2016). The spatiotemporal structure of diabatic processes governing the evolution of subantarctic mode water in the Southern Ocean. *Journal of Physical Oceanography*, *46*(2), 683–710. https://doi.org/10.1175/JPO-D-14-0243.1

Danilov, S., Sidorenko, D., Wang, Q., & Jung, T. (2017). The finite-volumE sea ice–ocean model (FESOM2). *Geoscientific Model Development*, *10*(2), 765–789. https://doi.org/10.5194/gmd-10-765-2017

De Baar, H. J., de Jong, J. T., Bakker, D. C., Löscher, B. M., Veth, C., Bathmann, U., & Smetacek, V. (1995). Importance of iron for plankton blooms and carbon dioxide drawdown in the Southern Ocean. *Nature*, *373*(6513), 412–415. https://doi.org/10.1038/373412a0

De Hoog, J. C., Gall, L., & Cornell, D. H. (2010). Trace-element geochemistry of mantle olivine and application to mantle petrogenesis and geothermobarometry. *Chemical Geology*, *270*(1), 196–215. https://doi.org/10.1016/j.chemgeo.2009.11.017

Dickson, R. R., & Brown, J. (1994). The production of North Atlantic deep water: Sources, rates, and pathways. *Journal of Geophysical Research*, *99*(C6), 12319–12341. https://doi.org/10.1029/94JC00530

Feng, E. Y., Koeve, W., Keller, D. P., & Oschlies, A. (2017). Model-based assessment of the CO$_2$ sequestration potential of coastal ocean alkalinization. *Earth's Future*, *5*(12), 1252–1266. https://doi.org/10.1002/2017EF000659

Friedlingstein, P., Jones, M. W., O'Sullivan, M., Andrew, R. M., Bakker, D. C. E., Hauck, J., et al. (2022). Global carbon budget 2021. *Earth System Science Data*, *14*(4), 1917–2005. https://doi.org/10.5194/essd-14-1917-2022

Fuss, S., Lamb, W. F., Callaghan, M. W., Hilaire, J., Creutzig, F., Amann, T., et al. (2018). Negative emissions—Part 2: Costs, potentials and side effects. *Environmental Research Letters*, *13*(6), 063002. https://doi.org/10.1088/1748-9326/aabf9f

Gattuso, J.-P., Magnan, A., Billé, R., Cheung, W. W. L., Howes, E. L., Joos, F., et al. (2015). Contrasting futures for ocean and society from different anthropogenic CO$_2$ emissions scenarios. *Science*, *349*(6243), aac4722. https://doi.org/10.1126/science.aac4722

Gattuso, J.-P., Williamson, P., Duarte, C. M., & Magnan, A. K. (2021). The potential for oceanocean-based climate action: Negative emissions technologies and beyond. *Frontiers in Climate*, *2*. https://doi.org/10.3389/fclim.2020.575716

González, M. F., & Ilyina, T. (2016). Impacts of artificial ocean alkalinization on the carbon cycle and climate in Earth system simulations. *Geophysical Research Letters*, *43*(12), 6493–6502. https://doi.org/10.1002/2016GL068576

Gruber, N., Clement, D., Carter, B. R., Feely, R. A., van Heuven, S., Hoppema, M., et al. (2019). The oceanic sink for anthropogenic $CO_2$ from 1994 to 2007. *Science*, *363*(6432), 1193–1199. https://doi.org/10.1126/science.aau5153

Gruber, N., Gloor, M., Mikaloff Fletcher, S. E., Doney, S. C., Dutkiewicz, S., Follows, M. J., et al. (2009). Oceanic sources, sinks, and transport of atmospheric $CO_2$. *Global Biogeochemical Cycles*, *23*(1). https://doi.org/10.1029/2008GB003349

Guo, J. A., Strzepek, R., Willis, A., Ferderer, A., & Bach, L. T. (2022). Investigating the effect of nickel concentration on phytoplankton growth to assess potential side-effects of ocean alkalinity enhancement. *Biogeosciences*, *19*(15), 3683–3697. https://doi.org/10.5194/bg-19-3683-2022

Gürses, O., Oziel, L., Karakuş, O., Sidorenko, D., Völker, C., Ye, Y., et al. (2023). Ocean biogeochemistry in the coupled ocean-sea ice-biogeochemistry model FESOM2.1-REcoM3. *Geoscientific Model Development Discussions*, 1–73. https://doi.org/10.5194/gmd-2023-2

Hartin, C. A., Fine, R. A., Sloyan, B. M., Talley, L. D., Chereskin, T. K., & Happell, J. (2011). Formation rates of Subantarctic mode water and Antarctic intermediate water within the South Pacific. *Deep Sea Research Part I: Oceanographic Research Papers*, *58*(5), 524–534. https://doi.org/10.1016/j.dsr.2011.02.010

Hartmann, J., West, A. J., Renforth, P., Köhler, P., De La Rocha, C. L., Wolf-Gladrow, D. A., et al. (2013). Enhanced chemical weathering as a geoengineering strategy to reduce atmospheric carbon dioxide, supply nutrients, and mitigate ocean acidification: Enhanced weathering. *Reviews of Geophysics*, *51*(2), 113–149. https://doi.org/10.1002/rog.20004

Hauck, J., Köhler, P., Wolf-Gladrow, D., & Völker, C. (2016). Iron fertilisation and century-scale effects of open ocean dissolution of olivine in a simulated $CO_2$ removal experiment. *Environmental Research Letters*, *11*(2), 024007. https://doi.org/10.1088/1748-9326/11/2/024007

He, J., & Tyka, M. D. (2023). Limits and $CO_2$ equilibration of near-coast alkalinity enhancement. *Biogeosciences*, *20*(1), 27–43. https://doi.org/10.5194/bg-20-27-2023

Hernández-Hernández, N., Bach, L. T., Montero, M. F., Taucher, J., Baños, I., Guan, W., et al. (2018). High $CO_2$ under nutrient fertilization increases primary production and biomass in subtropical phytoplankton communities: A mesocosm approach. *Frontiers in Marine Science*, *5*. https://doi.org/10.3389/fmars.2018.00213

Hinrichs, C., Köhler, P., Völker, C., & Hauck, J. (2023). Alkalinity biases in CMIP6 Earth system models and implications for simulated $CO_2$ drawdown via artificial alkalinity enhancement. *Biogeosciences*, *20*(18), 3717–3735. https://doi.org/10.5194/bg-20-3717-2023

Ilyina, T., Wolf-Gladrow, D., Munhoven, G., & Heinze, C. (2013). Assessing the potential of calcium-based artificial ocean alkalinization to mitigate rising atmospheric $CO_2$ and ocean acidification: Modeling mitigation potential of aoa. *Geophysical Research Letters*, *40*(22), 5909–5914. https://doi.org/10.1002/2013GL057981

Jeansson, E., Olsen, A., & Jutterström, S. (2017). Arctic intermediate water in the Nordic seas, 1991–2009. *Deep Sea Research Part I: Oceanographic Research Papers*, *128*, 82–97. https://doi.org/10.1016/j.dsr.2017.08.013

Jeansson, E., Tanhua, T., Olsen, A., Jr Smethie, W. M., Rajasakaren, B., Ólafsdóttir, S. R., & Ólafsson, J. (2023). Decadal changes in ventilation and anthropogenic carbon in the nordic seas. *Journal of Geophysical Research: Oceans*, *128*(3), e2022JC019318. https://doi.org/10.1029/2022JC019318

Jones, D. C., Ito, T., Takano, Y., & Hsu, W.-C. (2014). Spatial and seasonal variability of the air-sea equilibration timescale of carbon dioxide. *Global Biogeochemical Cycles*, *28*(11), 1163–1178. https://doi.org/10.1002/2014GB004813

Karakuş, O., Völker, C., Iversen, M., Hagen, W., Wolf-Gladrow, D., Fach, B., & Hauck, J. (2021). Modeling the impact of macrozooplankton on carbon export production in the Southern Ocean. *Journal of Geophysical Research: Oceans*, *126*(12). https://doi.org/10.1029/2021JC017315

Keller, D. P., Feng, E. Y., & Oschlies, A. (2014). Potential climate engineering effectiveness and side effects during a high carbon dioxide-emission scenario. *Nature Communications*, *5*(1), 3304. https://doi.org/10.1038/ncomms4304

Khatiwala, S., Primeau, F., & Hall, T. (2009). Reconstruction of the history of anthropogenic $CO_2$ concentrations in the ocean. *Nature*, *462*(7271), 346–349. https://doi.org/10.1038/nature08526

Kheshgi, H. S. (1995). Sequestering atmospheric carbon dioxide by increasing ocean alkalinity. *Energy*, *20*(9), 915–922. https://doi.org/10.1016/0360-5442(95)00035-F

Köhler, P. (2020). Anthropogenic $CO_2$ of high emission scenario compensated after 3500 Years of ocean alkalinization with an annually constant dissolution of 5 Pg of olivine. *Frontiers in Climate*, *2*, 575744. https://doi.org/10.3389/fclim.2020.575744

Köhler, P., Abrams, J. F., Völker, C., Hauck, J., & Wolf-Gladrow, D. A. (2013). Geoengineering impact of open ocean dissolution of olivine on atmospheric $CO_2$, surface ocean pH and marine biology. *Environmental Research Letters*, *8*(1), 014009. https://doi.org/10.1088/1748-9326/8/1/014009

Koldunov, N. V., Aizinger, V., Rakowsky, N., Scholz, P., Sidorenko, D., Danilov, S., & Jung, T. (2019). Scalability and some optimization of the finite-volumE sea ice–ocean model, version 2.0 (FESOM2). *Geoscientific Model Development*, *12*(9), 3991–4012. https://doi.org/10.5194/gmd-12-3991-2019

Lavender, K. L., Davis, R. E., & Owens, W. B. (2002). Observations of open-ocean deep convection in the Labrador Sea from subsurface floats. *Journal of Physical Oceanography*, *32*(2), 511–526. https://doi.org/10.1175/1520-0485(2002)032<0511:OOOODC>2.0.CO;2

Lenton, A., Matear, R. J., Keller, D. P., Scott, V., & Vaughan, N. E. (2018). Assessing carbon dioxide removal through global and regional ocean alkalinization under high and low emission pathways. *Earth System Dynamics*, *9*(2), 339–357. https://doi.org/10.5194/esd-9-339-2018

Lorbacher, K., Dommenget, D., Niiler, P., & Köhl, A. (2006). Ocean mixed layer depth: A subsurface proxy of ocean-atmosphere variability. *Journal of Geophysical Research*, *111*(C7). https://doi.org/10.1029/2003JC002157

Meinshausen, M., Vogel, E., Nauels, A., Lorbacher, K., Meinshausen, N., Etheridge, D. M., et al. (2017). Historical greenhouse gas concentrations for climate modelling CMIP6. *Geoscientific Model Development*, *10*(5), 2057–2116. https://doi.org/10.5194/gmd-10-2057-2017

Middelburg, J. J., Soetaert, K., & Hagens, M. (2020). Ocean alkalinity, buffering and biogeochemical processes. *Reviews of Geophysics*, *58*(3). https://doi.org/10.1029/2019RG000681

Moras, C. A., Bach, L. T., Cyronak, T., Joannes-Boyau, R., & Schulz, K. G. (2022). Ocean alkalinity enhancement – Avoiding runaway $CO_2$ precipitation during quick and hydrated lime dissolution. *Biogeosciences*, *19*(15), 3537–3557. https://doi.org/10.5194/bg-19-3537-2022

Nagwekar, T., Nissen, C., & Hauck, J. (2024a). FESOM2.1-REcoM3 model code for OAE. (Version expt_OAE) [Software]. *Zenodo*. https://doi.org/10.5281/zenodo.10967052

Nagwekar, T., Nissen, C., & Hauck, J. (2024b). Ocean alkalinity enhancement in deep water formation regions under low and high emission pathways. (Version v1) [Dataset]. *Zenodo*. https://doi.org/10.5281/zenodo.10056552

Nissen, C., Timmermann, R., Hoppema, M., Gürses, O., & Hauck, J. (2022). Abruptly attenuated carbon sequestration with Weddell Sea dense waters by 2100. *Nature Communications*, *13*(1), 3402. https://doi.org/10.1038/s41467-022-30671-3

O'Neill, B. C., Tebaldi, C., van Vuuren, D. P., Eyring, V., Friedlingstein, P., Hurtt, G., et al. (2016). The scenario model intercomparison project (ScenarioMIP) for CMIP6. *Geoscientific Model Development*, *9*(9), 3461–3482. https://doi.org/10.5194/gmd-9-3461-2016

Orr, J. C., & Epitalon, J.-M. (2015). Improved routines to model the ocean carbonate system: Mocsy 2.0. *Geoscientific Model Development*, *8*(3), 485–499. https://doi.org/10.5194/gmd-8-485-2015

Orsi, A., Johnson, G., & Bullister, J. (1999). Circulation, mixing, and production of Antarctic bottom water. *Progress in Oceanography*, *43*(1), 55–109. https://doi.org/10.1016/S0079-6611(99)00004-X

Oschlies, A., Koeve, W., Rickels, W., & Rehdanz, K. (2010). Side effects and accounting aspects of hypothetical large-scale Southern Ocean iron fertilization. *Biogeosciences*, *7*(12), 4017–4035. https://doi.org/10.5194/bg-7-4017-2010

Pellichero, V., Sallée, J.-B., Chapman, C. C., & Downes, S. M. (2018). The Southern Ocean meridional overturning in the sea-ice sector is driven by freshwater fluxes. *Nature Communications*, *9*(1), 1789. https://doi.org/10.1038/s41467-018-04101-2

Raven, J. A., & Falkowski, P. G. (1999). Oceanic sinks for atmospheric $CO_2$. *Plant, Cell and Environment*, *22*(6), 741–755. https://doi.org/10.1046/j.1365-3040.1999.00419.x

Renforth, P., & Henderson, G. (2017). Assessing ocean alkalinity for carbon sequestration: Ocean Alkalinity for C Sequestration. *Reviews of Geophysics*, *55*(3), 636–674. https://doi.org/10.1002/2016RG000533

Renforth, P., Jenkins, B., & Kruger, T. (2013). Engineering challenges of ocean liming. *Energy*, *60*, 442–452. https://doi.org/10.1016/j.energy.2013.08.006

Riahi, K., Schaeffer, R., Arango, J., Calvin, K., Guivarch, C., Hasegawa, T., et al. (2022). Mitigation pathways compatible with long-term goals. In *IPCC, 2022: Climate change 2022: Mitigation of climate change. Working group III contribution to the sixth assessment report of the intergovernmental panel on climate change* P. R. Shukla, J. Skea, R. Slade, A. Al Khourdajie, R. van Diemen, D. McCollum, M. Pathak, S. Some, P. Vyas, R. Fradera, M. Belkacemi, A. Hasija, G. Lisboa, S. Luz, & J. Malley, (Eds.), (pp. 295–408). Cambridge University Press. https://doi.org/10.1017/9781009157926.005

Rogge, A., Janout, M., Loginova, N., Trudnowska, E., Hörstmann, C., Wekerle, C., et al. (2023). Carbon dioxide sink in the Arctic Ocean from cross-shelf transport of dense Barents Sea water. *Nature Geoscience*, *16*(1), 82–88. https://doi.org/10.1038/s41561-022-01069-z

Sabine, C. L., Feely, R. A., Gruber, N., Key, R. M., Lee, K., Bullister, J. L., et al. (2004). The oceanic sink for anthropogenic $CO_2$. *Science*, *305*(5682), 367–371. https://doi.org/10.1126/science.1097403

Schartau, M., Engel, A., Schröter, J., Thoms, S., Völker, C., & Wolf-Gladrow, D. (2007). Modelling carbon overconsumption and the formation of extracellular particulate organic carbon. *Biogeosciences*, *4*(4), 433–454. https://doi.org/10.5194/bg-4-433-2007

Scholz, P., Sidorenko, D., Danilov, S., Wang, Q., Koldunov, N., Sein, D., & Jung, T. (2022). Assessment of the Finite-VolumE Sea ice–Ocean Model (FESOM2.0) – Part 2: Partial bottom cells, embedded sea ice and vertical mixing library CVMix. *Geoscientific Model Development*, *15*(2), 335–363. https://doi.org/10.5194/gmd-15-335-2022

Semmler, T., Danilov, S., Gierz, P., Goessling, H. F., Hegewald, J., Hinrichs, C., et al. (2020). Simulations for CMIP6 with the AWI climate model AWI-CM-1-1. *Journal of Advances in Modeling Earth Systems*, *12*(9), e2019MS002009. https://doi.org/10.1029/2019MS002009

Siegel, D. A., DeVries, T., Doney, S. C., & Bell, T. (2021). Assessing the sequestration time scales of some ocean-based carbon dioxide reduction strategies. *Environmental Research Letters*, *16*(10), 104003. https://doi.org/10.1088/1748-9326/ac0be0

Smetacek, V., Klaas, C., Strass, V. H., Assmy, P., Montresor, M., Cisewski, B., et al. (2012). Deep carbon export from a Southern Ocean iron-fertilized diatom bloom. *Nature*, *487*(7407), 313–319. https://doi.org/10.1038/nature11229

Talley, L. D. (2008). Freshwater transport estimates and the global overturning circulation: Shallow, deep and throughflow components. *Progress in Oceanography*, *78*(4), 257–303. https://doi.org/10.1016/j.pocean.2008.05.001

Tsujino, H., Urakawa, S., Nakano, H., Small, R. J., Kim, W. M., Yeager, S. G., et al. (2018). JRA-55 based surface dataset for driving ocean–sea-ice models (JRA55-do). *Ocean Modelling*, *130*, 79–139. https://doi.org/10.1016/j.ocemod.2018.07.002

UNFCCC. (2015). United nations framework on climate change (UNFCCC): Adoption of the Paris agreement, 21st conference of the parties. Retrieved from https://unfccc.int/sites/default/files/english_paris_agreement.pdf

Våge, K., Pickart, R. S., Thierry, V., Reverdin, G., Lee, C. M., Petrie, B., et al. (2009). Surprising return of deep convection to the subpolar North Atlantic Ocean in winter 2007–2008. *Nature Geoscience*, *2*(1), 67–72. https://doi.org/10.1038/ngeo382

Walin, G. (1982). On the relation between sea-surface heat flow and thermal circulation in the ocean. *Tellus*, *34*(2), 187–195. https://doi.org/10.1111/j.2153-3490.1982.tb01806.x

Wang, H., Pilcher, D. J., Kearney, K. A., Cross, J. N., Shugart, O. M., Eisaman, M. D., & Carter, B. R. (2023). Simulated impact of ocean alkalinity enhancement on atmospheric $CO_2$ removal in the Bering Sea. *Earth's Future*, *11*(1). https://doi.org/10.1029/2022EF002816

Xin, X., Faucher, G., & Riebesell, U. (2023). Phytoplankton response to increased nickel in the context of ocean alkalinity enhancement. *Biogeosciences Discussions*, 1–15. https://doi.org/10.5194/bg-2023-130

Zeebe, R. E., & Archer, D. (2005). Feasibility of ocean fertilization and its impact on future atmospheric $CO_2$ levels. *Geophysical Research Letters*, *32*(9). https://doi.org/10.1029/2005GL022449

EARTH'S FUTURE

# Supporting Information for "Ocean Alkalinity Enhancement in deep water formation regions under low and high emission pathways"

Tanvi Nagwekar [1], Cara Nissen [2], Judith Hauck [1]

[1]Alfred Wegener Institute for Polar and Marine Research, Bremerhaven, Germany.

[2]Department of Atmospheric and Oceanic Sciences and Institute of Arctic and Alpine Research, University of Colorado, Boulder, Boulder, CO, USA.

## Contents of this file

1. Supplementary Figures S1 to S8

**Introduction** Here, we present figures after simulating OAE globally and in the subduction regions of Southern Ocean, Northwest Atlantic Sea and the Norwegian-Barents Sea region under the SSP1-2.6 emission scenario from 2030-2100. The figures are detailing spatial patterns for the increase in $CO_2$ flux, surface alkalinity, calcification, Total Net Primary Production (NPPt), diatom productivity (NPPd), and small phytoplankton (NPPn) compared to the CTRL simulation. Additionally, we provide zonal averages for the increase in Dissolved Organic Carbon (DIC). The seasonal time series for olivine addition in the Southern Ocean and the Norwegian-Barents Sea region are based on the SSP1-2.6 scenario. Meanwhile, the Northwest Atlantic displays seasonal plots for both

---

SSP1-2.6 and SSP3-7.0 emission scenarios. All maps and seasonal variation time series are averaged over the last decade of the simulation, spanning 2090-2099.

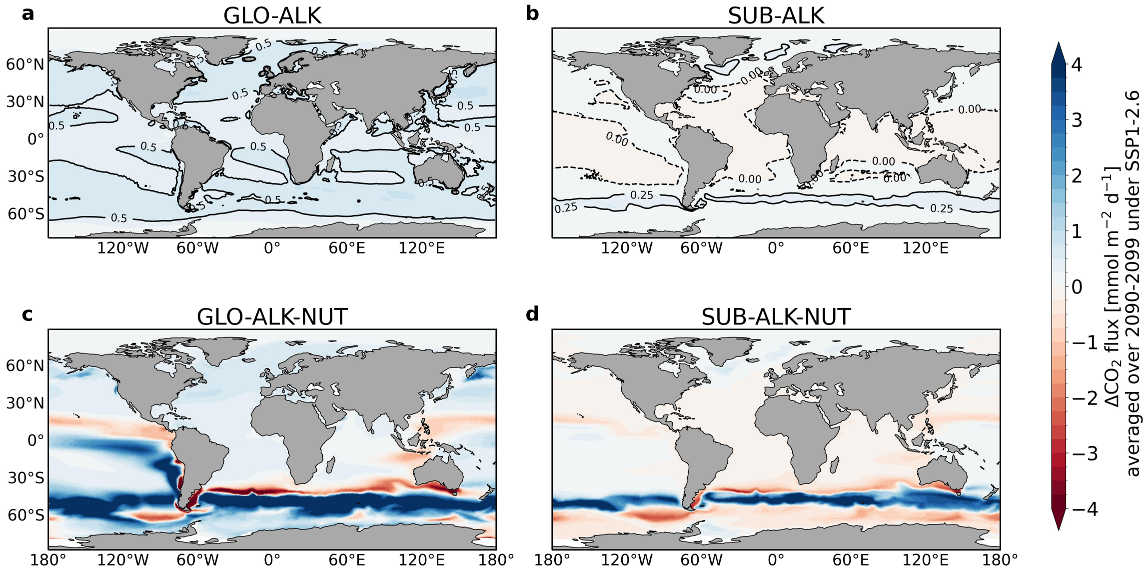

**Figure S1.** Spatial patterns of the difference in the $CO_2$ flux with respect to the CTRL run ($\Delta CO_2$ flux), averaged over 2090-2099 for the SSP1-2.6 scenario for four experiments: **(a)** GLO-ALK, **(b)** SUB-ALK. **(c)** GLO-ALK-NUT , **(d)** SUB-ALK-NUT. Positive values (blue color) represent enhanced $CO_2$ uptake and negative values (red color) represent reduced $CO_2$ uptake compared to the CTRL simulation.

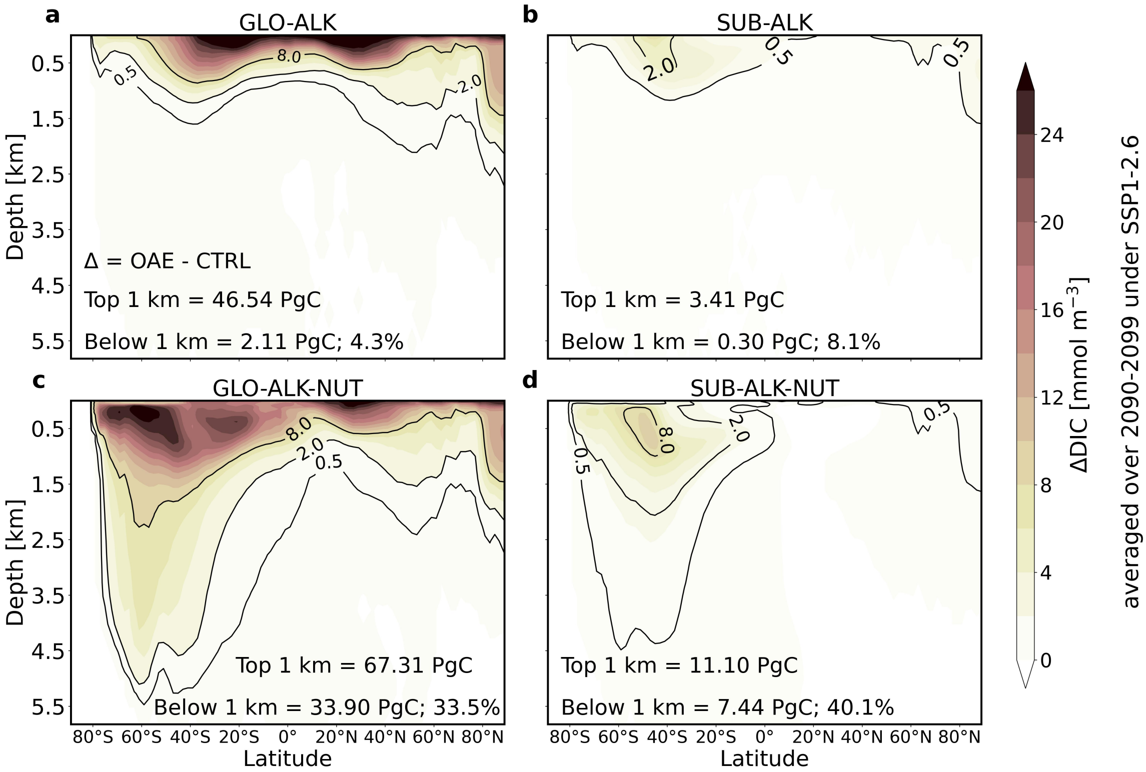

**Figure S2.** Zonal mean of ΔDIC in the ocean alkalinity enhancement experiments with respect to the CTRL run, averaged over 2090-2099 for SSP1-2.6 scenario for four experiments: **(a)** GLO-ALK, **(b)** SUB-ALK, **(c)** GLO-ALK-NUT and **(d)** SUB-ALK-NUT.

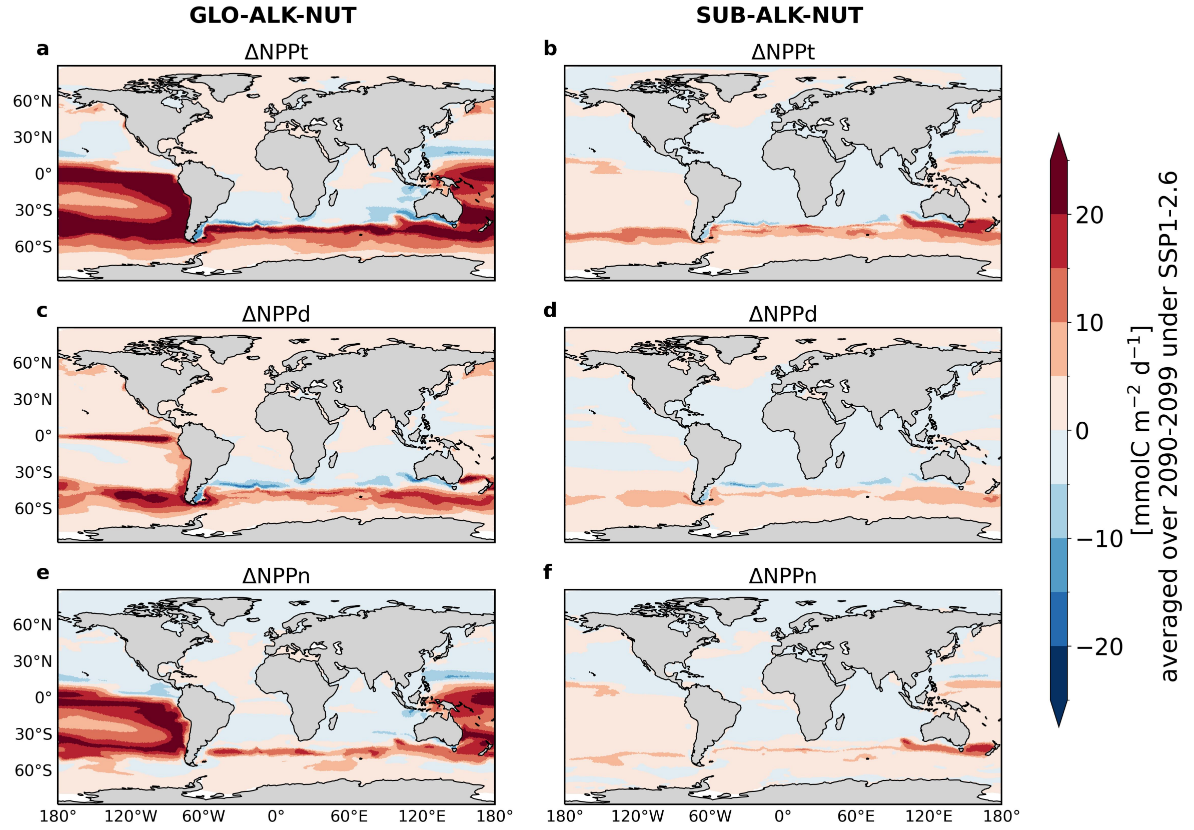

**Figure S3.** Spatial distribution of the excess total Net Primary Production (ΔNPPt), diatom NPP (ΔNPPd), and small phytoplankton NPP (ΔNPPn) in the ocean alkalinity enhancement experiments relative to the CTRL simulation, averaged over 2090-2099 for the SSP1-2.6 scenario. **(a,c,e)** ΔNPPt, ΔNPPd, and ΔNPPn for GLO-ALK-NUT. **(b,d,f)** ΔNPPt, ΔNPPd, andΔNPPn for SUB-ALK-NUT.

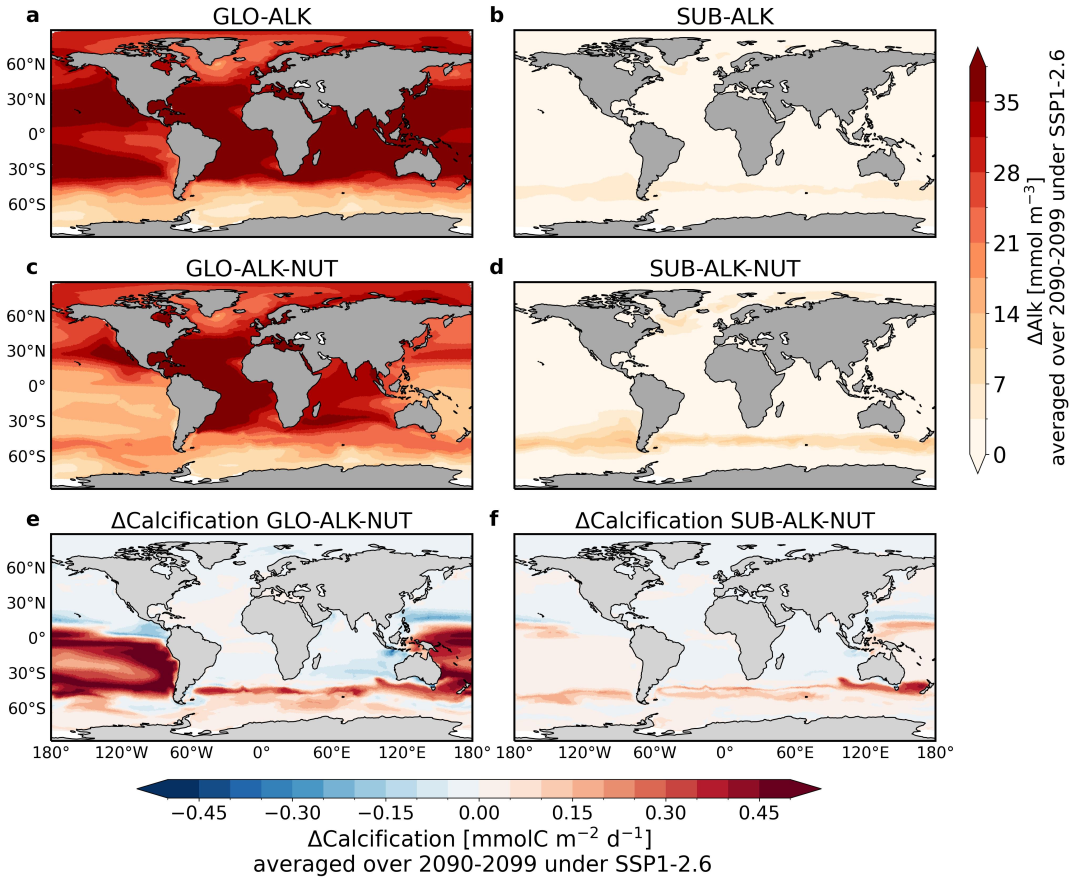

**Figure S4.** Spatial patterns of excess surface alkalinity and calcification in ocean alkalinity enhancement experiments relative to CTRL averaged over the years 2090-2099 under the SSP1-2.6 scenario. ΔAlk is shown for the experiments **(a)** GLO-ALK, **(b)** SUB-ALK, **(c)** GLO-ALK-NUT, **(d)** SUB-ALK-NUT and ΔCalcification for **(e)** GLO-ALK-NUT and **(f)** SUB-ALK-NUT.

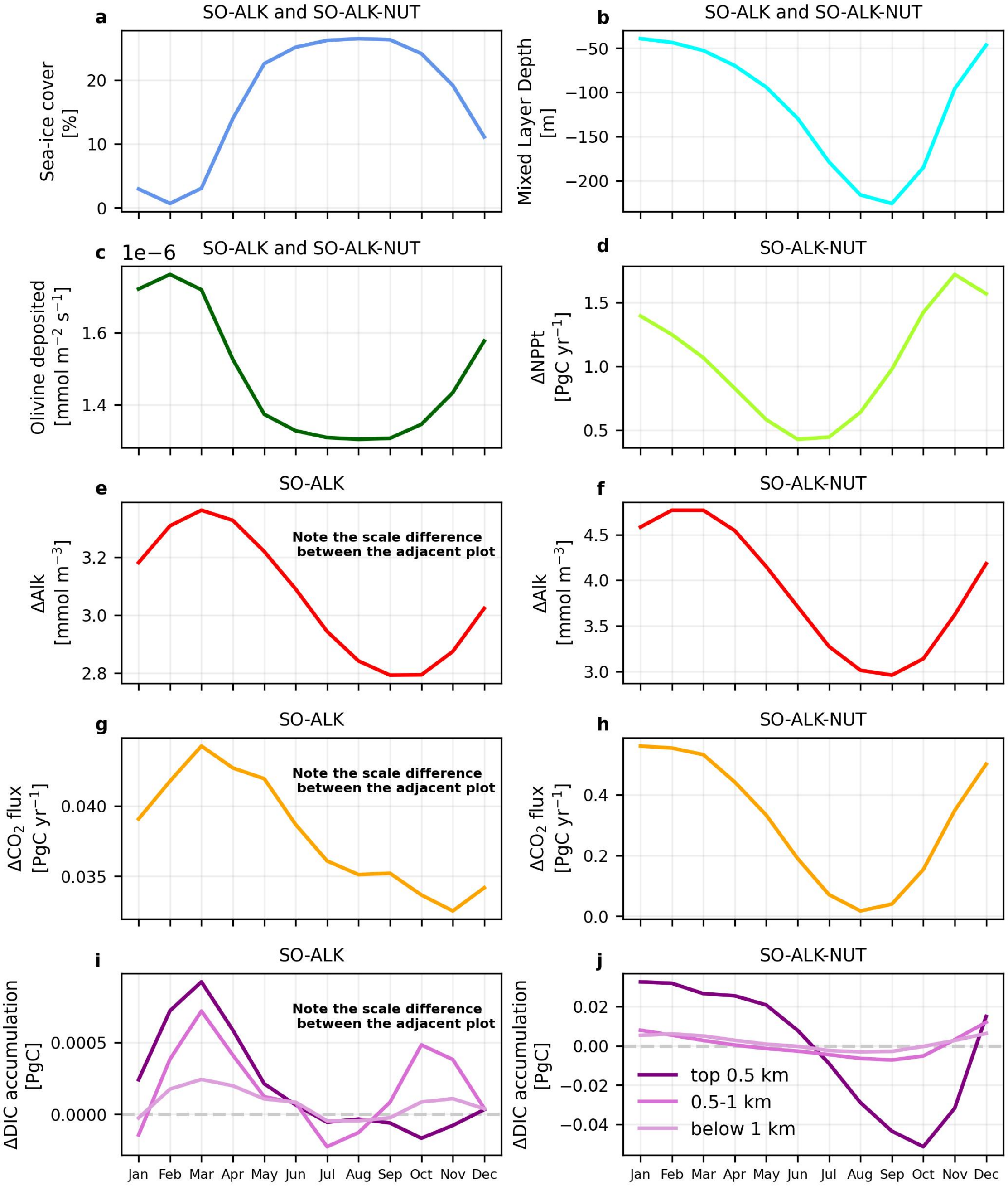

**Figure S5.** Seasonality for olivine deposition and biogeochemical responses in the ocean alkalinity enhancement experiments relative to CTRL in the Southern Ocean. The SO-ALK and SO-ALK-NUT simulations are shown and numbers are averaged over 2090-2099 under the SSP1-2.6 scenario. **(a,b,c)** Sea-ice cover [%], Mixed Layer Depth (MLD; m) Olivine deposition [mmol m$^{-2}$ s$^{-1}$] for SUB-ALK and SUB-ALK-NUT. **(d)** Excess Total Net Primary Production ΔNPPt [PgC yr$^{-1}$] for SUB-ALK-NUT. **(e,f)** Surface ΔAlk; [mmol m$^{-3}$] **(g,h)** ΔCO$_2$ flux [PgC yr$^{-1}$; positive: into the ocean, negative: reduced CO$_2$ uptake compared to CTRL] and **(i,j)** ΔDIC accumulation [PgC; positive: increase in DIC accumulation; negative: loss of DIC due to vertical and lateral transport] in top 0.5 km (dark purple), 0.5-1 km (orchid), below 1 km (light purple).

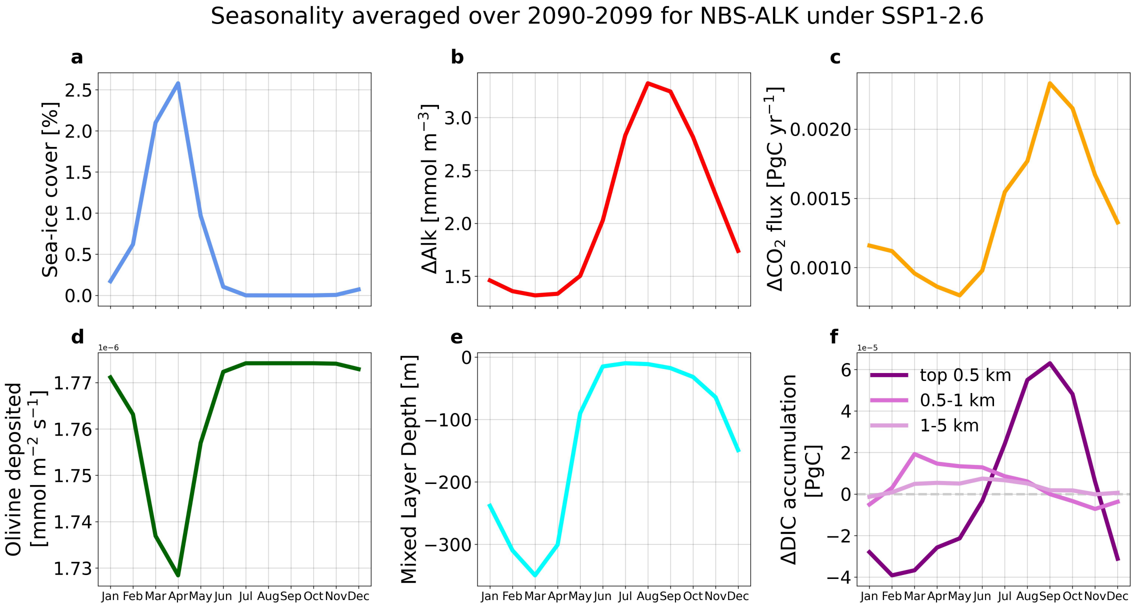

**Figure S6.** Seasonality for olivine deposition and biogeochemical responses in the ocean alkalinity enhancement experiments relative to CTRL in the Norwegian-Barents Sea region. The NBS-ALK simulation is shown and numbers are averaged over 2090-2099 under the SSP1-2.6 scenario. **(a)** Sea-ice cover [%], **(b)**Surface ΔAlk; [mmol $m^{-3}$], **(c)**$\Delta CO_2$ flux [PgC $yr^{-1}$; positive: into the ocean, negative: reduced $CO_2$ uptake compared to CTRL], **(d)**Olivine deposited [mmol $m^{-2}$ $s^{-1}$] **(e)**Mixed Layer Depth (MLD; m), and **(f)** ΔDIC accumulation [PgC; positive: increase in DIC accumulation; negative: loss of DIC due to vertical and lateral transport] in top 0.5 km (dark purple), 0.5-1 km (orchid), below 1 km (light purple).

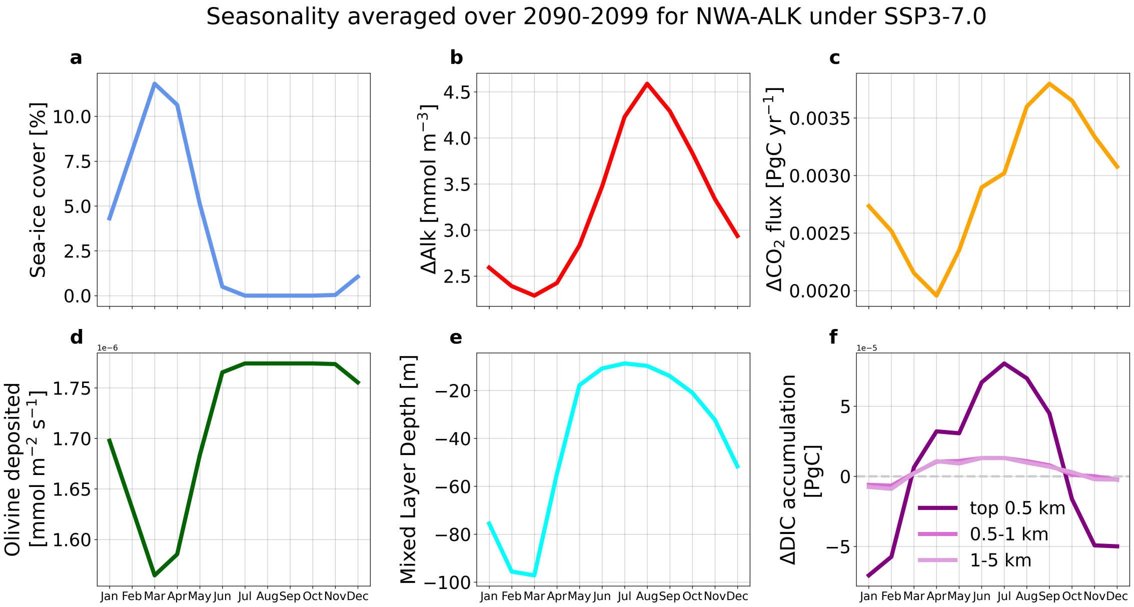

**Figure S7.** Seasonality for olivine deposition and biogeochemical responses in the ocean alkalinity enhancement experiments relative to CTRL in the Northwest Atlantic. The NWA-ALK simulation is shown and numbers are averaged over 2090-2099 under the SSP3-7.0 scenario. **(a)** Sea-ice cover [%], **(b)**Surface ΔAlk; [mmol $m^{-3}$], **(c)**Δ$CO_2$ flux [PgC $yr^{-1}$; positive: into the ocean, negative: reduced $CO_2$ uptake compared to CTRL], **(d)**Olivine deposited [mmol $m^{-2}$ $s^{-1}$] **(e)**Mixed Layer Depth (MLD; m), and **(f)** ΔDIC accumulation [PgC; positive: increase in DIC accumulation; negative: loss of DIC due to vertical and lateral transport] in top 0.5 km (dark purple), 0.5-1 km (orchid), below 1 km (light purple).

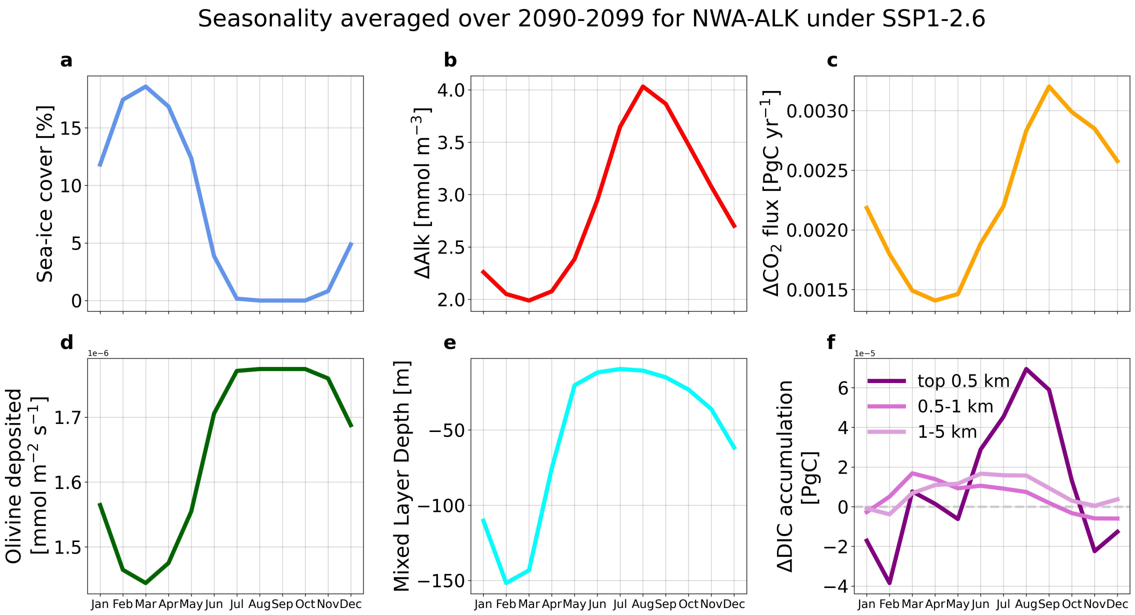

**Figure S8.** Seasonality for olivine deposition and biogeochemical responses in the ocean alkalinity enhancement experiments relative to CTRL in the Northwest Atlantic. The NWA-ALK simulation is shown and numbers are averaged over 2090-2099 under the SSP1-2.6 scenario. **(a)** Sea-ice cover [%], **(b)**Surface ΔAlk; [mmol m$^{-3}$], **(c)**Δ$CO_2$ flux [PgC yr$^{-1}$; positive: into the ocean, negative: reduced $CO_2$ uptake compared to CTRL], **(d)**Olivine deposited [mmol m$^{-2}$ s$^{-1}$] **(e)**Mixed Layer Depth (MLD; m), and **(f)** ΔDIC accumulation [PgC; positive: increase in DIC accumulation; negative: loss of DIC due to vertical and lateral transport] in top 0.5 km (dark purple), 0.5-1 km (orchid), below 1 km (light purple).

# 4

# PUBLICATION II

## ALKALINITY ENHANCEMENT IN THE SUBDUCTION REGIONS: EFFICIENCY, EARTH SYSTEM FEEDBACKS, AND DEEP OCEAN CARBON SEQUESTRATION

*in review at Environmental Research Letters*

# ALKALINITY ENHANCEMENT IN THE SUBDUCTION REGIONS: EFFICIENCY, EARTH SYSTEM FEEDBACKS, AND DEEP OCEAN CARBON SEQUESTRATION

Tanvi Nagwekar[1], Christopher Danek[1], Miriam Seifert[1], and Judith Hauck[1]

[1] Alfred-Wegener-Institut, Helmholtz-Zentrum für Polar- und Meeresforschung, Am Handelshafen 12, 27570 Bremerhaven, Germany

## ABSTRACT

Ocean Alkalinity Enhancement (OAE) is a carbon dioxide removal method that accelerates ocean carbon uptake, reduces atmospheric $CO_2$ concentrations, and thus supports the climate goals of the Paris Agreement. In this study, we compare OAE in the global ocean to OAE in subduction regions that are pivotal for anthropogenic carbon uptake and sequestration. Using an Earth System Model, we conducted emission-driven simulations under a high-emission scenario. From 2030 to 2100, we deposited 0.080 Pmol $yr^{-1}$ and 0.018 Pmol $yr^{-1}$ of alkalinity uniformly in the global ocean and subduction regions in the Southern Ocean, Northwest Atlantic and Norwegian-Barents Sea region, respectively. By 2100, OAE efficiency, calculated as the ratio of excess dissolved inorganic carbon to excess alkalinity, showed limited regional sensitivity, with comparable values in all simulations (0.72 ± 0.03). The Earth System Model simulations did not replicate the efficient downward carbon transport as found in previous ocean-only simulations because strong internal variability influenced deep ocean carbon storage. A strong linear relationship emerged between added alkalinity and the atmospheric $CO_2$ reduction across our simulations and previous studies. Global OAE reduced atmospheric $CO_2$ by 20.4 ± 0.6 ppm by 2100, while regional OAE in subduction regions reduced it by 3.6 ± 1.1 ppm. The land carbon sink weakened by 3.6 ± 3.4 PgC and by 2.0 ± 3.0 PgC in global and regional OAE, respectively. Climate feedbacks introduced high inter-annual and internal variability, illustrating the expected challenges to quantify OAE effects in real world applications. Overall, this study finds minimal differences in OAE efficiency between subduction regions and global ocean by the end of multi-decadal experiments. However, large uncertainties in the first decade of the regional application due to climate variability and Earth System Feedbacks pose challenges for Monitoring, Reporting and Verification of OAE.

Keywords: Ocean Alkalinity Enhancement, Subduction regions, Efficiency, Earth System Feedbacks

## INTRODUCTION

The oceans are pivotal in regulating atmospheric $CO_2$ concentrations and have taken up about a quarter of the anthropogenic $CO_2$ emitted since preindustrial times (Friedlingstein et al., 2022; Gruber et al., 2019). One of the main drivers for oceanic carbon uptake and outgassing is alkalinity, defined as the excess of proton acceptors over donors in seawater (Wolf-Gladrow et al., 2007; Zeebe and Wolf-Gladrow, 2001). Naturally, land weathering processes deposit alkalinity in the surface ocean, shifting carbonate equilibria by converting dissolved $CO_2$ into $HCO_3{}^-$ and $CO_3{}^{2-}$ ions, which are not directly exchangeable with the atmosphere, aiding long-term carbon sequestration. The chemical shift lowers the partial pressure of $CO_2$ ($pCO_2$) at the ocean surface, enhancing oceanic $CO_2$ uptake (Hartmann et al., 2013; Middelburg et al., 2020). However, the current rate of oceanic $CO_2$ uptake due to natural land weathering is almost two orders of magnitude lower than the anthropogenic $CO_2$ emission rates (Archer, 2005), and thus cannot mitigate rising atmospheric $CO_2$ levels and global warming. Hence, in order to achieve the climate goal by the Paris Agreement to limit the global temperature increase to 2°C above pre-industrial levels by 2100, drastic emission reductions will likely need to be accompanied by efforts of various Carbon Dioxide Removal (CDR) methods (UNFCCC, 2015). Ocean Alkalinity Enhancement (OAE) is an ocean-based CDR method that can artificially elevate the rate of oceanic $CO_2$ uptake (Hauck et al., 2016; Ilyina et al., 2013; Keller et al., 2021; Kheshgi, 1995). This can be achieved by spreading alkaline powder or solutions from various sources, such as lime, olivine, basalt, calcium carbonate or hydroxide over the ocean surface (Caserini et al., 2022).

Earth System Models (ESMs) demonstrate that OAE in high-emission scenarios strengthens the ocean carbon sink, while the land carbon sink weakens due to atmospheric $CO_2$ reduction (González and Ilyina, 2016; Jeltsch-Thömmes et al., 2024; Keller et al., 2014; Lenton et al., 2018; Palmiéri and Yool, 2024). Ocean-only models have also been used to explore OAE efficiencies in both global and regional applications, yielding varying results over the last decade after 75-80 years of deployment. For instance, OAE in large-scale biomes showed highest efficiencies in the Southern Ocean and lowest in the North Atlantic (Burt et al., 2021). Contrarily, similar efficiencies were found for global OAE and OAE along ship-tracks (Köhler et al., 2013), as well as for continuous OAE deployed globally and in the subduction regions of the Southern Ocean and North Atlantic. Notably, subduction regions could transfer $\sim$2 times more carbon to the deep ocean compared to OAE in the global ocean (Nagwekar et al., 2024). However, this contrasts with month-long pulsed OAE studies, which report low efficiencies in subduction regions due to low residence times of the water masses at the ocean surface and subsequent alkalinity loss to the deep ocean (Bach et al., 2023; He and Tyka, 2023; Jones et al., 2014). Note that ocean-only models estimate the 'capture efficiency' of OAE due to prescribed atmospheric $CO_2$ and exclusion of climate feedbacks and thus tend to overestimate OAE efficiency globally and regionally compared to ESMs ('Earth System efficiency', Schwinger et al., 2024).

This study quantifies the OAE efficiency of deep and bottom water formation regions in the Southern Ocean, Northwest Atlantic and Norwegian-Barents Sea region in response to OAE in the $21^{st}$ century in an ESM with a fully interactive carbon cycle. Through ensemble simulations, we also address uncertainties from internal climate variability, which may pose significant challenges for OAE's Monitoring, Reporting, and Verification (MRV; Ho et al., 2023).

## METHODS

### *Model Description*

The OAE simulations use the Alfred Wegener Institute Earth System Model (AWI-ESM-1-REcoM, Danek et al., 2023), based on the AWI Climate Model (AWI-CM1; Semmler et al., 2020) but includes the ocean biogeochemistry model REcoM and incorporates dynamic vegetation. The atmosphere component is modeled by ECHAM6.3 (Giorgetta et al., 2013; Stevens et al., 2013). Land vegetation and carbon dynamics are modeled with JSBACH3.20 (Reick et al., 2021), and the terrestrial hydrological discharge with HDMODEL (Hagemann and Dümenil, 1997). The ocean and sea-ice component is simulated with FESOM1.4 (Danilov et al., 2004; Wang et al., 2014), and the ocean biogeochemistry with REcoM2 (Hauck et al., 2013; Schourup-Kristensen et al., 2014). REcoM2 has 28 prognostic tracers and simulates marine carbonate chemistry and air-sea $CO_2$ exchange using the mocsy 2.0 routines (Orr and Epitalon, 2015). FESOM1.4 and REcoM2 are discretized on an unstructured mesh with 126859 surface nodes (the so-called CORE mesh) that has a finer resolution ($\sim$20-30 km) in the equatorial region, north of 60°N and in coastal Antarctica, and a coarser resolution ($\sim$120 km) in subtropical gyres. The mean horizontal resolution is $\sim$75 km, with 46 uneven vertical levels, varying from 5 m thickness at the surface to 250 m in the deep ocean (Wang et al., 2014).

### *Experimental Setup*

We start from a 970 years emission-driven spinup with preindustrial forcing following the CMIP6 protocol (Eyring et al., 2016) and select three years spaced 25 years apart to branch off three historical simulations from 1850 to 2014 (experiment 'esm-hist' from C4MIP protocol, Jones et al., 2016). These three ensemble members represent internal climate variability due to distinct initial climate conditions. Subsequently, future scenario simulations are carried out for the high-emission scenario SSP3-7.0 and for each ensemble member, following the scenario simulation C4MIP protocol (Jones et al., 2016). This scenario assumes inadequate climate policies to meet the Paris Agreement goal, with increasing $CO_2$ emissions that lead to an atmospheric $CO_2$ concentration of 867 ppm by 2100, and to global warming of 3-5°C above preindustrial levels (O'Neill et al., 2016). These future projection simulations (2015-2100) are termed as control (CTRL) simulations. The OAE simulations are branched off in 2030 from their respective CTRL and are computed until the end of 2100.

### *Identifying deep and bottom water formation regions*

Using the Water Mass Transformation (WMT) and Water Mass Formation (WMF) framework (Walin, 1982; Pellichero et al., 2018) we locate subduction regions in the Southern Ocean (SO; south of 40°S), Northwest Atlantic (NWA; Labrador Sea, Irminger Sea, Iceland Sea and shelf regions of Davis Strait collectively; 50°N-75°N; 70°W-17°W) and the Norwegian-Barents Sea (Gruber et al., 2009; Våge et al., 2009; NBS; 62°N–77°N; 60°E-10°W). The framework provides

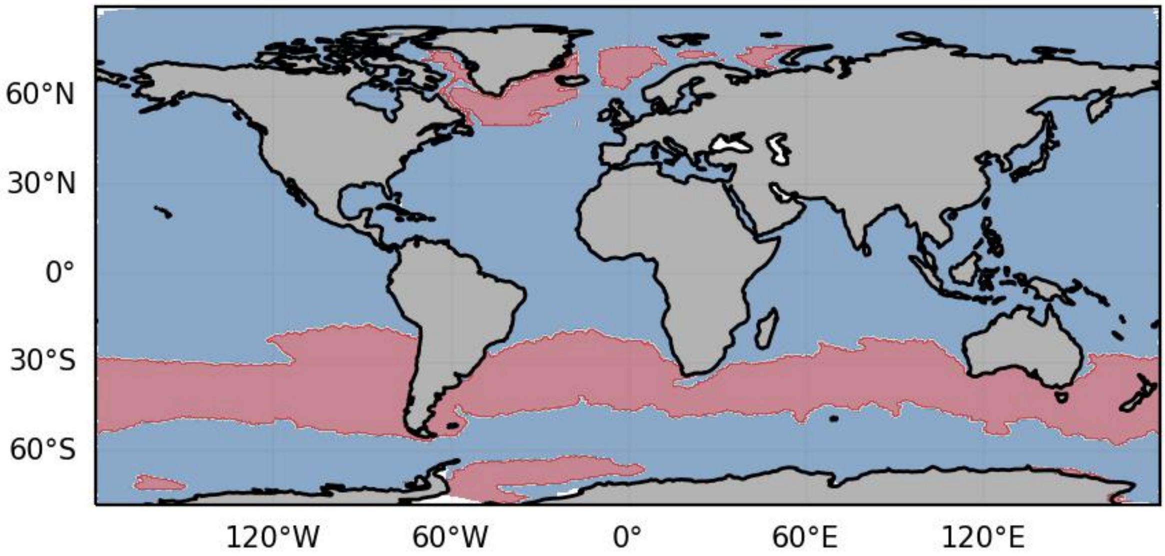

FIGURE 4.1: Red regions represent alkalinity deposition mask for the subduction regions in the Southern Ocean, Northwest Atlantic, and the Norwegian-Barents Sea region.

the magnitude at which a certain water mass is made denser or lighter due to diabatic processes like surface buoyancy fluxes, diapycnal mixing in the ocean interior and the rate of changes in lateral transport and mixing, ensuring mass conservation in a given density range (Abernathey et al., 2016; Pellichero et al., 2018; Nissen et al., 2022). As expected, it diagnoses deep, bottom and intermediate WMF regions based on the surface buoyancy fluxes in the Southern Ocean and the North Atlantic. Additionally, subduction is detected in Davis Strait shelves, a feature absent in observations (Jeansson et al., 2017; Jeansson et al., 2023) highlighting model limitations (also see Nagwekar et al., 2024). Further details on WMT/WMF calculations are given in the supplement (Text S1). Using the three historical ensemble members (1950-2014), we conduct the WMT/WMF analysis to identify subduction in the SO, NWA and NBS and create alkalinity deposition masks for each member. We choose the mask with the largest area of alkalinity deposition for OAE experiments in all ensemble members (Figure 4.1).

### *Ocean Alkalinity Enhancement Model Experiments and Efficiency*

We simulate the three ensemble members for global OAE (GLO-ALK) and subduction regions OAE (SUB-ALK) with continuous alkalinity addition from 2030 to 2100. For GLO-ALK, 0.082 Pmol $\mathrm{yr}^{-1}$ of alkalinity is deposited (equivalent to 3 Pg $\mathrm{yr}^{-1}$ olivine deposition; Hauck et al., 2016; Köhler et al., 2013). In SUB-ALK, using the subduction regions deposition mask (Figure 4.1), 0.018 Pmol $\mathrm{yr}^{-1}$ alkalinity is deposited (equivalent to 0.66 Pg $\mathrm{yr}^{-1}$ olivine). In both cases, added alkalinity is scaled with relative sea-ice cover in each grid cell and time-step, with no alkalinity addition in fully ice-covered cells. Hence, due to shrinking sea-ice cover towards the end of the century, ~1.9% more alkalinity was added in the 2090s compared to the 2030s (Table 4.1).

The OAE efficiency is calculated as the ratio of excess volume-integrated dissolved inorganic carbon (DIC) to excess volume-integrated alkalinity ($\eta CO_2$ = $\Delta$DIC/$\Delta$Alk; Renforth and Henderson, 2017). It accounts for the accumulated increase in DIC and alkalinity relative to the CTRL (Nagwekar et al., 2024). We report efficiencies calculated from globally integrated $\Delta$DIC and $\Delta$Alk for GLO-ALK and SUB-ALK (Table 4.1).

| Simulations | Alkalinity added [Pmol yr$^{-1}$] | | | $\Delta FCO_2$ [PgC yr$^{-1}$] | | $\eta$CO$_2$ ($\Delta$DIC/$\Delta$Alk) | | $\Delta$FCO$_2$ ocean cumulative [PgC] | | |
|---|---|---|---|---|---|---|---|---|---|---|
| | 2030s | 2090s | 2100 [Pmol] | 2030s | 2090s | 2030s | 2090s | 2030s | 2090s | 2100 |
| GLO-ALK | 0.078 | 0.080 | 5.57 | 0.53<br>±0.09 | 0.75<br>±0.16 | 0.46<br>±0.05 | 0.73<br>±0.01 | 2.67<br>±0.21 | 45.28<br>±0.76 | 49.54<br>±0.74 |
| SUB-ALK | 0.017 | 0.018 | 1.28 | 0.13<br>±0.10 | 0.20<br>±0.15 | 0.38<br>±0.20 | 0.71<br>±0.03 | 0.59<br>±0.22 | 10.10<br>±0.51 | 11.21<br>±0.54 |

| Simulations | $\Delta$FCO$_2$ land cumulative [PgC] | | | $\Delta$DIC top 1 km [PgC] | | | $\Delta$DIC below 1 km [PgC] | | |
|---|---|---|---|---|---|---|---|---|---|
| | 2030s | 2090s | 2100 | 2030s | 2090s | 2100 | 2030s | 2090s | 2100 |
| GLO-ALK | −0.14<br>±2.01 | −4.17<br>±2.66 | −3.56<br>±3.39 | 2.08<br>±0.45 | 41.27<br>±0.77 | 45.32<br>±1.29 | 0.11<br>±0.55 | 1.32<br>±0.50 | 1.16<br>±0.72 |
| SUB-ALK | −1.44<br>±3.11 | −0.73<br>±2.64 | −1.99<br>±3.0 | 0.26<br>±0.32 | 9.50<br>±1.0 | 10.23<br>±1.49 | 0.19<br>±0.25 | −0.084<br>±0.93 | 0.27<br>±1.79 |

| Simulations | $\Delta$DIC below 1 km [%] | | | Atmospheric CO$_2$ [ppm] | | | $\Delta$SAT [°C] | | |
|---|---|---|---|---|---|---|---|---|---|
| | 2030s | 2090s | 2100 | 2030s | 2090s | 2100 | 2030s | 2090s | 2100 |
| GLO-ALK | 5.02<br>±55.0 | 3.10<br>±39.4 | 2.50<br>±35.8 | −0.77<br>±0.64 | −18.57<br>±0.99 | −20.43<br>±0.59 | 0.005<br>±0.066 | −0.053<br>±0.092 | −0.043<br>±0.18 |
| SUB-ALK | 42.22<br>±43.9 | −0.89<br>±48.2 | 2.57<br>±45.4 | 0.28<br>±0.95 | −4.35<br>±0.89 | −3.6<br>±1.12 | 0.001<br>±0.088 | 0.016<br>±0.076 | 0.054<br>±0.053 |

Table 4.1: Amount of alkalinity added and response of the Earth System to the ocean alkalinity enhancement. We report added alkalinity after scaling with sea-ice cover, excess of oceanic CO$_2$ uptake ($\Delta$FCO$_2$), the efficiency metric $\eta$CO$_2$ that is calculated as the volume-integrated excess dissolved inorganic carbon (DIC) over volume-integrated excess alkalinity over the global ocean, the cumulative changes in air-sea ($\Delta$FCO$_2$ ocean cumulative) and air-land CO$_2$ flux (land CO$_2$ flux cumulative). We further list the increase in the DIC concentration in the top 1 km, below 1 km of the global ocean and percent of carbon stored below 1 km, changes in the atmospheric CO$_2$ mixing ratio and the Surface Air Temperature (SAT; 2 m). The numbers are calculated as OAE experiment minus CTRL and are reported as an average over the 2030s, 2090s and the year 2100. Alkalinity added in the year 2100 represents the cumulative value.

## RESULTS AND DISCUSSION

### *Variability in the oceanic $CO_2$ uptake in response to OAE*

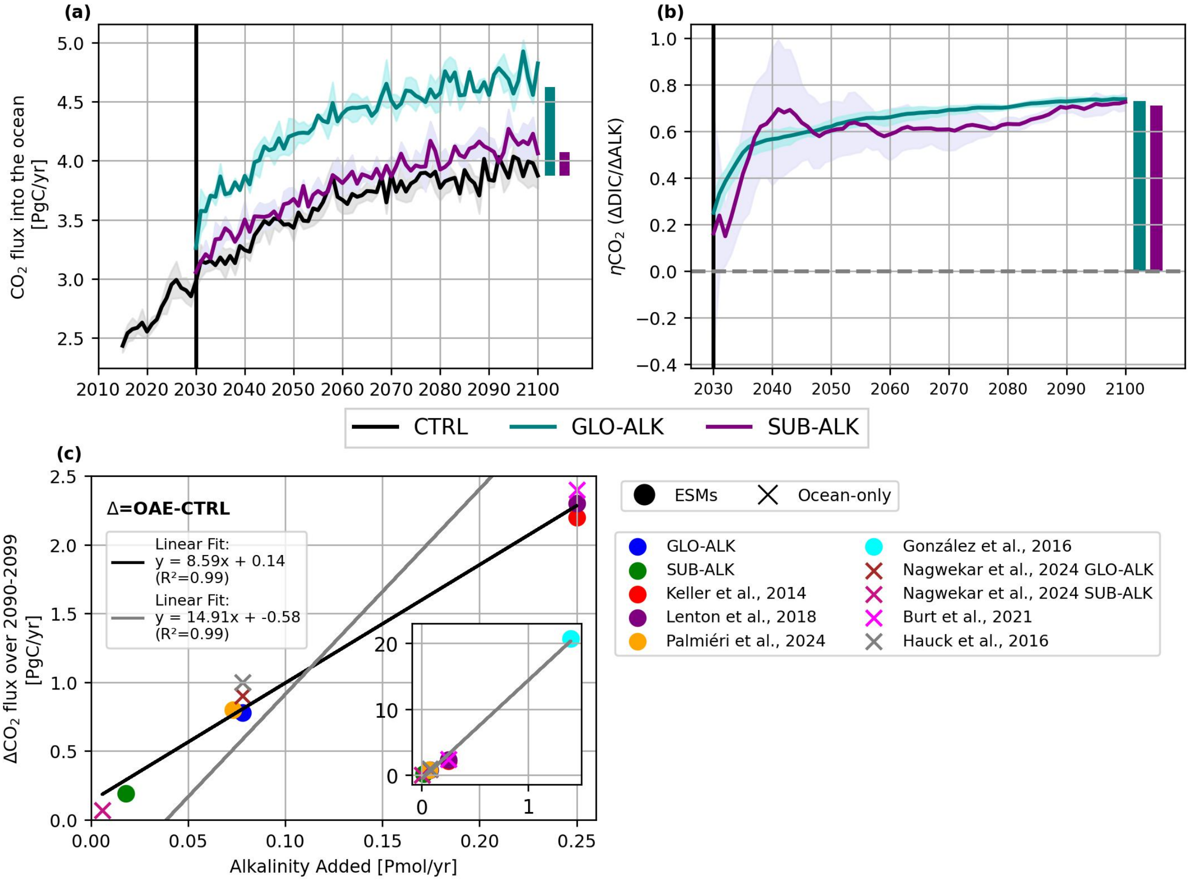

FIGURE 4.2: Ocean carbon response to ocean alkalinity enhancement for global (GLO-ALK) and subduction region (SUB-ALK) experiments. **(a)** Global oceanic $CO_2$ uptake in the Control (CTRL) and OAE simulations. The 2090-2099 mean difference between CTRL and GLO-ALK is shown by the green bar, and between CTRL and SUB-ALK by the purple bar. **(b)** OAE efficiency $\eta CO_2$, calculated as the volume-integrated increase in dissolved inorganic carbon (DIC) divided by the volume-integrated increase in alkalinity relative to the CTRL simulation. The average $\eta CO_2$ over the 2090s is indicated by a green bar for GLO-ALK and a purple bar for SUB-ALK. Shades around the lines represent the standard deviation of the ensemble members. **(c)** Increase in $CO_2$ flux relative to CTRL versus added alkalinity averaged over 2090-2099 for different studies using ocean-only and Earth System Models in a high emission scenario. Solid black and gray lines are the linear fits. Solid black linear fit is only for the studies with comparatively low levels of alkalinity addition and solid gray linear fit is for the studies with low as well as the study with a very high amount of alkalinity addition.

Alkalinity perturbation globally and in the subduction regions enhance $CO_2$ uptake throughout the century compared to the CTRL simulation (Figure 4.2a), although regional differences arise between ensemble members due to ocean-atmosphere interactions (Figure 4.3a-c). In GLO-ALK, $CO_2$ uptake relative to CTRL ($\Delta FCO_2$) is enhanced by 0.52 PgC $yr^{-1}$ in the 2030s and by 0.75 PgC $yr^{-1}$ in the 2090s. In SUB-ALK, $CO_2$ uptake rises by 0.13 PgC $yr^{-1}$ (2030s) and 0.20 PgC $yr^{-1}$ (2090s). The increase in $\Delta FCO_2$ over time results from delayed equilibration between ocean and atmosphere (Bach et al., 2023; Jones et al., 2014) and elevated ocean carbonate chemistry sensitivity to enhanced alkalinity at the end of the century in a high-$CO_2$ world (Hauck et al., 2016).

Our results show that by the end of the century, $CO_2$ uptake in GLO-ALK and SUB-ALK scales linearly with the amount of added alkalinity, as also seen in other ESMs and ocean-only models (Figure 4.2c). For instance, when adding as much alkalinity as in our GLO-ALK experiment to coastlines globally, the OAE-induced $CO_2$ uptake is comparable to our simulation (0.8 PgC $yr^{-1}$, Palmiéri and Yool, 2024). This implies that the ocean $CO_2$ response to OAE scales primarily with alkalinity input, while regional differences are secondary. Accordingly, higher alkalinity deposition globally or regionally (0.25 and 1.4 Pmol $yr^{-1}$) results in proportionally higher excess $CO_2$ uptake (González and Ilyina, 2016; Ilyina et al., 2013; Keller et al., 2014; Sonntag et al., 2018). However, the ocean-only models show higher excess $CO_2$ uptake than ESMs for the same alkalinity addition. For example, depositing 0.078 Pmol $^{-1}$ of alkalinity globally using an ocean-only setup increased the $CO_2$ uptake by 0.9-1.0 PgC $yr^{-1}$ (Hauck et al., 2016; Nagwekar et al., 2024), which is 0.1-0.2 PgC $yr^{-1}$ higher than in the emission-driven ESM simulation GLO-ALK. Similarly, Burt et al. (2021), using an ocean-only model with the same alkalinity addition (0.25 Pmol $yr^{-1}1$; 2020-2100) as in the ESM studies of Keller et al. (2014) and Lenton et al. (2018), reported a slightly higher $CO_2$ uptake by 0.1 PgC $yr^{-1}$ compared to the ESM studies. This difference is attributed to climate feedbacks in the ESMs and thus confirms that ocean-only studies provide an upper limit estimate of the increase in excess $CO_2$ uptake (Schwinger et al., 2024).

The OAE efficiencies of GLO-ALK and SUB-ALK converge in the 2090s (0.71-0.73), which is in line with other OAE studies using an ESM (e.g., 0.72-0.78; Feng et al., 2017; Palmiéri and Yool, 2024). However, efficiencies vary substantially in the first 20 years of the simulations (Figure 4.2b), due to different initial climate conditions in each ensemble member that influence the earth system response to OAE. Compared to GLO-ALK (8.5% standard deviation around the mean), SUB-ALK shows explicitly high variability among its ensemble members (±55.5%). Since the initial decades are key for real-world applications, the high uncertainty in efficiency of regional applications during this period will be a challenge for MRV. Following the larger OAE-induced ocean $CO_2$ uptake in ocean-only models, they also reported higher efficiencies, ranging from 0.85 to 0.95 for global and regional OAE (Burt et al., 2021; He and Tyka, 2023; Nagwekar et al., 2024; Wang et al., 2023). This again underlines the role of climate feedbacks in determining the OAE efficiency.

In an ocean-only setup, global and subduction regions OAE revealed nearly uniform spatial patterns of $CO_2$ flux changes relative to CTRL ($\Delta FCO_2$), with consistent positive anomalies (Nagwekar et al., 2024). In contrast, ESM simulations for GLO-ALK and SUB-ALK display more regional heterogeneity in $\Delta FCO_2$, with negative anomalies ($FCO_2$ lower in OAE than in CTRL) caused by climate feedbacks (Figure 4.3a-f). Consequently, each ensemble member exhibits distinct regional patterns due to specific land-ocean-atmosphere interactions. For instance, in SUB-ALK, positive $\Delta FCO_2$ ($FCO_2$ higher in OAE than in CTRL) occurs predominantly in the Southern Ocean, where we deposit alkalinity, but the Weddell Sea response varies across ensemble members. The North Atlantic also shows ensemble member-dependent results, with

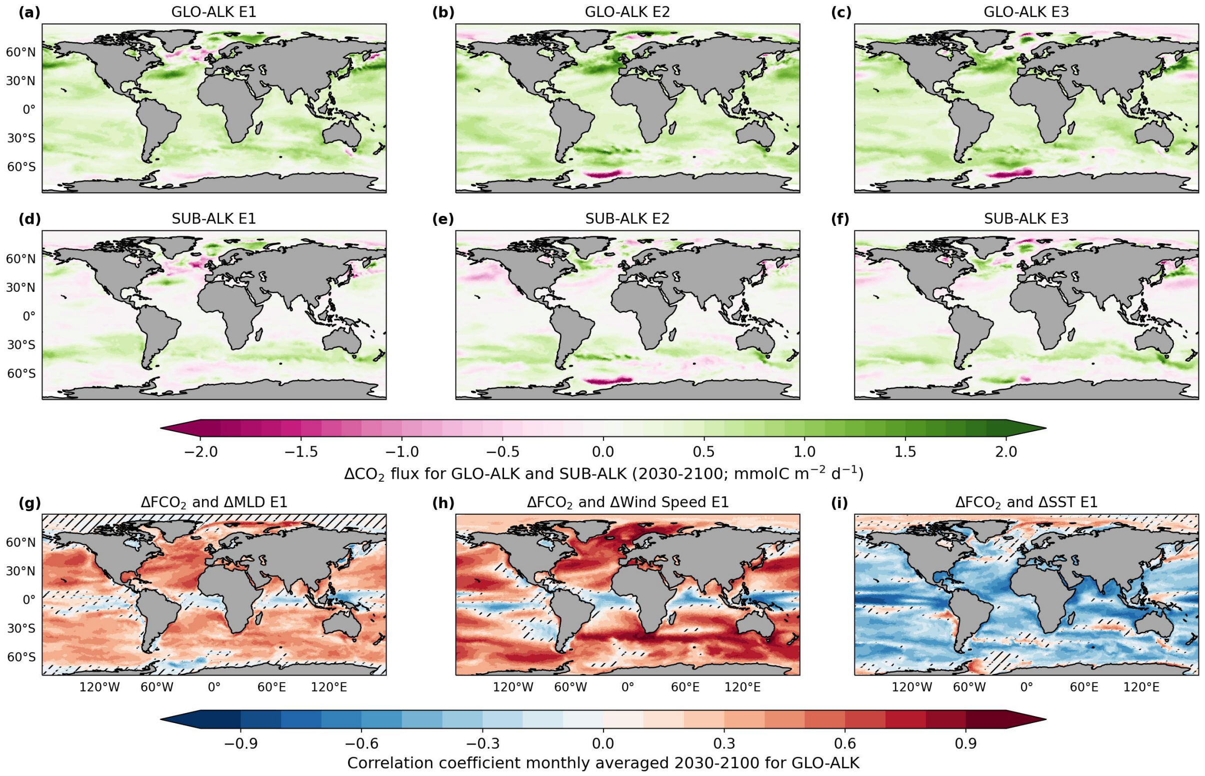

FIGURE 4.3: Spatial patterns for changes in the air-sea $CO_2$ flux relative to CTRL ($\Delta FCO_2$) for each ensemble member averaged over 2030-2100 in **(a,b,c)** GLO-ALK and **(d,e,f)** SUB-ALK. $CO_2$ flux in CTRL is positive for uptake and negative for outgassing. In the $\Delta FCO_2$ maps, positive indicates an increase in $FCO_2$ relative to CTRL and negative indicates a decrease in $FCO_2$ relative to CTRL. Correlation coefficients for GLO-ALK in the first ensemble member (E1) between $CO_2$ flux anomalies and **(g)** Mixed Layer Depth (MLD) anomalies, **(h)** Wind Speed anomalies and **(i)** Sea Surface Temperature (SST) anomalies, respectively. The hatched regions show where the correlation coefficient is not statistically significant (confidence level=0.95). All correlations are calculated from monthly means over 2030-2100. See supplement Figure S3 and S4 for the correlation patterns in other ensemble members for GLO-ALK and SUB-ALK.

the first ensemble member in SUB-ALK exhibiting a negative $\Delta FCO_2$, while the other two ensemble members show a positive anomaly (Figure 4.3d-f). This response is likely linked to the variable deep mixing in the Southern Ocean and North Atlantic. In summary, these experiments illustrate how the spatial $CO_2$ flux response to OAE is modified by internal climate variability.

The differences of $CO_2$ flux anomalies between ensemble members can be explained through well-known drivers of air-sea $CO_2$ fluxes that seemingly vary between ensemble members (e.g., Takahashi et al., 2009). Here, we illustrate this through maps of correlations between $CO_2$ flux anomalies with MLD (as a proxy for mixing), wind speed (as the major driver of gas-exchange) and SST anomalies (as a proxy for solubility). We find significant correlations throughout most of the global ocean (Figure 4.3g-i) that are robust across ensemble members (Figure S3-S4). Higher $CO_2$ uptake in response to OAE occurs when the MLD is shallower, wind speeds are stronger, and SST is lower compared to the CTRL.

*Long-term carbon storage in form of Dissolved Inorganic Carbon*

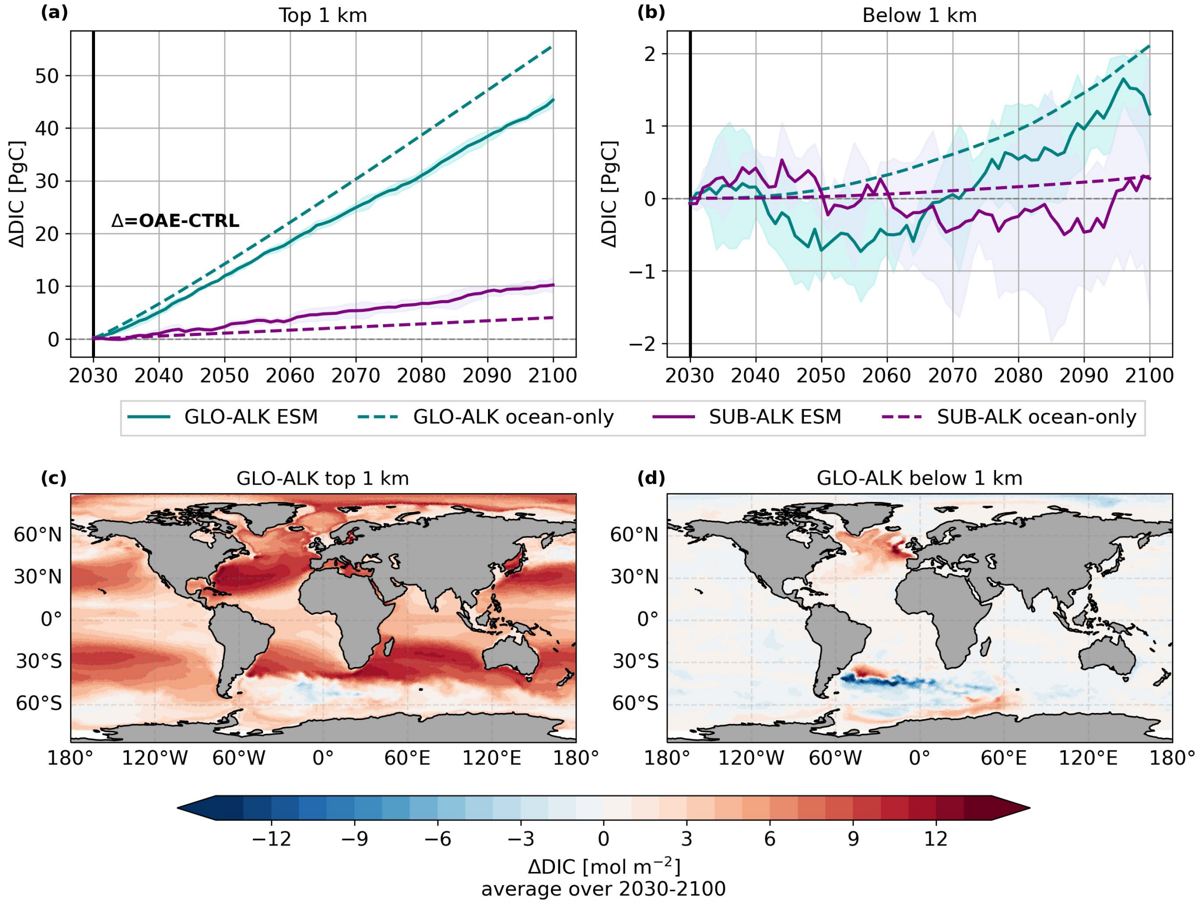

FIGURE 4.4: Volume-integrated dissolved inorganic carbon (DIC) relative to CTRL **(a)** in the top 1 km and **(b)** below 1 km for global OAE (GLO-ALK; green) and subduction regions OAE (SUB-ALK; purple). Solid lines represent the Earth System Model (ESM) simulations (this study) and dashed lines show ocean-only simulations (Nagwekar et al., 2024). Shades around the lines represent the standard deviation of the ensemble members. **(c,d)** Spatial patterns for changes in DIC in the GLO-ALK experiment relative to CTRL using the ESM in the top 1 km and below 1 km, respectively. See supplementary Figures S5 and S6 for ΔDIC spatial patterns in individual ensemble members of GLO-ALK and SUB-ALK respectively.

We next assess changes in the DIC inventory (ΔDIC) to evaluate the OAE impact on deep ocean carbon storage in subduction regions versus the global ocean. In the top 1 km of the water column, 41.3 ± 0.8 PgC of DIC is accumulated in GLO-ALK and 9.5 ± 1.0 PgC in SUB-ALK until 2090s (relative to CTRL, Table 4.1). Carbon accumulation is positive throughout the top 1 km, with a low interannual variability and ensemble spread (Figure 4.4a). The maximum accumulation is found in the top 100 m depth in both the experiments. Below 1 km, ΔDIC shows high annual fluctuations and variability across the ensemble members, with lower accumulation than CTRL during certain decades (Figure 4.4b). This variability on a global and regional scale arises from climate feedbacks to OAE and internal climate variability in the ESM. The role of climate feedbacks is illustrated by SUB-ALK relatively transferring on average 8.4 times more excess carbon below 1 km than GLO-ALK in the 2030s, but accumulating less excess carbon below 1 km compared to GLO-ALK in the 2090s with large variability across the ensemble. In an ocean-only setup without climate feedbacks, SUB-ALK could transfer ∼2 times more carbon to the deep ocean than GLO-ALK by the 2090s (Nagwekar et al., 2024). Internal climate variability is depicted by the fact that for the first ensemble member, SUB-ALK accumulates more carbon than GLO-ALK in 2090s, whereas the other two ensemble members render the opposite. This illustrates that without ensemble simulations, the impact of internal climate variability on storage efficiency would be overlooked.

Along with temporal variability, $\Delta$DIC also exhibited spatial variability (Figure 4.4c-d). Positive $\Delta$DIC occurs in the top 1 km, with maximum accumulation in the gyre system, the Arctic, and the Southern Ocean. Below 1 km, $\Delta$DIC increases prominently in the North Atlantic and along the Antarctic coast. Surprisingly, both the upper 1 km and the layer below 1 km have negative $\Delta$DIC anomalies, i.e., the DIC is lower in OAE simulations compared to the CTRL. As this is not found in the ocean-only simulations, this must be driven by climate feedbacks that leads to redistribution of DIC within the water column. Possible processes that may play a role in these feedbacks are altered ocean circulation, mixing, biological productivity in the euphotic zone, and shifts of ocean fronts (Clement and Gruber, 2018; Keppler et al., 2023; Doney et al., 2009). These confounding effects present a challenge for MRV that rely on measurements of changes in DIC and alkalinity inventories due to OAE.

### *Impact of OAE on Atmospheric $CO_2$, Surface Air Temperature (SAT), and Land Carbon Fluxes*

A crucial outcome of OAE for climate change mitigation is the atmospheric $CO_2$ reduction. GLO-ALK and SUB-ALK reduce atmospheric $CO_2$ by 20.4 ± 0.6 ppm and 3.6 ± 1.1 ppm, respectively, in 2100 (Figure 4.5a). The reduction in atmospheric $CO_2$ scales linearly with the added amount of alkalinity (Figure 4.5c, $R^2 = 1$). This linear relationship persists across various studies, despite differences in model configuration, resolution, and underlying assumptions, such as the region, period, method and material used for OAE deployment. Palmiéri and Yool (2024), simulated a decrease of 20.8 ppm in atmospheric $CO_2$ by 2100 from OAE along global coasts, which is comparable in terms of added alkalinity (0.078 Pmol $yr^{-1}$) and $CO_2$ reduction to our GLO-ALK experiment. This suggests a limited regional sensitivity in atmospheric $CO_2$ reduction, consistent with findings by Lenton et al. (2018), who reported a $CO_2$ reduction of 82-86 ppm for 0.25 Pmol $yr^{-1}$ alkalinity addition globally and regionally by the end of the 21st century. However, the atmospheric $CO_2$ reduction simulated in our experiments and in other studies is small compared to the historical atmospheric $CO_2$ increase due to fossil fuel emissions and land-use change. This re-emphasizes the need for drastic emission reduction prior to application of a portfolio of negative emissions technologies, to which OAE could contribute. It is common sense that OAE would be more effective in mitigating climate change and minimizing negative impacts on marine ecology in low-emission pathways, as these align better with emission reduction strategies and net-zero targets (Ho, 2023). To reduce atmospheric $CO_2$ by 450 ppm and limit temperature rise to 1.5°C within a high-emission scenario, an unrealistically large amount of alkalinity (1.4 Pmol $yr^{-1}$) addition would be needed (González and Ilyina, 2016). While OAE modeling studies often use high-emission scenarios,

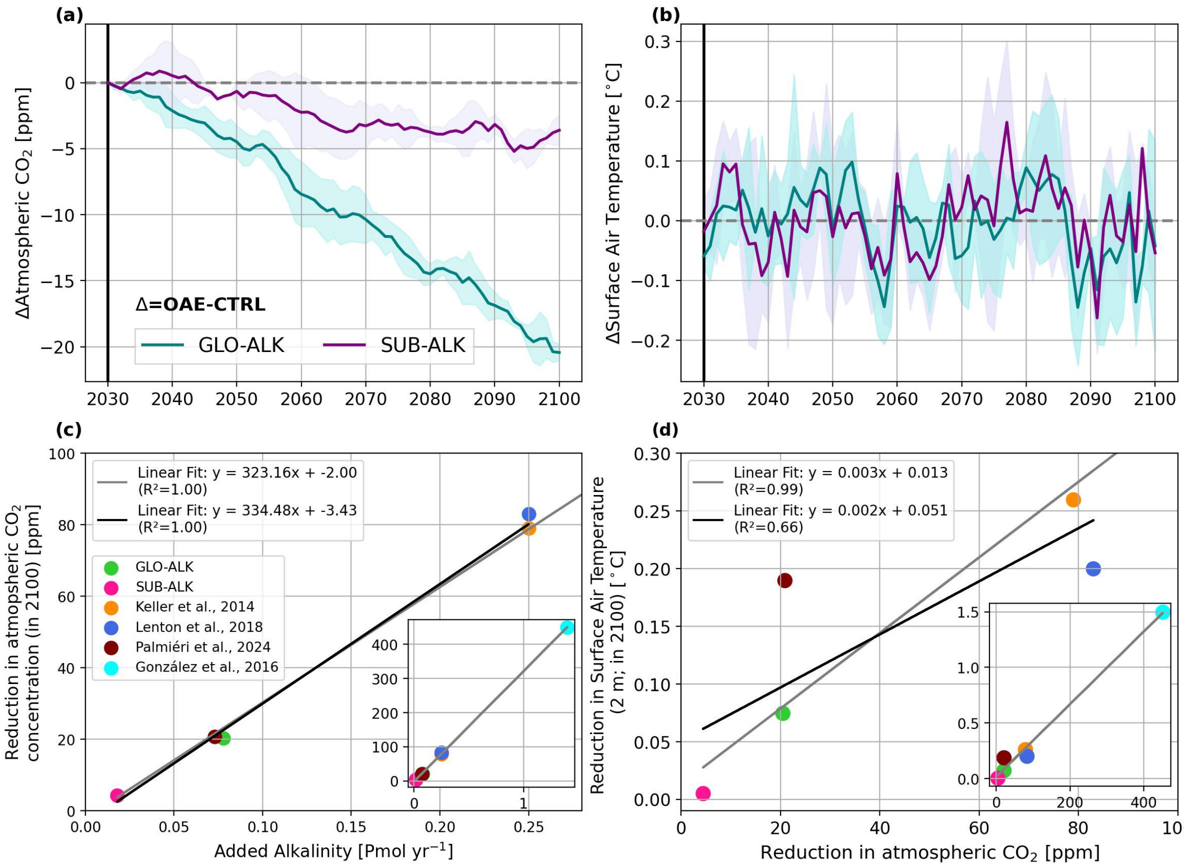

FIGURE 4.5: Time series for the change in **(a)** atmospheric $CO_2$ and **(b)** surface air temperature relative to the CTRL in global OAE (GLO-ALK; green) and subduction region OAE (SUB-ALK; purple). Shades around the lines represent the standard deviation of the ensemble members. Scatter plots showing the relationship between **(c)** added alkalinity and the corresponding reduction in atmospheric $CO_2$ concentration, and **(d)** atmospheric $CO_2$ reduction and the decrease in surface air temperature (SAT; 2 m) across different studies using various Earth System Models. Solid black linear fit is only for the studies with comparatively low levels of alkalinity addition or atmospheric $CO_2$ reduction and solid gray linear fit is for the studies with low as well as the study with a very high amount of alkalinity addition or atmospheric $CO_2$ reduction.

the scenario dependence of OAE is relatively low, hence the results will be transferable to other emission pathways (Lenton et al., 2018; Nagwekar et al., 2024).

The atmospheric $CO_2$ reduction stimulated fluctuations in SAT (2 m). Compared to the CTRL simulation, SAT is reduced by a statistically insignificant 0.053 ± 0.092°C (GLO-ALK) and 0.016 ± 0.076°C (SUB-ALK) in the 2090s. In addition, the interannual variability is strong and SAT can at times also become higher than in the CTRL simulation. A comparison with other studies indicates that the response of SAT to atmospheric $CO_2$ reduction is highly model dependent (Figure 4.5d). In contrast to the well understood carbon system response to OAE (Figure 4.5c), the SAT signal depends on the model's equilibrium climate sensitivity (ECS). For instance, Palmiéri and Yool (2024) show a higher SAT reduction for a similar decrease in atmospheric $CO_2$ as our GLO-ALK (Figure 4.5d), due to the higher ECS of UK-ESM (5.4°C; Sellar et al., 2019) compared to AWI-ESM (3.2°C; Semmler et al., 2020). Further, a lag of approximately a decade in SAT response following $CO_2$ decline due to OAE has been reported (Jeltsch-Thömmes et al., 2024). However, over a 70-years simulation, this lag probably has only a small effect on the relationship between ΔSAT and atmospheric $CO_2$ reduction by 2100. Our simulations as well as previous studies suggest that the scale of OAE applied here (0.018-0.25 Pmol $yr^{-1}$) results in a negligible SAT decrease by 2100 (Figure 4.5d). Thus, at this scale, OAE can only be effective if implemented along with drastic emission reductions and with a portfolio of other CDR techniques.

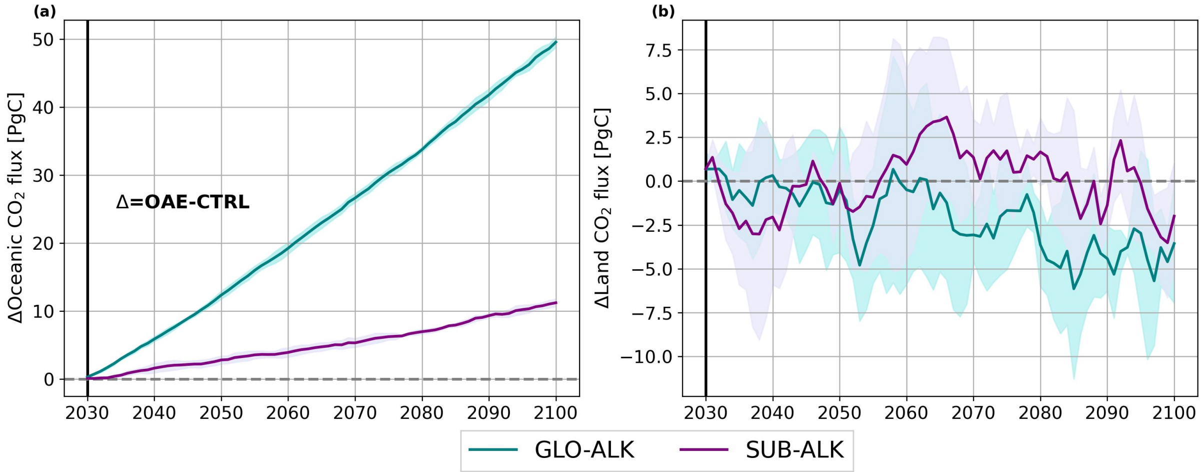

FIGURE 4.6: Time series for the cumulative change in **(a)** the oceanic $CO_2$ flux and **(b)** the land $CO_2$ flux changes. Positive: strengthening of the carbon sinks. Both global OAE (GLO-ALK) and subduction region OAE (SUB-ALK) are relative to the CTRL simulation. Solid lines represent the ensemble mean and the shading is the standard deviation of the three ensemble members.

In our GLO-ALK simulation, the atmospheric $CO_2$ is reduced by 43.4 ± 1.3 PgC relative to CTRL by 2100, of which 49.5 ± 0.7 PgC is taken up by the oceans and the land uptake is reduced by 3.6 ± 3.4 PgC. SUB-ALK results in removal of 7.6 ± 2.4 PgC atmospheric $CO_2$ relative to CTRL by 2100, with the oceans taking up 11.2 ± 0.5 PgC and land uptake weakening by 2.0 ± 3.0 PgC (Figure 4.6a,b). This implies that the ocean's response to OAE is robust, whereas the land response is weaker and more variable. In SUB-ALK, changes in the land carbon sink remain indistinguishable from zero throughout the $21^{st}$ century due to lower alkalinity addition. Contrarily, in GLO-ALK, the differences deviate from zero after 2080, implying that the effect of alkalinity addition has a time of emergence of 50 years. Generally, OAE can affect the land carbon cycle through alterations in the atmospheric $CO_2$ and SAT. A reduction in atmospheric $CO_2$ diminishes the $CO_2$ fertilization effect, leading to a lower rate of carbon uptake by vegetation (Jeltsch-Thömmes et al., 2024). Additionally, changes in the SAT and precipitation influence the vegetation dynamics and soil carbon storage, further affecting the land carbon cycle (Adloff et al., 2018). In our simulations, the higher reduction in atmospheric $CO_2$ and SAT in GLO-ALK, resulting from higher total alkalinity addition, leads to a stronger weakening of the land carbon sink compared to SUB-ALK over the $21^{st}$ century. Our results are in line with previous studies that reported a weakening of the land carbon sink in both global and regional OAE experiments of varying magnitude based on amount of added alkalinity and corresponding atmospheric $CO_2$ and SAT reduction (González and Ilyina, 2016; Keller et al., 2014; Lenton et al., 2018; Palmiéri and Yool, 2024). Our simulations also point to a large internal variability of the land carbon sink that will complicate its quantification if that is considered necessary as part of MRV.

### *Limitations*

We conducted idealized OAE experiments assuming instantaneous and complete dissolution of the added alkaline mineral in the surface ocean. While being consistent with prior studies using prescribed alkalinity addition rates (Butenschön et al., 2021; Hauck et al., 2016; Keller et al., 2014; Lenton et al., 2018), it eludes how ambient seawater temperature, pH and mineral grain size affect the dissolution dynamics. Maximum dissolution rate is achieved with finely ground minerals ($\sim 1$ $\mu$m) are dissolved in warmer, more acidic seawater (Feng et al., 2017; Köhler et al., 2013; Palmiéri and Yool, 2024). However, the energy consumption in mining, grinding, transportation, and distribution of the minerals reduces the overall efficiency, which is not considered in this study. Another unaddressed risk in our study is secondary calcium carbonate precipitation at high alkalinity concentrations, that may result in runaway precipitation and reduced OAE efficiency (Hartmann et al., 2023; Moras et al., 2022). Suitner et al. (2024) observed runaway precipitation when aragonite saturation states ($\Omega_a$) exceeded a threshold of 2.5-5.0. In another experiment, secondary precipitation reduced the OAE efficiency from 0.8 to 0.1 mol $CO_2$ per mol alkalinity above an $\Omega_a$ threshold of $\sim 7$ (Moras et al., 2022). Our model simulations reached a maximum value of 1.5 ± 0.03 over 2090s at the ocean surface, suggesting our global and regional experiments could be a safe limit in terms of runaway precipitation.

While we added pure alkalinity to our model without accounting for potential biological effects, the different alkaline minerals used for OAE can differ considerably in terms of efficiency, and may have a negative effect on marine ecosystems. Reported effects include species-specific reduction in growth rates of diatoms and phytoplankton (Ferderer et al., 2022; Guo et al., 2022) and disruption of seafloor ecosystem due to sinking of undissolved alkaline mineral grains used for OAE (Feng et al., 2017; Fuhr et al., 2022). However, the extent and nature of these effects are not yet fully understood and require further investigation. Assessing these biological impacts falls outside the scope of this study, but future research should integrate potential ecological effects into biogeochemical models.

## CONCLUSION

Ocean Alkalinity Enhancement experiments in the global ocean (GLO-ALK) and in subduction regions (SUB-ALK) resulted in similar efficiencies over the 2090s (0.72 ± 0.03) in an emission-driven Earth System Model (ESM). However, climate feedbacks introduced high inter-annual and internal variability, which was strongest in SUB-ALK during the initial decades of deployment. These feedbacks also modified the OAE effects on atmospheric $CO_2$ reduction and, in turn, land carbon fluxes. Notably, land fluxes offset the enhanced ocean carbon sink by 7.3 ± 6.8% (GLO-ALK) and 17.8 ± 26.6% (SUB-ALK) in the 2090s. The OAE levels in our simulations had no significant effect on surface air temperature. While the capture efficiency of OAE, derived from ocean-only models with prescribed atmospheric $CO_2$, is more comparable with the current carbon accounting practices (Schwinger et al., 2024), our ESM simulations highlight the importance of understanding climate feedbacks for effective Monitoring, Reporting, and Verification of OAE.

## ACKNOWLEDGEMENTS

This study was funded by Federal Ministry of Education and Research of Germany (BMBF) in the framework of RETAKE-B, one of the six research consortia of German Marine Research Alliance (DAM) research mission "Marine carbon sinks on decarbonization pathways" (CDRmare); Grant: 03F0895B. JH was funded by the Initiative and Networking Fund of the Helmholtz Association (Helmholtz Young Investigator Group Marine Carbon and Ecosystem Feedbacks in the Earth System [MarESys], Grant VH-NG-1301). MS was funded by the European Union's Horizon 2020 research and innovation program under Grant Agreement No. 869357 (project OceanNETs). The work reflects only the author's view; the European Commission and their executive agency are not responsible for any use that may be made of the information the work contains. None of the authors have any competing interest.

# BIBLIOGRAPHY

Abernathey, R. P., Cerovecki, I., Holland, P. R., Newsom, E., Mazloff, M., and Talley, L. D. (2016). "Water-mass transformation by sea ice in the upper branch of the Southern Ocean overturning". In: *Nature Geoscience* 9.8, pp. 596–601. ISSN: 1752-0894, 1752-0908. DOI: `10.1038/ngeo2749`.

Adloff, M., Reick, C. H., and Claussen, M. (2018). "Earth system model simulations show different feedback strengths of the terrestrial carbon cycle under glacial and interglacial conditions". In: *Earth System Dynamics* 9.2, pp. 413–425. ISSN: 2190-4979. DOI: `10.5194/esd-9-413-2018`.

Archer, D. (2005). "Fate of fossil fuel CO2 in geologic time". In: *Journal of Geophysical Research: Oceans* 110 (C9). ISSN: 2156-2202. DOI: `10.1029/2004JC002625`.

Bach, L. T., Ho, D. T., Boyd, P. W., and Tyka, M. D. (2023). "Toward a consensus framework to evaluate air–sea CO2 equilibration for marine CO2 removal". In: *Limnology and Oceanography Letters* 8.5, pp. 685–691. ISSN: 2378-2242. DOI: `10.1002/lol2.10330`.

Burt, D. J., Fröb, F., and Ilyina, T. (2021). "The Sensitivity of the Marine Carbonate System to Regional Ocean Alkalinity Enhancement". In: *Frontiers in Climate* 3. ISSN: 2624-9553. URL: `https://www.frontiersin.org/articles/10.3389/fclim.2021.624075`.

Butenschön, M., Lovato, T., Masina, S., Caserini, S., and Grosso, M. (2021). "Alkalinization Scenarios in the Mediterranean Sea for Efficient Removal of Atmospheric CO2 and the Mitigation of Ocean Acidification". In: *Frontiers in Climate* 3. ISSN: 2624-9553. URL: `https://www.frontiersin.org/articles/10.3389/fclim.2021.614537`.

Caserini, S., Storni, N., and Grosso, M. (2022). "The Availability of Limestone and Other Raw Materials for Ocean Alkalinity Enhancement". In: *Global Biogeochemical Cycles* 36.5, e2021GB007246. ISSN: 1944-9224. DOI: `10.1029/2021GB007246`.

Clement, D. and Gruber, N. (2018). "The eMLR(C*) Method to Determine Decadal Changes in the Global Ocean Storage of Anthropogenic CO2". In: *Global Biogeochemical Cycles* 32.4, pp. 654–679. ISSN: 1944-9224. DOI: `10.1002/2017GB005819`.

Danek, C., Gürses, Ö., Gierz, P., Andrés-Martínez, M., and Hauck, J. (2023). *AWI AWI-ESM1REcoM model output prepared for CMIP6 C4MIP*. DOI: `10.22033/ESGF/CMIP6.17721`.

Danilov, S., Kivman, G., and Schröter, J. (2004). "A finite-element ocean model: principles and evaluation". In: *Ocean Modelling* 6.2, pp. 125–150. ISSN: 1463-5003. DOI: `10.1016/S1463-5003(02)00063-X`.

Doney, S. C., Lima, I., Feely, R. A., Glover, D. M., Lindsay, K., Mahowald, N., Moore, J. K., and Wanninkhof, R. (2009). "Mechanisms governing interannual variability in upper-ocean inorganic carbon system and air–sea CO2 fluxes: Physical climate and atmospheric dust". In: *Deep Sea Research Part II: Topical Studies in Oceanography*. Surface Ocean CO2 Variability and Vulnerabilities 56.8, pp. 640–655. ISSN: 0967-0645. DOI: `10.1016/j.dsr2.2008.12.006`.

Eyring, V., Bony, S., Meehl, G. A., Senior, C. A., Stevens, B., Stouffer, R. J., and Taylor, K. E. (2016). "Overview of the Coupled Model Intercomparison Project Phase 6 (CMIP6) experimental design and organization". In: *Geoscientific Model Development* 9.5, pp. 1937–1958. ISSN: 1991-959X. DOI: `10.5194/gmd-9-1937-2016`.

Feng, E. Y., Koeve, W., Keller, D. P., and Oschlies, A. (2017). "Model-Based Assessment of the CO2 Sequestration Potential of Coastal Ocean Alkalinization". In: *Earth's Future* 5.12, pp. 1252–1266. ISSN: 2328-4277. DOI: `10.1002/2017EF000659`.

Ferderer, A., Chase, Z., Kennedy, F., Schulz, K. G., and Bach, L. T. (2022). "Assessing the influence of ocean alkalinity enhancement on a coastal phytoplankton community". In: *Biogeosciences* 19.23, pp. 5375–5399. ISSN: 1726-4170. DOI: `10.5194/bg-19-5375-2022`.

Friedlingstein, P., Jones, M. W., O'Sullivan, M., Andrew, R. M., Bakker, D. C. E., Hauck, J., Le Quéré, C., Peters, G. P., Peters, W., Pongratz, J., Sitch, S., Canadell, J. G., Ciais, P., Jackson, R. B., Alin, S. R., et al. (2022). "Global Carbon Budget 2021". In: *Earth System Science Data* 14.4, pp. 1917–2005. ISSN: 1866-3508. DOI: `10.5194/essd-14-1917-2022`.

Fuhr, M., Geilert, S., Schmidt, M., Liebetrau, V., Vogt, C., Ledwig, B., and Wallmann, K. (2022). "Kinetics of Olivine Weathering in Seawater: An Experimental Study". In: *Frontiers in Climate* 4. ISSN: 2624-9553. URL: `https://www.frontiersin.org/articles/10.3389/fclim.2022.831587`.

Giorgetta, M. A., Jungclaus, J., Reick, C. H., Legutke, S., Bader, J., Böttinger, M., Brovkin, V., Crueger, T., Esch, M., Fieg, K., Glushak, K., Gayler, V., Haak, H., Hollweg, H.-D., Ilyina, T., et al. (2013). "Climate and carbon cycle changes from 1850 to 2100 in MPI-ESM simulations for the Coupled Model Intercomparison Project phase 5". In: *Journal of Advances in Modeling Earth Systems* 5.3, pp. 572–597. ISSN: 1942-2466. DOI: `10.1002/jame.20038`.

González, M. F. and Ilyina, T. (2016). "Impacts of artificial ocean alkalinization on the carbon cycle and climate in Earth system simulations". In: *Geophysical Research Letters* 43.12, pp. 6493–6502. ISSN: 1944-8007. DOI: `10.1002/2016GL068576`.

Gruber, N., Clement, D., Carter, B. R., Feely, R. A., Heuven, S. van, Hoppema, M., Ishii, M., Key, R. M., Kozyr, A., Lauvset, S. K., Lo Monaco, C., Mathis, J. T., Murata, A., Olsen, A., Perez, F. F., et al. (2019). "The oceanic sink for anthropogenic CO $_2$ from 1994 to 2007". In: *Science* 363.6432, pp. 1193–1199. ISSN: 0036-8075, 1095-9203. DOI: `10.1126/science.aau5153`.

Gruber, N., Gloor, M., Mikaloff Fletcher, S. E., Doney, S. C., Dutkiewicz, S., Follows, M. J., Gerber, M., Jacobson, A. R., Joos, F., Lindsay, K., Menemenlis, D., Mouchet, A., Müller, S. A., Sarmiento, J. L., and Takahashi, T. (2009). "Oceanic sources, sinks, and transport of atmospheric CO2". In: *Global Biogeochemical Cycles* 23.1. ISSN: 1944-9224. DOI: `10.1029/2008GB003349`.

Guo, J. A., Strzepek, R., Willis, A., Ferderer, A., and Bach, L. T. (2022). "Investigating the effect of nickel concentration on phytoplankton growth to assess potential side-effects of ocean alkalinity enhancement". In: *Biogeosciences* 19.15, pp. 3683–3697. ISSN: 1726-4170. DOI: `10.5194/bg-19-3683-2022`.

Hagemann, S. and Dümenil, L. (1997). "A parametrization of the lateral waterflow for the global scale". In: *Climate Dynamics* 14.1, pp. 17–31. ISSN: 1432-0894. DOI: `10.1007/s003820050205`.

Hartmann, J., Suitner, N., Lim, C., Schneider, J., Marín-Samper, L., Arístegui, J., Renforth, P., Taucher, J., and Riebesell, U. (2023). "Stability of alkalinity in ocean alkalinity enhancement (OAE) approaches – consequences for durability of $CO_2$ storage". In: *Biogeosciences* 20.4, pp. 781–802. ISSN: 1726-4170. DOI: `10.5194/bg-20-781-2023`.

Hartmann, J., West, A. J., Renforth, P., Köhler, P., De La Rocha, C. L., Wolf-Gladrow, D. A., Dürr, H. H., and Scheffran, J. (2013). "Enhanced chemical weathering as a geoengineering strategy to reduce atmospheric carbon dioxide, supply nutrients, and mitigate ocean acidification: ENHANCED WEATHERING". In: *Reviews of Geophysics* 51.2, pp. 113–149. ISSN: 87551209. DOI: `10.1002/rog.20004`.

Hauck, J., Völker, C., Wang, T., Hoppema, M., Losch, M., and Wolf-Gladrow, D. A. (2013). "Seasonally different carbon flux changes in the Southern Ocean in response to the southern annular mode". In: *Global Biogeochemical Cycles* 27.4, pp. 1236–1245. ISSN: 0886-6236, 1944-9224. DOI: `10.1002/2013GB004600`.

Hauck, J., Köhler, P., Wolf-Gladrow, D., and Völker, C. (2016). "Iron fertilisation and century-scale effects of open ocean dissolution of olivine in a simulated $CO_2$ removal experiment". In: *Environmental Research Letters* 11.2, p. 024007. ISSN: 1748-9326. DOI: `10.1088/1748-9326/11/2/024007`.

He, J. and Tyka, M. D. (2023). "Limits and $CO_2$ equilibration of near-coast alkalinity enhancement". In: *Biogeosciences* 20.1, pp. 27–43. ISSN: 1726-4170. DOI: `10.5194/bg-20-27-2023`.

Ho, D. T. (2023). "Carbon dioxide removal is not a current climate solution — we need to change the narrative". In: *Nature* 616.7955, pp. 9–9. DOI: `10.1038/d41586-023-00953-x`.

Ho, D. T., Bopp, L., Palter, J. B., Long, M. C., Boyd, P. W., Neukermans, G., and Bach, L. T. (2023). "Monitoring, reporting, and verification for ocean alkalinity enhancement". In: *State of the Planet* 2-oae2023, pp. 1–12. DOI: `10.5194/sp-2-oae2023-12-2023`. URL: `https://sp.copernicus.org/articles/2-oae2023/12/2023/`.

Ilyina, T., Wolf-Gladrow, D., Munhoven, G., and Heinze, C. (2013). "Assessing the potential of calcium-based artificial ocean alkalinization to mitigate rising atmospheric $CO_2$ and ocean acidification: MODELING MITIGATION POTENTIAL OF AOA". In: *Geophysical Research Letters* 40.22, pp. 5909–5914. ISSN: 00948276. DOI: `10.1002/2013GL057981`.

Jeansson, E., Olsen, A., and Jutterström, S. (2017). "Arctic Intermediate Water in the Nordic Seas, 1991–2009". In: *Deep Sea Research Part I: Oceanographic Research Papers* 128, pp. 82–97. ISSN: 0967-0637. DOI: `10.1016/j.dsr.2017.08.013`.

Jeansson, E., Tanhua, T., Olsen, A., Smethie Jr., W. M., Rajasakaren, B., Ólafsdóttir, S. R., and Ólafsson, J. (2023). "Decadal Changes in Ventilation and Anthropogenic Carbon in the Nordic Seas". In: *Journal of Geophysical Research: Oceans* 128.3, e2022JC019318. ISSN: 2169-9291. DOI: `10.1029/2022JC019318`.

Jeltsch-Thömmes, A., Tran, G., Lienert, S., Keller, D. P., Oschlies, A., and Joos, F. (2024). "Earth system responses to carbon dioxide removal as exemplified by ocean alkalinity enhancement: tradeoffs and lags". In: *Environmental Research Letters* 19.5, p. 054054. ISSN: 1748-9326. DOI: `10.1088/1748-9326/ad4401`.

Jones, C. D., Ciais, P., Davis, S. J., Friedlingstein, P., Gasser, T., Peters, G. P., Rogelj, J., Vuuren, D. P. v., Canadell, J. G., Cowie, A., Jackson, R. B., Jonas, M., Kriegler, E., Littleton, E., Lowe, J. A., et al. (2016). "Simulating the Earth system response to negative emissions". In: *Environmental Research Letters* 11.9, p. 095012. ISSN: 1748-9326. DOI: `10.1088/1748-9326/11/9/095012`.

Jones, D. C., Ito, T., Takano, Y., and Hsu, W.-C. (2014). "Spatial and seasonal variability of the air-sea equilibration timescale of carbon dioxide". In: *Global Biogeochemical Cycles* 28.11, pp. 1163–1178. ISSN: 1944-9224. DOI: `10.1002/2014GB004813`.

Keller, D. P., Brent, K., Bach, L. T., and Rickels, W. (2021). "Editorial: The Role of Ocean-Based Negative Emission Technologies for Climate Mitigation". In: *Frontiers in Climate* 3, p. 743816. ISSN: 2624-9553. DOI: `10.3389/fclim.2021.743816`.

Keller, D. P., Feng, E. Y., and Oschlies, A. (2014). "Potential climate engineering effectiveness and side effects during a high carbon dioxide-emission scenario". In: *Nature Communications* 5.1, p. 3304. ISSN: 2041-1723. DOI: `10.1038/ncomms4304`.

Keppler, L., Landschützer, P., Lauvset, S. K., and Gruber, N. (2023). "Recent Trends and Variability in the Oceanic Storage of Dissolved Inorganic Carbon". In: *Global Biogeochemical Cycles* 37.5, e2022GB007677. ISSN: 1944-9224. DOI: `10.1029/2022GB007677`.

Kheshgi, H. S. (1995). "Sequestering atmospheric carbon dioxide by increasing ocean alkalinity". In: *Energy* 20.9, pp. 915–922. ISSN: 0360-5442. DOI: `10.1016/0360-5442(95)00035-F`.

Köhler, P., Abrams, J. F., Völker, C., Hauck, J., and Wolf-Gladrow, D. A. (2013). "Geoengineering impact of open ocean dissolution of olivine on atmospheric CO $_2$ , surface ocean pH and marine biology". In: *Environmental Research Letters* 8.1, p. 014009. ISSN: 1748-9326. DOI: `10.1088/1748-9326/8/1/014009`.

Lenton, A., Matear, R. J., Keller, D. P., Scott, V., and Vaughan, N. E. (2018). "Assessing carbon dioxide removal through global and regional ocean alkalinization under high and low emission pathways". In: *Earth System Dynamics* 9.2, pp. 339–357. ISSN: 2190-4987. DOI: `10.5194/esd-9-339-2018`.

Middelburg, J. J., Soetaert, K., and Hagens, M. (2020). "Ocean Alkalinity, Buffering and Biogeochemical Processes". In: *Reviews of Geophysics* 58.3, e2019RG000681. ISSN: 1944-9208. DOI: `10.1029/2019RG000681`.

Moras, C. A., Bach, L. T., Cyronak, T., Joannes-Boyau, R., and Schulz, K. G. (2022). "Ocean alkalinity enhancement – avoiding runaway CaCO $_3$ precipitation during quick and hydrated lime dissolution". In: *Biogeosciences* 19.15, pp. 3537–3557. ISSN: 1726-4189. DOI: `10.5194/bg-19-3537-2022`.

Nagwekar, T., Nissen, C., and Hauck, J. (2024). "Ocean Alkalinity Enhancement in Deep Water Formation Regions Under Low and High Emission Pathways". In: *Earth's Future* 12.10, e2023EF004213. ISSN: 2328-4277. DOI: `10.1029/2023EF004213`.

Nissen, C., Timmermann, R., Hoppema, M., Gürses, Ö., and Hauck, J. (2022). "Abruptly attenuated carbon sequestration with Weddell Sea dense waters by 2100". In: *Nature Communications* 13.1, p. 3402. ISSN: 2041-1723. DOI: `10.1038/s41467-022-30671-3`.

O'Neill, B. C., Tebaldi, C., Vuuren, D. P. van, Eyring, V., Friedlingstein, P., Hurtt, G., Knutti, R., Kriegler, E., Lamarque, J.-F., Lowe, J., Meehl, G. A., Moss, R., Riahi, K., and Sanderson, B. M. (2016). "The Scenario Model Intercomparison Project (ScenarioMIP) for CMIP6". In: *Geoscientific Model Development* 9.9, pp. 3461–3482. ISSN: 1991-959X. DOI: `10.5194/gmd-9-3461-2016`.

Orr, J. C. and Epitalon, J.-M. (2015). "Improved routines to model the ocean carbonate system: mocsy 2.0". In: *Geoscientific Model Development* 8.3, pp. 485–499. ISSN: 1991-959X. DOI: `10.5194/gmd-8-485-2015`. URL: `https://gmd.copernicus.org/articles/8/485/2015/`.

Palmiéri, J. and Yool, A. (2024). "Global-Scale Evaluation of Coastal Ocean Alkalinity Enhancement in a Fully Coupled Earth System Model". In: *Earth's Future* 12.3, e2023EF004018. ISSN: 2328-4277. DOI: `10.1029/2023EF004018`.

Pellichero, V., Sallée, J.-B., Chapman, C. C., and Downes, S. M. (2018). "The southern ocean meridional overturning in the sea-ice sector is driven by freshwater fluxes". In: *Nature Communications* 9.1, p. 1789. ISSN: 2041-1723. DOI: `10.1038/s41467-018-04101-2`.

Reick, C. H., Gayler, V., Goll, D., Hagemann, S., Heidkamp, M., Nabel, J. E. M. S., Raddatz, T., Roeckner, E., Schnur, R., and Wilkenskjeld, S. (2021). "JSBACH 3 - The land component of the MPI Earth System Model: documentation of version 3.2". In: DOI: `10.17617/2.3279802`.

Renforth, P. and Henderson, G. (2017). "Assessing ocean alkalinity for carbon sequestration: Ocean Alkalinity for C Sequestration". In: *Reviews of Geophysics* 55.3, pp. 636–674. ISSN: 87551209. DOI: `10.1002/2016RG000533`.

Schourup-Kristensen, V., Sidorenko, D., Wolf-Gladrow, D. A., and Völker, C. (2014). "A skill assessment of the biogeochemical model REcoM2 coupled to the Finite Element Sea Ice–Ocean

Model (FESOM 1.3)". In: *Geoscientific Model Development* 7.6, pp. 2769–2802. ISSN: 1991-9603. DOI: `10.5194/gmd-7-2769-2014`.

Schwinger, J., Bourgeois, T., and Rickels, W. (2024). "On the emission-path dependency of the efficiency of ocean alkalinity enhancement". In: *Environmental Research Letters* 19.7, p. 074067. ISSN: 1748-9326. DOI: `10.1088/1748-9326/ad5a27`.

Sellar, A. A., Jones, C. G., Mulcahy, J. P., Tang, Y., Yool, A., Wiltshire, A., O'Connor, F. M., Stringer, M., Hill, R., Palmieri, J., Woodward, S., Mora, L. de, Kuhlbrodt, T., Rumbold, S. T., Kelley, D. I., et al. (2019). "UKESM1: Description and Evaluation of the U.K. Earth System Model". In: *Journal of Advances in Modeling Earth Systems* 11.12, pp. 4513–4558. ISSN: 1942-2466. DOI: `10.1029/2019MS001739`.

Semmler, T., Danilov, S., Gierz, P., Goessling, H. F., Hegewald, J., Hinrichs, C., Koldunov, N., Khosravi, N., Mu, L., Rackow, T., Sein, D. V., Sidorenko, D., Wang, Q., and Jung, T. (2020). "Simulations for CMIP6 With the AWI Climate Model AWI-CM-1-1". In: *Journal of Advances in Modeling Earth Systems* 12.9, e2019MS002009. ISSN: 1942-2466. DOI: `10.1029/2019MS002009`.

Sonntag, S., Ferrer González, M., Ilyina, T., Kracher, D., Nabel, J. E. M. S., Niemeier, U., Pongratz, J., Reick, C. H., and Schmidt, H. (2018). "Quantifying and Comparing Effects of Climate Engineering Methods on the Earth System". In: *Earth's Future* 6.2, pp. 149–168. ISSN: 2328-4277. DOI: `10.1002/2017EF000620`.

Stevens, B., Giorgetta, M., Esch, M., Mauritsen, T., Crueger, T., Rast, S., Salzmann, M., Schmidt, H., Bader, J., Block, K., Brokopf, R., Fast, I., Kinne, S., Kornblueh, L., Lohmann, U., et al. (2013). "Atmospheric component of the MPI-M Earth System Model: ECHAM6". In: *Journal of Advances in Modeling Earth Systems* 5.2, pp. 146–172. ISSN: 1942-2466. DOI: `10.1002/jame.20015`.

Suitner, N., Faucher, G., Lim, C., Schneider, J., Moras, C. A., Riebesell, U., and Hartmann, J. (2024). "Ocean alkalinity enhancement approaches and the predictability of runaway precipitation processes: results of an experimental study to determine critical alkalinity ranges for safe and sustainable application scenarios". In: *Biogeosciences* 21.20, pp. 4587–4604. ISSN: 1726-4170. DOI: `10.5194/bg-21-4587-2024`.

Takahashi, T., Sutherland, S. C., Wanninkhof, R., Sweeney, C., Feely, R. A., Chipman, D. W., Hales, B., Friederich, G., Chavez, F., Sabine, C., Watson, A., Bakker, D. C. E., Schuster, U., Metzl, N., Yoshikawa-Inoue, H., et al. (2009). "Climatological mean and decadal change in surface ocean pCO2, and net sea–air CO2 flux over the global oceans". In: *Deep Sea Research Part II: Topical Studies in Oceanography*. Surface Ocean CO2 Variability and Vulnerabilities 56.8, pp. 554–577. ISSN: 0967-0645. DOI: `10.1016/j.dsr2.2008.12.009`.

UNFCCC (2015). "United Nations Framework Convention on Climate Change (UNFCCC): Adoption of the Paris Agreement, 21st Conference of the Parties." In: URL: `https://unfccc.int/sites/default/files/english_paris_agreement.pdf`.

Våge, K., Pickart, R. S., Thierry, V., Reverdin, G., Lee, C. M., Petrie, B., Agnew, T. A., Wong, A., and Ribergaard, M. H. (2009). "Surprising return of deep convection to the subpolar North Atlantic Ocean in winter 2007–2008". In: *Nature Geoscience* 2.1, pp. 67–72. ISSN: 1752-0908. DOI: `10.1038/ngeo382`.

Walin, G. (1982). "On the relation between sea-surface heat flow and thermal circulation in the ocean". In: *Tellus* 34.2, pp. 187–195. ISSN: 00402826, 21533490. DOI: `10.1111/j.2153-3490.1982.tb01806.x`.

Wang, H., Pilcher, D. J., Kearney, K. A., Cross, J. N., Shugart, O. M., Eisaman, M. D., and Carter, B. R. (2023). "Simulated Impact of Ocean Alkalinity Enhancement on Atmospheric CO $_2$ Removal in the Bering Sea". In: *Earth's Future* 11.1. ISSN: 2328-4277, 2328-4277. DOI: `10.1029/2022EF002816`.

Wang, Q., Danilov, S., Sidorenko, D., Timmermann, R., Wekerle, C., Wang, X., Jung, T., and Schröter, J. (2014). "The Finite Element Sea Ice-Ocean Model (FESOM) v.1.4: formulation of an ocean general circulation model". In: *Geoscientific Model Development* 7.2, pp. 663–693. ISSN: 1991-959X. DOI: `10.5194/gmd-7-663-2014`.

Wolf-Gladrow, D. A., Zeebe, R. E., Klaas, C., Körtzinger, A., and Dickson, A. G. (2007). "Total alkalinity: The explicit conservative expression and its application to biogeochemical processes". In: *Marine Chemistry*. Special issue: Dedicated to the memory of Professor Roland Wollast 106.1, pp. 287–300. ISSN: 0304-4203. DOI: `10.1016/j.marchem.2007.01.006`.

Zeebe, R. E. and Wolf-Gladrow, D. (2001). *CO2 in Seawater: Equilibrium, Kinetics, Isotopes*. Gulf Professional Publishing. 382 pp. ISBN: 978-0-444-50946-8.

# Supplementary Material

## Alkalinity Enhancement in the Subduction Regions: Efficiency, Earth System Feedbacks, and Deep Ocean Carbon Sequestration

**Tanvi Nagwekar[1], Christopher Danek[1], Miriam Seifert[1], and Judith Hauck[1]**

[1]Alfred Wegener Institute for Polar and Marine Research, Bremerhaven, Germany

E-mail: tanvi.nagwekar@awi.de

### Text S1: Water Mass Transformation and Water Mass Formation

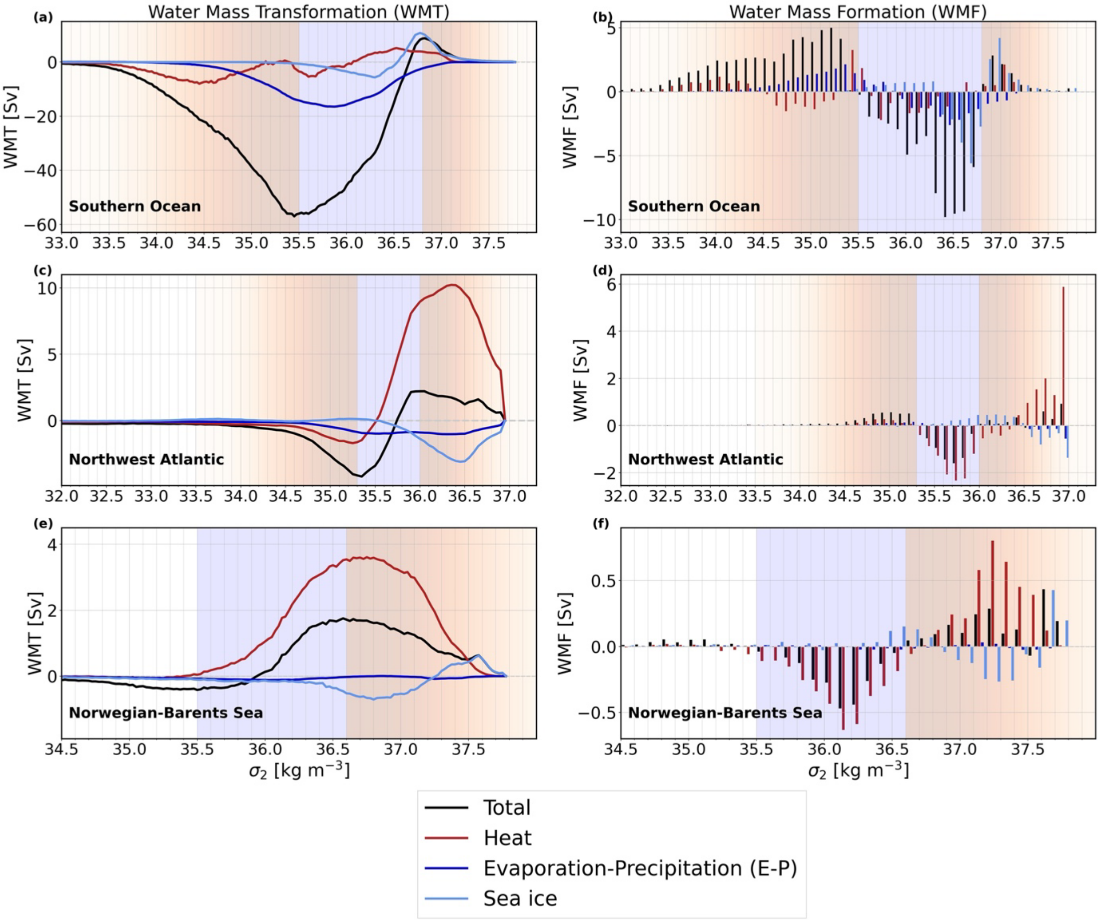

***Figure S1:*** *Water Mass Transformation (WMT, left) and Water Mass Formation (WMF, right) rates for the subduction regions.* ***(a,c, and e)*** *The annual mean surface WMT rates (Sv) integrated over 0.025 kg/m³ density bins in panel* ***(a)*** *the*

*Southern Ocean,* ***(c)*** *the Northwest Atlantic, and* ***(e)*** *the Norwegian-Barents Sea region as a function of the potential density anomaly $\sigma_2$ (kg/m$^3$) due to the total buoyancy flux (black), heat flux (red), evaporation minus precipitation (E-P; dark blue), and the sea-ice induced freshwater flux (light blue). The shading marks the density ranges of downwelling (red) and upwelling (blue).* ***(b, d, and f)*** *The annual mean surface WMF rates (Sv) for the different subduction regions are integrated over 0.1 kg/m$^3$ density bins. The total WMF (black bars) results from the contribution of the heat flux (red bars) and the two components of the freshwater flux, that is E-P (dark blue bars) and sea-ice (light blue bars). Positive values represent subduction/downwelling (red shaded regions) and negative values represent upwelling (blue shaded regions).*

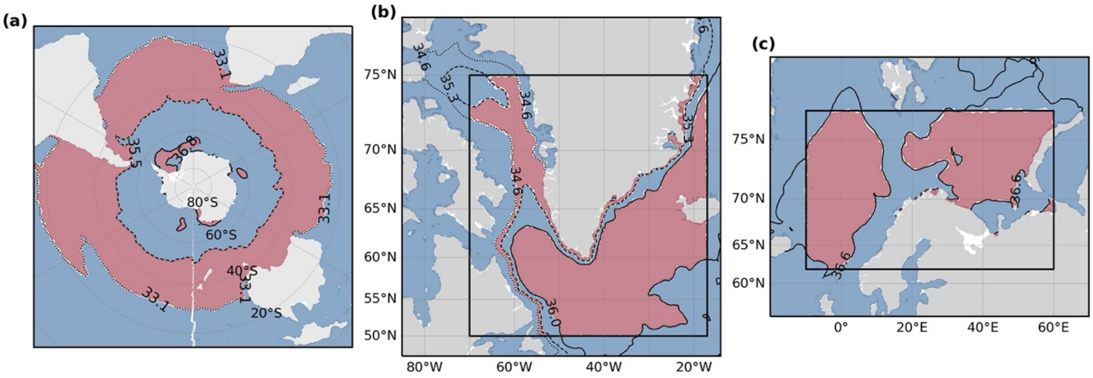

***Figure S2****: The regional mask for alkalinity deposition, obtained by using the isopycnal outcrops for deep and bottom water formation areas from the water mass formation analysis.* ***(a)*** *Southern Ocean,* ***(b)*** *Northwest Atlantic, and* ***(c)*** *Norwegian-Barents Sea regions. The black boxes for the Northwest Atlantic and the Norwegian-Barents Sea region denote the areas considered for the water mass transformation analysis. For the Southern Ocean, we consider the areas south of 40°S.*

We relate the monthly surface buoyancy fluxes, i.e., heat flux, freshwater flux decomposed into sea-ice formation and melting and evaporation minus precipitation (E-P), to the surface density distribution to derive Water Mass Transformation (WMT) rates (Nagwekar et al., 2024; Nissen et al., 2022; Figure S1). Water Mass Formation (WMF) rate, is the derivative of WMT with respect to density, and shows where water masses converge (WMF>0; downwelling) or diverge (WMF<0; upwelling) in given density bins (Pellichero et al., 2018). In the Southern Ocean subduction occurs primarily due to sea-ice formation and loss of heat in the density bins >36.8 kg/m$^3$ (red shaded region in Figure S1a and S1b). This density range is representative of the Antarctic Bottom Water (AABW) formation in the Weddell and Ross Sea basins (Orsi et al., 1999). The Antarctic Intermediate and Subantarctic Mode Water (AAIW and SAMW) masses are found between 45 and 60°S characterized by the freshwater flux (Cerovečki & Mazloff, 2016; Hartin et al., 2011; Talley, 2008). Accordingly, our model simulations suggest the E-P component of freshwater flux leads to subduction in the density bins between 33.1 and 35.5 kg/m$^3$ (Figure S1a and S1b) which represent the AAIW and SAMW formation regions in the Subantarctic (Figure S2a). Buoyancy induced upwelling occurs in between 35.5 and 36.8 kg/m$^3$ (blue shaded regions in Figure S1a and S1b). In the North Atlantic the formation of North Atlantic Deep Water mainly occurs due heat loss (Dickson & Brown, 1994; Jeansson et al., 2017; Våge et al., 2009). Similarly, our model also suggests heat loss to be the main driver of subduction in the Northwest Atlantic in the density bins >36 kg/m$^3$ and in density bins between 34.6 and 35.4 kg/m$^3$ (Figure S1c and S1d). Similarly, in the Norwegian-Barents Sea regions subduction occurs in the density bins >36.6 kg/m$^3$ primarily due to heat loss (Figure S1e and S1f). The density thresholds obtained from the WMF analysis are then used to locate the subduction regions in the Southern Ocean, Northwest Atlantic and Norwegian-Barents Sea regions (Figures S2a, S2b and S2c).

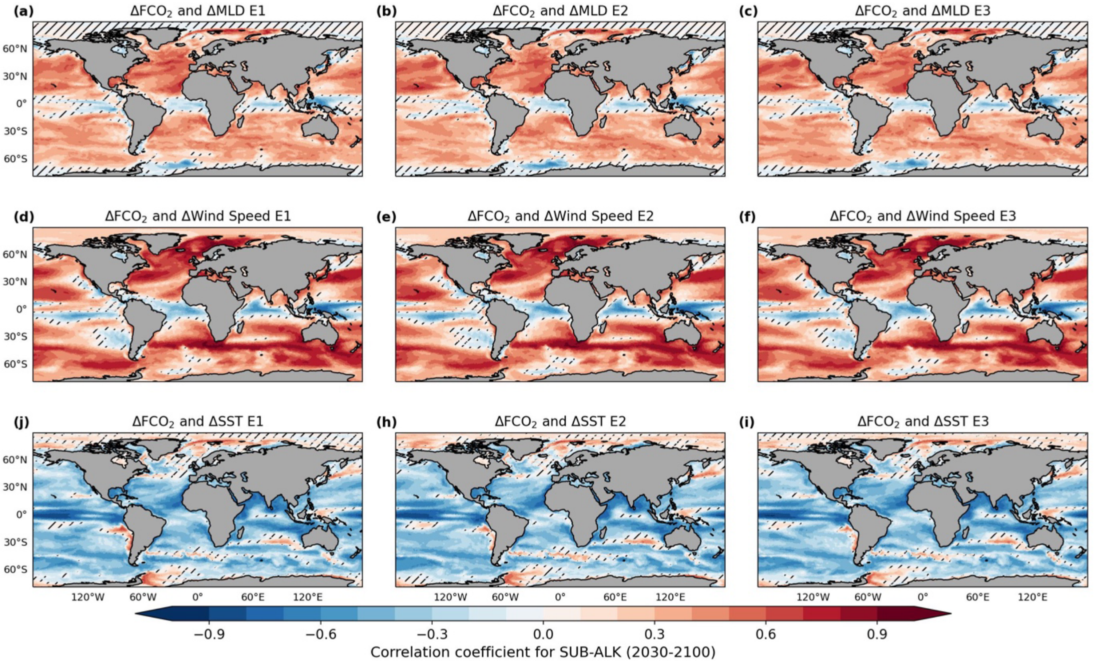

***Figure S3:*** *Correlation coefficient across the three ensemble members in the SUB-ALK experiment between the I flux anomalies and* ***(a,b,c)*** *Mixed Layer depth anomalies,* ***(d,e,f)*** *Wind Speed anomalies and,* ***(j,h,i)*** *Sea Surface Temperature anomalies. The hatched regions show where the correlation coefficient is not statistically significant (confidence level=0.95). All correlations are calculated from monthly means over 2030-2100.*

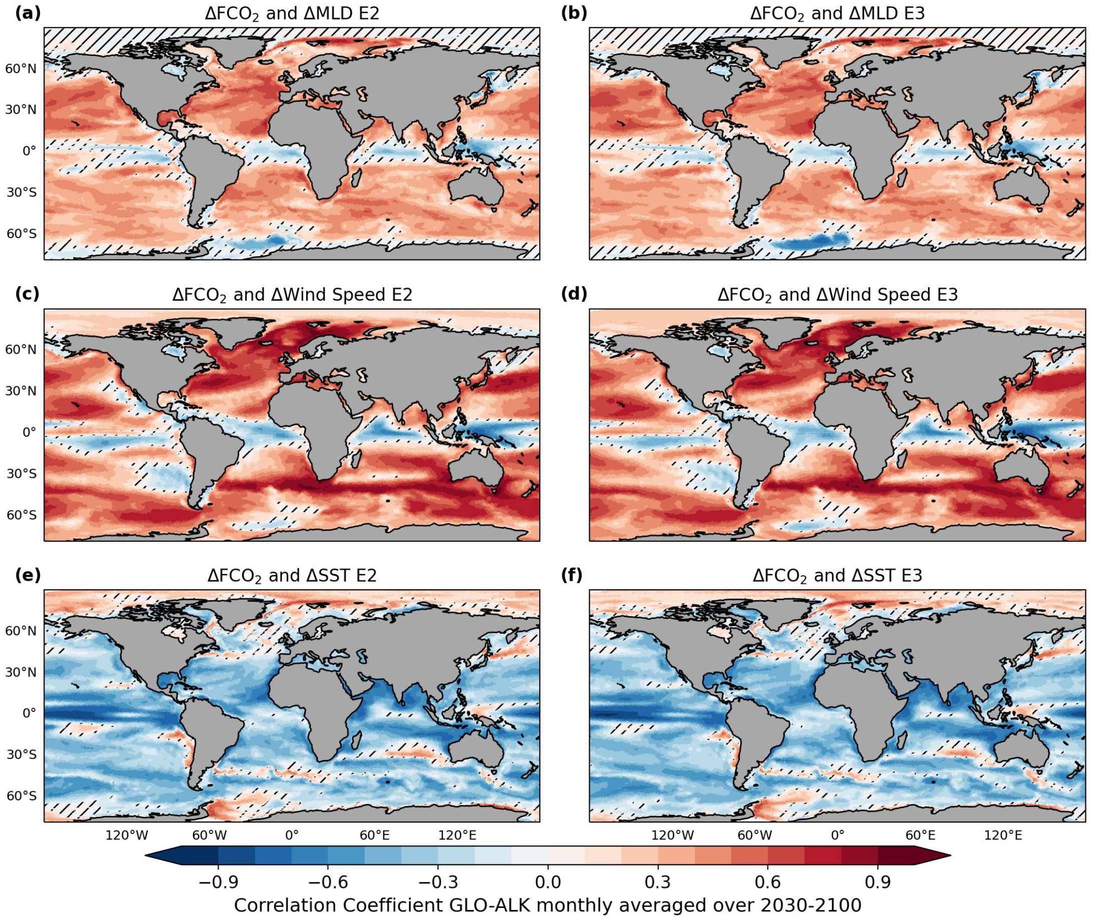

***Figure S4***: *Correlation coefficient across the two ensemble members in the GLO-ALK experiment between the* $CO_2$ *flux anomalies and* ***(a,b)*** *Mixed Layer depth anomalies,* ***(c,d)*** *Wind Speed anomalies and,* ***(e,f)*** *Sea Surface Temperature anomalies. The hatched regions show where the correlation coefficient is not statistically significant (confidence level=0.95). All correlations are calculated from monthly means over 2030-2100.*

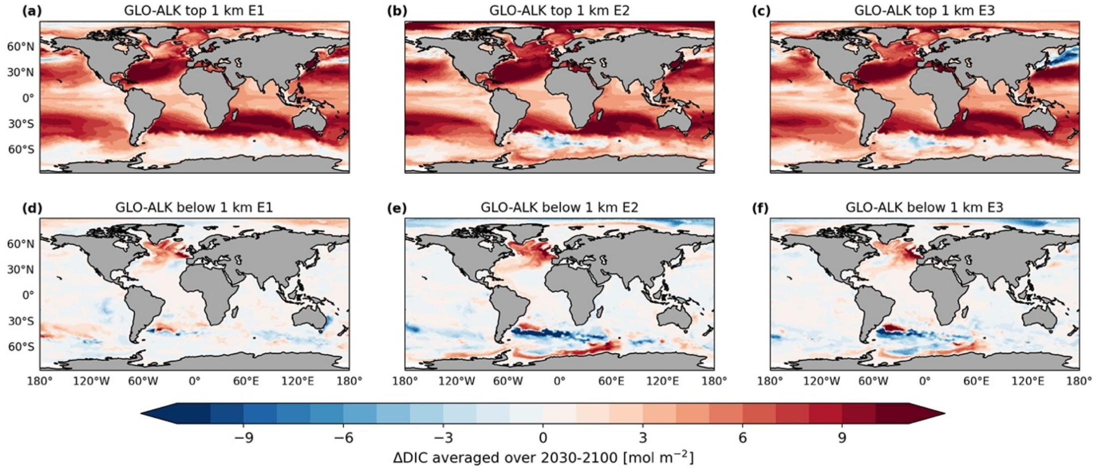

***Figure S5***: *Spatial patterns for changes in deph-integrated DIC in the GLO-ALK experiment relative to CTRL for the three ensemble members in* ***(a,b,c)*** *top 1 km and* ***(d,e,f)*** *below 1 km.*

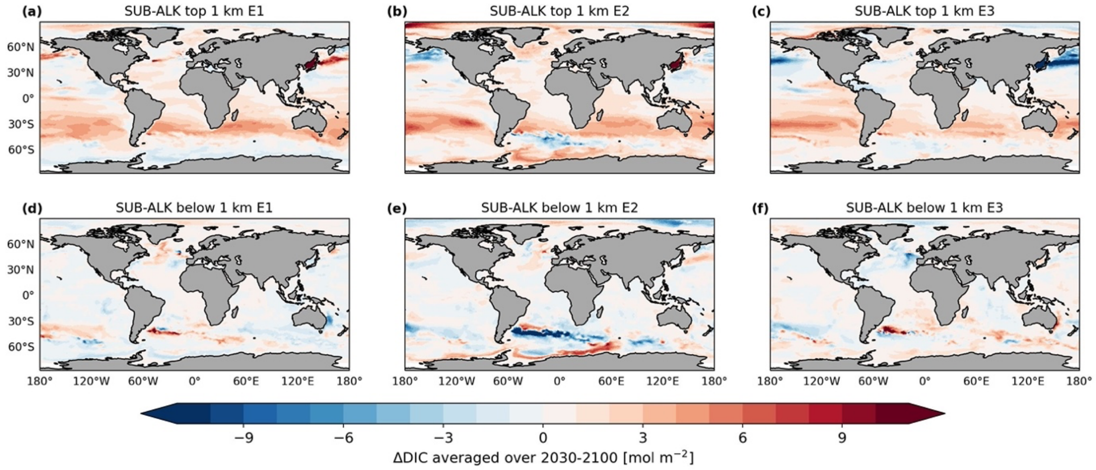

***Figure S6:*** *Spatial patterns for changes in depth-integrated DIC in the SUB-ALK experiment relative to CTRL for the three ensemble members in* ***(a,b,c)*** *top 1 km and* ***(d,e,f)*** *below 1 km.*

## References

Cerovečki, I., & Mazloff, M. R. (2016). The Spatiotemporal Structure of Diabatic Processes Governing the Evolution of Subantarctic Mode Water in the Southern Ocean. *Journal of Physical Oceanography*, *46*(2), 683–710. https://doi.org/10.1175/JPO-D-14-0243.1

Dickson, R. R., & Brown, J. (1994). The production of North Atlantic Deep Water: Sources, rates, and pathways. *Journal of Geophysical Research: Oceans*, *99*(C6), 12319–12341. https://doi.org/10.1029/94JC00530

Hartin, C. A., Fine, R. A., Sloyan, B. M., Talley, L. D., Chereskin, T. K., & Happell, J. (2011). Formation rates of Subantarctic mode water and Antarctic intermediate water within the South Pacific. *Deep Sea Research Part I: Oceanographic Research Papers*, *58*(5), 524–534. https://doi.org/10.1016/j.dsr.2011.02.010

Jeansson, E., Olsen, A., & Jutterström, S. (2017). Arctic Intermediate Water in the Nordic Seas, 1991–2009. *Deep Sea Research Part I: Oceanographic Research Papers*, *128*, 82–97. https://doi.org/10.1016/j.dsr.2017.08.013

Nagwekar, T., Nissen, C., & Hauck, J. (2024). Ocean Alkalinity Enhancement in Deep Water Formation Regions Under Low and High Emission Pathways. *Earth's Future*, *12*(10), e2023EF004213. https://doi.org/10.1029/2023EF004213

Nissen, C., Timmermann, R., Hoppema, M., Gürses, Ö., & Hauck, J. (2022). Abruptly attenuated carbon sequestration with Weddell Sea dense waters by 2100. *Nature Communications*, *13*(1), Article 1. https://doi.org/10.1038/s41467-022-30671-3

Orsi, A. H., Johnson, G. C., & Bullister, J. L. (1999). Circulation, mixing, and production of Antarctic Bottom Water. *Progress in Oceanography*, *43*(1), 55–109. https://doi.org/10.1016/S0079-6611(99)00004-X

Pellichero, V., Sallée, J.-B., Chapman, C. C., & Downes, S. M. (2018). The southern ocean meridional overturning in the sea-ice sector is driven by freshwater fluxes. *Nature Communications*, *9*(1), 1789. https://doi.org/10.1038/s41467-018-04101-2

Talley, L. D. (2008). Freshwater transport estimates and the global overturning circulation: Shallow, deep and throughflow components. *Progress in Oceanography*, *78*(4), 257–303. https://doi.org/10.1016/j.pocean.2008.05.001

Våge, K., Pickart, R. S., Thierry, V., Reverdin, G., Lee, C. M., Petrie, B., Agnew, T. A., Wong, A., & Ribergaard, M. H. (2009). Surprising return of deep convection to the subpolar North Atlantic Ocean in winter 2007–2008. *Nature Geoscience*, *2*(1), 67–72. https://doi.org/10.1038/ngeo382

# 5

## PUBLICATION III

### EFFECT OF MODEL RESOLUTION ON OCEAN ALKALINITY ENHANCEMENT IN THE SUBDUCTION REGIONS AND THE GLOBAL OCEAN

*In preparation*

# EFFECT OF MODEL RESOLUTION ON OCEAN ALKALINITY ENHANCEMENT IN THE SUBDUCTION REGIONS AND THE GLOBAL OCEAN

Tanvi Nagwekar[1], Christopher Danek[1], Cara Nissen[3], Miriam Seifert[1], and Judith Hauck[1,2]

[1] Alfred-Wegener-Institut, Helmholtz-Zentrum für Polar- und Meeresforschung, Am Handelshafen 12, 27570 Bremerhaven, Germany

[2] Universität Bremen, FB2, Leobener Strasse, 28359 Bremen, Germany

[3] Department of Freshwater and Marine Ecology, Institute for Biodiversity and Ecosystem Dynamics, University of Amsterdam, Netherlands

## ABSTRACT

Ocean Alkalinity Enhancement (OAE) has emerged as a promising ocean-based carbon dioxide removal strategy to augment oceanic $CO_2$ uptake. Ocean models are used to assess the efficiency and the effects of OAE, but how sensitive the model-based estimates to OAE are to model resolution remains uncertain. Here, we compare OAE simulations using the global ocean biogeochemistry model FESOM2.1-REcoM3 in low- and high-resolution (LR and HR) configurations. Experiments are conducted under the SSP3-7.0 emission scenario, with continuous, uniform alkalinity deployment applied globally as well as in the subduction regions of the Southern Ocean and North Atlantic from 2030 to 2100. We find that century-scale, basin-wide increases in $CO_2$ flux and final OAE efficiencies are only modestly affected by horizontal resolution, particularly when alkalinity is introduced globally with OAE efficiency ranging over 0.57-0.56 (2030s) and 0.85-0.86 (2090s) on the two setups. However, in the early phase (2030s) of OAE applied to subduction regions HR simulations reveal 11.1% higher (0.70) OAE efficiencies than LR (0.63), highlighting the potential effect of finer-scale processes that seam to matter more on a shorter timescale and taper off by the end of the century. Beyond OAE efficiency, HR and LR runs also differ in their simulated distributions of dissolved inorganic carbon (DIC), with more carbon transferred to the ocean interior in the HR configuration under both global (5.5%) and subduction regions (7.7%) deployments than the LR simulations. Total net primary production, in particular when coupled with added nutrients (iron and silicic acid) to mimic olivine addition as an alkaline substance, shows a broadly similar basin-wide increase in both resolutions but exhibits subtle differences tied to background nutrient availability in the HR setup. Seasonal response in OAE-induced changes is similar in both setups, where the regional OAE simulations indicates that the timing of deployment can be crucial, with summertime shallow mixed layer depth resulting in higher excess surface alkalinity and higher increase in carbon uptake compared to the winter months. Overall, while the LR models capture long-term, large-scale OAE trends well, the HR simulations could provide valuable insights into initial variability in regional OAE efficiency and deep ocean DIC storage. However, robust model evaluation is the prerequisite for the future modeling studies in order to inform near-term monitoring, reporting, and verification (MRV) needs.

## INTRODUCTION

Carbon Dioxide Removal (CDR) refers to artificially removing carbon from the atmosphere and storing it in geological formations, land or ocean carbon reservoirs, or in products (Intergovernmental Panel on Climate Change IPCC, 2018). Although phasing out fossil fuels remains paramount to stabilize and ultimately reduce the atmospheric $CO_2$ concentration, CDR is deemed necessary as a complementary effort particularly in the second half of this century to remove residual and legacy $CO_2$ emissions (IPCC, 2023). Together, these efforts aid in reaching the climate goal set by the Paris Agreement to limit the rise of global temperature to well below 2°C and preferably below 1.5°C by 2100 (UNFCCC, 2015). Currently, the majority of the climate mitigation pathways by the IPCC considers various land-based CDR methods like afforestation and reforestation, bioenergy with carbon capture and storage, and soil carbon sequestration (Pongratz et al., 2024). However, they exhibit limitations regarding competition for land use, carbon storage durability, and ecosystem disruption (Fuss et al., 2018). Hence, ocean-based CDR methods are receiving increasing attention (Ho and Bopp, 2024). These methods leverage the vast capacity of the ocean to take up and store carbon. Ocean Alkalinity Enhancement (OAE) is one such ocean-based CDR method that enhances the oceanic carbon uptake capacity by manipulating the carbonate chemistry. This method offers a substantial potential for carbon uptake and sequestration while, to date, showing minimal adverse effects on marine ecosystems (Gattuso et al., 2021; Keller et al., 2014). However, further research is essential to fully evaluate its long-term effectiveness, ecological impacts, and feasibility (Oschlies et al., 2023). Additionally, developing a comprehensive monitoring, reporting, and verification (MRV) framework is critical for ensuring its responsible implementation (Ho et al., 2023).

Historically, the ocean has played a pivotal role in the global carbon cycle, acting as a major regulator of the Earth's climate (Gruber et al., 2009). Since the Industrial Revolution, the ocean has absorbed approximately one-quarter of anthropogenic $CO_2$ emissions (Friedlingstein et al., 2024). A key control on oceanic carbon cycling is alkalinity, defined as the excess of proton acceptors over proton donors (Wolf-Gladrow et al., 2007). Naturally, alkalinity is introduced into the surface ocean through rock weathering, a process that shifts the carbonate equilibrium toward bicarbonate ($HCO_3^-$) and carbonate ($CO_3^{2-}$) ions, thereby reducing the concentration of aqueous $CO_2$ (Zeebe and Wolf-Gladrow, 2001). This reduction in aqueous $CO_2$ concentration lowers the partial pressure of $CO_2$ ($pCO_2$) at the ocean surface. When surface ocean $pCO_2$ falls below atmospheric $pCO_2$, the resulting gradient drives net $CO_2$ uptake by the oceans (Middelburg et al., 2020). However, this natural weathering process operates on geological timescales, making it insufficient to counterbalance the current pace of anthropogenic emissions (Archer, 2005). OAE seeks to accelerate this process by artificially increasing ocean alkalinity. This can be achieved by spreading finely pulverized rock powders, such as olivine, basalt, or lime, in the surface ocean or by depositing alkalinity generated through electrolysis of seawater or brine solutions (Bach et al., 2019; Eisaman et al., 2023; Hartmann et al., 2013; Renforth et al., 2013).

Modeling studies have illustrated varying degrees of regional response to OAE deployment. For instance, Köhler et al. (2013) observed similar excess carbon uptake ($\sim$7 PgC) in both global OAE and OAE along ship-track over 2000-2010, assuming a uniform annual deposition of 3 Pg olivine. Likewise, Lenton et al. (2018) reported small regional variability when comparing global OAE with latitudinal band-specific applications, noting an excess carbon uptake of 184 PgC over the period 2020-2100 with a yearly addition of 0.25 Pmol alkalinity. In contrast, Burt et al. (2021) found regional differences in OAE-induced carbon uptake over a 75-year period, where the Southern Ocean sequestered 175 PgC, compared to 82 PgC in the North Atlantic under identical alkalinity addition rates but with different deployment areas compared to Lenton et al. (2018). The corresponding OAE efficiencies ($\eta CO_2 = \Delta DIC/\Delta Alk$; Renforth and Henderson, 2017) were 0.89 for the Southern Ocean and 0.65 for the North Atlantic. Further, Butenschön et al. (2021) simulated OAE along ship tracks in the Mediterranean Sea over a 50-year period and reported a low efficiency of 0.5 by the end of the experiment. Both studies attributed the lower efficiencies in the North Atlantic and Mediterranean Sea to rapid alkalinity loss to the deep ocean. He and Tyka (2023) investigated month-long pulsed OAE deployments along global coastlines, reporting efficiencies between 0.6 and 0.8. They, along with Bach et al. (2023), noted that regions with strong downwelling (e.g., around Iceland and in the Labrador Sea) are unsuitable for OAE, as water masses here are exported to the deep ocean before equilibration with atmospheric $CO_2$ can occur. This results in reduction of about half of the carbon uptake potential of OAE. In contrast to these findings, Nagwekar et al. (2024) reported comparable efficiencies ($\sim$0.85) for continuous OAE deployment in both the global oceans and subduction regions of the Southern Ocean and the North Atlantic. Their study also found that subduction regions transferred nearly twice the relative amount of carbon to the deep ocean compared to global OAE, though the absolute amount was lower due to their smaller surface area. These contrasting findings underscore the need for more detailed investigations into the regional dynamics of subduction areas. To achieve this, high-resolution models can be employed to simulate the physical and biogeochemical processes critical to OAE with consideration of regionally important smaller scale processes.

Intermediate, deep, and bottom water formation is a crucial component of the ocean overturning circulation, as it transfers anthropogenic carbon-laden surface water masses into the ocean interior resulting in carbon sequestration on centennial to millennial timescales (Gruber et al., 2009; Gruber et al., 2019). Accordingly, the Southern Ocean and North Atlantic are associated with 40% and 23% of ocean anthropogenic carbon uptake, respectively (Gruber et al., 2019; Khatiwala et al., 2009; Sabine et al., 2004). A range of physical processes impact the anthropogenic carbon uptake and storage, including mesoscale eddies which can be better represented using high resolution eddy permitting or resolving models. Eddies are characterized by typical radii of 40 to 100 km and an average lifetime of 16 to 32 weeks (Chelton et al., 2011). They are ubiquitous in the global ocean and induce changes in vertical and horizontal mixing, heat distribution, gas exchange and circulation patterns (Beech et al., 2022; Gnanadesikan et al., 2015; Meredith and Hogg, 2006; Smith et al., 2000). By altering these dynamics, they facilitate transport of carbon, oxygen and nutrients, thus modifying physical carbon uptake and storage as well as primary productivity in the oceans (Dufour et al., 2015; Oschlies and

Garçon, 1998). Furthermore, cyclonic and anticyclonic eddies were shown to exert differing impacts on carbon uptake. For instance, integrated over the Southern Ocean, anticyclonic eddies contributed ∼0.03 PgC $yr^{-1}$ to total carbon uptake and cyclonic eddies offset this by ∼0.01 PgC $yr^{-1}$ (Keppler et al., 2024). Previous studies comparing models of different resolutions demonstrated that high-resolution models (1/6°, 1/10°) outperform coarse-resolution models by resolving small-scale processes and thus providing a more precise representation of upper ocean dynamics, deep water formation, and mixed layer depth (Oschlies, 2002; Sidorenko et al., 2020). Further, Langlais et al. (2017) reported that coarse-resolution models underestimate the anthropogenic carbon sequestration in the Southern Ocean intermediate water masses by 40% as compared to high resolution models. However, the high computational cost and long runtimes of high resolution models could come at the cost of shorter spin-ups, which may cause errors in estimation of anthropogenic carbon uptake (Beech et al., 2024; Terhaar et al., 2024).

Despite the recognized importance of high-resolution modeling for capturing small-scale processes, studies investigating OAE predominantly rely on coarse resolution simulations. Moreover, high resolution model estimates complementing direct observations would be essential for effective Monitoring, Reporting, and Verification (MRV) of OAE (Fennel et al., 2023; Ho et al., 2023). Therefore, this study seeks to address this gap by employing high-resolution modeling to simulate OAE globally and in subduction regions and comparing the results with those from coarse-resolution simulations by Nagwekar et al. (2024).By doing so, we aim to distinguish the impact of model resolution on simulated OAE-induced changes in OAE efficiency, oceanic carbon uptake and storage.

## METHODS

### *Model Description*

Simulations for OAE are carried out using the global ocean general circulation Finite-volumE Sea Ice-Ocean Model (FESOM2.1; Koldunov et al., 2019; Scholz et al., 2022; Scholz et al., 2019) coupled to the global biogeochemistry Regulated Ecosystem Model (REcoM3; Gürses et al., 2023). REcoM3 has 28 prognostic tracers and simulates the marine carbonate system and air-sea CO2 exchange using the mocsy 2.0 routines (Orr and Epitalon, 2015). It consists of two phytoplankton classes (silicifying diatoms and small phytoplankton with an implicit representation of calcifiers) and three zooplankton groups (microzooplankton, mesozooplankton, and polar macrozooplankton; Karakuş et al., 2021). It resolves the cycling of the macronutrients dissolved inorganic nitrogen (DIN) and silicic acid (DSi) and of the trace metal iron (DFe). REcoM3 incorporates a variable stoichiometry approach, that is, variable C:N:Chl:Si ratios for diatoms and C:N:Chl:$CaCO_3$ ratios for small phytoplankton, which can help to simulate the physiological response of phytoplankton to changing environmental conditions such as light and nutrient availability (Hohn, 2008; Schartau et al., 2007).

*Experimental Setup*

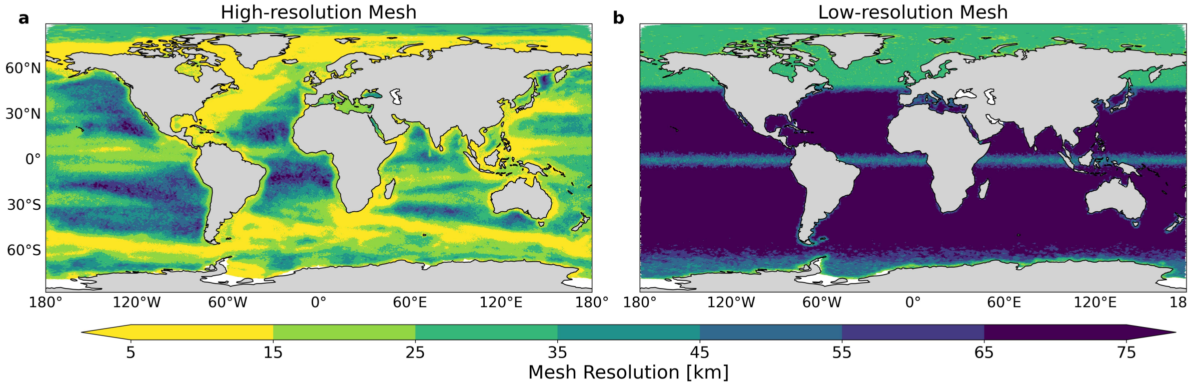

FIGURE 5.1: Mesh Resolution in km **(a)** High-resolution and **(b)** Low-resolution.

High-resolution simulations are carried out with the so-called BOLD mesh (hereafter High-resolution: HR). It has 1,306,775 surface nodes and 47 unevenly spaced vertical z levels, where layer thickness varies from 5 m at the surface to 250 m in the ocean interior. It has an increased horizontal resolution of about 5 to 10 km in the Southern Ocean, North Atlantic, Arctic, equatorial Pacific, and Indian Ocean (Figure 5.1a). The resolution is coarsened to 50-60 km in the tropics and the subtropical gyres in the Pacific and Atlantic Ocean (Figure 5.1a; Sein et al., 2018). The HR mesh is a globally eddy permitting mesh. Hence, by using this mesh we can study the effect of high resolution on the OAE-induced changes as compared to the OAE simulations carried out on the relatively coarse resolution CORE mesh (hereafter Low-resolution: LR; Figure 5.1b; Nagwekar et al., 2024). The LR mesh has 126,858 surface nodes and the horizontal resolution is 20 km along the Antarctic coast, in the equatorial regions and north of 50°N and ~75 km in the subtropical ocean basins. It has the same vertical resolution as the HR mesh.

For this study we first ran 104 years of physics-only spin-up on the HR mesh. The drift in the circulation was assessed by quantifying the volume transport across the Drake Passage, which reached a quasi-steady state within 100 years. We interpolated the biogeochemical fields from an existing spin-up of 150 years on the LR mesh to the HR mesh. With these initial conditions, we started the historical simulation from 1950 to 2014. Considering the first 40 years of the historical simulation as further spin-up time, physical and biogeochemical tracers have experienced a total of 144 and 40 years of spin-up on the HR mesh, respectively. Following the spin-up and the historical simulation, we performed future scenario simulations from 2014 to 2100. As in Nissen et al. (2022) and Nagwekar et al. (2024), all simulations at the ocean surface were forced with atmospheric output from the AWI Climate Model, in particular from its contribution to the "Coupled Model Intercomparison Project Phase 6 (CMIP6)" (Semmler et al., 2020). The simulations are forced with 3-hourly atmospheric momentum fluxes, freshwater fluxes, radiation, and daily output of terrestrial freshwater runoff from the first member of the historical simulation from 1950 to 2014 and of the Shared Socioeconomic Pathways SSP3-7.0 experiment from 2015 to 2100 (O'Neill et al., 2016). The SSP3-7.0 scenario has inadequate climate policies and assumes a continuous increase in emissions, leading to an atmospheric

$CO_2$ mixing ratio of 867.2 ppm and global warming of ∼5°C by the end of the 21st century (Semmler et al., 2020).

### *Identification of deep and bottom water formation regions*

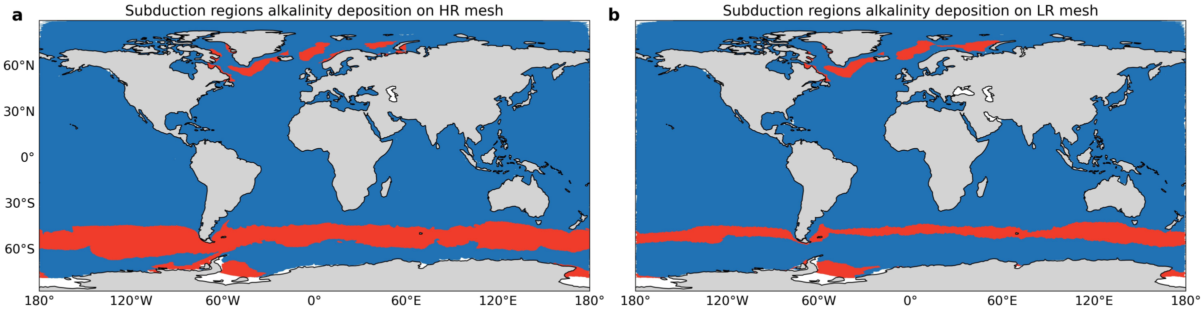

FIGURE 5.2: Alkalinity deposition masks obtained from the water mass transformation and formation analysis for **(a)** High-resolution mesh and **(b)** Low-resolution mesh.

The Water Mass Transformation (WMT) and Water Mass Formation (WMF) framework is utilized to identify subduction regions in the Southern Ocean (SO; south of 40°S), the Northwest Atlantic (NWA; 50°N–75°N; 70°W–17°W), and the Norwegian-Barents Sea (NBS; 62°N–77°N; 60°E–10°W) using the historical simulations spanning the period from 1950 to 2014. Originally proposed by Walin (1982), this framework provides a means to quantify the extent to which water within a specific density class becomes either denser or lighter due to diabatic processes, including surface fluxes, diapycnal mixing in the ocean's interior, and changes in lateral transport and mixing rates (Nissen et al., 2022; Abernathey et al., 2016). Consequently, the transformation rate serves as a measure of the net volume flux through isopycnal surfaces. This is crucial because water masses must either subduct or upwell within defined density ranges to maintain mass continuity at the ocean surface (Abernathey et al., 2016; Walin, 1982; Pellichero et al., 2018).

Using this framework, WMT rates are derived by accounting for the contributions of surface buoyancy fluxes comprising heat and freshwater exchanges to changes in surface density. These rates yield density thresholds above or below which the water masses are made denser or lighter. Based on these thresholds, we locate subduction regions in the SO, NWA, and NBS and generate the alkalinity deposition mask for OAE experiments (Figure 5.2a). A similar analysis was carried out using the CORE mesh simulations to obtain the alkalinity deposition mask (Figure 5.2b; Nagwekar et al., 2024). Notably, the mask from the HR mesh covers a total area of $42.87 \text{x} 10^{12}$ $m^2$, which is substantially larger than the $27.16 \text{x} 10^{12}$ $m^2$ covered by the LR mesh mask. Both configurations indicate subduction on the Davis Strait shelves, a feature that is not captured by observational studies (Jeansson et al., 2023; Jeansson et al., 2017 see also Nagwekar et al., 2024). Additional details on WMT/WMF calculations, including the equations used, are provided in the supplement (Text S1; Figure S1 and Figure S2).

### *OAE Model Experiments*

Following the historical simulation, a CTRL run (without alkalinity addition) is performed from 2014 to 2100 under the SSP3-7.0 high-emission scenario. Previous studies have shown that the dependency of OAE on the emission scenario is small, making results highly transferable across scenarios (Lenton et al., 2018; Nagwekar et al., 2024). Therefore, we limit our high-resolution simulations to the SSP3-7.0 scenario. OAE simulations are branched off from the CTRL run in 2030 and continue until 2100. Three distinct OAE experiments are conducted with uniform and continuous alkalinity deposition: global OAE (GLO-ALK), OAE in subduction regions (SUB-ALK), and global OAE with nutrient fertilization (GLO-ALK-NUT). In the SUB-ALK experiment, alkalinity is deposited across all three subduction regions collectively to evaluate their combined potential for carbon uptake and storage. Previous simulations of OAE in individual subduction regions on the LR mesh showed approximately additive effects (Nagwekar et al., 2024), supporting the rationale for combined regional simulations here.

In all simulations, the added alkalinity and nutrients are scaled according to the relative sea-ice cover in each grid cell at each time step, ensuring that no additions occur in the fully ice-covered regions. As sea-ice extent declines towards the end of the century, alkalinity and nutrient deposition increases in the 2090s compared to the 2030s. For global OAE experiments the alkalinity addition rates are similar between LR and HR and amount to 77.82 Tmol yr$^{-1}$ over the 2030s, increasing slightly to 79.46 Tmol yr$^{-1}$ during the 2090s. This amount of added alkalinity would be equivalent to deposition of 3 Pg olivine per year, where 1 mol of olivine dissolved in seawater releases 4 mol of alkalinity (Hauck et al., 2016; Köhler et al., 2013). In the SUB-ALK experiments, alkalinity deposition is consistently higher in the HR setup throughout the century due to its finer resolution, which captures larger subduction regions. Accordingly, during the 2030s, the HR SUB-ALK simulation applies 9.25 Tmol yr$^{-1}$ of alkalinity, compared to 5.71 Tmol yr$^{-1}$ in the LR setup. By the 2090s, alkalinity deposition in the HR simulation increases slightly to 9.52 Tmol yr$^{-1}$, while the LR rate remains nearly unchanged at 5.72 Tmol yr$^{-1}$. The olivine equivalent for the alkalinity released in the HR setup is 0.36 Pg yr$^{-1}$, whereas in the LR setup, it amounts to 0.22 Pg yr$^{-1}$. In GLO-ALK-NUT simulation, nutrient fertilization accompanies alkalinity addition in both setups, reflecting the composition of olivine used as an alkaline feedstock. Along with alkalinity release, olivine dissolution also introduces silicic acid and iron, with 1 mol of olivine releasing 1 mol of silicic acid and 0.2 moles of iron. Given the identical global addition of alkalinity, both the HR and LR setups exhibit equal deposition rates of nutrients. In the 2030s, these rates are 19.44 Tmol of silicic acid per year and 3.88 Tmol of iron per year, which increase to 19.84 Tmol of silicic acid per year and 3.97 Tmol of iron per year by the 2090s.

The OAE efficiency $\eta CO_2 = \Delta DIC/\Delta Alk$ is calculated as the global ratio of the volume-integrated increases in dissolved inorganic carbon (DIC) and alkalinity, both relative to the CTRL simulation (Renforth and Henderson, 2017). This efficiency metric is independent of the mode of OAE deployment and material used for OAE. It accounts for an accumulated increase in DIC and alkalinity as a result of alkalinity enhancement relative to CTRL.

TABLE 5.1: Excess oceanic $CO_2$ uptake ($\Delta CO_2f$), Ocean alkalinity enhancement efficiency ($\eta CO_2$) calculated as the ratio of volume integrated excess dissolved inorganic carbon (DIC) over volume-integrated excess alkalinity, increase in total net primary production ($\Delta$NPPt), and increase in DIC ($\Delta$) in top 1 km and >1 km of the ocean depth with respect to CTRL simulations, on the high-resolution (HR) and low-resolution (LR) model setups. All numbers are calculated as an average over the global ocean, Southern, Pacific, Atlantic, Indian, and Arctic Ocean over the 2030s and 2090s. $\Delta$DIC values are only given for the Global Ocean.

| **Global Ocean** | | | | | | | |
|---|---|---|---|---|---|---|---|
| **Variable** | **Year** | **GLO-ALK** | | **SUB-ALK** | | **GLO-ALK-NUT** | |
| | | HR | LR | HR | LR | HR | LR |
| $\Delta CO_2f$ [PgC $yr^{-1}$] | 2030s | 0.65 | 0.63 | 0.09 | 0.05 | 2.45 | 2.39 |
| | 2090s | 0.92 | 0.90 | 0.11 | 0.065 | 1.26 | 1.24 |
| $\eta CO_2$ [$\Delta$DIC/$\Delta$Alk] | 2030s | 0.57 | 0.56 | 0.68 | 0.63 | - | - |
| | 2090s | 0.86 | 0.85 | 0.90 | 0.85 | - | - |
| $\Delta$NPPt [PgC $yr^{-1}$] | 2030s | - | - | - | - | 12.21 | 13.15 |
| | 2090s | - | - | - | - | 8.90 | 9.50 |
| $\Delta$DIC top 1 km [PgC] | 2030s | 2.94 | 2.89 | 0.39 | 0.24 | 9.29 | 8.85 |
| | 2090s | 51.80 | 50.95 | 6.01 | 3.70 | 72.41 | 69.51 |
| $\Delta$DIC >1 km [PgC] | 2030s | 0.0073 | 0.0034 | 0.0015 | 0.0007 | 2.22 | 2.03 |
| | 2090s | 3.0 | 1.73 | 0.50 | 0.25 | 35.08 | 32.43 |
| **Southern Ocean** | | | | | | | |
| **Variable** | **Year** | **GLO-ALK** | | **SUB-ALK** | | **GLO-ALK-NUT** | |
| | | HR | LR | HR | LR | HR | LR |
| $\Delta CO_2f$ [PgC $yr^{-1}$] | 2030s | 0.15 | 0.14 | 0.074 | 0.041 | 1.06 | 1.05 |
| | 2090s | 0.21 | 0.20 | 0.10 | 0.05 | 0.81 | 0.71 |
| $\eta CO_2$ [$\Delta$DIC/$\Delta$Alk] | 2030s | 0.66 | 0.65 | 0.68 | 0.63 | - | - |

| Continued | | | | | | | |
|---|---|---|---|---|---|---|---|
| Variable | Year | GLO-ALK | | SUB-ALK | | GLO-ALK-NUT | |
| | | HR | LR | HR | LR | HR | LR |
| | 2090s | 0.89 | 0.88 | 0.91 | 0.85 | - | - |
| $\Delta$NPPt [PgC yr$^{-1}$] | 2030s | - | - | - | - | 2.83 | 3.17 |
| | 2090s | - | - | - | - | 3.34 | 3.72 |
| **Pacific Ocean** | | | | | | | |
| Variable | Year | GLO-ALK | | SUB-ALK | | GLO-ALK-NUT | |
| | | HR | LR | HR | LR | HR | LR |
| $\Delta$CO$_2$f [PgC yr$^{-1}$] | 2030s | 0.28 | 0.27 | 0.006 | 0.004 | 1.19 | 1.13 |
| | 2090s | 0.39 | 0.37 | 0.008 | 0.005 | 0.32 | 0.33 |
| $\eta$CO$_2$ [$\Delta$DIC/$\Delta$Alk] | 2030s | 0.56 | 0.55 | 0.68 | 0.63 | - | - |
| | 2090s | 0.86 | 0.85 | 0.89 | 0.84 | - | - |
| $\Delta$NPPt [PgC yr$^{-1}$] | 2030s | - | - | - | - | 9.13 | 9.50 |
| | 2090s | - | - | - | - | 5.63 | 5.96 |
| **Atlantic Ocean** | | | | | | | |
| Variable | Year | GLO-ALK | | SUB-ALK | | GLO-ALK-NUT | |
| | | HR | LR | HR | LR | HR | LR |
| $\Delta$CO$_2$f [PgC yr$^{-1}$] | 2030s | 0.13 | 0.12 | 0.004 | 0.003 | 0.12 | 0.12 |
| | 2090s | 0.18 | 0.17 | 0.005 | 0.004 | 0.14 | 0.15 |
| $\eta$CO$_2$ [$\Delta$DIC/$\Delta$Alk] | 2030s | 0.55 | 0.54 | 0.63 | 0.61 | - | - |
| | 2090s | 0.85 | 0.84 | 0.86 | 0.83 | - | - |
| $\Delta$NPPt [PgC yr$^{-1}$] | 2030s | - | - | - | - | 0.11 | 0.17 |

**Continued**

| **Variable** | **Year** | **GLO-ALK** | | **SUB-ALK** | | **GLO-ALK-NUT** | |
|---|---|---|---|---|---|---|---|
| | | HR | LR | HR | LR | HR | LR |
| | 2090s | - | - | - | - | −0.24 | 0.05 |

**Indian Ocean**

| **Variable** | **Year** | **GLO-ALK** | | **SUB-ALK** | | **GLO-ALK-NUT** | |
|---|---|---|---|---|---|---|---|
| | | HR | LR | HR | LR | HR | LR |
| $\Delta CO_2f$ [PgC $yr^{-1}$] | 2030s | 0.08 | 0.08 | $4.5e^{-5}$ | $5.7e^{-5}$ | 0.05 | 0.05 |
| | 2090s | 0.11 | 0.11 | $6.4e^{-5}$ | $9.3e^{-5}$ | −0.03 | 0.02 |
| $\eta CO_2$ [ΔDIC/ΔAlk] | 2030s | 0.54 | 0.52 | 0.79 | 0.74 | - | - |
| | 2090s | 0.87 | 0.85 | 0.86 | 0.86 | - | - |
| ΔNPPt [PgC $yr^{-1}$] | 2030s | - | - | - | - | 0.04 | 0.14 |
| | 2090s | - | - | - | - | −0.66 | −0.32 |

**Arctic Ocean**

| **Variable** | **Year** | **GLO-ALK** | | **SUB-ALK** | | **GLO-ALK-NUT** | |
|---|---|---|---|---|---|---|---|
| | | HR | LR | HR | LR | HR | LR |
| $\Delta CO_2f$ [PgC $yr^{-1}$] | 2030s | 0.008 | 0.008 | 0.001 | 0.0009 | 0.008 | 0.008 |
| | 2090s | 0.02 | 0.019 | 0.002 | 0.002 | 0.02 | 0.02 |
| $\eta CO_2$ [ΔDIC/ΔAlk] | 2030s | 0.65 | 0.64 | 0.54 | 0.48 | - | - |
| | 2090s | 0.90 | 0.89 | 0.82 | 0.80 | - | - |
| ΔNPPt [PgC $yr^{-1}$] | 2030s | - | - | - | - | 0.009 | 0.01 |
| | 2090s | - | - | - | - | −0.01 | 0.0004 |

## RESULTS

### *Oceanic $CO_2$ uptake and OAE efficiency in the high- and low-resolution model setups*

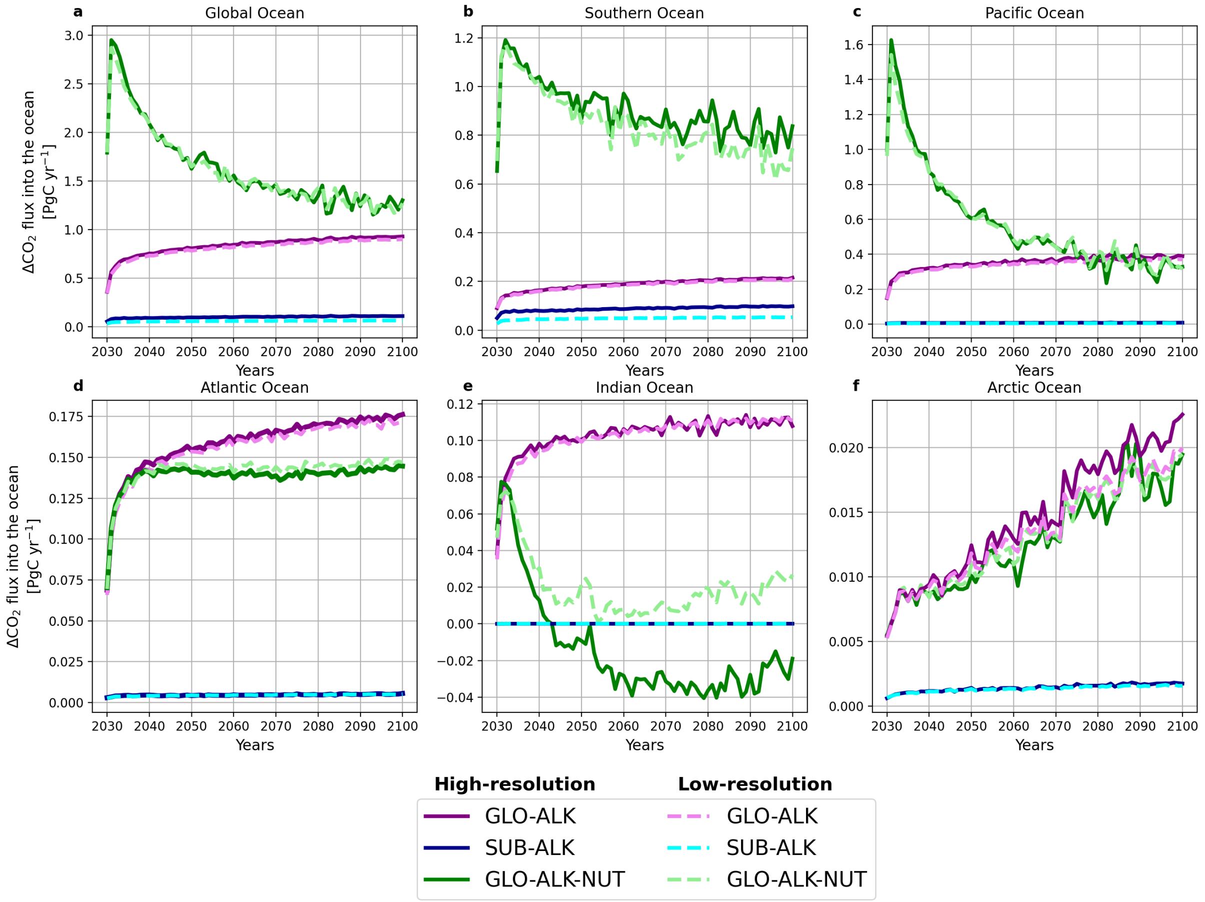

Figure 5.3: Time series of the increase in oceanic $CO_2$ uptake (PgC yr$^{-1}$) due to Ocean Alkalinity Enhancement (OAE) in global and subduction region OAE experiments under the SSP3-7.0 emission scenario, averaged over **(a)** the global ocean and **(b-f)** individual ocean basins where the region definition is based on RECCAP (DeVries et al., 2023). Solid lines represent high-resolution simulations, while dashed lines represent low-resolution simulations. Colors denote different experiments: global alkalinity addition (solid dark purple for high-resolution, dashed light purple for low-resolution), subduction region alkalinity addition (solid dark blue for high-resolution, dashed light blue for low-resolution), and global alkalinity with nutrient fertilization (solid dark green for high-resolution, dashed light green for low-resolution). The zoomed-in version of the SUB-ALK experiments is provided in Figure 4. Note the difference in the scales on the y-axis for each panel.

The GLO-ALK simulation on the HR setup exhibits a higher increase in oceanic $CO_2$ uptake relative to CTRL ($\Delta CO_2$f) than the LR setup, with a 3.7% greater uptake when averaged over the full simulation period (Figure 5.3a). During the 2030s, global $\Delta CO_2$f reaches 0.65 PgC yr$^{-1}$ in HR GLO-ALK, slightly exceeding the 0.63 PgC yr$^{-1}$ in LR (Figure 5.3a; Table 5.1). By the end of the century, as atmospheric $CO_2$ concentrations rise under the SSP3-7.0 scenario, $\Delta CO_2$f increases to 0.92 PgC yr$^{-1}$ in HR and 0.90 PgC yr$^{-1}$ in LR, maintaining a small but consistent difference. Regionally, the Pacific Ocean exhibits the highest increase in carbon uptake in both setups, with HR showing a 3.4% greater $\Delta CO_2$f than LR over the 2030s (Figure 5.3c). The Southern

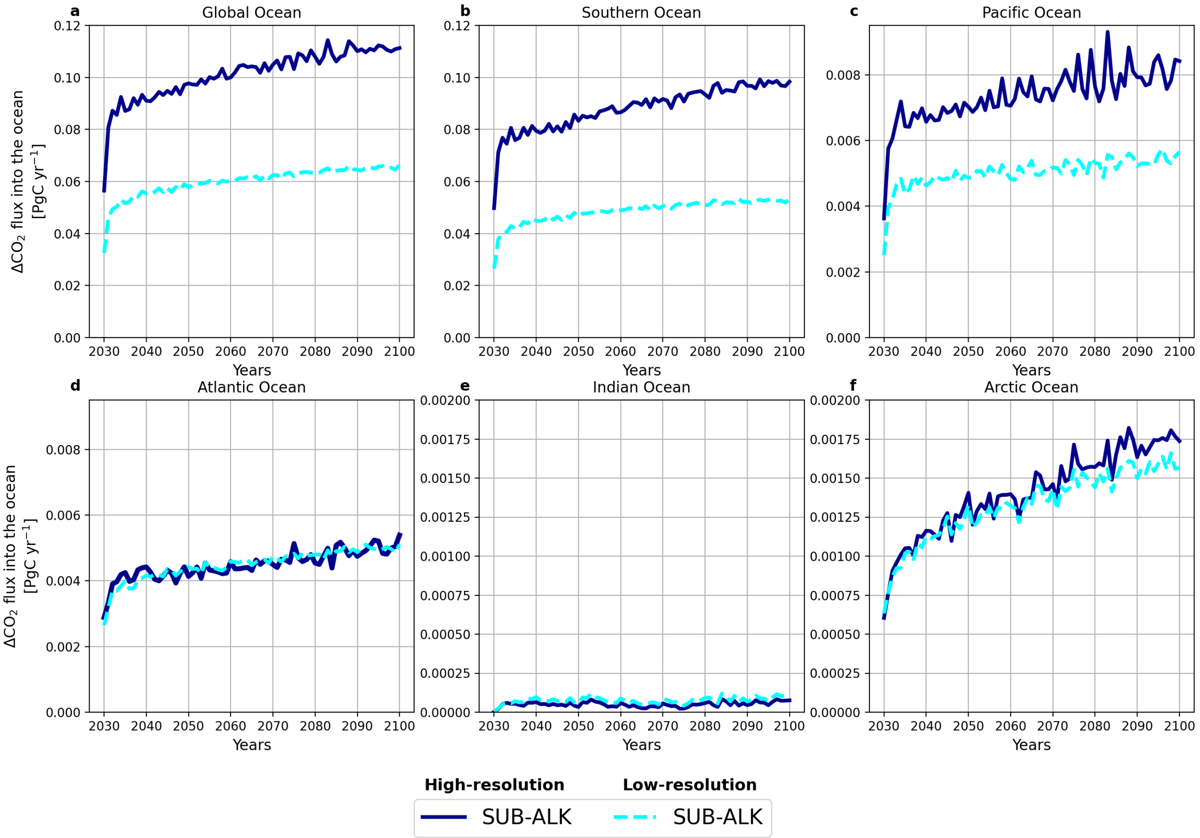

FIGURE 5.4: Time series of the increase in oceanic $CO_2$ uptake (PgC yr$^{-1}$) relative to the CTRL simulation due to Ocean Alkalinity Enhancement (OAE) for the subduction region OAE (SUB-ALK) under the SSP3-7.0 emission scenario, averaged over **(a)** the global ocean, and **(b-f)** individual ocean basins using the high-resolution setup (solid dark blue lines) and low-resolution setup (dashed light-blue lines). Note the difference in the scales on the y-axis for each panel.

Ocean follows, with uptake ranging from 0.20 to 0.21 PgC yr$^{-1}$ in both setups (Figure 5.3b). The Atlantic and Indian Oceans show increases of 0.10-0.17 PgC yr$^{-1}$ (Figure 5.3d-e), while the Arctic Ocean exhibits the lowest uptake (∼0.02 PgC yr$^{-1}$) with minimal differences between resolutions (Figure 5.3f). While HR consistently shows slightly higher carbon uptake than LR, the differences remain small across all regions and timescales. Given that both simulations receive identical global alkalinity additions, the increase in oceanic $CO_2$ uptake is primarily a function of the added alkalinity rather than model resolution. This indicates that the effect of resolution on global and regional $\Delta CO_2$f is overall small.

The higher oceanic $CO_2$ uptake in the HR SUB-ALK simulation is primarily due to greater alkalinity addition compared to the LR setup. The HR configuration has a 66.3% larger subduction area for alkalinity deposition, leading to a 63.8% higher alkalinity input in these regions over the simulation period. As a result, HR exhibits a 66.7% higher $\Delta CO_2$f (0.10 PgC yr$^{-1}$) than LR (0.06 PgC yr$^{-1}$) when averaged globally over the full simulation period (Figure 5.4a). Regionally, the Southern Ocean shows the largest difference, with $\Delta CO_2$f in HR being nearly twice as high as in LR during both the 2030s and 2090s (Figure 5.4b; Table 5.1). The Pacific Ocean follows, where $\Delta CO_2$f is 50–60% higher in HR compared to LR (Figure 5.4c). In contrast, the Atlantic Ocean shows only minor differences in $\Delta CO_2$f between the two setups,

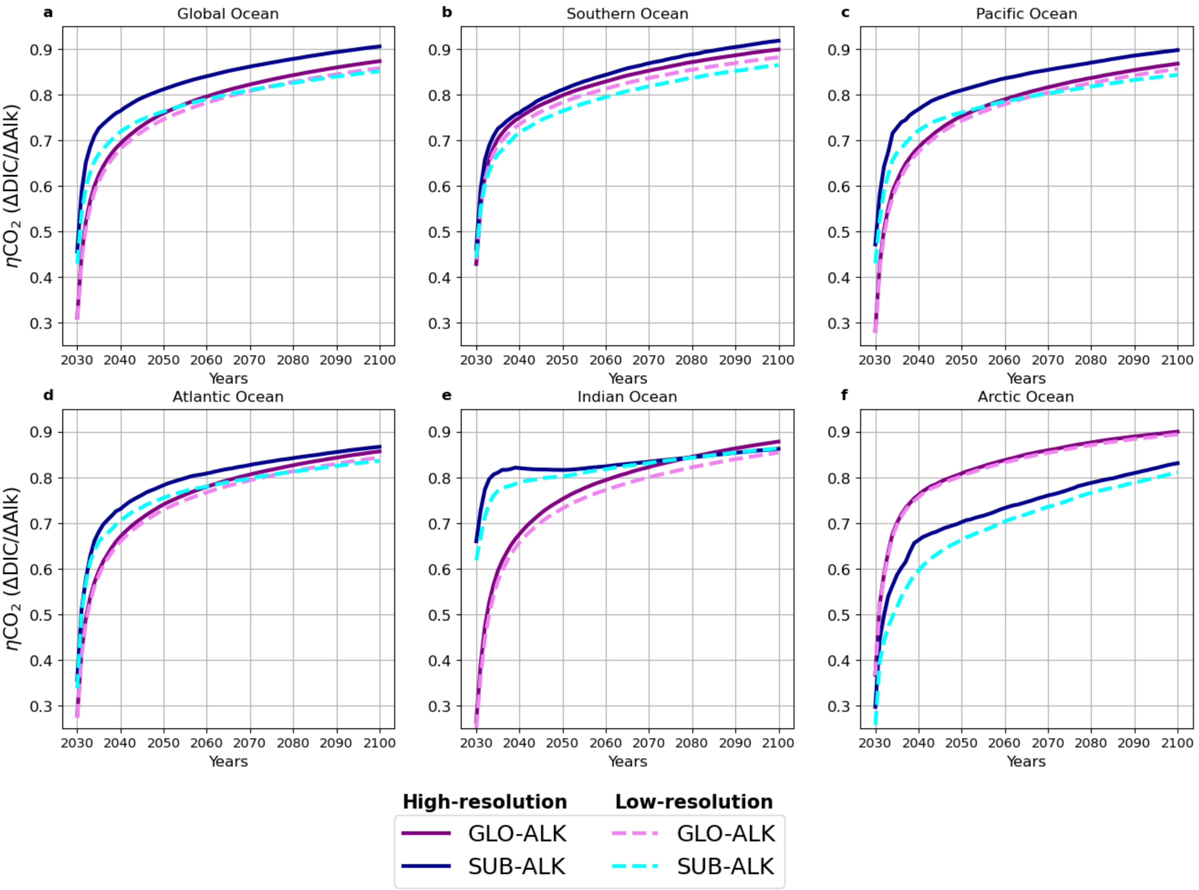

FIGURE 5.5: Time series of Ocean Alkalinity Enhancement (OAE) efficiency ($\eta CO_2$ = ΔDIC/ΔAlk) across **(a)** the global ocean and **(b-f)** individual ocean basins. Solid lines represent high-resolution simulations, while dashed lines represent low-resolution simulations. Colors indicate different OAE experiments: global OAE (GLO-ALK: solid dark purple for high-resolution, dashed light purple for low-resolution) and subduction region OAE (SUB-ALK: solid dark blue for high-resolution, dashed light blue for low-resolution).

with values of 0.004 and 0.003 PgC $yr^{-1}$ in the 2030s and 0.005 and 0.004 PgC $yr^{-1}$ in the 2090s (Figure 5.4d; Table 5.1). These results for the SUB-ALK experiment also indicate that the primary driver of increased oceanic $CO_2$ uptake is the amount of added alkalinity, while the effect of model resolution appears to be of secondary importance.

The nutrient fertilization simulations in HR and LR result in a similar global carbon uptake increase (1.24-1.26 PgC $yr^{-1}$) relative to CTRL over the $21^{st}$ century. In the HR setup, $\Delta CO_2f$ increases by 2.45 PgC $yr^{-1}$ in the 2030s and 1.26 PgC $yr^{-1}$ in the 2090s, while LR shows slightly lower values of 2.39 PgC $yr^{-1}$ and 1.24 PgC $yr^{-1}$, respectively (Figure 5.3a; Table 5.1). Regional variations are, however, evident, particularly in the Indian Ocean, where HR exhibits a decline in $CO_2$ uptake compared to LR and even falls below the CTRL, resulting in negative values of $\Delta CO_2f$. By the 2090s, $\Delta CO_2f$ in the Indian Ocean decreases by 0.03 PgC $yr^{-1}$ in the HR setup, whereas it increases by 0.02 PgC $yr^{-1}$ in LR (Figure 5.3e; Table 5.1). This Indian Ocean $\Delta CO_2f$ reduction in the HR setup is likely due to differences in nutrient utilization in other basins, particularly in the Pacific and Southern Oceans on the two setups. The Southern Ocean exhibits highly comparable carbon uptake in the HR and LR setup over the 2030s, with the value being slightly higher (by 0.95%) in the HR setup. However, by the 2090s, the increase in carbon uptake on HR setup in the Southern Ocean is higher by 14.1% than the LR setup. The Pacific Ocean shows nearly identical $\Delta CO_2f$ in both configurations throughout the simulation period (Figure 5.3b and c). Since both setups receive identical alkalinity and nutrient inputs, discrepancies in nutrient utilization and their impact on carbon uptake in the Indian and Southern Oceans stem from differences in model configuration and the representation of nutrients in the mean state of the HR and LR setups. Additionally, over time, differences in particulate organic carbon transport between the LR and HR setups can lead to varying outgassing patterns in the Atlantic, Indian, and Pacific Oceans over time (Harrison et al., 2018).

Despite the seamingly similar $CO_2$ flux response to alkalinity addition in both the setups, the HR simulations indicate that subduction regions exhibit higher OAE efficiencies than the global ocean, reaching 0.68 in the 2030s and 0.90 in the 2090s (Figure 6.1a). Throughout the simulation period, both GLO-ALK and SUB-ALK in the HR setup consistently exhibit higher globally averaged efficiencies than their LR counterparts (Figure 6.1a). The largest efficiency differences between GLO-ALK and SUB-ALK occur in the initial phase of OAE deployment. In the 2030s, SUB-ALK in the HR setup is 19.3% more efficient than GLO-ALK, whereas in the LR setup, this difference is 12.5%. By the 2090s, the efficiency gap narrows to 3.5% in the HR setup, with SUB-ALK reaching 0.90 and GLO-ALK 0.87, while both experiments in the LR setup stabilize at 0.85. Across individual ocean basins in the 2090s, GLO-ALK efficiencies in the HR setup range from 0.85 to 0.89, compared to a narrower range of 0.84 to 0.85 in the LR setup (Figure 6.1b–f). Similarly, SUB-ALK efficiencies in the HR setup vary between 0.81 and 0.91, with the highest in the Southern Ocean (0.91; Figure 6.1b) and the lowest in the Arctic Ocean (0.81; Figure 6.1f). The LR setup follows the same pattern but with lower values, ranging from 0.79 to 0.85. Efficiency differences between global and regional experiments tend to diminish toward the end of the century, but substantial differences persist in the early years of deployment (Figure 6.1a-f). These initial disparities may arise from the finer model resolution in the HR setup and differences in the background carbonate chemistry state between the two setups (Figure S5, S6 to S10). In the early phase of alkalinity deployment, local dynamics specific to the deployment regions can play a substantial role in shaping the efficiency differences. However, as the alkalinity perturbation signal spreads beyond the application site, the impact of resolution differences weakens, leading to more similar efficiencies between the two setups.

### *Increase in Net Primary Production in the high- and low-resolution model setups*

The addition of iron and silicic acid alongside alkalinity enhances global total net primary production (NPPt) in both HR and LR simulations compared to their respective control (CTRL) states (Figure 5.6a). However, the magnitude of this increase varies between the two setups. When averaged globally, the increase in total NPP (ΔNPPt) relative to CTRL is marginally higher in the HR setup (42.3%) than in the LR setup (41.4%) over the 2030s (Figure 5.6b). In contrast, during the 2090s, the HR setup exhibits a lower ΔNPPt (28.5%) than the LR setup (30.2%; Figure 5.6b). Globally, the LR setup has a 9.2% higher NPPt (31.6 PgC $yr^{-1}$) in its CTRL simulation than the HR setup (28.7 PgC $yr^{-1}$) averaged over the entire simulation period, whereas the HR setup has marginally higher values of NPPt ($\sim$0.2 PgC $yr^{-1}$) than the LR setup

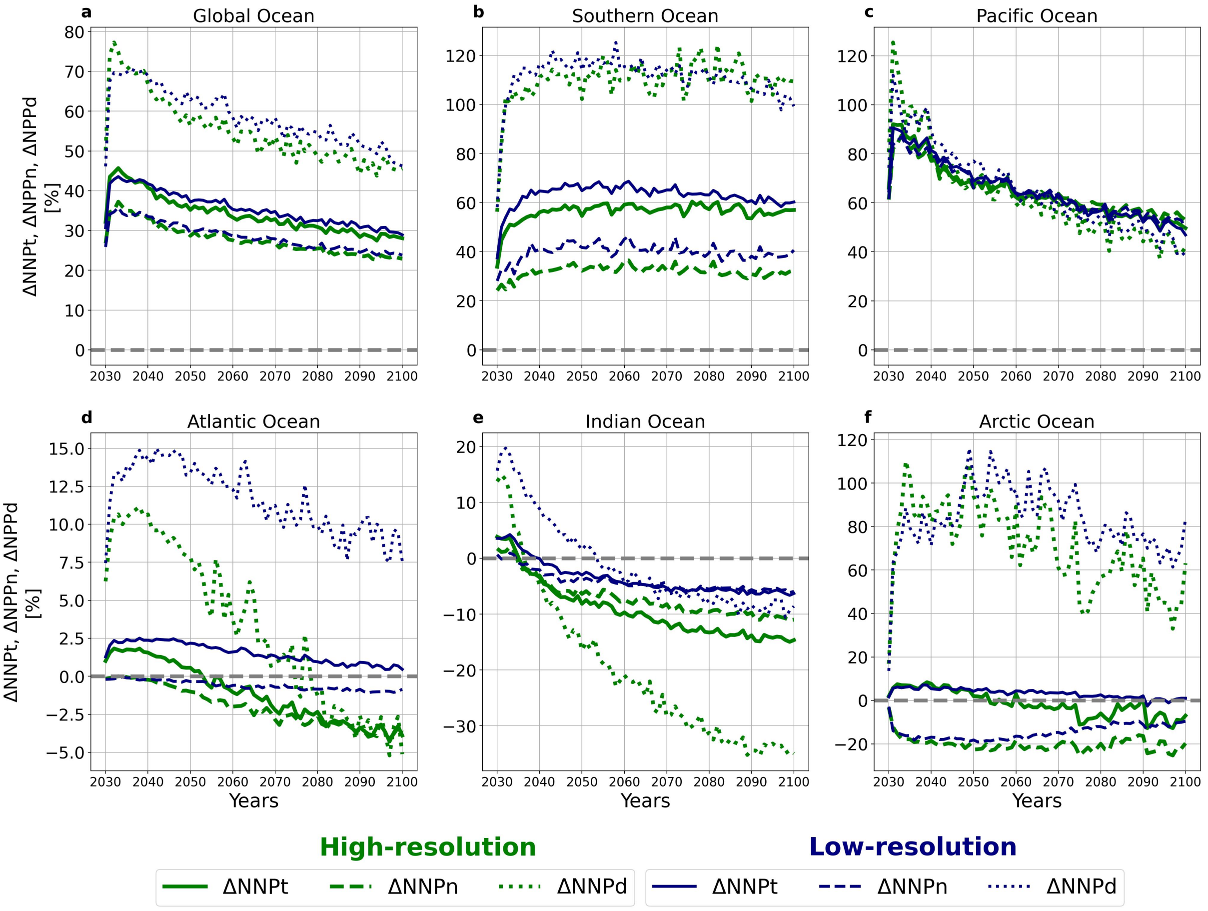

FIGURE 5.6: Time series for the percent increase in total net primary production (ΔNPPt; solid lines), small phytoplankton NPP (ΔNPPn; dashed lines), and diatom NPP (ΔNPPd; dotted lines) relative to CTRL on the high-resolution setup (green color) and low-resolution setup (blue color) in the **(a)** global ocean and **(b-f)** individual ocean basins.

in the Southern Ocean (Figure 5.7c). These small differences in the relative changes of NPPt caused by OAE may stem from variations in the baseline state of nutrient distributions and hence the nutrient limitation of phytoplankton growth between the two setups, resulting in different sensitivities to the nutrient addition.

Regional variations in NPPt further highlight differences in nutrient utilization across ocean basins. The Southern Ocean and Pacific Ocean exhibit the highest increases in NPPt relative to CTRL in both setups as they are to large-extent iron limited (Figure 6b-c). In particular, ΔNPPt in the Southern Ocean of both setups is consistent throughout the simulation period with the HR setup exhibiting an increase of 56.3% (3.3 PgC yr$^{-1}$) and the LR setup of 63% (3.7 PgC yr$^{-1}$; Figure 5.6b; Table 5.1). In the Pacific Ocean, ΔNPPt is also large and positive due to iron limitation in the South Pacific, but declines over time. ΔNPPt values in the Pacific Ocean are comparable between the two setups with values ranging between 84.3% and 85.3% (9.1-9.5 PgC yr$^{-1}$) in the 2030s and reducing to 51.4-52.2% (5.6-5.9 PgC yr$^{-1}$) in the 2090s (Figure 5.6c; Table 5.1). While the NPPt in the CTRL simulation on both setups in the Pacific Ocean remains largely unchanged throughout the simulation period, the decline in ΔNPPt over time could be due to the saturation reached by the additional nutrients deposited and by the nutrient robbing in the Southern Ocean. That means that as iron and silicic acid are added, more DIN is used

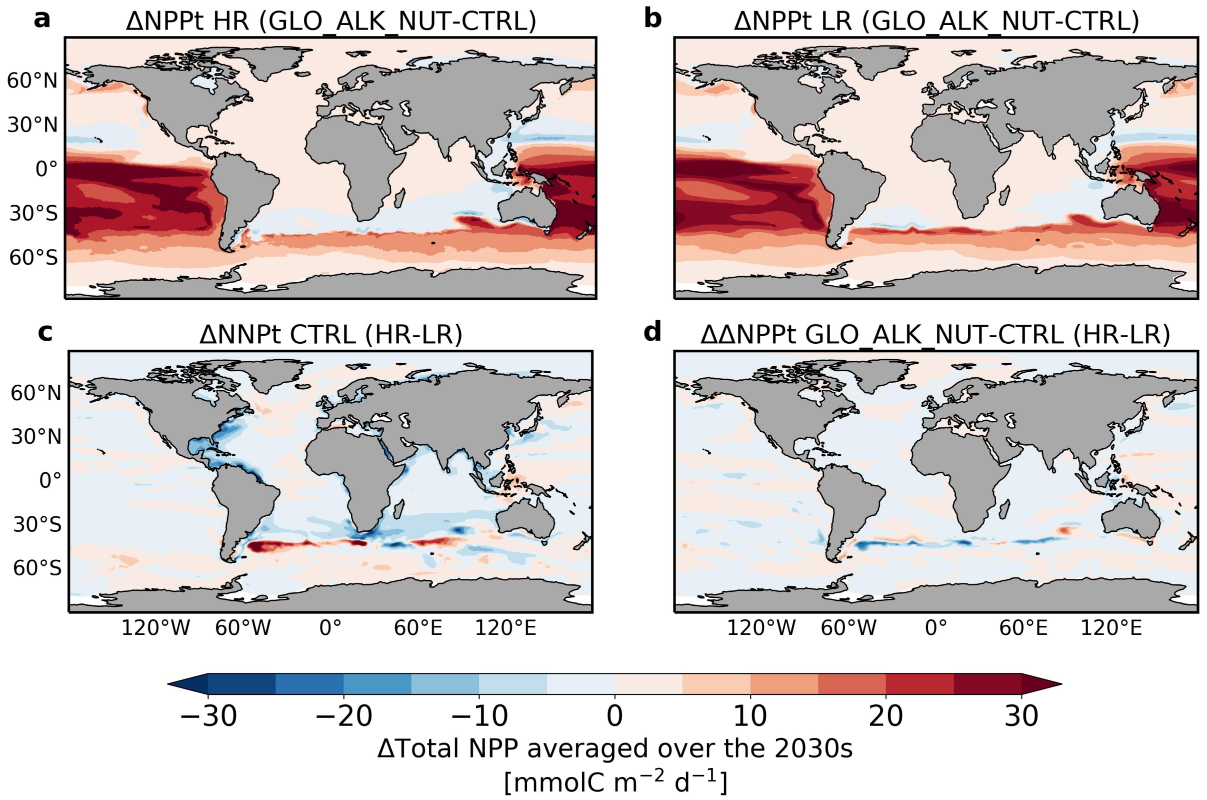

FIGURE 5.7: Spatial maps for differences in total net primary production (ΔNPPt) between different simulations. All maps are calculated as an average over the 2030s. **(a,b)** Differences between GLO-ALK-NUT and their respective CTRL (ΔNPPt) and differences between the high-resolution and low-resolution simulations for **(c)** the control simulations, and **(d)** increase in NPPt (ΔNPPt).

locally in the Southen Ocean, making less DIN available for export to the global ocean, thus, reducing NPP outside of the Southern Ocean as compared to the unperturbed state (Hauck et al., 2016). Consequently, the Southern Ocean exhibits a consistently positive effect due to permanent iron fertilization. In the Pacific, there is a positive increase in NPPt because of the strong fertilization in the South Pacific, but this positive increase declines over time likely due to nutrient robbing in the Southern Ocean, and possibly due to disturbed nutrient cycles in the North Pacific. In contrast, the Atlantic, Indian, and Arctic Oceans experience continuous declines in ΔNPPt, with values falling below their respective CTRL states (Figure 5.6d–f) as these basins respond less to DSi and DFe fertilization and receive progressively less DIN. However, the decrease in NPPt relative to the CTRL simulations in these basins is outweighed by the strong positive responses in the Southern and Pacific Ocean, leading to a net positive increase in global NPPt in both setups.

The differences in the response of small phytoplankton NPP (NPPn), diatom NPP (NPPd), and total NPP between the HR and LR setups primarily arise from variations in background nutrient distributions (Figure S3 and S4). The dissolved iron (DFe) concentration on the HR setup in its CTRL simulation is higher than the LR setup globally (Figure S3). Particularly, in the Southern Ocean the higher background DFe in HR CTRL results in higher NPPt than the CTRL simulation on the LR setup over the 2030s (Figure 5.7c). As a consequence, the HR simulation exhibits a weaker response to additional iron deposition in the OAE experiment, leading to a smaller increase in NPPt relative to the LR simulation (Figure 5.6b). Similarly, the HR CTRL simulation has higher dissolved silicic acid (DSi) concentrations in the Southern Ocean than the LR setup (Figure S4). This greater nutrient availability in the HR CTRL state reduces nutrient limitation for both diatoms and small phytoplankton, thereby dampening the response to additional nutrient fertilization both globally and across different ocean basins compared to the LR simulation.

*Dissolved Inorganic Carbon (DIC) in the high- and low-resolution model setups*

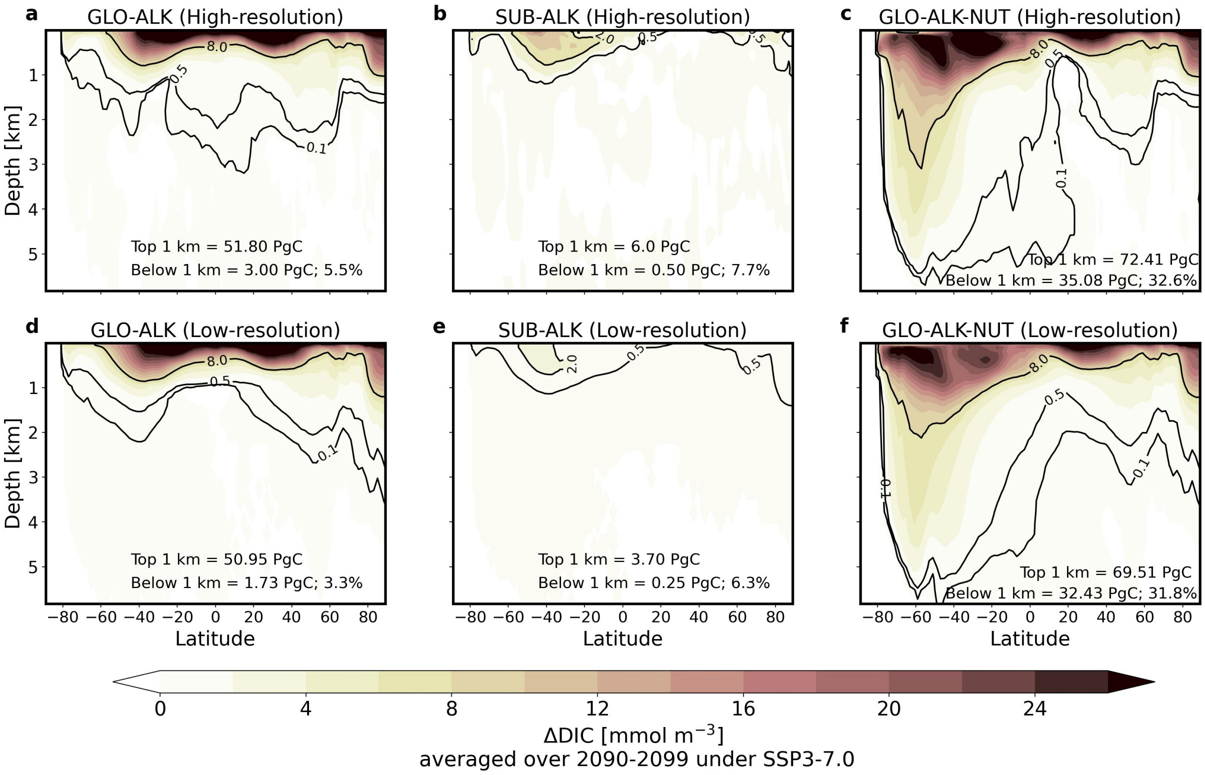

FIGURE 5.8: Zonal mean increase in dissolved inorganic carbon relative to the control simulation (ΔDIC), averaged over 2090-2099, for **(a, d)** GLO-ALK, **(b, e)** SUB-ALK, and **(c, f)** GLO-ALK-NUT in **(a-c)** the high-resolution setup and **(d-f)** the low-resolution setup.

In all experiments, the HR simulations transfer a larger fraction of carbon below 1 km than their LR counterparts (Figure 5.8a-f). In the GLO-ALK experiments, where both the HR and LR setups receive the same alkalinity additions, the HR simulations transfers 5.5% of the total increase in DIC relative to the the CTRL to the depths below 1 km over the 2090s, while the LR simulations transfers only 3.3% (Figure 5.8a and 5.8d). In the SUB-ALK experiments, the HR simulation transports 7.7% of the carbon taken up below 1 km, in contrast to 6.3% in the LR simulation (Figure 5.8b and 5.8e). In the GLO-ALK-NUT experiments, where both nutrients and alkalinity additions are similar between HR and LR, the HR simulation transports 32.6% of the excess carbon to the depths below 1 km, slightly higher than the 31.8% observed in the LR simulation (Figure 5.8c and 5.8f). Moreover, both HR and LR models reveal that subduction regions facilitate the transport of approximately 1-2 times more excess carbon to depths below 1 km than observed in the corresponding GLO-ALK experiments. It is important to note, however, that the absolute increase in DIC for SUB-ALK experiments amounts to only 7-11% of that in the GLO-ALK cases due to smaller surface areas of the subduction regions as identified with the water mass transformation framework and thus resulting in lower total alkalinity additions than in the GLO-ALK experiments.

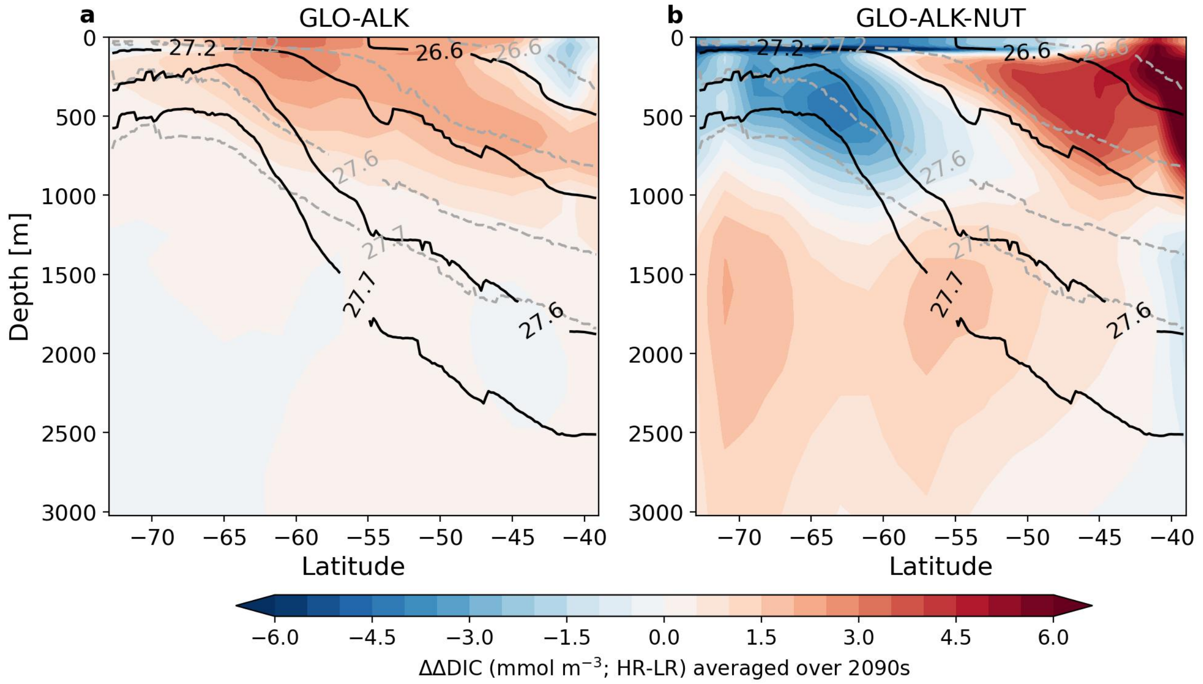

Figure 5.9: Zonal mean differences in the increase of dissolved inorganic carbon (ΔΔDIC = OAE-CTRL) between the high and low resolution simulations for **(a)** only alkalinity addition in the global ocean (GLO-ALK) and, **(b)** global alkalinity addition with nutrient fertilization (GLO-ALK-NUT), averaged over 2090–2099. Solid black lines indicate neutral density isopycnals in the high-resolution simulation, while dashed gray lines represent isopycnals in the low-resolution simulation.

Comparing the DIC accumulation in response to OAE between the high and low resolution simulations (ΔΔDIC) highlights the key role of the Southern Ocean in shaping this global signal (Figure 5.9). Neutral density contours reveal structural differences in isopycnal slopes, which strongly influence deep ocean carbon transport pathways (Chen et al., 2022). In the high resolution simulation, steeper isopycnal slopes indicate stronger vertical transport, leading to a greater penetration of carbon into the ocean interior. This is particularly evident in the top 500 m depth, where elevated ΔΔDIC values align with major subduction pathways. Accordingly, the amount of carbon transferred to 1-3 km in the Southern Ocean for GLO-ALK of HR is 0.88 PgC while that in the LR is 0.39 PgC over the 2090s.

Furthermore, nutrient fertilization in the GLO-ALK-NUT experiment amplifies the increase in deep ocean DIC in the HR simulation relative to the LR setup, due to larger biological productivity and thus larger carbon storage (Figure 5.9b). This difference arises from distinct initial nutrient limitations, which lead to different NPP responses and carbon storage outcomes. In the HR simulation, stronger vertical transport redistributes carbon more efficiently from the surface to deeper layers, resulting in 14.92 PgC being transferred below 1 km over the 2090s compared to 11.93 PgC in the LR experiment. The primary factor behind this enhanced transfer is the higher NPP observed in the HR control simulation, particularly between 40°S and 50°S, relative to the LR control (Figure 5.7c). In addition, the particularly negative ΔΔDIC values in the surface layer indicate that, although DIC increases in both HR and LR after nutrient addition, the increase is less pronounced in HR. These findings underscore that variations in initial nutrient conditions and potential differences in spin-up times or initial states can substantially influence carbon sequestration efficiency under nutrient fertilization.

### *Seasonal response of OAE in the subduction regions using the high- and low-resolution model setups*

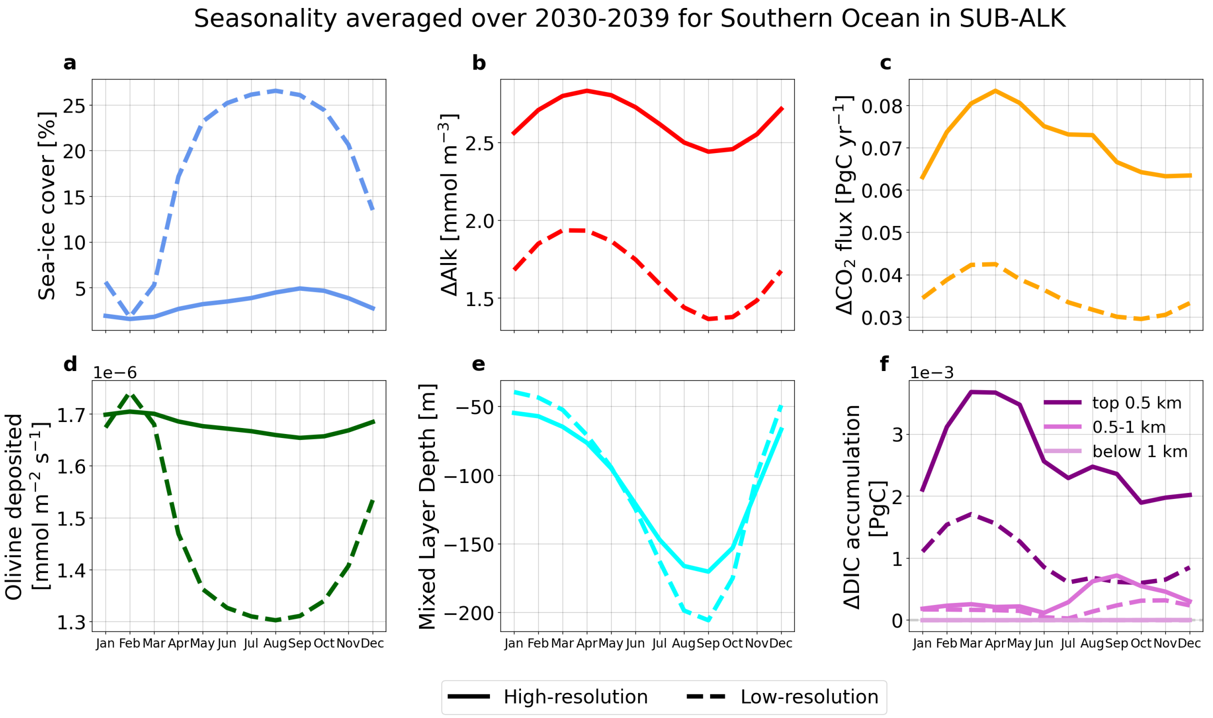

FIGURE 5.10: Seasonal response for ocean alkalinity enhancement (OAE) in the Northwest Atlantic for regional OAE (SUB-ALK) on the high-resolution (solid lines) and low-resolution (dashed lines) setups. The numbers are averaged over 2030-2039 under the SSP3-7.0 emission scenario. **(a)** Sea-ice cover [%], **(b)** Excess surface alkalinity ΔAlk [mmol m$^{-3}$], **(c)** Excess $CO_2$ flux $\Delta CO_2f$ [PgC yr$^{-1}$], **(d)** Amount of alkalinity (olivine) deposited [mmol m$^{-2}$ s$^{-1}$], **(e)** Mixed Layer Depth (MLD; m), and **(f)** Excess dissolved inorganic carbon (DIC) accumulation (ΔDIC; PgC) in the top 0.5 km (dark purple), 0.5-1 km (orchid), and below 1 km (light purple).

The increase in surface alkalinity (ΔAlk), $CO_2$ uptake ($\Delta CO_2f$), and DIC accumulation (ΔDIC) relative to CTRL show a consistent seasonal response across both HR and LR regional OAE simulations (SUB-ALK) in both hemispheres (Figure 5.10 and 5.11). As the alkalinity addition is scaled with sea-ice cover, a seasonal peak occurs when sea ice is at its minimum (Figure 5.10a and 5.10d; Figure 5.11a and 5.11d). In the SO, this peak occurs between January and March (Figure 5.10d), while in the NWA, it is observed from July to November (Figure 5.11d). Although the HR simulation generally exhibits greater sea-ice cover than the LR setup, the effective

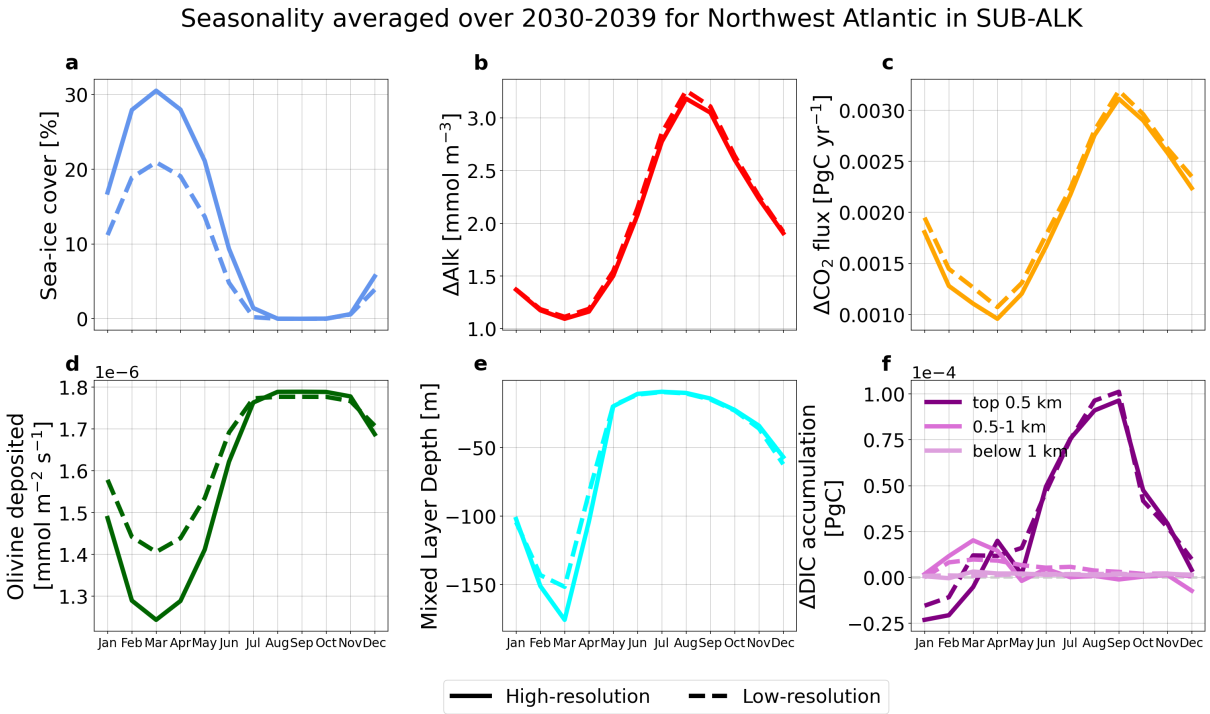

FIGURE 5.11: Seasonal response for ocean alkalinity enhancement (OAE) in the Northwest Atlantic for regional OAE (SUB-ALK) on the high-resolution (solid lines) and low-resolution (dashed lines) setups. The numbers are averaged over 2030-2039 under the SSP3-7.0 emission scenario. **(a)** Sea-ice cover [%], **(b)** Excess surface alkalinity ΔAlk [mmol $m^{-3}$], **(c)** Excess $CO_2$ flux $\Delta CO_2f$ [PgC $yr^{-1}$], **(d)** Amount of alkalinity (olivine) deposited [mmol $m^{-2}$ $s^{-1}$], **(e)** Mixed Layer Depth (MLD; m), and **(f)** Excess dissolved inorganic carbon (DIC) accumulation (ΔDIC; PgC) in the top 0.5 km (dark purple), 0.5-1 km (orchid), and below 1 km (light purple).

sea-ice-covered area within the alkalinity deposition mask is lower when considering only the Southern Ocean subduction regions (Figure 5.10a). This is because the alkalinity deposition area in the HR setup is 63% larger than the LR setup, reducing the relative fraction of the region covered by sea-ice (Figure 5.2a). In contrast, in the NWA, the alkalinity deposition mask is 9% smaller in the HR setup than in the LR setup, leading to 10% greater sea-ice cover in the HR simulation during February–April (Figure 5.11a).

The seasonal cycle of ΔAlk is closely linked to variations in mixed layer depth (MLD; Figure 5.10b and 5.10e and Figure 5.11b and 5.11e). When the MLD is shallow, excess surface alkalinity reaches its maximum. This pattern is observed during February–April in the SO (Figure 5.10b) and June–August in the NWA (Figure 5.11b). Conversely, in winter months—July–October in the SO and January–March in the NWA—the deepening of the MLD leads to a reduction in excess surface alkalinity. The magnitude of these variations differs between the two setups, particularly in the Southern Ocean where the larger alkalinity deposition area and lower sea-ice cover in the HR setup leads to higher alkalinity addition than the LR setup (Figure 5.10a and 5.10d). Additionally, when averaged over the alkalinity deposition mask in the Southern Ocean, the MLD results in being shallower in the HR than the LR setup (Figure 5.10e). These factors contribute to differences in the surface ΔAlk between the two resolutions, with HR having stronger anomalies than the LR (Figure 5.10b). In contrast, in the

NWA, the alkalinity deposition regions in the HR and LR setups differ by 9%, resulting in similar alkalinity addition in the ice-free regions (Figure 5.11d). Since the MLD is very similar between the two setups, the surface ΔAlk is also very similar (Figure 5.11b and 5.11e).

The seasonal changes in $CO_2$ flux relative to CTRL follow the pattern of excess alkalinity in both hemispheres (Figure 5.10c and 5.11c). Higher $\Delta CO_2f$ values occur during the summer months—February–April in the SO and June–August in the NWA—coinciding with peaks in excess alkalinity. Since increased alkalinity enhances $CO_2$ uptake, the high-resolution setup, which exhibits a higher excess alkalinity and lower sea-ice cover, also shows a stronger $CO_2$ flux anomaly compared to the low-resolution model in the Southern Ocean (Figure 5.10b and 5.10c). In NWA, where ΔAlk is similar in both setups, the increase in $CO_2$ uptake is also comparable (Figure 5.11b and 5.11c). This demonstrates that the primary driver of $\Delta CO_2f$ is the amount of excess alkalinity governed by the MLD seasonality, for which model resolution seems to play a secondary role.

The seasonal cycle of ΔDIC follows that of $\Delta CO_2f$, with the strongest accumulation in the upper 0.5 km occurring during February–May in the SO (Figure 5.10f) and June–August in the NWA (Figure 5.11f). The deeper layers (0.5–1 km and >1 km), show only a weak seasonal cycle. In the SO, where $\Delta CO_2f$ is higher in the high-resolution setup, ΔDIC accumulation is also greater compared to the low-resolution model (Figure 5.10f). In the NWA, where $CO_2$ uptake is similar between the two setups, ΔDIC accumulation is also similar. However, during January–March in the NWA, negative ΔDIC values appear in the upper 0.5 km (Figure 5.11f). This can be attributed to the deep winter MLD, which reduces OAE-induced surface $CO_2$ uptake, preventing a net increase in DIC relative to CTRL. Additionally, lateral advection of water masses out of the alkalinity addition region may contribute to localized ΔDIC values falling below baseline levels in both setups. Overall, the seasonal dynamics of surface alkalinity, $CO_2$ uptake, and DIC accumulation are primarily governed by the MLD variability and the effect of model resolution on the overall seasonal cycle seems not to affect these substantially.

## DISCUSSION AND CONCLUSION

Our study examines the impact of enhanced horizontal resolution on the simulated efficiency of OAE at global scales and within the subduction regions of the Southern Ocean and the North Atlantic. To assess the resolution effect, we compared our HR simulations with those of Nagwekar et al. (2024), who used the same model on a LR mesh. Our historical (1950-2014) and future projection CTRL (no-OAE; 2015-2100) simulations under the SSP3-7.0 scenario show nearly identical global carbon uptake in both the HR and LR configurations, with values of 1.2-1.3 PgC $yr^{-1}$ during the historical period and 3.9-4.0 PgC $yr^{-1}$ for the future period. These results indicate that large-scale air-sea $CO_2$ fluxes in our model are only marginally sensitive to horizontal resolution. In contrast, previous studies have reported different impacts of mesoscale processes on surface carbon uptake, which can only be resolved by HR meshes. For example, Ford et al. (2023) used in-situ observations and a Lagrangian eddy atlas to show that long-lived eddies in the South Atlantic can enhance regional carbon uptake by approximately 0.06 MtC $yr^{-1}$. Guo and Timmermans (2024) estimated the net mesoscale-driven $CO_2$ uptake to be on the order of 105 tC $yr^{-1}$ using a HR global model. Gnanadesikan et al. (2015) further demonstrated that variations in eddy-induced mixing parameters can modify carbon uptake by about 15%. Our results align with the modest net mesoscale effect reported by Guo and Timmermans (2024) and Ford et al. (2023) but differ from the larger discrepancies observed by Gnanadesikan et al. (2015).

In our OAE experiments, differences in $CO_2$ uptake between HR and LR configurations primarily reflect the amount of added alkalinity and its coupling with large-scale circulation. In the global OAE (GLO-ALK) experiments, where the same alkalinity input is applied in both resolutions, the increase in $CO_2$ uptake relative to the control is nearly identical, ranging from 0.63 to 0.65 PgC $yr^{-1}$ in the 2030s and from 0.90 to 0.92 PgC $yr^{-1}$ in the 2090s, with HR exhibiting a modestly higher uptake than LR (by 2-3%). In contrast, the subduction region OAE (SUB-ALK) experiments reveal more pronounced differences. In the 2030s, HR yields an increase in $CO_2$ uptake of 0.09 PgC $yr^{-1}$ compared to 0.05 PgC $yr^{-1}$ in LR which is a 80% higher value, while in the 2090s, HR attains 0.11 PgC $yr^{-1}$ versus 0.07 PgC $yr^{-1}$ in LR, corresponding to a 57.1% increase. This disparity is likely driven but cannot be fully explained by a 63.8% higher alkalinity addition in HR and may also stem from differences in the dynamical processes between the two configurations. Our results for global and regional OAE demonstrate that the increase in oceanic $CO_2$ uptake in both the setups scales linearly with the added amount of alkalinity by the end of the century, which is consistent with the Publication II of this thesis (Nagwekar et al., submitted). Overall, both our CTRL (non-OAE) and OAE simulations show minimal sensitivity of large-scale air-sea $CO_2$ fluxes to horizontal model resolution. In OAE simulations, the increase in $CO_2$ uptake is primarily determined by the amount of alkalinity added, while differences in the background state of each model can further modulate the response (Figure S9, S10).

Notable differences between global and regional OAE efficiencies emerge in the initial phase of deployment (2030s), which could be crucial for MRV strategies. In our simulations, the HR SUB-ALK experiment reaches the highest efficiency of 0.70, exceeding the LR SUB-ALK by 7.9%. These early disparities likely reflect fine-scale processes resolved by the HR mesh and the differences in the background state of alkalinity and DIC. By the end of the century, however, resolution effects on OAE efficiency diminish. In the 2090s, the HR GLO-ALK efficiency is 0.86 versus 0.85 in LR, and the SUB-ALK experiment reaches 0.90 in HR compared to 0.85 in LR. These values align with estimates from Burt et al. (2021) who used a coarse-resolution model for global and regional OAE simulations with a higher alkalinity addition of 250 Tmol $yr^{-1}$, reporting a global efficiency of 0.83 after 70 years and a Southern Ocean efficiency of 0.89. Our SUB-ALK Southern Ocean results (0.85 in LR to 0.91 in HR) closely match that range. Across other ocean basins, our $\eta CO_2$ values are also consistent with the findings of Burt et al. (2021), although our Arctic Ocean values (0.80-0.82) fall somewhat below the 0.87 reported by them. This is likely because we do not explicitly add alkalinity in the Arctic Ocean resulting in lower oceanic $CO_2$ uptake and thus lower OAE efficiency. Wang et al. (2023), using a high-resolution ($\sim$10 km) Bering Sea model with 0.0167 Tmol $yr^{-1}$ of alkalinity addition, found an efficiency of 0.96 after three years of deployment. They attribute this high efficiency to the shallow ocean depth in the Bering Sea and to higher background DIC and alkalinity values in the region.

Other coarse-resolution studies also report efficiencies between 0.85 and 0.95 (He and Tyka, 2023; Zhou et al., 2025; Yankovsky et al., 2024), indicating that over large spatial and temporal scales, resolution exerts a relatively modest effect. Nonetheless, our study shows that focusing solely on the final decade can obscure important initial contrasts and overlook substantial early-phase uncertainty in the OAE experiments.

Based on our results, large discrepancies in OAE efficiency during the first years of deployment introduce considerable uncertainty into MRV during those years. If short-term variability and uncertainty is overlooked, carbon removal may be over- or undercounted, compromising both the credibility of early-phase life cycle assessments and the integrity of associated carbon credit schemes. High-resolution modeling can alleviate these risks by capturing fine-scale physical and biogeochemical processes, such as localized mesoscale dynamics and the rapid, initial shifts in alkalinity concentration that occur immediately after OAE implementation and often drive outsized fluxes. By more accurately replicating these transient responses, high-resolution simulations can help pinpoint the timing and location of critical measurement needs, thereby guiding targeted observations. This, in turn, supports a robust MRV framework that can possibly reflect an improved trajectory of carbon sequestration capacity of OAE deployed in a particular region and can ensure that carbon credits more reliably mirror actual $CO_2$ removal.

Irrespective of model resolution, both HR and LR setups exhibit a similar seasonal response to OAE-induced changes, primarily driven by seasonal variations in MLD. During summer, a shallower MLD enhances the retention of excess alkalinity, leading to increased oceanic $CO_2$ uptake, whereas in winter, a deeper MLD reduces surface alkalinity levels, subsequently lowering $CO_2$ uptake (Nagwekar et al., 2024). This pattern aligns with findings from multiple studies that simulated pulsed OAE across various regions and the open ocean (He and Tyka, 2023; Zhou et al., 2025; Yankovsky et al., 2024). These studies primarily applied alkalinity pulses in January (a winter month in the Northern Hemisphere) and reported that subduction regions in the North Atlantic, including the Labrador Sea, Nordic Seas, and areas around Iceland, are unsuitable for OAE, as alkalinity is rapidly transported to the deep ocean before having a substantial impact on enhancing oceanic $CO_2$ uptake. Zhou et al. (2025) further simulated pulsed OAE globally in January, April, July, and October, demonstrating a similar seasonal response in OAE efficiency to that observed in our simulations. In the Labrador Sea, the efficiency increased from 0.2 in winter to 0.7 in summer, highlighting the importance of seasonal timing in OAE deployment. Based on these findings, our results suggest that subduction regions can be viable for OAE if deployment strategies account for seasonal variability. Future studies should focus on comparing different alkalinity deployment modes (pulsed vs. continuous), as pulsed deployment is more representative of real-world implementation and holds particular relevance for the MRV framework of OAE.

In this study, we also examined how horizontal resolution influences total NPP over the 21st century. In the CTRL (no-OAE) simulations, the HR setup in the Southern Ocean exhibits about 4% higher NPPt than the LR setup during the initial 20 years, yet by the end of the century it becomes 5% lower. Outside the Southern Ocean, NPPt in the CTRL simulation on HR remains consistently lower by roughly 17.13% compared to LR. These findings partially align with previous HR studies that show eddies can enhance production but do not always produce uniformly higher values. For instance, Lévy et al. (2012) reported a temporary phytoplankton boost upon moving from 1/9° to 1/54° resolution, followed by a 10-20% decline in basin-wide production over 50 years. Oschlies (2002) also found that mesoscale eddies increase production relative to coarse-resolution runs, though the net impact falls short of geochemical estimates.

Turning to the nutrient-enhanced simulations (iron and silicic acid) combined with alkalinity addition (GLO-ALK-NUT), we observe a global NPPt increase in both HR and LR. Initially, HR shows a slightly stronger increase relative to its CTRL simulation in the 2030s (by 0.9%), yet it ends up being 1.8% lower than LR over the 2090s. These contrasting responses stem from the higher background iron and silicic acid concentrations of the HR setup (Figure S11, and S12), which reduce the sensitivity of primary production to added nutrients. Such resolution-driven discrepancies in nutrient supply are consistent with the work of Mahadevan and Archer (2000), who observed a two- to three fold rise in nutrient flux to the euphotic zone when grid spacing was reduced from 40 km to 10 km, and Lévy et al. (2001), who recorded similarly large increases in upward nutrient transport when moving from a 6 km to a 2 km grid. These findings show that finer grid spacing resolves nutrient injections and can alter simulated primary production, sometimes enhancing local growth but, in other cases, reducing productivity on broader regional or decadal scales. However, as our evaluation indicates that the HR model exhibits stronger biases in DSi concentrations than the LR model with respect to the observational data, it does not necessarily provide a more reliable representation of nutrient dynamics (Figure S11, and S12). Given these biases, a more robust model evaluation against observations is essential in order to determine the most reliable setup for nutrient-enhanced OAE simulations

Our CTRL simulations for 2030-2100 show that the HR configuration yields slightly lower DIC concentrations than the LR setup. Specifically, HR has 1.6% lower DIC in the upper 1 km and 1.2% lower DIC below 1 km compared to LR. This result contrasts with previous studies. For example, Langlais et al., 2017 reported that coarse-resolution models underestimate anthropogenic carbon sequestration in intermediate water masses by nearly 40% compared to the high-resolution simulations. Resplandy et al. (2019) reported that eddy-driven subduction transports carbon to depths of 500-1000 m but contributes less than 5% to the annual basin-scale flux because upward and downward fluxes nearly counterbalance. In the Southern Ocean, Matear (2001) demonstrated that mesoscale eddies enhance the efficiency and alter the spatial pattern of carbon uptake by intensifying subduction and mixing. In contrast, our baseline experiments indicate that small-scale processes resolved in HR do not lead to enhanced DIC concentrations relative to LR.

In our OAE experiments, the resolution effect on DIC concentrations becomes more pronounced. In the GLO-ALK simulation, with equal alkalinity additions in both setups, HR exhibits 1.7% higher increase in DIC concentrations relative to CTRL (ΔDIC) in the upper 1 km and striking 73.4% higher ΔDIC concentrations below 1 km compared to LR. In the Southern Ocean of the GLO-ALK experiments, the carbon transfer to below 1 km in HR is nearly twice that in LR. This outcome is primarily attributed to steeper and deeper isopycnal structures in HR, which allow for more efficient vertical transport. In the SUB-ALK experiments, the larger increases in DIC concentrations observed in HR in both the upper 1 km and below are likely due to a higher alkalinity addition compared to LR, rendering the resolution effect secondary in this case. Overall, while our CTRL results contrasts the conventional view of enhanced deep carbon sequestration via mesoscale eddies, our OAE experiments underscore that, under equal alkalinity forcing, high-resolution modeling displays a pronounced, region-specific impact on how deep ocean carbon storage.

In conclusion, our results indicate that the most pronounced differences in OAE efficiency appear during the initial deployment phase of regional OAE, presumably due to differences in how ocean carbonate chemistry is represented in each setup. Over multi-decadal timescales, however, OAE efficiency and additional carbon uptake remain largely driven by the amount of alkalinity added, making the net resolution effect relatively modest. Although the HR configuration exhibits greater carbon sequestration below 1 km than LR in the global and regional OAE experiments, complexities arising from differences in small-scale dynamics, spin-up strategies, and biases in the mean state complicate direct comparisons. Furthermore, the substantial computational cost of HR modeling can constrain spin-up duration and the feasibility of extensive multi-decadal experiments, potentially introducing further uncertainties. While HR may capture more detailed short-term and regional processes, it does not fundamentally alter large-scale trends relative to LR (Gnanadesikan et al., 2015). Taken together, these insights underscore the difficulty in disentangling resolution-driven effects and the necessity for robust model evaluation, regardless of the chosen resolution, when assessing OAE outcomes.

## SUPPLEMENTAL MATERIAL

### *Text S1*

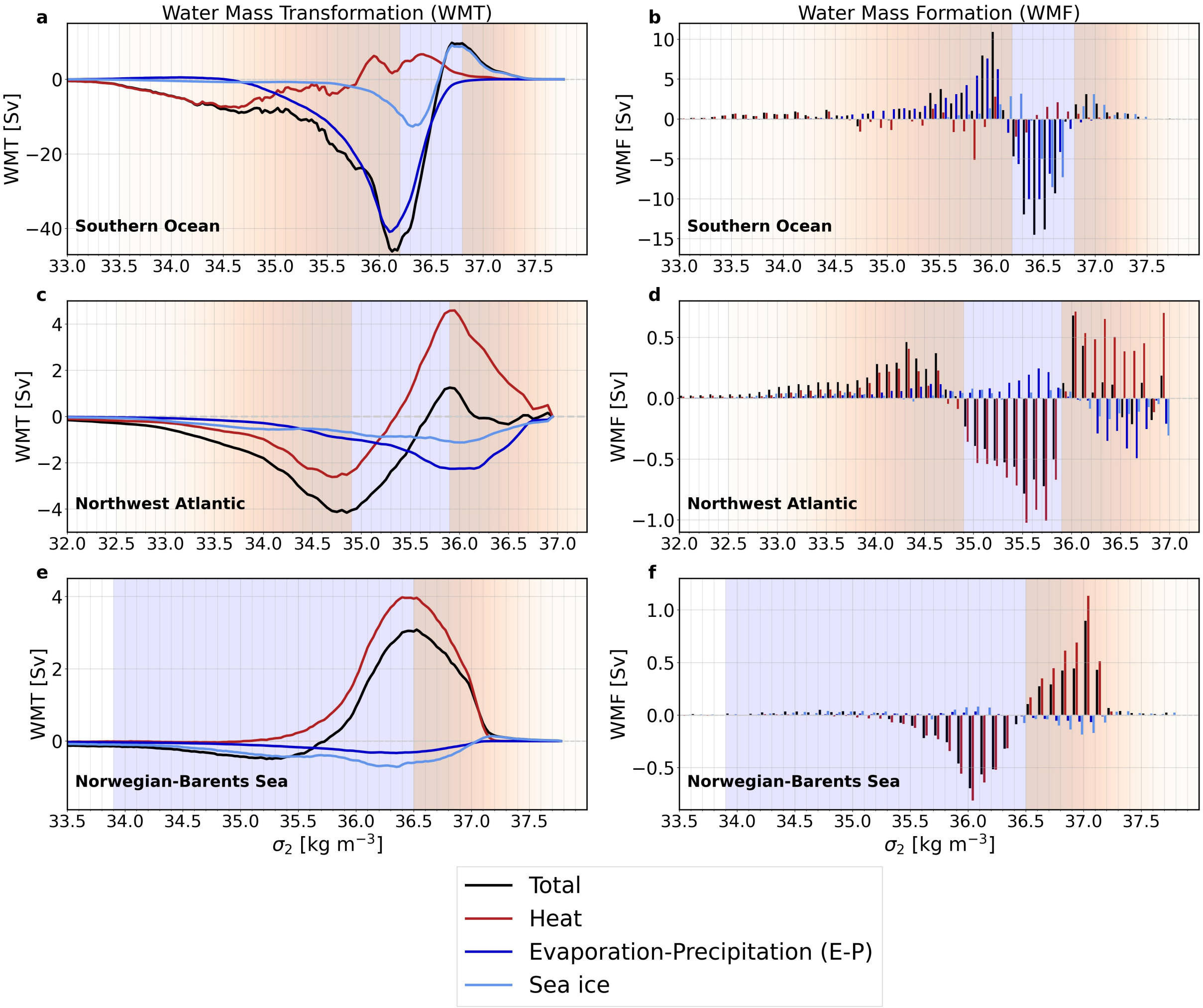

FIGURE S1: Water Mass Transformation (WMT, left) and Water Mass Formation (WMF, right) rates for the subduction regions. **(a,c,e)** The annual mean surface WMT rates (Sv) integrated over 0.025 kg m$^{-3}$ density bins in panel (a) the Southern Ocean, (c) the Northwest Atlantic, and (e) the Norwegian-Barents Sea region as a function of the potential density anomaly $\rho_2$ (kg m$^{-3}$) due to the total buoyancy flux (black), heat flux (red), evaporation minus precipitation (E-P; dark blue), and the sea-ice induced freshwater flux (light blue). The shading marks the density ranges of downwelling (red) and upwelling (blue). **(b,d,f)** The annual mean surface WMF rates (Sv) for the different subduction regions are integrated over 0.1 kg m$^{-3}$ density bins. The total WMF (black bars) results from the contribution of the heat flux (red bars) and the two components of the freshwater flux, that is E-P (dark blue bars) and sea-ice (light blue bars). Positive values represent subduction/downwelling (red shaded regions) and negative values represent upwelling (blue shaded regions).

We relate the monthly surface buoyancy fluxes, i.e., heat flux, freshwater flux decomposed into sea-ice formation and melting and evaporation minus precipitation (E-P), to the surface density distribution to derive Water Mass Transformation (WMT) rates (Nagwekar et al., 2024; Nissen et al., 2022; Figure S1) following the below equation.

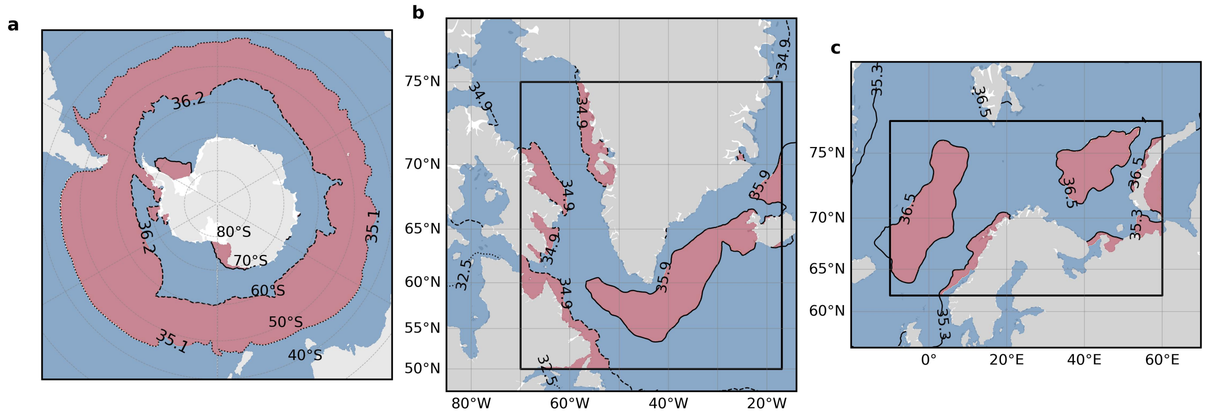

Figure S2: The regional mask for alkalinity deposition, obtained by using the isopycnal outcrops for deep and bottom water formation areas from the water mass formation analysis. **(a)** Southern Ocean, **(b)** Northwest Atlantic, and **(c)** Norwegian-Barents Sea regions. The black boxes for the Northwest Atlantic and the Norwegian-Barents Sea region denote the areas considered for the water mass transformation analysis. For the Southern Ocean, we consider the areas south of 40°S.

$$WMT(\rho_k, t) = -\frac{1}{\rho_{k+1} - \rho_k} \iint_A \frac{\alpha Q_{net}}{\rho_0 C_p} \, dA + \frac{1}{\rho_{k+1} + \rho_k} \iint_A \frac{\beta S F_{net}}{\rho_0} \, dA \quad . \tag{5.1}$$

Here, A is the outcrop area between two consecutive density bins k and k+1, $\rho_0$ is the reference density (35 kg m$^{-3}$) and S is surface salinity. The coefficients $\alpha$, $C_p$ (3994 J kg$^{-1}$ K$^{-1}$), and $\beta$ are the thermal expansion coefficient, heat capacity, and haline contraction, respectively. The values for $\alpha$, $\beta$ and S were calculated as monthly means over the analysis period (1950-2014). $F_{net}$ is decomposed into freshwater fluxes between atmosphere and ocean ($F_{atm \rightarrow ocean}$, evaporation minus precipitation) and between sea ice and ocean ($F_{seaice \rightarrow ocean}$, sea-ice formation or melting):

$$F_{net} = F_{atm \rightarrow ocean} + F_{sea\ ice \rightarrow ocean} \tag{5.2}$$

Water Mass Formation (WMF) rate, is the derivative of WMT with respect to density, and shows where water masses converge (WMF>0; downwelling) or diverge (WMF<0; upwelling) in given density bins (Pellichero et al., 2018). Following Pellichero et al. (2018) and Abernathey et al. (2016), the WMF rates are calculated by integrating over density bins of width 0.1 kg m$^{-3}$ for the subduction regions in the Southern Ocean, Northwest Atlantic and the Norwegian-Barents Sea region. In the Southern Ocean subduction occurs primarily due to sea-ice formation in the density bins >36.8 kg m$^{-3}$ (red shaded region in Figure S1a and S1b). This density range is representative of the Antarctic Bottom Water (AABW) formation in the Weddell and Ross Sea basins (Orsi et al., 1999). The Antarctic Intermediate and Subantarctic Mode Water (AAIW and SAMW) masses are found between 45 and 60°S characterized by the freshwater flux (Cerovečki and Mazloff, 2016; Hartin et al., 2011; Talley, 2008). Accordingly, our model simulations suggest the E-P component of freshwater flux leads to subduction in the density bins between 35.1 and 36.2 kg m$^{-3}$ (Figure S1a and S1b) which represent the AAIW and SAMW formation regions in the Subantarctic (Figure S2a). Buoyancy induced upwelling occurs in between 36.2 and 36.8 kg m$^{-3}$ (blue shaded regions in Figure S1a and S1b). In the North Atlantic the formation of

North Atlantic Deep Water mainly occurs due heat loss (Dickson and Brown, 1994; Våge et al., 2009; Jeansson et al., 2017). Similarly, our model also suggests heat loss to be the main driver of subduction in the Northwest Atlantic in the density bins >35.9 kg $m^{-3}$ and in density bins between 32.5 and 34.9 kg $m^{-3}$ (Figure S1c and S1d). Similarly, in the Norwegian-Barents Sea regions subduction occurs in the density bins >36.5 kg $m^{-3}$ and in the density bins between 33.9 and 35.3 kg $m^{-3}$ primarily due to heat loss (Figure S1e and S1f). The density thresholds obtained from the WMF analysis are then used to locate the subduction regions in the Southern Ocean, Northwest Atlantic and Norwegian-Barents Sea regions (Figures S2a, S2b and S2c).

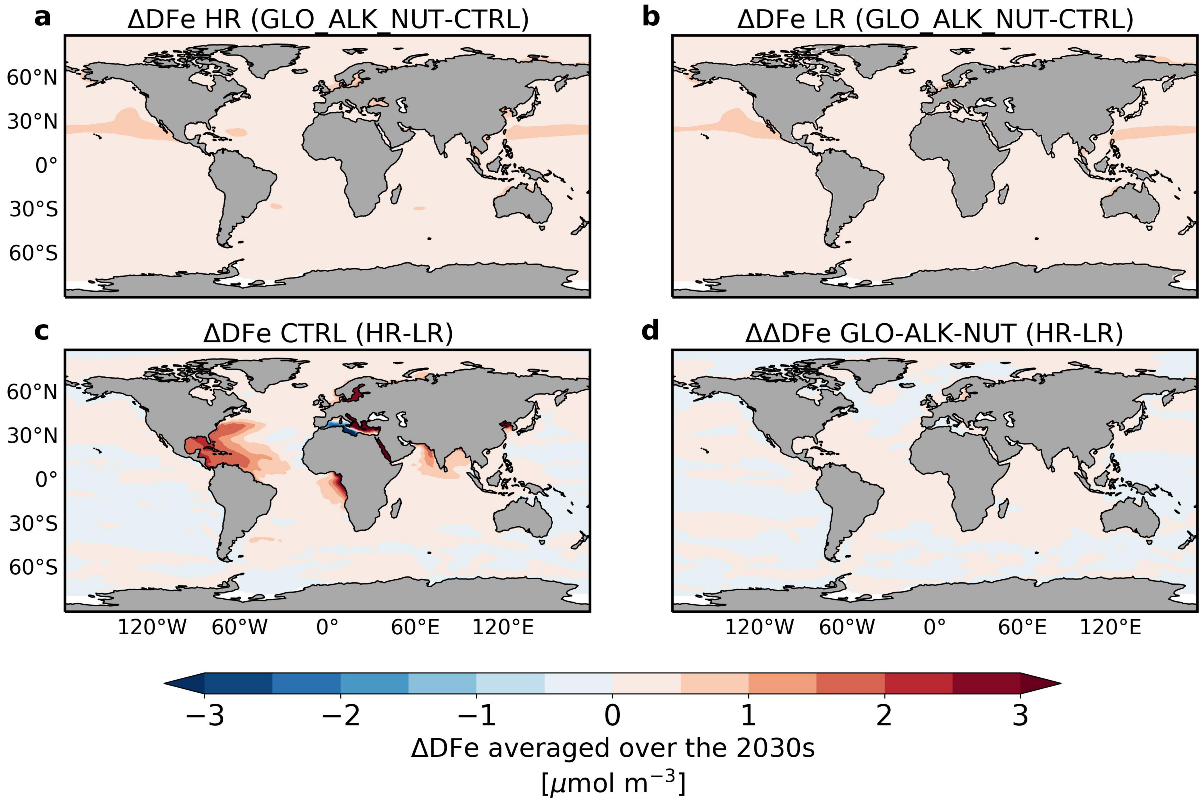

Figure S3: Spatial maps for differences in dissolved iron (ΔDFe) between different simulations. All maps are calculated as an average over the 2030s. **(a,b)** Differences between GLO-ALK-NUT and their respective CTRL (ΔDFe) and differences between the high-resolution and low-resolution simulations for **(c)** the control simulations, and **(d)** increase in DFe (ΔDFe).

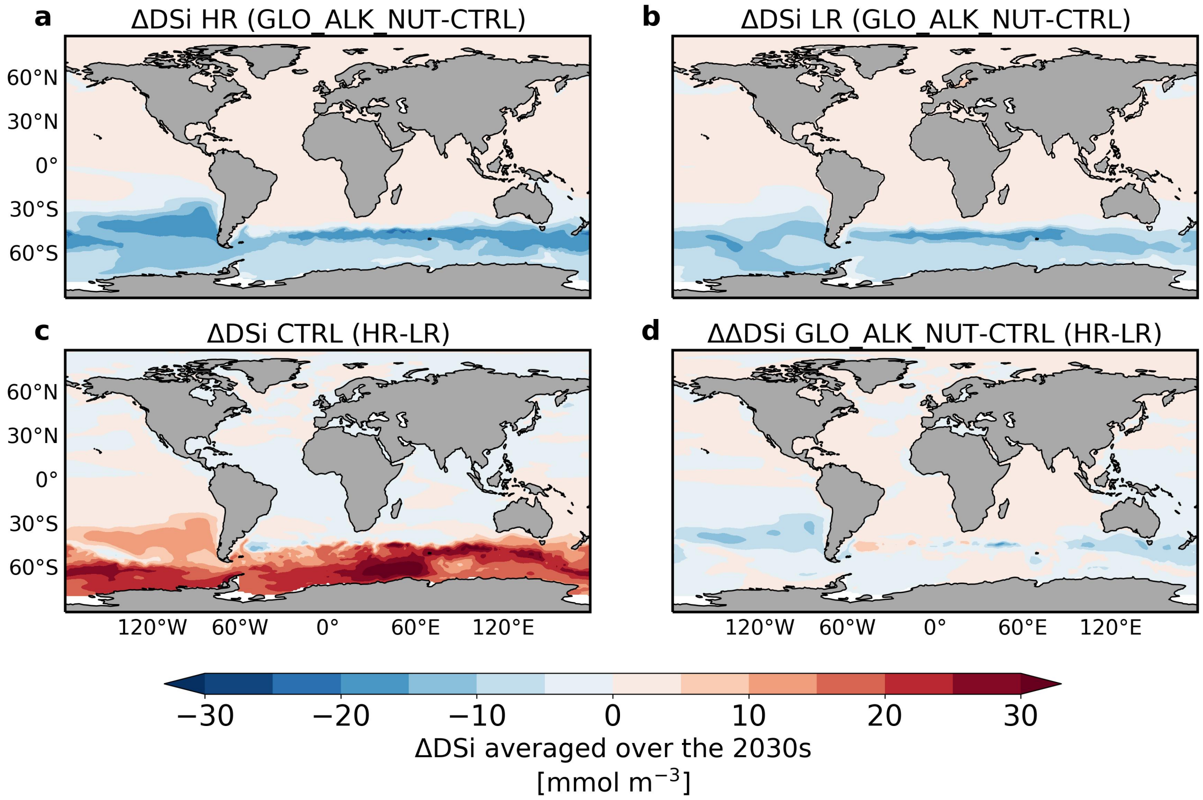

FIGURE S4: Spatial maps for differences in dissolved iron (ΔDSi) between different simulations. All maps are calculated as an average over the 2030s. **(a,b)** Differences between GLO-ALK-NUT and their respective CTRL (ΔDSi) and differences between the high-resolution and low-resolution simulations for **(c)** the control simulations, and **(d)** increase in DSi (ΔDSi).

| **Parameters** | **Correlation Coefficient** | |
|---|---|---|
| | **High-resolution** | **Low-resolution** |
| Alkalinity (top 100 m) with GLODAP | 0.94 | 0.97 |
| DIC (top 100 m) with GLODAP | 0.94 | 0.97 |
| Air-sea $CO_2$ flux with Chau et al., 2020 | 0.72 | 0.58 |
| DSi (top 100 m) with WOA | 0.69 | 0.84 |

TABLE 5.2: Correlation coefficients for Alkalinity, dissolved inorganic carbon (DIC), air-sea $CO_2$ flux and DSi in the high-resolution and low-resolution models with the observational datasets. All the correlation coefficients are calculated over the period 2000 to 2009.

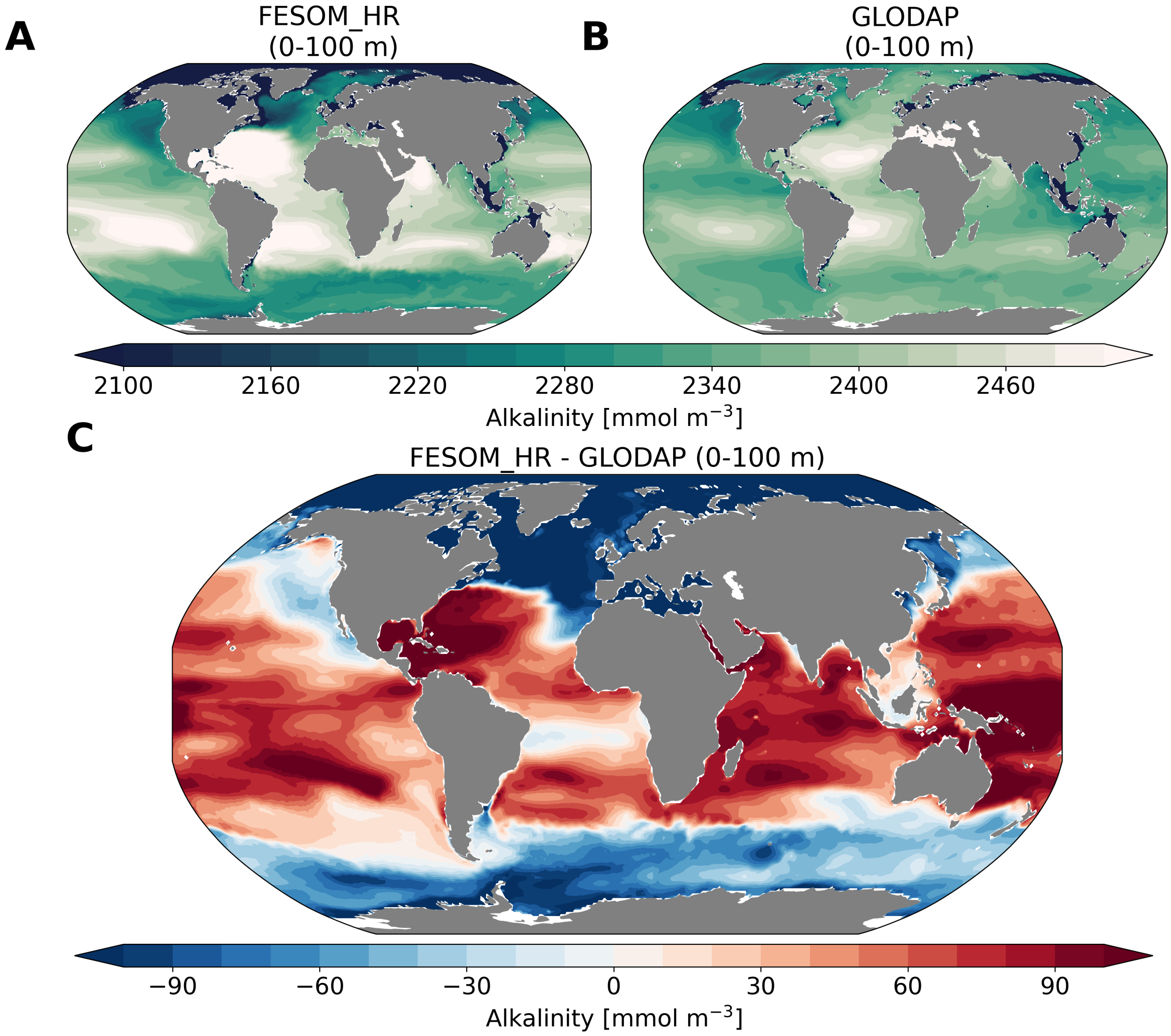

FIGURE S5: Evaluation of alkalinity concentration [mmol m$^{-3}$] in top 100 m against the GLODAP data over the period 2000 to 2009 on the high-resolution (HR) setup. **(A)** Alkalinity in the HR setup, **(B)** Alkalinity from GLODAP, and **(C)** Alkalinity anomaly between HR setup and GLODAP.

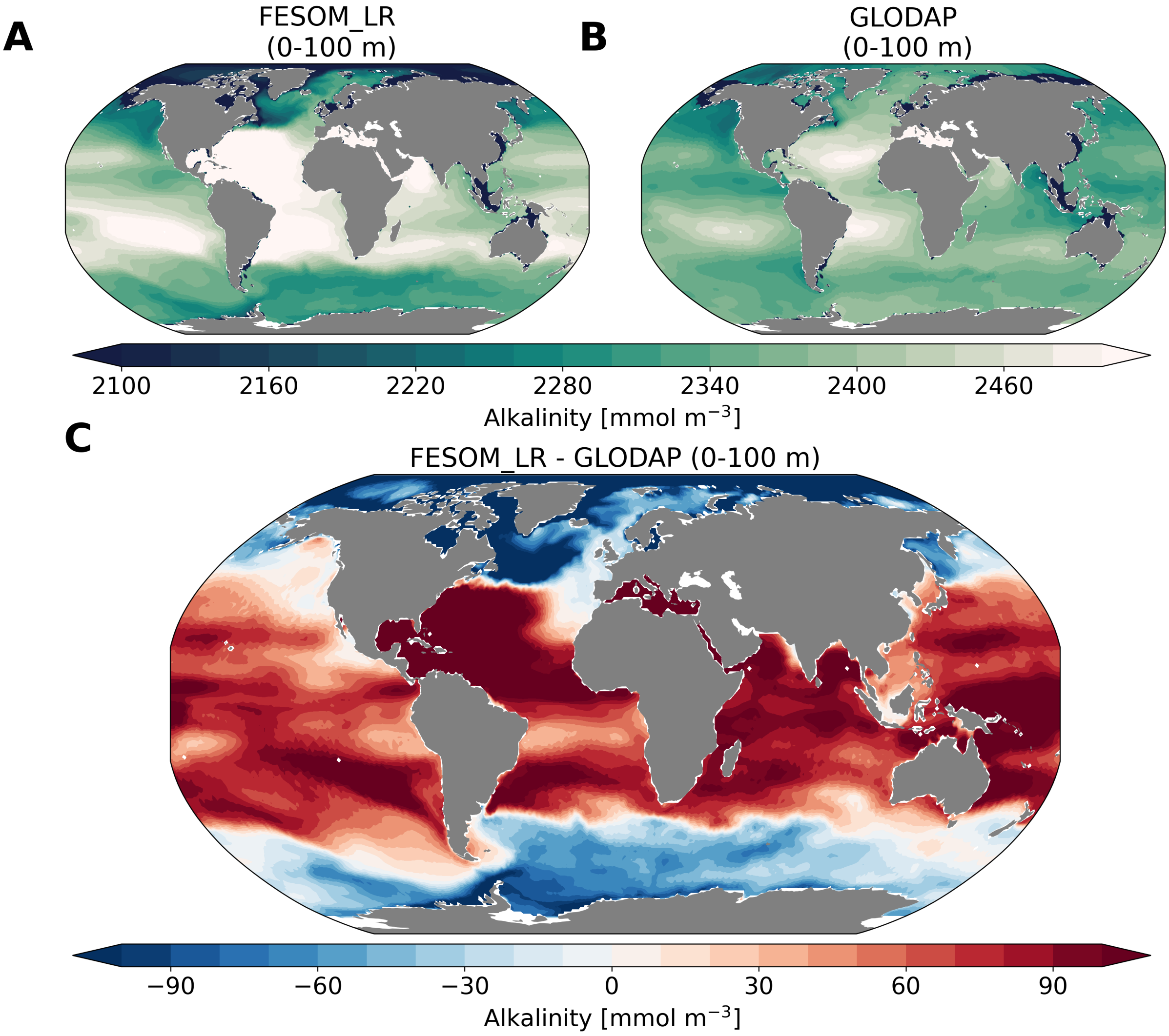

Figure S6: Evaluation of alkalinity concentration [mmol m$^{-3}$] in top 100 m against the GLODAP data over the period 2000 to 2009 on the low-resolution (LR) setup. **(A)** Alkalinity in the LR setup, **(B)** Alkalinity from GLODAP, and **(C)** Alkalinity anomaly between LR setup and GLODAP.

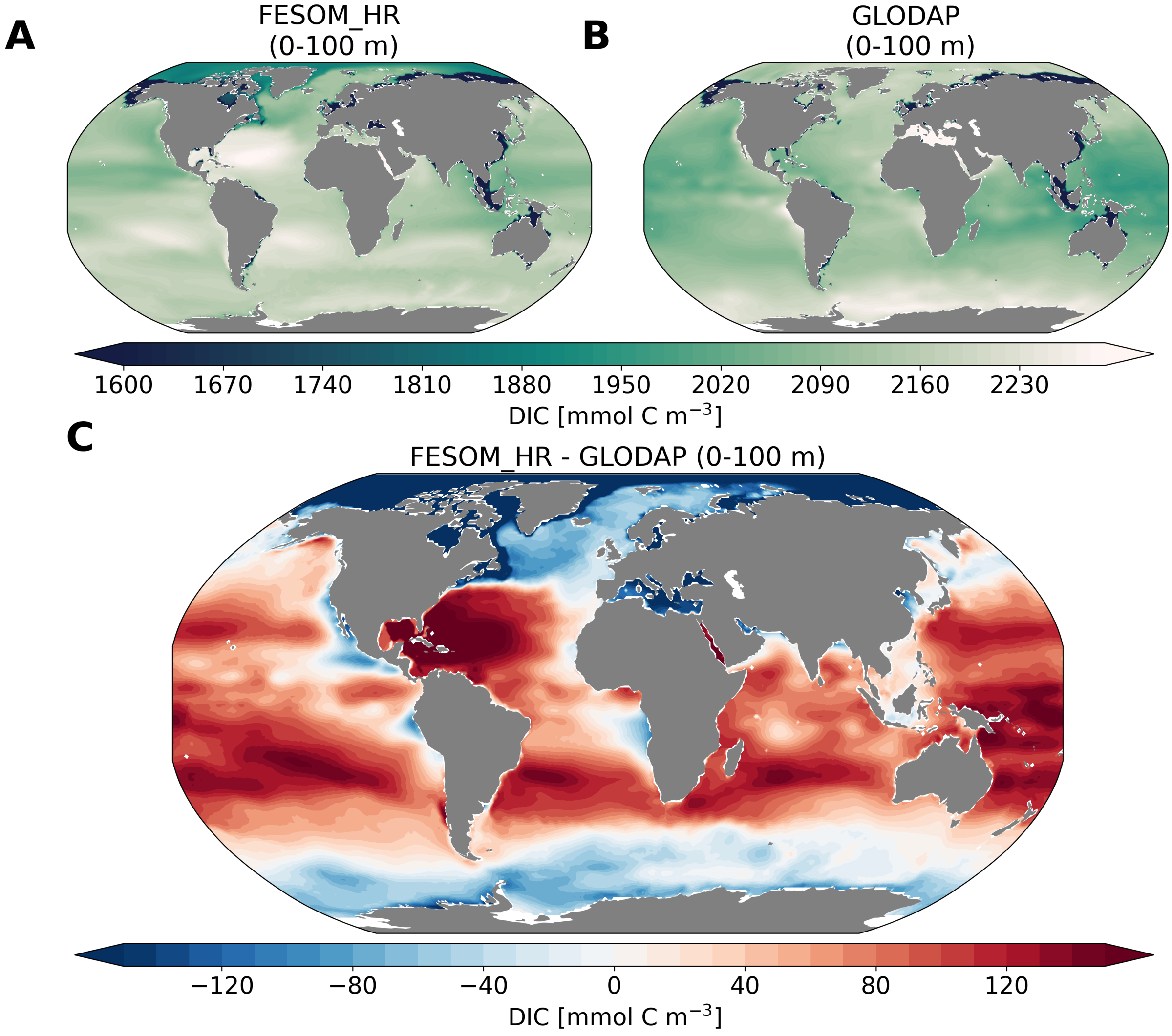

Figure S7: Evaluation of dissolved inorganic carbon (DIC) concentration [mmol m$^{-3}$] in top 100 m against the GLODAP data over the period 2000 to 2009 on the high-resolution (HR) setup. **(A)** DIC in the HR setup, **(B)** DIC from GLODAP, and **(C)** DIC anomaly between HR setup and GLODAP.

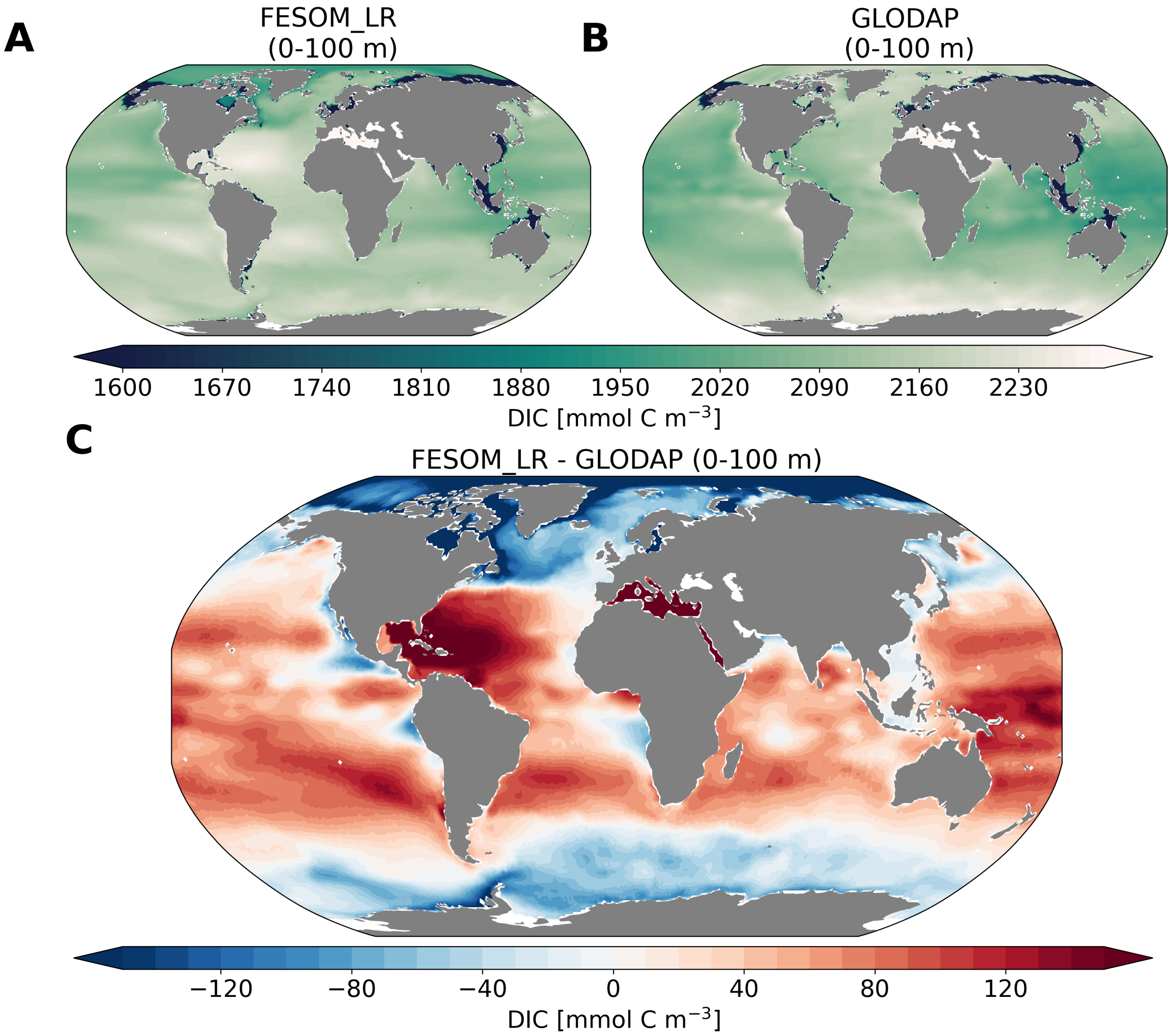

Figure S8: Evaluation of dissolved inorganic carbon (DIC) concentration [mmol m$^{-3}$] in top 100 m against the GLODAP data over the period 2000 to 2009 on the low-resolution (LR) setup. **(A)** DIC in the LR setup, **(B)** DIC from GLODAP, and **(C)** DIC anomaly between LR setup and GLODAP.

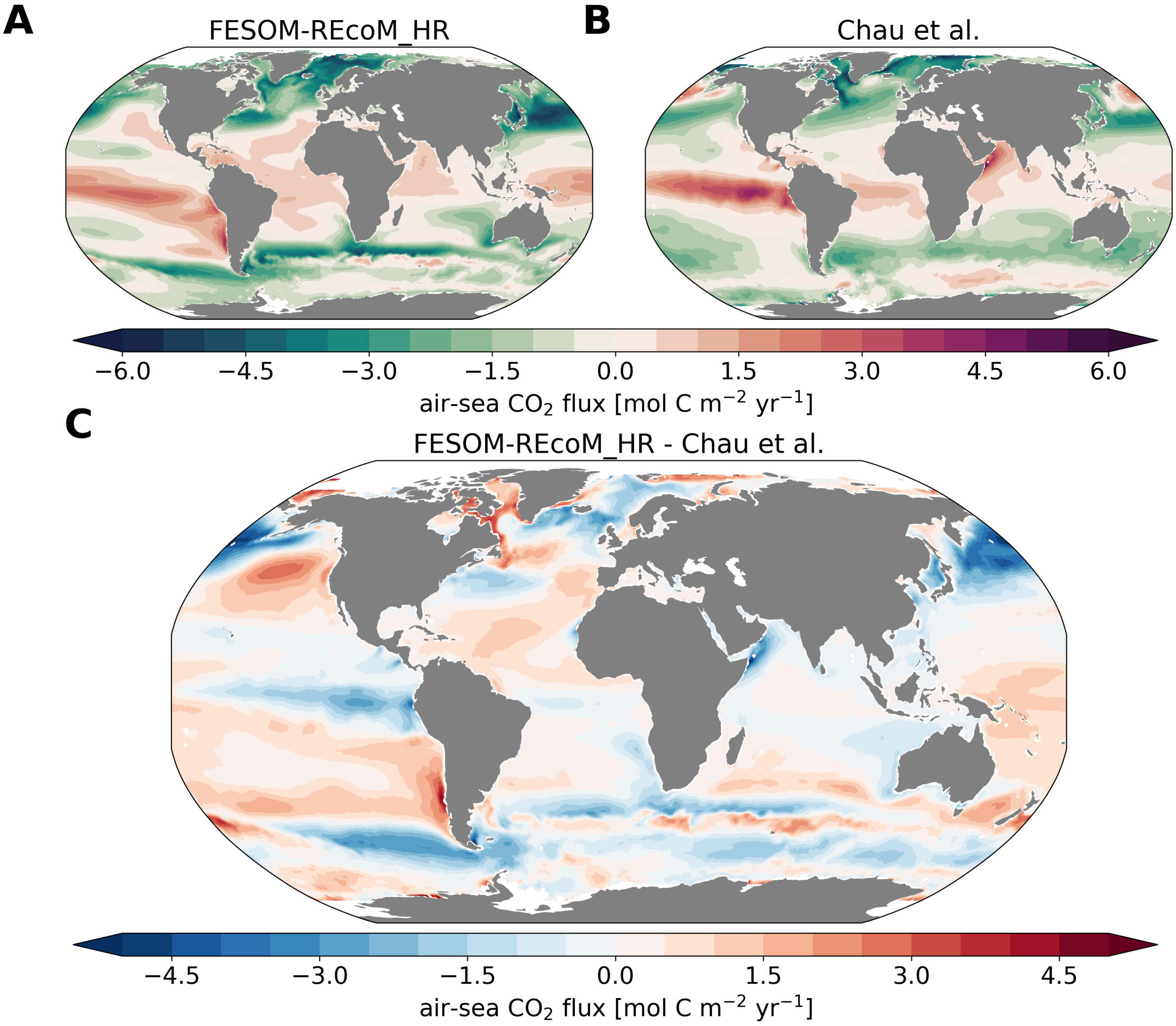

FIGURE S9: Evaluation of air-sea $CO_2$ flux [molC $m^{-2}$ $yr^{-1}$] against Chau et al. (2020) over the period 2000 to 2009 on the high-resolution (HR) setup. **(A)** Air-sea $CO_2$ flux in the HR setup, **(B)** Air-sea $CO_2$ flux from Chau et al. (2020), and **(C)** Air-sea $CO_2$ flux anomaly between HR setup and Chau et al. (2020). Negative values mean flux into the ocean.

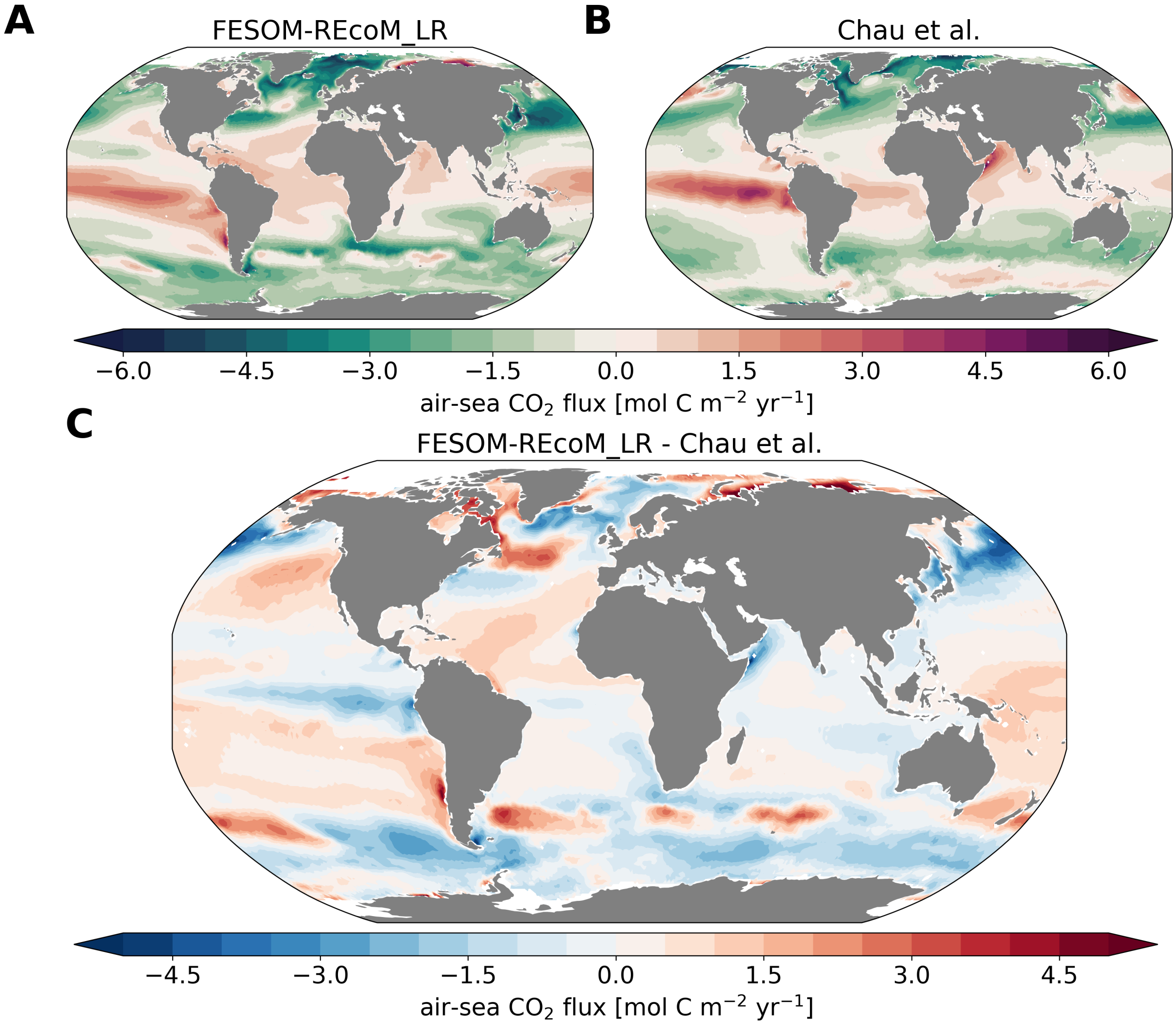

Figure S10: Evaluation of air-sea CO$_2$ flux [molC m$^{-2}$ yr$^{-1}$] against Chau et al. (2020) over the period 2000 to 2009 on the low-resolution (LR) setup. **(A)** Air-sea CO$_2$ flux in the LR setup, **(B)** Air-sea CO$_2$ flux from Chau et al. (2020), and **(C)** Air-sea CO$_2$ flux anomaly between LR setup and Chau et al. (2020). Negative values mean flux into the ocean.

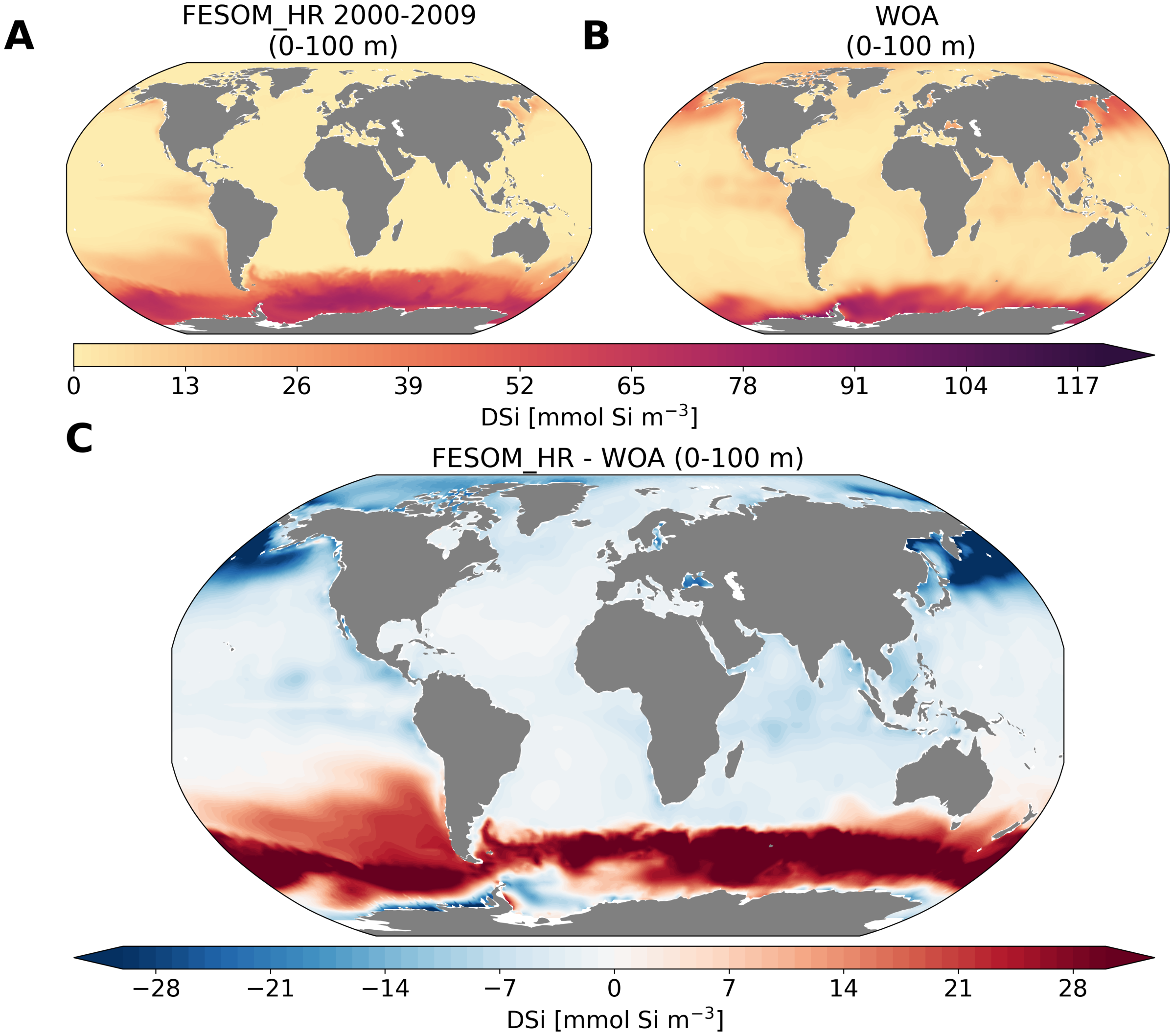

FIGURE S11: Evaluation of dissolved silicate (DSi) concentration [mmol Si $m^{-3}$] in top 100 m against the World Ocean Atlans (WOA) over the period 2000 to 2009 on the high-resolution (HR) setup. **(A)** DSi in the HR setup, **(B)** DSi in WOA, and **(C)** DSi anomaly between HR setup and WOA.

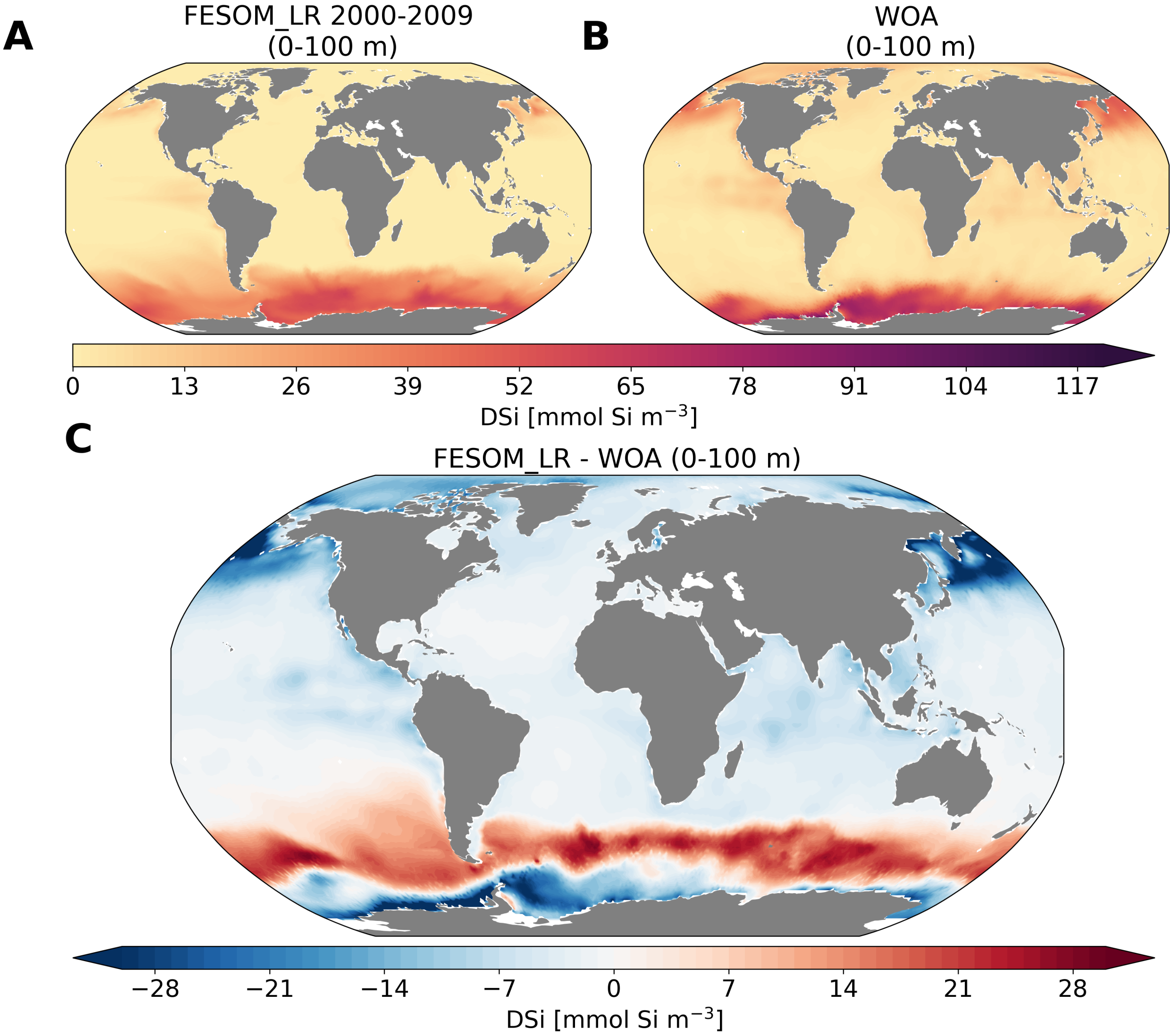

FIGURE S12: Evaluation of dissolved silicate (DSi) concentration [mmol Si m$^{-3}$] in top 100 m against the World Ocean Atlans (WOA) over the period 2000 to 2009 on the low-resolution (LR) setup. **(A)** DSi in the LR setup, **(B)** DSi in WOA, and **(C)** DSi anomaly between LR setup and WOA.

# BIBLIOGRAPHY

Abernathey, R. P., Cerovecki, I., Holland, P. R., Newsom, E., Mazloff, M., and Talley, L. D. (2016). "Water-mass transformation by sea ice in the upper branch of the Southern Ocean overturning". In: *Nature Geoscience* 9.8, pp. 596–601. ISSN: 1752-0894, 1752-0908. DOI: `10.1038/ngeo2749`.

Archer, D. (2005). "Fate of fossil fuel CO2 in geologic time". In: *Journal of Geophysical Research: Oceans* 110 (C9). ISSN: 2156-2202. DOI: `10.1029/2004JC002625`.

Bach, L. T., Gill, S. J., Rickaby, R. E. M., Gore, S., and Renforth, P. (2019). "CO2 Removal With Enhanced Weathering and Ocean Alkalinity Enhancement: Potential Risks and Co-benefits for Marine Pelagic Ecosystems". In: *Frontiers in Climate* 1. ISSN: 2624-9553. DOI: `10.3389/fclim.2019.00007`.

Bach, L. T., Ho, D. T., Boyd, P. W., and Tyka, M. D. (2023). "Toward a consensus framework to evaluate air–sea CO2 equilibration for marine CO2 removal". In: *Limnology and Oceanography Letters* 8.5, pp. 685–691. ISSN: 2378-2242. DOI: `10.1002/lol2.10330`.

Beech, N., Rackow, T., Semmler, T., Danilov, S., Wang, Q., and Jung, T. (2022). "Long-term evolution of ocean eddy activity in a warming world". In: *Nature Climate Change* 12.10, pp. 910–917. ISSN: 1758-6798. DOI: `10.1038/s41558-022-01478-3`.

Beech, N., Rackow, T., Semmler, T., and Jung, T. (2024). "Exploring the ocean mesoscale at reduced computational cost with FESOM 2.5: efficient modeling strategies applied to the Southern Ocean". In: *Geoscientific Model Development* 17.2, pp. 529–543. ISSN: 1991-959X. DOI: `10.5194/gmd-17-529-2024`.

Burt, D. J., Fröb, F., and Ilyina, T. (2021). "The Sensitivity of the Marine Carbonate System to Regional Ocean Alkalinity Enhancement". In: *Frontiers in Climate* 3. ISSN: 2624-9553. URL: `https://www.frontiersin.org/articles/10.3389/fclim.2021.624075`.

Butenschön, M., Lovato, T., Masina, S., Caserini, S., and Grosso, M. (2021). "Alkalinization Scenarios in the Mediterranean Sea for Efficient Removal of Atmospheric CO2 and the Mitigation of Ocean Acidification". In: *Frontiers in Climate* 3. ISSN: 2624-9553. URL: `https://www.frontiersin.org/articles/10.3389/fclim.2021.614537`.

Cerovečki, I. and Mazloff, M. R. (2016). "The Spatiotemporal Structure of Diabatic Processes Governing the Evolution of Subantarctic Mode Water in the Southern Ocean". In: *Journal of Physical Oceanography* 46.2, pp. 683–710. ISSN: 0022-3670, 1520-0485. DOI: `10.1175/JPO-D-14-0243.1`.

Chelton, D. B., Schlax, M. G., and Samelson, R. M. (2011). “Global observations of nonlinear mesoscale eddies”. In: *Progress in Oceanography* 91.2, pp. 167–216. ISSN: 0079-6611. DOI: `10.1016/j.pocean.2011.01.002`.

Chen, H., Haumann, F. A., Talley, L. D., Johnson, K. S., and Sarmiento, J. L. (2022). “The Deep Ocean’s Carbon Exhaust”. In: *Global Biogeochemical Cycles* 36.7, e2021GB007156. DOI: `https://doi.org/10.1029/2021GB007156`.

DeVries, T., Yamamoto, K., Wanninkhof, R., Gruber, N., Hauck, J., Müller, J. D., Bopp, L., Carroll, D., Carter, B., Chau, T.-T.-T., Doney, S. C., Gehlen, M., Gloege, L., Gregor, L., Henson, S., et al. (2023). “Magnitude, Trends, and Variability of the Global Ocean Carbon Sink From 1985 to 2018”. In: *Global Biogeochemical Cycles* 37.10, e2023GB007780. ISSN: 1944-9224. DOI: `10.1029/2023GB007780`.

Dickson, R. R. and Brown, J. (1994). “The production of North Atlantic Deep Water: Sources, rates, and pathways”. In: *Journal of Geophysical Research: Oceans* 99 (C6), pp. 12319–12341. ISSN: 2156-2202. DOI: `10.1029/94JC00530`.

Dufour, C. O., Griffies, S. M., Souza, G. F. d., Frenger, I., Morrison, A. K., Palter, J. B., Sarmiento, J. L., Galbraith, E. D., Dunne, J. P., Anderson, W. G., and Slater, R. D. (2015). “Role of Mesoscale Eddies in Cross-Frontal Transport of Heat and Biogeochemical Tracers in the Southern Ocean”. In: DOI: `10.1175/JPO-D-14-0240.1`.

Eisaman, M. D., Geilert, S., Renforth, P., Bastianini, L., Campbell, J., Dale, A. W., Foteinis, S., Grasse, P., Hawrot, O., Löscher, C. R., Rau, G. H., and Rønning, J. (2023). “Assessing the technical aspects of ocean-alkalinity-enhancement approaches”. In: *State of the Planet* 2-oae2023, pp. 1–29. DOI: `10.5194/sp-2-oae2023-3-2023`.

Fennel, K., Long, M. C., Algar, C., Carter, B., Keller, D., Laurent, A., Mattern, J. P., Musgrave, R., Oschlies, A., Ostiguy, J., Palter, J. B., and Whitt, D. B. (2023). “Modelling considerations for research on ocean alkalinity enhancement (OAE)”. In: *State of the Planet* 2-oae2023, pp. 1–29. DOI: `10.5194/sp-2-oae2023-9-2023`.

Ford, D. J., Tilstone, G. H., Shutler, J. D., Kitidis, V., Sheen, K. L., Dall’Olmo, G., and Orselli, I. B. M. (2023). “Mesoscale Eddies Enhance the Air-Sea CO2 Sink in the South Atlantic Ocean”. In: *Geophysical Research Letters* 50.9, e2022GL102137. ISSN: 1944-8007. DOI: `10.1029/2022GL102137`.

Friedlingstein, P., O’Sullivan, M., Jones, M. W., Andrew, R. M., Hauck, J., Landschützer, P., Le Quéré, C., Li, H., Luijkx, I. T., Olsen, A., Peters, G. P., Peters, W., Pongratz, J., Schwingshackl, C., Sitch, S., et al. (2024). “Global Carbon Budget 2024”. In: *Earth System Science Data Discussions*, pp. 1–133. DOI: `10.5194/essd-2024-519`.

Fuss, S., Lamb, W. F., Callaghan, M. W., Hilaire, J., Creutzig, F., Amann, T., Beringer, T., Garcia, W. d. O., Hartmann, J., Khanna, T., Luderer, G., Nemet, G. F., Rogelj, J., Smith, P., Vicente, J. L. V., et al. (2018). “Negative emissions—Part 2: Costs, potentials and side effects”.

In: *Environmental Research Letters* 13.6, p. 063002. ISSN: 1748-9326. DOI: `10.1088/1748-9326/aabf9f`.

Gattuso, J.-P., Williamson, P., Duarte, C. M., and Magnan, A. K. (2021). “The Potential for Ocean-Based Climate Action: Negative Emissions Technologies and Beyond”. In: *Frontiers in Climate* 2. ISSN: 2624-9553. DOI: `10.3389/fclim.2020.575716`.

Gnanadesikan, A., Pradal, M.-A., and Abernathey, R. (2015). “Isopycnal mixing by mesoscale eddies significantly impacts oceanic anthropogenic carbon uptake”. In: *Geophysical Research Letters* 42.11, pp. 4249–4255. ISSN: 1944-8007. DOI: `10.1002/2015GL064100`.

Gruber, N., Clement, D., Carter, B. R., Feely, R. A., Heuven, S. van, Hoppema, M., Ishii, M., Key, R. M., Kozyr, A., Lauvset, S. K., Lo Monaco, C., Mathis, J. T., Murata, A., Olsen, A., Perez, F. F., et al. (2019). “The oceanic sink for anthropogenic CO $_2$ from 1994 to 2007”. In: *Science* 363.6432, pp. 1193–1199. ISSN: 0036-8075, 1095-9203. DOI: `10.1126/science.aau5153`.

Gruber, N., Gloor, M., Mikaloff Fletcher, S. E., Doney, S. C., Dutkiewicz, S., Follows, M. J., Gerber, M., Jacobson, A. R., Joos, F., Lindsay, K., Menemenlis, D., Mouchet, A., Müller, S. A., Sarmiento, J. L., and Takahashi, T. (2009). “Oceanic sources, sinks, and transport of atmospheric CO2”. In: *Global Biogeochemical Cycles* 23.1. ISSN: 1944-9224. DOI: `10.1029/2008GB003349`.

Guo, Y. and Timmermans, M.-L. (2024). “The Role of Ocean Mesoscale Variability in Air-Sea CO2 Exchange: A Global Perspective”. In: *Geophysical Research Letters* 51.10, e2024GL108373. ISSN: 1944-8007. DOI: `10.1029/2024GL108373`.

Gürses, Ö., Oziel, L., Karakuş, O., Sidorenko, D., Völker, C., Ye, Y., Zeising, M., Butzin, M., and Hauck, J. (2023). “Ocean biogeochemistry in the coupled ocean–sea ice–biogeochemistry model FESOM2.1–REcoM3”. In: *Geoscientific Model Development* 16.16, pp. 4883–4936. ISSN: 1991-959X. DOI: `10.5194/gmd-16-4883-2023`.

Harrison, C. S., Long, M. C., Lovenduski, N. S., and Moore, J. K. (2018). “Mesoscale Effects on Carbon Export: A Global Perspective”. In: *Global Biogeochemical Cycles* 32.4, pp. 680–703. DOI: `https://doi.org/10.1002/2017GB005751`.

Hartin, C. A., Fine, R. A., Sloyan, B. M., Talley, L. D., Chereskin, T. K., and Happell, J. (2011). “Formation rates of Subantarctic mode water and Antarctic intermediate water within the South Pacific”. In: *Deep Sea Research Part I: Oceanographic Research Papers* 58.5, pp. 524–534. ISSN: 0967-0637. DOI: `10.1016/j.dsr.2011.02.010`.

Hartmann, J., West, A. J., Renforth, P., Köhler, P., De La Rocha, C. L., Wolf-Gladrow, D. A., Dürr, H. H., and Scheffran, J. (2013). “Enhanced chemical weathering as a geoengineering strategy to reduce atmospheric carbon dioxide, supply nutrients, and mitigate ocean acidification: ENHANCED WEATHERING”. In: *Reviews of Geophysics* 51.2, pp. 113–149. ISSN: 87551209. DOI: `10.1002/rog.20004`.

Hauck, J., Köhler, P., Wolf-Gladrow, D., and Völker, C. (2016). "Iron fertilisation and century-scale effects of open ocean dissolution of olivine in a simulated $CO_2$ removal experiment". In: *Environmental Research Letters* 11.2, p. 024007. ISSN: 1748-9326. DOI: `10.1088/1748-9326/11/2/024007`.

He, J. and Tyka, M. D. (2023). "Limits and $CO_2$ equilibration of near-coast alkalinity enhancement". In: *Biogeosciences* 20.1, pp. 27–43. ISSN: 1726-4170. DOI: `10.5194/bg-20-27-2023`.

Ho, D. T. and Bopp, L. (2024). "Marine carbon dioxide removal may be a future climate solution". In: *Dialogues on Climate Change* 1.1, pp. 56–62. ISSN: 2976-8659. DOI: `10.1177/29768659241293223`.

Ho, D. T., Bopp, L., Palter, J. B., Long, M. C., Boyd, P. W., Neukermans, G., and Bach, L. T. (2023). "Monitoring, reporting, and verification for ocean alkalinity enhancement". In: *State of the Planet* 2-oae2023, pp. 1–12. DOI: `10.5194/sp-2-oae2023-12-2023`. URL: `https://sp.copernicus.org/articles/2-oae2023/12/2023/`.

Hohn, S. (2008). "Coupling and decoupling of biogeochemical cycles in marine ecosystems". In.

IPCC (2018). "Annex I: Glossary [Matthews, J.B.R. (ed.)]. Global Warming of 1.5°C. An IPCC Special Report on the impacts of global warming of 1.5°C above pre-industrial levels and related global greenhouse gas emission pathways, in the context of strengthening the global response to the threat of climate change, sustainable development, and efforts to eradicate poverty [Masson-Delmotte, V., P. Zhai, H.-O. Pörtner, D. Roberts, J. Skea, P.R. Shukla, A. Pirani, W. Moufouma-Okia, C. Péan, R. Pidcock, S. Connors, J.B.R. Matthews, Y. Chen, X. Zhou, M.I. Gomis, E. Lonnoy, T. Maycock, M. Tignor, and T. Waterfield (eds.)]." In: pp. 541–562. DOI: `10.1017/9781009157940.008`.

– (2023). *Climate Change 2023: Synthesis Report. Contribution of Working Groups I, II and III to the Sixth Assessment Report of the Intergovernmental Panel on Climate Change*. Ed. by C. W. Team, H. Lee, and J. Romero. Geneva, Switzerland: IPCC, p. 184. DOI: `10.59327/IPCC/AR6-9789291691647`.

Jeansson, E., Olsen, A., and Jutterström, S. (2017). "Arctic Intermediate Water in the Nordic Seas, 1991–2009". In: *Deep Sea Research Part I: Oceanographic Research Papers* 128, pp. 82–97. ISSN: 0967-0637. DOI: `10.1016/j.dsr.2017.08.013`.

Jeansson, E., Tanhua, T., Olsen, A., Smethie Jr., W. M., Rajasakaren, B., Ólafsdóttir, S. R., and Ólafsson, J. (2023). "Decadal Changes in Ventilation and Anthropogenic Carbon in the Nordic Seas". In: *Journal of Geophysical Research: Oceans* 128.3, e2022JC019318. ISSN: 2169-9291. DOI: `10.1029/2022JC019318`.

Karakuş, O., Völker, C., Iversen, M., Hagen, W., Wolf-Gladrow, D., Fach, B., and Hauck, J. (2021). "Modeling the Impact of Macrozooplankton on Carbon Export Production in the Southern Ocean". In: *Journal of Geophysical Research: Oceans* 126.12. ISSN: 2169-9275, 2169-9291. DOI: `10.1029/2021JC017315`.

Keller, D. P., Feng, E. Y., and Oschlies, A. (2014). “Potential climate engineering effectiveness and side effects during a high carbon dioxide-emission scenario”. In: *Nature Communications* 5.1, p. 3304. ISSN: 2041-1723. DOI: `10.1038/ncomms4304`.

Keppler, L., Eddebbar, Y. A., Gille, S. T., Guisewhite, N., Mazloff, M. R., Tamsitt, V., Verdy, A., and Talley, L. D. (2024). “Effects of Mesoscale Eddies on Southern Ocean Biogeochemistry”. In: *AGU Advances* 5.6, e2024AV001355. ISSN: 2576-604X. DOI: `10.1029/2024AV001355`.

Khatiwala, S., Primeau, F., and Hall, T. (2009). “Reconstruction of the history of anthropogenic CO2 concentrations in the ocean”. In: *Nature* 462.7271, pp. 346–349. ISSN: 1476-4687. DOI: `10.1038/nature08526`.

Köhler, P., Abrams, J. F., Völker, C., Hauck, J., and Wolf-Gladrow, D. A. (2013). “Geoengineering impact of open ocean dissolution of olivine on atmospheric CO $_2$ , surface ocean pH and marine biology”. In: *Environmental Research Letters* 8.1, p. 014009. ISSN: 1748-9326. DOI: `10.1088/1748-9326/8/1/014009`.

Koldunov, N. V., Aizinger, V., Rakowsky, N., Scholz, P., Sidorenko, D., Danilov, S., and Jung, T. (2019). “Scalability and some optimization of the Finite-volumE Sea ice–Ocean Model, Version 2.0 (FESOM2)”. In: *Geoscientific Model Development* 12.9, pp. 3991–4012. ISSN: 1991-9603. DOI: `10.5194/gmd-12-3991-2019`.

Langlais, C. E., Lenton, A., Matear, R., Monselesan, D., Legresy, B., Cougnon, E., and Rintoul, S. (2017). “Stationary Rossby waves dominate subduction of anthropogenic carbon in the Southern Ocean”. In: *Scientific Reports* 7.1, p. 17076. ISSN: 2045-2322. DOI: `10.1038/s41598-017-17292-3`.

Lenton, A., Matear, R. J., Keller, D. P., Scott, V., and Vaughan, N. E. (2018). “Assessing carbon dioxide removal through global and regional ocean alkalinization under high and low emission pathways”. In: *Earth System Dynamics* 9.2, pp. 339–357. ISSN: 2190-4987. DOI: `10.5194/esd-9-339-2018`.

Lévy, M., Iovino, D., Resplandy, L., Klein, P., Madec, G., Tréguier, A.-M., Masson, S., and Takahashi, K. (2012). “Large-scale impacts of submesoscale dynamics on phytoplankton: Local and remote effects”. In: *Ocean Modelling* 43-44, pp. 77–93. ISSN: 1463-5003. DOI: `https://doi.org/10.1016/j.ocemod.2011.12.003`.

Lévy, M., Klein, P., and Treguier, A.-M. (2001). “Impact of sub-mesoscale physics on production and subduction of phytoplankton in an oligotrophic regime”. In: *Journal of Marine Research* 59.4. URL: `https://elischolar.library.yale.edu/journal_of_marine_research/2401`.

Mahadevan, A. and Archer, D. (2000). “Modeling the impact of fronts and mesoscale circulation on the nutrient supply and biogeochemistry of the upper ocean”. In: *Journal of Geophysical Research: Oceans* 105 (C1), pp. 1209–1225. ISSN: 2156-2202. DOI: `10.1029/1999JC900216`.

Matear, R. J. (2001). "Effects of numerical advection schemes and eddy parameterizations on ocean ventilation and oceanic anthropogenic CO2 uptake". In: *Ocean Modelling* 3.3, pp. 217–248. ISSN: 1463-5003. DOI: `10.1016/S1463-5003(01)00010-5`.

Meredith, M. P. and Hogg, A. M. (2006). "Circumpolar response of Southern Ocean eddy activity to a change in the Southern Annular Mode". In: *Geophysical Research Letters* 33.16. ISSN: 1944-8007. DOI: `10.1029/2006GL026499`.

Middelburg, J. J., Soetaert, K., and Hagens, M. (2020). "Ocean Alkalinity, Buffering and Biogeochemical Processes". In: *Reviews of Geophysics* 58.3, e2019RG000681. ISSN: 1944-9208. DOI: `10.1029/2019RG000681`.

Nagwekar, T., Nissen, C., and Hauck, J. (2024). "Ocean Alkalinity Enhancement in Deep Water Formation Regions Under Low and High Emission Pathways". In: *Earth's Future* 12.10, e2023EF004213. ISSN: 2328-4277. DOI: `10.1029/2023EF004213`.

Nissen, C., Timmermann, R., Hoppema, M., Gürses, Ö., and Hauck, J. (2022). "Abruptly attenuated carbon sequestration with Weddell Sea dense waters by 2100". In: *Nature Communications* 13.1, p. 3402. ISSN: 2041-1723. DOI: `10.1038/s41467-022-30671-3`.

O'Neill, B. C., Tebaldi, C., Vuuren, D. P. van, Eyring, V., Friedlingstein, P., Hurtt, G., Knutti, R., Kriegler, E., Lamarque, J.-F., Lowe, J., Meehl, G. A., Moss, R., Riahi, K., and Sanderson, B. M. (2016). "The Scenario Model Intercomparison Project (ScenarioMIP) for CMIP6". In: *Geoscientific Model Development* 9.9, pp. 3461–3482. ISSN: 1991-959X. DOI: `10.5194/gmd-9-3461-2016`.

Orr, J. C. and Epitalon, J.-M. (2015). "Improved routines to model the ocean carbonate system: mocsy 2.0". In: *Geoscientific Model Development* 8.3, pp. 485–499. ISSN: 1991-959X. DOI: `10.5194/gmd-8-485-2015`. URL: `https://gmd.copernicus.org/articles/8/485/2015/`.

Orsi, A., Johnson, G., and Bullister, J. (1999). "Circulation, mixing, and production of Antarctic Bottom Water". In: *Progress in Oceanography* 43.1, pp. 55–109. ISSN: 00796611. DOI: `10.1016/S0079-6611(99)00004-X`.

Oschlies, A. (2002). "Improved Representation of Upper-Ocean Dynamics and Mixed Layer Depths in a Model of the North Atlantic on Switching from Eddy-Permitting to Eddy-Resolving Grid Resolution". In: ISSN: 1520-0485. URL: `https://journals.ametsoc.org/view/journals/phoc/32/8/1520-0485_2002_032_2277_irouod_2.0.co_2.xml`.

Oschlies, A., Bach, L. T., Rickaby, R. E. M., Satterfield, T., Webb, R., and Gattuso, J.-P. (2023). "Climate targets, carbon dioxide removal, and the potential role of ocean alkalinity enhancement". In: *State of the Planet* 2-oae2023, pp. 1–9. DOI: `10.5194/sp-2-oae2023-1-2023`.

Oschlies, A. and Garçon, V. (1998). "Eddy-induced enhancement of primary production in a model of the North Atlantic Ocean". In: *Nature* 394.6690, pp. 266–269. ISSN: 1476-4687. DOI: `10.1038/28373`.

Pellichero, V., Sallée, J.-B., Chapman, C. C., and Downes, S. M. (2018). “The southern ocean meridional overturning in the sea-ice sector is driven by freshwater fluxes”. In: *Nature Communications* 9.1, p. 1789. ISSN: 2041-1723. DOI: `10.1038/s41467-018-04101-2`.

Pongratz, J., Smith, S., Schwingshackl, C., Dayathilake, L., Gasser, T., Grassi, G., and Pilli, R. (2024). “Chapter 7: Current levels of CDR, The State of Carbon Dioxide Removal - 2nd Edition.” In: in collab. with Center For Open Science. Publisher: OSF. DOI: `10.17605/OSF.IO/ZXSKB`.

Renforth, P., Jenkins, B. G., and Kruger, T. (2013). “Engineering challenges of ocean liming”. In: *Energy* 60, pp. 442–452. ISSN: 0360-5442. DOI: `10.1016/j.energy.2013.08.006`.

Renforth, P. and Henderson, G. (2017). “Assessing ocean alkalinity for carbon sequestration: Ocean Alkalinity for C Sequestration”. In: *Reviews of Geophysics* 55.3, pp. 636–674. ISSN: 87551209. DOI: `10.1002/2016RG000533`.

Resplandy, L., Lévy, M., and McGillicuddy Jr., D. J. (2019). “Effects of Eddy-Driven Subduction on Ocean Biological Carbon Pump”. In: *Global Biogeochemical Cycles* 33.8, pp. 1071–1084. ISSN: 1944-9224. DOI: `10.1029/2018GB006125`.

Sabine, C. L., Feely, R. A., Gruber, N., Key, R. M., Lee, K., Bullister, J. L., Wanninkhof, R., Wong, C. S., Wallace, D. W. R., Tilbrook, B., Millero, F. J., Peng, T.-H., Kozyr, A., Ono, T., and Rios, A. F. (2004). “The Oceanic Sink for Anthropogenic CO $_2$”. In: *Science* 305.5682, pp. 367–371. ISSN: 0036-8075, 1095-9203. DOI: `10.1126/science.1097403`.

Schartau, M., Engel, A., Schröter, J., Thoms, S., Völker, C., and Wolf-Gladrow, D. (2007). “Modelling carbon overconsumption and the formation of extracellular particulate organic carbon”. In: *Biogeosciences* 4.4, pp. 433–454. ISSN: 1726-4170. DOI: `10.5194/bg-4-433-2007`.

Scholz, P., Sidorenko, D., Danilov, S., Wang, Q., Koldunov, N., Sein, D., and Jung, T. (2022). “Assessment of the Finite-VolumE Sea ice–Ocean Model (FESOM2.0) – Part 2: Partial bottom cells, embedded sea ice and vertical mixing library CVMix”. In: *Geoscientific Model Development* 15.2, pp. 335–363. ISSN: 1991-9603. DOI: `10.5194/gmd-15-335-2022`.

Scholz, P., Sidorenko, D., Gurses, O., Danilov, S., Koldunov, N., Wang, Q., Sein, D., Smolentseva, M., Rakowsky, N., and Jung, T. (2019). “Assessment of the Finite-volumE Sea ice-Ocean Model (FESOM2.0) – Part 1: Description of selected key model elements and comparison to its predecessor version”. In: *Geoscientific Model Development* 12.11, pp. 4875–4899. ISSN: 1991-9603. DOI: `10.5194/gmd-12-4875-2019`.

Sein, D. V., Koldunov, N. V., Danilov, S., Sidorenko, D., Wekerle, C., Cabos, W., Rackow, T., Scholz, P., Semmler, T., Wang, Q., and Jung, T. (2018). “The Relative Influence of Atmospheric and Oceanic Model Resolution on the Circulation of the North Atlantic Ocean in a Coupled Climate Model”. In: *Journal of Advances in Modeling Earth Systems* 10.8, pp. 2026–2041. ISSN: 19422466. DOI: `10.1029/2018MS001327`.

Semmler, T., Danilov, S., Gierz, P., Goessling, H. F., Hegewald, J., Hinrichs, C., Koldunov, N., Khosravi, N., Mu, L., Rackow, T., Sein, D. V., Sidorenko, D., Wang, Q., and Jung, T. (2020). "Simulations for CMIP6 With the AWI Climate Model AWI-CM-1-1". In: *Journal of Advances in Modeling Earth Systems* 12.9, e2019MS002009. ISSN: 1942-2466. DOI: `10.1029/2019MS002009`.

Sidorenko, D., Danilov, S., Fofonova, V., Cabos, W., Koldunov, N., Scholz, P., Sein, D. V., and Wang, Q. (2020). "AMOC, Water Mass Transformations, and Their Responses to Changing Resolution in the Finite-VolumE Sea Ice-Ocean Model". In: *Journal of Advances in Modeling Earth Systems* 12.12. ISSN: 1942-2466, 1942-2466. DOI: `10.1029/2020MS002317`.

Smith, R. D., Maltrud, M. E., Bryan, F. O., and Hecht, M. W. (2000). "Numerical Simulation of the North Atlantic Ocean at 1/10°". In: ISSN: 1520-0485. URL: `https://journals.ametsoc.org/view/journals/phoc/30/7/1520-0485_2000_030_1532_nsotna_2.0.co_2.xml`.

Talley, L. D. (2008). "Freshwater transport estimates and the global overturning circulation: Shallow, deep and throughflow components". In: *Progress in Oceanography* 78.4, pp. 257–303. ISSN: 0079-6611. DOI: `https://doi.org/10.1016/j.pocean.2008.05.001`.

Terhaar, J., Goris, N., Müller, J. D., DeVries, T., Gruber, N., Hauck, J., Perez, F. F., and Séférian, R. (2024). "Assessment of Global Ocean Biogeochemistry Models for Ocean Carbon Sink Estimates in RECCAP2 and Recommendations for Future Studies". In: *Journal of Advances in Modeling Earth Systems* 16.3, e2023MS003840. ISSN: 1942-2466. DOI: `10.1029/2023MS003840`.

UNFCCC (2015). "United Nations Framework Convention on Climate Change (UNFCCC): Adoption of the Paris Agreement, 21st Conference of the Parties." In: URL: `https://unfccc.int/sites/default/files/english_paris_agreement.pdf`.

Våge, K., Pickart, R. S., Thierry, V., Reverdin, G., Lee, C. M., Petrie, B., Agnew, T. A., Wong, A., and Ribergaard, M. H. (2009). "Surprising return of deep convection to the subpolar North Atlantic Ocean in winter 2007–2008". In: *Nature Geoscience* 2.1, pp. 67–72. ISSN: 1752-0908. DOI: `10.1038/ngeo382`.

Walin, G. (1982). "On the relation between sea-surface heat flow and thermal circulation in the ocean". In: *Tellus* 34.2, pp. 187–195. ISSN: 00402826, 21533490. DOI: `10.1111/j.2153-3490.1982.tb01806.x`.

Wang, H., Pilcher, D. J., Kearney, K. A., Cross, J. N., Shugart, O. M., Eisaman, M. D., and Carter, B. R. (2023). "Simulated Impact of Ocean Alkalinity Enhancement on Atmospheric CO $_2$ Removal in the Bering Sea". In: *Earth's Future* 11.1. ISSN: 2328-4277, 2328-4277. DOI: `10.1029/2022EF002816`.

Wolf-Gladrow, D. A., Zeebe, R. E., Klaas, C., Körtzinger, A., and Dickson, A. G. (2007). "Total alkalinity: The explicit conservative expression and its application to biogeochemical processes". In: *Marine Chemistry*. Special issue: Dedicated to the memory of Professor Roland Wollast 106.1, pp. 287–300. ISSN: 0304-4203. DOI: `10.1016/j.marchem.2007.01.006`.

Yankovsky, E., Zhou, M., Tyka, M., Bachman, S., Ho, D., Karspeck, A., and Long, M. (2024). "Impulse response functions as a framework for quantifying ocean-based carbon dioxide removal". In: *EGUsphere*, pp. 1–26. DOI: `10.5194/egusphere-2024-2697`.

Zeebe, R. E. and Wolf-Gladrow, D. (2001). *CO2 in Seawater: Equilibrium, Kinetics, Isotopes*. Gulf Professional Publishing. 382 pp. ISBN: 978-0-444-50946-8.

Zhou, M., Tyka, M. D., Ho, D. T., Yankovsky, E., Bachman, S., Nicholas, T., Karspeck, A. R., and Long, M. C. (2025). "Mapping the global variation in the efficiency of ocean alkalinity enhancement for carbon dioxide removal". In: *Nature Climate Change* 15.1, pp. 59–65. ISSN: 1758-6798. DOI: `10.1038/s41558-024-02179-9`.

# 6

# SYNTHESIS

## SYNTHESIS

The atmospheric $CO_2$ inventory has been rising at a rate of 5.2 PgC $yr^{-1}$ from 2014 to 2023 (Friedlingstein et al., 2024), bringing the planet closer to the 2°C global warming limit above preindustrial levels specified by the Paris Agreement (UNFCCC, 2015; Pörtner et al., 2022). Avoiding this requires not only rapid emission reductions by phasing out fossil fuel usage, but also the deployment of various land and ocean-based CDR methods (IPCC, 2023). Among these methods, Ocean Alkalinity Enhancement stands out for its high potential for durable carbon storage (Gattuso et al., 2021; Oschlies et al., 2023). It leverages the ocean's natural capacity to absorb $CO_2$ by accelerating the natural weathering process that would otherwise occur over geological timescales. Thus, by artificially enhancing alkalinity, OAE shifts the carbonate equilibrium by promoting the conversion of $CO_2$ to more stable carbonate and bicarbonate ions (Hartmann et al., 2013; Renforth and Henderson, 2017). Although OAE shows promise, uncertainties regarding its scalability, efficiency, and ecological effects necessitate further research, including laboratory studies, field experiments, and numerical modeling (Eisaman et al., 2023; Iglesias-Rodríguez et al., 2023; Riebesell et al., 2023).

Although numerical ocean models are simplified representations of natural processes and subject to inherent uncertainties, they are critical for evaluating the diverse impacts of OAE on oceanic and biogeochemical processes. For instance, fit-for-purpose models provide valuable insights into the regional and global dynamics of OAE deployment (Fennel et al., 2023). Ocean-only models, by prescribing atmospheric $CO_2$ levels, isolate oceanic responses to OAE interventions, providing insights into the upper limits of carbon uptake efficiency (Burt et al., 2021; Hauck et al., 2016; Köhler et al., 2013; Butenschön et al., 2021; He and Tyka, 2023; Wang et al., 2023). In contrast, ESMs account for the coupled interactions between the ocean, atmosphere, and land, capturing feedbacks that influence OAE efficiency (Fakhraee et al., 2023; González and Ilyina, 2016; Jeltsch-Thömmes et al., 2024; Keller et al., 2014; Lenton et al., 2018; Palmiéri and Yool, 2024; Schwinger et al., 2024). Together, these modeling approaches are vital for quantifying uncertainties, evaluating ecological impacts, and informing the design of robust MRV frameworks critical for ensuring transparency and reliability in carbon accounting (Fennel et al., 2023; Ho et al., 2023).

Despite advancements in modeling understanding of OAE, substantial gaps remain, particularly concerning its efficiency in subduction regions, such as those in the Southern Ocean, Northwest Atlantic, and Norwegian-Barents Sea. These regions naturally transfer surface carbon to deeper ocean layers and isolate it from the atmosphere for multi-decadal to centennial time-scales (Gruber et al., 2019). However, some studies have suggested that these regions are not ideal for OAE as the subduction process limits the residence time of water masses at the ocean surface resulting in loss of $CO_2$-deficient waters to deep ocean before it can equilibrate with the atmosphere (Bach et al., 2023; He and Tyka, 2023; Jones et al., 2014). This would lead to reduction of about half of the carbon uptake efficiency of OAE. However, the complexities of the processes in these regions and their response to OAE remain inadequately studied and motivates further research.

This thesis thus addresses this research gap by simulating OAE globally and in subduction regions utilizing both coarse- and high-resolution ocean-only models, as well as a fully coupled ESM. Alkalinity is enhanced continuously and uniformly from 2030 to 2100 under a low and high emission scenario. By integrating these modeling approaches, the findings enhance the understanding of how subduction regions respond to OAE in terms of carbon uptake and deep ocean carbon sequestration. This synthesis chapter summarizes the key findings, their implications for future OAE deployment, and discusses limitations and recommendations for advancing modeling approaches for OAE.

## 6.1 MAJOR FINDINGS OF THE THESIS

### 6.1.1 *Q1: How do the subduction regions, individually and collectively, perform in terms of carbon uptake and OAE efficiency to global OAE and what are the uncertainty estimates?*

#### ***Effect of alkalinity addition on oceanic carbon uptake***

Publications I, II, and III present OAE simulations performed globally and in subduction regions under the SSP3-7.0 emission scenario over the $21^{st}$ century. They allow quantification and comparison of oceanic $CO_2$ uptake across various model configurations. Publications I and III utilize ocean-only models (FESOM2.1-REcoM3) with coarse and high spatial resolutions respectively, whereas Publication II employs the fully coupled emission-driven ESM AWI-ECM-1-REcoM. Robust results emerge across these different model configurations which consistently demonstrate a significant linear relationship between the amount of alkalinity added and the resulting increase in oceanic $CO_2$ uptake, applicable to both global and regional deployments. Notably, Publication II extends this analysis by comparing alkalinity addition rates and $CO_2$ uptake responses from multiple independent OAE studies employing ocean-only models and ESMs (Burt et al., 2021; Hauck et al., 2016; Keller et al., 2014; Lenton et al., 2018; Nagwekar et al., 2024; Palmiéri and Yool, 2024). This comparative assessment reinforces the robustness of the linear scaling behavior across diverse model types and experimental designs. It further highlights that the first-order carbonate chemistry effects governing $CO_2$ uptake are well understood and consistently scale linearly with the magnitude of alkalinity addition, reinforcing confidence that the basic concept of OAE works and that other effects (e.g., choice of model) are secondary on global spatial and centennial time-scale. However, this linear relationship may change or may not hold when biological effects, mineral dissolution, or secondary precipitation are explicitly included in the models. Since current models do not represent these processes, their influence on OAE induced carbon uptake remains unknown. Future modeling studies should therefore focus on parametrizing these processes to improve the $CO_2$ uptake estimates.

Despite the overall agreement among the models used in this thesis, subtle differences emerge in their simulated $CO_2$ uptake responses. In global OAE simulations, Publications I and III report $CO_2$ uptake increases of 0.85-0.86 PgC $yr^{-1}$ during the 2090s, whereas Publication II, which accounts for climate feedbacks, reports a lower uptake of 0.75 PgC $yr^{-1}$. This result is consistent with Schwinger et al. (2024) showing that climate feedbacks can reduce the carbon uptake induced by OAE simulated using an ESM as compared to ocean-only models. Publication III further evaluates $CO_2$ uptake differences for global alkalinity addition across major ocean basins and finds results comparable to those of Publication I, indicating that model resolution has a limited effect on the global-scale uptake. For subduction region deployments, differences in $CO_2$ uptake are primarily attributed to differences in the alkalinity deposition area, obtained from water mass transformation analysis, leading to different amounts of added alkalinity in each setup. Among the three studies, $CO_2$ uptake over the 2090s is highest in Publication II (0.20 PgC $yr^{-1}$), lowest in Publication I (0.07 PgC $yr^{-1}$), and intermediate in Publication III (0.11 PgC $yr^{-1}$). Publication III also compares effects of regional alkalinity addition across different ocean basins with results from Publication I and finds that only the Southern Ocean shows consistently higher $CO_2$ uptake in the high-resolution model. In particular, the $CO_2$ uptake in the Southern Ocean in the high-resolution model is twice as high as in the low-resolution simulation during the 2090s. However, this increase can be primarily attributed to the 63.8% higher alkalinity deposition in Publication III while the resolution effect is secondary. Overall, these results imply that the primary driver of oceanic $CO_2$ uptake globally or in the subduction regions is the amount of added alkalinity with further uncertainties introduced by the climate feedbacks while the effect of model resolution being only of second order importance by the end of the century.

Publication I also investigates the scenario dependency of OAE by performing simulations under SSP1-2.6 along with SSP3-7.0 emission scenario. Consistent with Lenton et al. (2018) the results indicate a small scenario dependency, with slightly higher $CO_2$ uptake (0.1 PgC $yr^{-1}$; 12.5% for global OAE and 0.01 PgC $yr^{-1}$; 16.6% for regional OAE) in SSP3-7.0 than SSP1-2.6 due to reduced ocean buffer capacity in a high-$CO_2$ environment. However, the first-order effect, the linearity between added alkalinity and increase in $CO_2$ uptake is also observed across different emission scenarios, making the results highly transferable. Additionally, Publication I examines the seasonal response of OAE and finds that shallow mixed layer depths (MLD) during summer enhance surface alkalinity and, consequently, carbon uptake and storage in both hemispheres. This finding contrasts with previous studies that either reported no seasonal response Lenton et al. (2018) or associated deeper MLDs, particularly in the North Atlantic, with higher alkalinity retention and carbon uptake (Köhler et al., 2013). These differences highlight the need for further research to refine deployment strategies for optimal deployment in order to increase OAE efficiency.

### *OAE Efficiency*

OAE efficiency is defined as the ratio of volume-integrated increase in DIC to volume-integrated increase in alkalinity ($\eta CO_2 = \Delta DIC/\Delta Alk$; Renforth and Henderson, 2017). It captures changes in ocean carbonate chemistry since the onset of OAE and can thus be considered a metric for long-term efficiency. Publication I demonstrated that under the SSP3-7.0 and SSP1-2.6 scenarios, OAE efficiency in subduction regions was identical to that of the global ocean, with values of 0.85 and 0.80, respectively, during the 2090s. The slightly higher efficiency under SSP3-7.0 is attributed to the reduced buffer capacity of the ocean at higher atmospheric $CO_2$ levels. Publications II and III, both focused on the SSP3-7.0 scenario, and further assessed OAE efficiency at global and regional scales. Publication II reported comparable global and

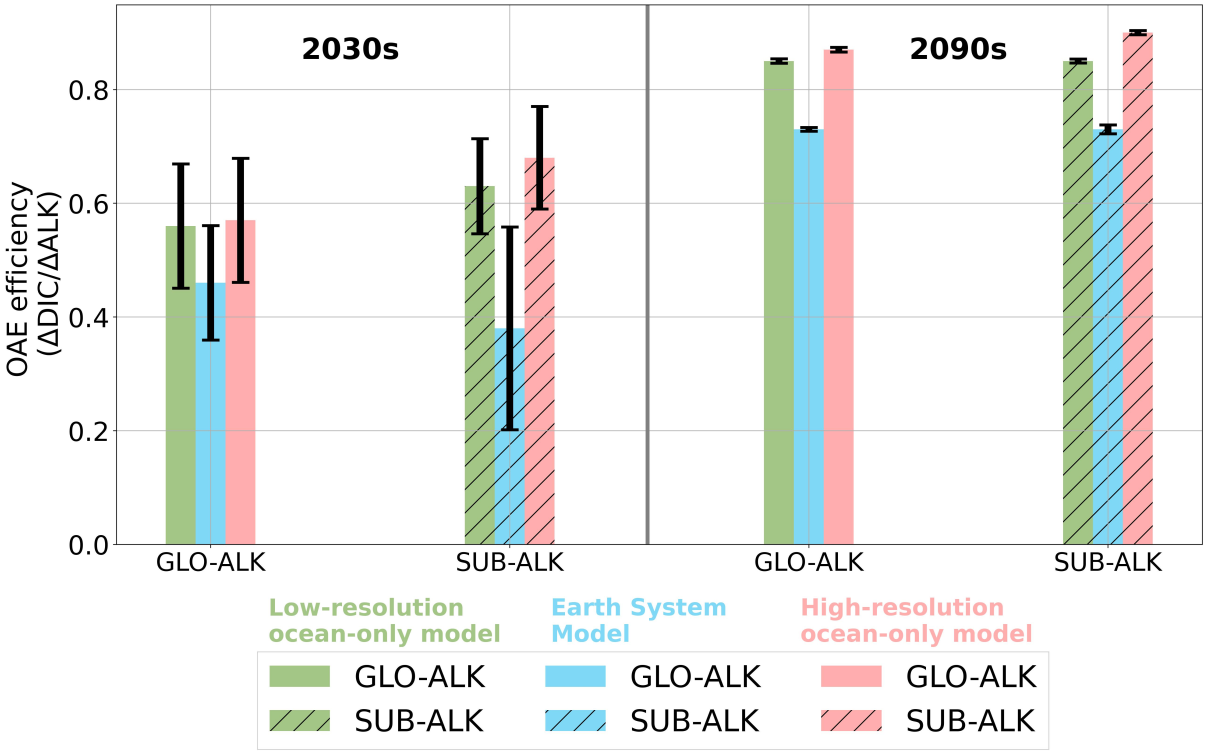

FIGURE 6.1: Efficiency of ocean alkalinity enhancement (OAE; $\eta CO_2 = \Delta DIC/\Delta Alk$) for the three model setups averaged over the 2030s and 2090s under SSP3-7.0 emission scenario. Solid bars represent global OAE experiments (GLO-ALK) while the dashed bars represent the subduction regions OAE experiments. Low-resolution ocean-only model (Publication I; green bars), fully coupled Earth System Model (Publication II; blue bars), and high-resolution ocean-only model (Publication III; pink bars).

regional efficiency (0.71-0.73), while Publication III reported global efficiency of 0.85 and regional efficiency of 0.91. This contrasts with earlier studies that suggested subduction regions are inefficient for OAE, attributing the low efficiency to rapid loss of alkalinity and $CO_2$ deficient waters to the deep ocean via strong downwelling (Bach et al., 2023; He and Tyka, 2023). A possible explanation for this discrepancy is the difference in alkalinity addition methods: previous studies applied pulsed additions, while my approach used continuous, uniform additions over 70 years. If so, this would point to the importance of developing optimal deployment scenarios. However, whether this methodological difference directly influences OAE efficiency requires further study (see section 6.2.1).

Although all three publications report comparable OAE efficiencies between the global ocean and subduction regions, Publication II reports the lowest efficiency of 0.71-0.73. This difference stems from its ESM configuration, which allows the atmospheric $CO_2$ reservoir to interact dynamically with land and ocean reservoirs, incorporating the effects of climate feedbacks on OAE-induced changes. In contrast, ocean-only models, which use prescribed atmospheric $pCO_2$, do not account for these feedbacks. Consequently, the efficiency estimated using an ESM is termed "earth system efficiency," while that from ocean-only models is referred to as "capture efficiency" (Schwinger et al., 2024). The distinction between these metrics is particularly relevant when evaluating CDR deployment within different policy frameworks. In a cost-benefit analysis of climate policies, earth system efficiency is the appropriate metric, as it provides a comprehensive measure of net carbon removal by considering the earth system feedbacks. However, when a climate target is already established and policy instruments such as emission trading are in place, the focus shifts to a cost-effective approach. Here the CDR methods (OAE in this case) must be compared based on their cost per unit of carbon captured. In this context, capture efficiency becomes a relevant measure, as it quantifies the directly sequestered carbon and determines the amount of carbon offset credits assigned for a given CDR approach (Schwinger et al., 2024).

Most notably, during the initial deployment phase in the 2030s, all three publications reveal pronounced differences and uncertainties in global and regional OAE efficiencies (Figure 6.1). In ocean-only models, subduction regions show higher efficiencies compared to global OAE simulations, with the high-resolution SUB-ALK simulation achieving an efficiency of 0.7. Conversely, Publication II indicates that regional efficiencies are lower than the global average while reporting the highest uncertainty (±55% around the mean) during the 2030s. Over time, the lateral and vertical spread of alkalinity perturbations in the ocean leads to a gradual decrease in uncertainty by the end of the simulation period. Furthermore, Publication II with the ensemble simulations capture the model internal variability which is higher in the regional OAE compared to global OAE. This variability indicates that the response of OAE is sensitive to the initial climate conditions, and varying these conditions can yield different outcomes. Given the prominent differences in the global and regional efficiencies and higher uncertainties across all model setups during the initial years of OAE deployment which are the most critical for real-world implementation, this may pose a potential challenge for MRV of OAE. Therefore, future modeling studies should focus more on the immediate impacts of OAE on global as well as regional scale.

### *Effect of nutrient (iron and silcic acid) fertilization of oceanic $CO_2$ uptake and surface CDR potential*

Publications I and III account for the dual effect of nutrient fertilization and alkalinity addition on oceanic $CO_2$ uptake and storage. In these studies, nutrient fertilization results from the assumed deposition of olivine, as an alkaline feedstock for OAE, which releases iron and silicic acid into surface waters. Publication I simulates nutrient fertilization globally, in three subduction regions combined, and exclusively in the Southern Ocean subduction region. In Publication III, solely global-scale deposition is considered. Both Publications reported that the magnitude of oceanic $CO_2$ uptake with nutrient fertilization is notably ($\sim$37%) higher than only alkalinity addition experiments. For global deposition, both studies report a comparable nutrient-induced increase in $CO_2$ uptake of 1.24-1.26 PgC yr$^{-1}$ over the 2090s. This indicates that, when averaged at a global scale, differences in model resolution do not have substantial influence on the nutrient-induced carbon uptake. Publication III demonstrates that while global averages align, differences are observed in region specific nutrient-induced carbon uptake. Particularly, the Southern Ocean in the high-resolution setup shows a 14.1% higher increase in carbon uptake than the low-resolution setup over the 2090s. In the Indian Ocean, however, uptake decreases substantially in the high-resolution simulation, with values falling below those in the CTRL (no OAE) simulation. Similarly, the Atlantic Ocean in the high-resolution setup also exhibits marginally reduced carbon uptake compared to low-resolution simulations. This disparity primarily arises due to difference in representation of nutrients in the mean state of the high-resolution and low-resolution model setups. When compared to observational data, the high-resolution simulation exhibited a stronger bias and a lower correlation (0.69) in DSi distribution than the low-resolution model, which achieved a correlation of (0.84). These results suggest that the low-resolution model may be sufficient for nutrient fertilization experiments, as the high-resolution setup does not demonstrate a clear advantage while also being more computationally demanding.

The surface CDR potential is defined as the amount of carbon sequestered per unit amount of dissolved alkaline material (in this case olivine; Hauck et al., 2016; Köhler et al., 2013). This metric represents a short-term efficiency measure by focusing solely on surface ocean carbon uptake. Unlike $\eta CO_2$, which exclusively accounts for carbon uptake driven by carbonate chemistry alterations from OAE, the surface CDR potential also captures the contribution of nutrient fertilization effects associated with olivine dissolution. While only alkalinity addition experiments demonstrated comparable $\eta CO_2$ between global and subduction regions, the additional influence of nutrient fertilization introduces substantial regional variability in CDR potential. Notably, Publication I reported that the Southern Ocean exhibits the highest CDR potential, reaching approximately 1 PgC per Pg olivine which is 2.5 times higher than the CDR potential reported for global nutrient fertilization simulations. This elevated response is primarily attributed to iron fertilization, as the Southern Ocean is naturally iron-limited (Baar et al., 1995; Smetacek et al., 2012). Iron deposition thus enhances primary productivity, resulting in increased carbon uptake. Notably, about 97% of the total increase in nutrient-induced carbon uptake occurs in the Southern Ocean, while the contribution from North Atlantic subduction regions is small. The efficiency of nutrient fertilization is highest during the initial few years of the simulation but declines toward the end of the century. This decline occurs due to the saturation of fertilization effect, reduced nutrient consumption over time, and release of carbon via remineralization, leading to a gradual decrease in carbon uptake. Similar findings have been discussed in previous studies, such as Hauck et al. (2016) and Köhler et al. (2013), which emphasize the transient nature of nutrient fertilization efficiency. Although nutrient fertilization itself is recognized as a potential CDR method (Aumont and Bopp, 2006; Zeebe and Archer, 2005), studies have reported associated side effects, including potential ecological disruptions and altered biogeochemical cycles, warranting careful consideration before large-scale implementation (Keller et al., 2014; Oschlies et al., 2010a; Tagliabue et al., 2023).

### 6.1.2 *Q2: Can subduction regions increase deep ocean carbon sequestration due to OAE and what are the associated uncertainty estimates?*

The primary rationale for targeting subduction regions for OAE lies in their natural capacity to transport dissolved carbon from the surface ocean to the interior, enabling sequestration over multi-decadal to centennial timescales (Gruber et al., 2019; Sabine et al., 2004). To evaluate

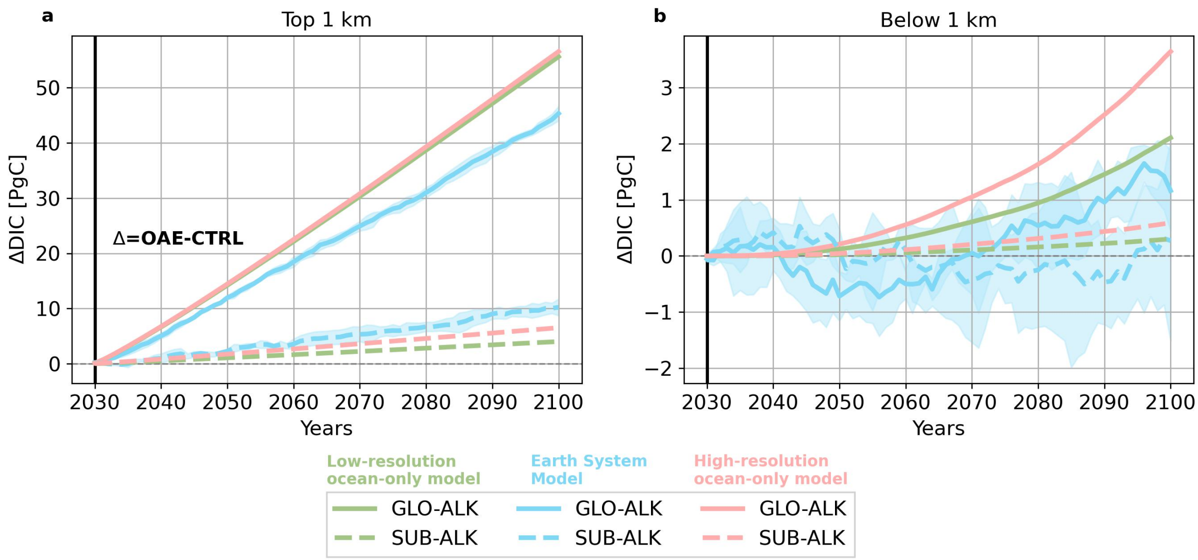

FIGURE 6.2: Time series for increase in dissolved inorganic carbon relative to the CTRL (ΔDIC) in the **(a)** top 1 km and **(b)** below 1 km ocean depth for all the model setups. Low-resolution ocean-only model (Publication I; green color), fully coupled Earth System Model (Publication II; blue color), and high-resolution ocean-only model (Publication III; pink color). Solid lines represent global OAE experiments (GLO-ALK) and dashed lines represent regional OAE experiments (SUB-ALK).

this hypothesis, I analyzed the increase in DIC in the upper 1 km and below 1 km of the water column following OAE deployment in both global and subduction regions across three model setups (Figure 6.2a and b). In the global OAE experiments, where an equal amount of alkalinity is deposited across all setups, the ocean-only models in Publications I and III report comparable increases in DIC in the upper 1 km, with the high-resolution simulation showing higher accumulation (54.80 PgC) than the low-resolution simulation (50.95 PgC) over the 2090s. In contrast, the global OAE experiment in Publication II shows the lowest increase in DIC (41.27 ± 0.77 PgC) in this layer due to the influence of climate feedbacks, which are not accounted for in the ocean-only models. For regional OAE experiments, the amount of alkalinity added varies across setups based on the extent of subduction regions in each configuration. The regional OAE experiment in Publication II, which receives the highest alkalinity input, leads to the largest increase in $CO_2$ uptake and, consequently, the highest increase in DIC (9.50 ± 1.0 PgC) in the upper 1 km during the 2090s. This is followed by the high-resolution regional OAE simulation, which receives the second-highest alkalinity input and results in a DIC increase of 6.00 PgC. The low-resolution regional OAE simulation in Publication I, which receives the least alkalinity input, shows the lowest increase in DIC (3.70 PgC) in the top 1 km over the last decade of the century.

For deep ocean carbon sequestration (below 1 km depth; Figure 6.2b), both ocean-only setups show a consistent positive increase in DIC throughout the simulation period for both global and regional OAE deployments. Among all simulations, the global OAE experiment in Publication III reports the highest DIC accumulation (3.00 PgC), which can be attributed to a steeper and deeper neutral density isopycnal structure, indicating stronger vertical transport and greater penetration of carbon into the ocean interior. In the regional OAE experiments, the higher

DIC accumulation in Publication III is primarily due to a 63.8% greater alkalinity addition compared to the simulations in Publication I, with model resolution playing only a minor role in this case. Notably, both ocean-only setups in Publications I and III show that subduction regions transfer a $\sim$1–2 times higher fraction of the total carbon taken up to depths below 1 km compared to their respective global OAE experiments. However, this efficient downward transport of carbon is not reflected in the findings of Publication II.

Publication II concludes that subduction regions may not be as efficient as the global ocean in sequestering carbon in the deep ocean. While DIC changes in the upper 1 km exhibit a consistent positive increase with low uncertainty for both global and subduction region OAE, DIC changes below 1 km show substantial interannual and internal variability. Notably, during several years of the simulation period, deep ocean DIC concentrations fall below baseline levels (CTRL; no OAE), a pattern not observed in either the high- or low-resolution ocean-only simulations. This variability, along with occasional reductions in DIC relative to the CTRL, arises from climate feedbacks and model internal variability, contributing to elevated uncertainty in both global and regional OAE outcomes. These findings highlight the necessity of accounting for Earth system feedbacks when assessing OAE-induced carbon uptake and storage potential, as neglecting these factors could lead to misleading conclusions. At the same time, incorporating such feedbacks remains both a challenge and a prerequisite for developing reliable carbon management strategies and designing a robust MRV framework.

Publication I and III investigated the combined effect of nutrient fertilization and alkalinity addition on carbon sequestration in the global ocean, both identifying the Southern Ocean as the most effective region for deep ocean carbon storage. However, the absolute amount of carbon stored below 1 km differs between the two simulations. The CTRL simulation in Publication III exhibits higher net primary productivity than the low-resolution CTRL simulation, amplifying the efficiency of biological carbon sequestration. As a result, Publication III reports a greater (14.92 PgC) absolute amount of carbon sequestered compared to Publication I, which sequestered 11.93 PgC. However, preliminary evaluation indicates that the high-resolution model overestimates nutrient availability, which may ultimately affect net primary production and consequently influence carbon uptake and storage. Therefore, further research and comprehensive model evaluation are required to ensure robust assessments of model performance in the context of OAE. Beyond the global ocean experiments, Publication I also examined nutrient fertilization in subduction regions and found similar trends, with the Southern Ocean subduction region demonstrating the highest efficiency among all subduction regions. However, despite its effectiveness, the total carbon sequestered in subduction regions remained lower than in the global ocean experiment, primarily due to their smaller spatial extent, which limited alkalinity addition and, consequently, reduced the overall carbon uptake.

Overall the findings suggest that the primary driver for increase in DIC in the top 1 km depth for the regional OAE is the amount of added alkalinity. For global OAE with similar alkalinity input, the deciding factor is the influence of the climate feedbacks, while the role of model resolution is only secondary. In terms of deep ocean carbon sequestration, for global OAE experiments, the better representation of surface to deep ocean connecting pathways in the high-resolution potentially results in higher deep ocean DIC, however, we see that the consideration of climate feedbacks and internal climate variability will also be equally or more important in order to have a realistic estimate of deep ocean carbon sequestration for global as well as regional OAE deployment scenarios.

### 6.1.3 *Q3. How do the global and regional OAE deployments affect land and ocean carbon sinks, atmospheric $CO_2$ concentration, and surface air temperature?*

Unlike ocean-only models in Publications I and III, which are tailored to investigate ocean-specific processes and responses to OAE, the ESM in Publication II integrates terrestrial and atmospheric components, offering a broader implication of OAE on the earth system. Global OAE deployment was found to lower atmospheric $CO_2$ concentration by approximately 20.43 ± 0.59 ppm by 2100, while OAE confined to subduction regions achieved a reduction of 3.6 ± 1.12 ppm. A notable finding was the significant linear relationship between the reduction in atmospheric $CO_2$ and the quantity of alkalinity added for OAE in the last year of deployment (2100). This relationship is consistent across multiple ESM-based studies, irrespective of variations in model configurations, resolutions, and assumptions regarding OAE deployment regions (González and Ilyina, 2016; Keller et al., 2014; Lenton et al., 2018; Palmiéri and Yool, 2024). This consistency suggests that large-scale OAE responses are reliably captured across models. However, further research should prioritize refining small-scale deployment strategies by identifying optimal sites for real-world OAE implementation.

Publication II concluded that the reductions in atmospheric $CO_2$ achieved through both global and regional OAE deployments are insufficient to have any substantial impact on reduction in surface air temperature by the end of the century. Globally, alkalinity addition resulted in an insignificant surface temperature reduction of 0.043 ± 0.18°C, while deployment in subduction regions achieved a decrease of 0.054 ± 0.053°C by 2100. These temperature changes exhibited high interannual variability and uncertainty throughout the simulation period, with several years showing temperature increases above the CTRL simulation. This variability is consistent with findings of the studies that implemented alkalinity addition rates ranging from 0.02 to 0.25 Pmol $yr^{-1}$ (González and Ilyina, 2016; Keller et al., 2014; Lenton et al., 2018; Palmiéri and Yool, 2024). Additionally, a comparatively weaker linear relationship was identified between atmospheric $CO_2$ reduction and surface air temperature changes across different studies. In contrast to the air-sea $CO_2$ fluxes, this weak correlation is due to the dominant influence of equilibrium climate sensitivity in determining the temperature response, which varies depending on the model used in each study.

Publication II reported that the land carbon sink weakened over the simulation period, with reductions of 0.73 ± 2.64 PgC for SUB-ALK and 4.17 ± 2.66 PgC for GLO-ALK during the 2090s. This aligns with other studies that also documented a decrease in land sink ranging from 1-5 PgC by the end of the century (González and Ilyina, 2016; Palmiéri and Yool, 2024). The weakening is attributed to reduced atmospheric $CO_2$ levels, which diminish the $CO_2$ fertilization effect on vegetation, and to temperature variations that alter precipitation patterns, impacting vegetation and soil carbon storage (Adloff et al., 2018; Jeltsch-Thömmes et al., 2024). In the subduction region simulations, the impact on the land sink was small, with changes remaining near zero (0.02 ± 3.0 PgC) over the multiple years. Conversely, global alkalinity addition led to significant deviations from zero after 35-40 years (3.6 ± 3 PgC), reflecting a lag time of approximately three to four decades before the effects of OAE on the land sink became apparent. Throughout the simulation period, the land carbon sink exhibited pronounced interannual variability and considerable uncertainty, contrasting with the relatively consistent and robust response observed in the ocean carbon sink. This variability underscores challenges if the land sink is to be integrated into MRV frameworks and highlights the need for further investigation to improve predictive accuracy.

## 6.2 LIMITATIONS AND FUTURE OUTLOOK

### 6.2.1 *Mode of Alkalinity Addition*

Alkalinity addition was continuously applied in all OAE experiments reported in Publications I, II, and III. Simulations employed models with 15-minute time-steps, during which 0.21 mol $m^{-2}$ of alkalinity was uniformly distributed across the global oceans and the subduction regions over a 70-year period. This approach, provides an upper limit estimate of carbon sequestration for the amount of added alkalinity. The global-scale experiments assumed an addition of 78.80 Tmol of alkalinity annually, while subduction-region experiments in Publications I, II, and III modeled annual inputs of 5.72 Tmol, 17.99 Tmol, and 9.37 Tmol, respectively. Such volumes vastly exceed the current global production capacity of 5–6 Mt $yr^{-1}$, necessitating an unprecedented expansion of mining infrastructure, which would in turn introduce substantial additional carbon emissions and erode the overall efficacy of the method (Caserini et al., 2022).

An alternative and more practical approach is the pulsed/discontinuous addition of alkalinity. Several modeling studies have examined this approach under particular seasonal timing and regional characteristics. Zhou et al. (2025) simulated OAE pulse in January, April, July, and October globally and reported a seasonal response of OAE efficiency with summer months having higher efficiency than winter months. For instance, a pulse in July in the Labrador Sea achieved an efficiency of 0.7, while a pulse in January resulted in a much lower efficiency of 0.2, both efficiencies calculated 15 years after the pulse was deployed. They attributed this to deep winter mixing, which removes alkalinity from the surface ocean. In general, they report that the polar regions (deep and bottom water formation areas) in both hemispheres have persistent lower efficiencies as compared to the subpolar water masses which are deemed to be the best regions for OAE as they achieve efficiencies of 0.8 within 8 years of deployment. Similarly, He and Tyka (2023) and Yankovsky et al. (2024) also simulated a month-long pulsed OAE in January at different coastal and open ocean locations. Their results also concluded that the regions around Iceland and Labrador Sea, are not suitable for OAE, again due to the limited time for $CO_2$-deficient waters to equilibrate with the atmosphere. Yamamoto et al. (2024) also conducted a pulsed OAE experiment over the global ocean, but using a coupled ocean-atmosphere linearized model. Their results mirrored those of the previous studies, with low OAE efficiencies in regions around the Labrador Sea and the Southern Ocean deep-water formation zones. However, Yamamoto et al. (2024) also highlighted a distinct feature in the subpolar mode water regions which are north of the polar front. In these areas, mode waters that are subducted into the deeper ocean resurface more quickly than deep waters, allowing for a secondary phase of $CO_2$ uptake. This resurfacing dynamic facilitates continued atmospheric $CO_2$ ingassing, partially mitigating the inefficiency caused by initial alkalinity loss to deeper ocean layers.

These findings contrast with the results of Publications I and III, which reported sustained high efficiencies (0.85–0.90) in subduction regions by the end of the century, under continuous alkalinity addition over 70 years. The apparent contradiction may stem from differences in alkalinity addition mode (pulsed vs continuous) and the seasonal dependence of efficiency (Publication I), however, this remains to be tested. Notably, Publication I and III aligns with Zhou et al. (2025) in identifying higher $CO_2$ uptake during summer, reinforcing the critical role of seasonality in OAE efficiency. This underscores the need for further investigation into how application mode modulates OAE outcomes, particularly in subduction regions.

### 6.2.2 *Alkaline Mineral Dissolution*

The only-alkalinity addition experiments across all three publications are independent of the specific alkaline mineral and method for OAE, meaning dissolution kinetics is not a concern when alkalinity is introduced in solution form. In contrast, the nutrient fertilization experiments assume olivine as the source, where dissolution kinetics influence the extent of carbon uptake due to the particulate nature of the material. These simulations assume complete and instantaneous dissolution, an unrealistic scenario in natural ocean conditions. This assumption arises due to the absence of comprehensive dissolution kinetics data, which limits its explicit representation in models. Consequently, the reported carbon uptake and OAE efficiencies represent upper-bound estimates. In reality, mineral dissolution rates are influenced by factors such as particle size, ambient seawater temperature, and pH (Feng et al., 2017; Oelkers, 2001). Smaller particle sizes enhance dissolution rates due to their higher surface area-to-volume ratio, with particles smaller than 10 $\mu$m being optimal for near-complete dissolution in the surface ocean (Köhler et al., 2013). In case of olivine, mineral composition also affects dissolution, with magnesium-rich olivine dissolving 20–30% faster than its iron-rich counterpart under similar conditions (Hangx and Spiers, 2009; Oelkers et al., 2018; Olsen, 2007). Furthermore, dissolution rates are generally higher in warmer and more acidic waters. For instance, in high latitudes, dissolution rates can decrease by a factor of 2.5-3.6 compared to those in low to intermediate latitudes (45°S to 45°N) due to colder water temperatures (Geerts et al., 2025; Hangx and Spiers, 2009). This implies that if olivine would be used for OAE in subduction regions, the colder water masses in these areas would significantly reduce dissolution rates and the upper-bound estimate of the model simulations would not be reached. Thus, if any alkaline rock powder feedstock is used for OAE, then accounting for such factors in future modeling efforts will be crucial for refining the accuracy of predicted OAE impacts and better aligning them with real-world scenarios.

Currently, no global or regional models incorporate the effects of near-field dynamics on OAE. To address this gap, parameterization schemes must be developed based on insights from near-field models, such as direct numerical simulations or large eddy simulations, which resolve processes at scales of micrometers to meters (Fennel et al., 2023). These models capture processes under varying turbulence intensities, where increased particle suspension and mixing enhance effective dissolution and thus is relevant for OAE (Mensa et al., 2015; Taylor et al., 2020). Additionally, near-field models can simulate localized pH buffering and dynamics at the injection site, where alkalinity addition can temporarily elevate pH by 0.1-0.3 units (Hartmann et al., 2013), impacting dissolution efficiency (Fornari et al., 2016). They can also account for particle aggregation, especially for fine particles ($<10\ \mu$m), which, despite their rapid dissolution potential, are prone to aggregation. This process reduces effective surface area and dissolution efficiency, highlighting the need for precise parametrization of such interactions. However, near-field models are computationally demanding, resulting in a low feasibility for long-term simulations. Moreover, the current lack of validation against observational data and field experiments restricts the reliability of these models. To overcome these challenges, multi-scale modeling frameworks are needed to couple near-field dynamics with regional dispersal models, ensuring consistent dissolution predictions across spatial and temporal scales. Validation through field experiments should be prioritized to enhance model accuracy and applicability for future OAE research (Fennel et al., 2023).

### 6.2.3 *Secondary Mineral Precipitation*

Secondary calcium carbonate ($CaCO_3$) precipitation occurs when seawater becomes supersaturated with carbonate ions ($\Omega > 1$; Zeebe and Westbroek, 2003). During OAE, if the addition of alkalinity results in oversaturation, this phenomenon could counteract the intended effects by consuming the added alkalinity to form $CaCO_3$ (Bach et al., 2019; Schulz et al., 2023). To mitigate this risk, the critical $\Omega$ values at the deployment site should be determined in order to estimate the amount of alkalinity that can be safely introduced (Hartmann et al., 2023). Saturation states, which vary with salinity and temperature, are typically higher in mid- and low-latitude regions compared to the polar oceans (Schulz et al., 2023). The three publications in this thesis did not account for secondary precipitation, and therefore, the upper limit of alkalinity addition in either the global ocean or subduction regions was not explicitly tested. Current understanding suggests that maintaining $\Omega$ below a threshold of approximately 5 to 7 is essential to avoid secondary mineral precipitation (Fuhr et al., 2022; Moras et al., 2022; Suitner et al., 2024). In our simulations, 0.034 $\mu$mol kg$^{-1}$ of alkalinity was added globally and in subduction regions over the 21st century. This amount remains well below levels applied in some experimental studies, where extreme alkalinity additions ($>2700\ \mu$mol kg$^{-1}$) led to surpassing the $\Omega$ threshold and triggered secondary precipitation (Gately et al., 2023). Notably, Publications I identified increased calcification in the southern subtropical Pacific Ocean and certain areas of the Southern Ocean during nutrient addition experiments. This elevated calcification, driven by enhanced productivity of small phytoplankton with implicit calcification processes, reduced surface alkalinity compared to experiments with only alkalinity addition. Collectively, both inorganic precipitation and biologically driven $CaCO_3$ production constitute a form of "$CaCO_3$ leakage," where alkalinity is removed from the ocean surface, thereby constraining the OAE efficiency.

Overall, the alkalinity additions in our studies falls well within what can be considered a safe range. However, critical $\Omega$ values are region-specific, influenced by local physical, chemical, and biological conditions (Bach et al., 2019; Hartmann et al., 2023), and therefore, further laboratory and field experiments are needed to refine these thresholds. Moreover, a key limitation of global ocean models is the large grid cells which cannot capture processes at a few meter to kilometre scale and thus leads to rapid dilution of added alkalinity. In real ocean conditions, point-source alkalinity addition would not experience such swift dilution, which may alter local saturation levels. Hence, to improve the understanding of regional impacts, high-resolution near-field models are essential to capture small-scale processes that influence OAE efficiency. Such insights could support the development of parameterizations for secondary mineral precipitation, enabling more robust and accurate OAE simulations in future modeling efforts (Fennel et al., 2023).

### 6.2.4 *Biological response to OAE*

The three publications in this thesis do not consider the biological impacts of OAE, which are crucial for determining the permissible alkalinity addition at a given site based on its background biological conditions. While field experiments involving varying levels of alkalinity addition, have not yet reported drastic adverse effects on marine ecosystems, these findings remain preliminary. A more critical assessment of how different phytoplankton functional types (PFTs) respond to alkalinity addition is essential (See section 2.7.2). Publications I and III, in the nutrient fertilization experiments, report an increase in net primary productivity; however, the models used here are not equipped to capture potential impacts on higher trophic levels, such as changes in energy transfer within marine food webs. Additionally, the parameterizations used in these studies do not explicitly account for how OAE might affect the growth rates of specific phytoplankton and zooplankton groups.

Incorporating a full range of biological and ecological processes into global ocean models remains a significant challenge due to the intricate interactions involved. For example, while REcoM simulates nutrient limitations, such as those related to iron and silicic acid for small phytoplankton and diatoms Hauck et al. (2016), the model version used for the thesis does not account for the effects of changes in carbonate chemistry caused by alkalinity addition on these species. Moreover, no current models simulate the ecological consequences of Ni release from olivine-based OAE. Biological impacts of OAE are often subtle and can be obscured by natural variability, further complicating their representation in global models (Fennel et al., 2023). If the electrochemical approach is employed for OAE, the primary biological feedback to consider would be the changes in carbonate chemistry, particularly its impact on biogenic calcification rates and phytoplankton growth (Eisaman et al., 2023; Ringham et al., 2024). These effects could potentially be easier to include in global models compared to the crushed rock feedstock approach, as the latter involves additional complexities. Specifically, it not only alters the carbonate chemistry but also introduces physical dissolution dynamics and the risk of heavy metal contamination, which are more difficult to parameterize in models due to a lack of sufficient data (Bach et al., 2019; Fennel et al., 2023; Fennel et al., 2023; Hartmann et al., 2013). Therefore, further field studies are required to enhance model accuracy and develop the necessary parametrizations to account for the biological impacts of OAE.

### 6.2.5 *Model Validation*

The accurate representation of total alkalinity and DIC is critical for assessing the efficiency of OAE as a negative emissions technology using an ocean model. An evaluation of CMIP6 models against the GLODAPv2 dataset indicated that the models underestimated surface alkalinity, with global mean biases ranging from –85 mmol $m^{-3}$ (–3.6%) to +50 mmol $m^{-3}$ (+2.1%). Surface DIC biases ranged from –55 mmol $m^{-3}$ (–2.6%) to +53 mmol $m^{-3}$ (+2.5%; Hinrichs et al., 2023). These biases affect the modeled carbonate system response to OAE, leading to discrepancies in the estimated efficiency of $CO_2$ removal. Consequently, a hypothetical addition of 100 $\mu$mol $kg^{-1}$ of alkalinity produced $pCO_2$ reductions between 91 and 104 $\mu$atm instead of the observed 92 $\mu$atm, resulting in an overestimate of up to 13%, even though the $CO_2$ uptake efficiency ($\eta CO_2$) remained within $-0.1\%$ to $+1.1\%$ of observations (Hinrichs et al., 2023).

These coupled biases affect deep and bottom water formation regions. Errors in preformed alkalinity in the upper 1 km, combined with calcium carbonate dissolution in deeper layers, can shift surface underestimations into overestimations at depth with alkalinity biases exceeding +100 mmol $m^{-3}$ below 4000 m. Deep water formation is crucial for transporting carbon into the ocean interior for long-term sequestration, so even small inaccuracies in alkalinity and DIC have significant implications for estimates of carbon storage over centennial to millennial timescales (Hinrichs et al., 2023). These uncertainties can compromise MRV systems that depend on precise representations of carbonate chemistry and water mass transport. However, such uncertainties can be effectively reduced through data assimilation techniques, which integrate observational data with model simulations to produce optimized state estimates. This approach aligns model outputs more closely with real-world conditions (Fennel et al., 2023). Validated models are thus indispensable for refining OAE efficiency estimates and meeting MRV requirements necessary for real-world implementation (Fennel et al., 2023; Ho et al., 2023).

## 6.3 CONCLUSION

Ocean Alkalinity Enhancement (OAE) was investigated to test the hypothesis that intermediate, deep and bottom water formation regions in the Southern Ocean and North Atlantic, crucial for anthropogenic carbon uptake, can act as effective sites for OAE deployment by leveraging their natural ability to sequester carbon away from the atmosphere over multi-decadal to centennial timescales. Using low- and high-resolution ocean-only models and a fully coupled emission driven Earth System Model (ESM), this study assessed the efficiency of OAE in these regions compared to global applications, under high and low emission pathways.

The results show that the choice of model has a greater impact on OAE efficiency in the initial decade of alkalinity deployment than on long-term estimates, with all models projecting high uncertainties during this phase. This highlights the need for future studies to focus on the immediate impacts of OAE and conduct robust model evaluations during this period to refine monitoring, reporting, and verification (MRV) formulations. While all models show a significant linear relationship between the amount of alkalinity added and the increase in oceanic $CO_2$ uptake, this linearity only becomes evident after approximately 60 years of alkalinity addition and may not exist at smaller spatial and temporal scales. Furthermore, biological implications, effects of mineral dissolution, and secondary mineral precipitation are not accounted for in the models and may further influence this linearity, necessitating future efforts to parametrize these processes for more realistic carbon uptake estimates. Results show that the subduction regions can be a viable option for OAE but are subject to a strong seasonal variability. Thus, future studies should consider seasonal dynamics for regional OAE applications and develop more optimal deployment strategies by investigating the impact of pulsed versus continuous alkalinity addition and comparing coastal versus open-ocean applications. Additionally, the results also elucidate that Earth system feedbacks substantially impact both short-term regional OAE efficiencies and deep ocean carbon sequestration, underscoring the need for a better understanding of post-OAE ocean-atmosphere interactions and their implications for achieving climate targets. Addressing these uncertainties through improved model parametrization and evaluation is crucial to refining OAE efficiency estimates, which in turn will contribute to the development of a robust MRV system that supports effective, sustainable, and safe implementation of OAE.

# BIBLIOGRAPHY

# BIBLIOGRAPHY

---

Adloff, M., Reick, C. H., and Claussen, M. (2018). “Earth system model simulations show different feedback strengths of the terrestrial carbon cycle under glacial and interglacial conditions”. In: *Earth System Dynamics* 9.2, pp. 413–425. ISSN: 2190-4979. DOI: `10.5194/esd-9-413-2018`.

Amundson, R. (2001). “The Carbon Budget in Soils”. In: *Annual Review of Earth and Planetary Sciences* 29 (Volume 29, 2001), pp. 535–562. ISSN: 0084-6597, 1545-4495. DOI: `10.1146/annurev.earth.29.1.535`.

Archer, D. (2010). *The Global Carbon Cycle*. Princeton University Press. ISBN: 978-1-4008-3707-6. DOI: `10.1515/9781400837076`.

Archer, D., Kheshgi, H., and Maier-Reimer, E. (1997). “Multiple timescales for neutralization of fossil fuel CO2”. In: *Geophysical Research Letters* 24.4, pp. 405–408. ISSN: 0094-8276. DOI: `10.1029/97GL00168`.

Arrhenius, S. and Holden, E. S. (1897). “On the Influence of Carbonic Acid in the Air Upon the Temperature of the Earth”. In: *Publications of the Astronomical Society of the Pacific* 9.54. Publisher: [University of Chicago Press, Astronomical Society of the Pacific], pp. 14–24. ISSN: 0004-6280. URL: `https://www.jstor.org/stable/40670917`.

Aumont, O. and Bopp, L. (2006). “Globalizing results from ocean in situ iron fertilization studies: GLOBALIZING IRON FERTILIZATION”. In: *Global Biogeochemical Cycles* 20.2. ISSN: 08866236. DOI: `10.1029/2005GB002591`.

Baar, H. J. W. de, Jong, J. T. M. de, Bakker, D. C. E., Löscher, B. M., Veth, C., Bathmann, U., and Smetacek, V. (1995). “Importance of iron for plankton blooms and carbon dioxide drawdown in the Southern Ocean”. In: *Nature* 373.6513, pp. 412–415. ISSN: 1476-4687. DOI: `10.1038/373412a0`.

Babiker, M., Berndes, G., Blok, K., Cohen, B., Cowie, A., Geden, O., Ginzburg, V., Leip, A., Smith, P., Sugiyama, M., and Yamba, F. (2022). “Cross-sectoral perspectives”. In: *In IPCC 2022: Mitigation of Climate Change. Contribution of Working Group III to the Sixth Assessment Report of the Intergovernmental Panel on Climate Change*. Ed. by P. R. Shukla, J. Skea, R. Slade, A. Al Khourdajie, R. van Diemen, D. McCollum, M. Pathak, S. Some, P. Vyas, R. Fradera, M. Belkacemi, A. Hasija, G. Lisboa, S. Luz, and J. Malley. Cambridge, UK and New York, NY, USA: Cambridge University Press. DOI: `10.1017/9781009157926.014`.

Bach, L. T., Gill, S. J., Rickaby, R. E. M., Gore, S., and Renforth, P. (2019). “CO2 Removal With Enhanced Weathering and Ocean Alkalinity Enhancement: Potential Risks and Co-benefits for Marine Pelagic Ecosystems”. In: *Frontiers in Climate* 1. ISSN: 2624-9553. DOI: `10.3389/fclim.2019.00007`.

Bach, L. T., Ho, D. T., Boyd, P. W., and Tyka, M. D. (2023). “Toward a consensus framework to evaluate air–sea CO2 equilibration for marine CO2 removal”. In: *Limnology and Oceanography Letters* 8.5, pp. 685–691. ISSN: 2378-2242. DOI: `10.1002/lol2.10330`.

Barkakaty, B., Sumpter, B. G., Ivanov, I. N., Potter, M. E., Jones, C. W., and Lokitz, B. S. (2017). “Emerging materials for lowering atmospheric carbon”. In: *Environmental Technology and Innovation* 7, pp. 30–43. ISSN: 2352-1864. DOI: `10.1016/j.eti.2016.12.001`.

Beerling, D. J., Kantzas, E. P., Lomas, M. R., Wade, P., Eufrasio, R. M., Renforth, P., Sarkar, B., Andrews, M. G., James, R. H., Pearce, C. R., Mercure, J.-F., Pollitt, H., Holden, P. B., Edwards, N. R., Khanna, M., et al. (2020). “Potential for large-scale CO2 removal via enhanced rock weathering with croplands”. In: *Nature* 583.7815, pp. 242–248. ISSN: 1476-4687. DOI: `10.1038/s41586-020-2448-9`.

Berelson, W. M., Balch, W. M., Najjar, R., Feely, R. A., Sabine, C., and Lee, K. (2007). “Relating estimates of CaCO3 production, export, and dissolution in the water column to measurements of CaCO3 rain into sediment traps and dissolution on the sea floor: A revised global carbonate budget”. In: *Global Biogeochemical Cycles* 21.1. ISSN: 1944-9224. DOI: `10.1029/2006GB002803`.

Berger, A. (1988). “Milankovitch Theory and climate”. In: *Reviews of Geophysics* 26.4, pp. 624–657. ISSN: 1944-9208. DOI: `10.1029/RG026i004p00624`.

Berner, E. K. and Berner, R. A. (2012). *Global Environment: Water, Air, and Geochemical Cycles - Second Edition*. Princeton University Press. ISBN: 978-1-4008-4276-6. DOI: `10.1515/9781400842766`.

Berner, R. A. (1990). “Atmospheric Carbon Dioxide Levels Over Phanerozoic Time”. In: *Science* 249.4975, pp. 1382–1386. DOI: `10.1126/science.249.4975.1382`.

Blain, S., Quéguiner, B., Armand, L., Belviso, S., Bombled, B., Bopp, L., Bowie, A., Brunet, C., Brussaard, C., Carlotti, F., Christaki, U., Corbière, A., Durand, I., Ebersbach, F., Fuda, J.-L., et al. (2007). “Effect of natural iron fertilization on carbon sequestration in the Southern Ocean”. In: *Nature* 446.7139, pp. 1070–1074. ISSN: 1476-4687. DOI: `10.1038/nature05700`.

Bloom, A. A., Exbrayat, J.-F., Velde, I. R. van der, Feng, L., and Williams, M. (2016). “The decadal state of the terrestrial carbon cycle: Global retrievals of terrestrial carbon allocation, pools, and residence times”. In: *Proceedings of the National Academy of Sciences* 113.5, pp. 1285–1290. DOI: `10.1073/pnas.1515160113`.

Boudreau, B. P., Middelburg, J. J., and Luo, Y. (2018). “The role of calcification in carbonate compensation”. In: *Nature Geoscience* 11.12, pp. 894–900. ISSN: 1752-0908. DOI: `10.1038/s41561-018-0259-5`.

Boudreau, B. P., Middelburg, J. J., and Meysman, F. J. R. (2010). “Carbonate compensation dynamics”. In: *Geophysical Research Letters* 37.3. ISSN: 1944-8007. DOI: `10.1029/2009GL041847`.

Boyd, P. W. and Trull, T. W. (2007). “Understanding the export of biogenic particles in oceanic waters: Is there consensus?” In: *Progress in Oceanography* 72.4, pp. 276–312. ISSN: 0079-6611. DOI: `10.1016/j.pocean.2006.10.007`.

Boyd, P. W., Claustre, H., Levy, M., Siegel, D. A., and Weber, T. (2019). “Multi-faceted particle pumps drive carbon sequestration in the ocean”. In: *Nature* 568.7752, pp. 327–335. ISSN: 1476-4687. DOI: `10.1038/s41586-019-1098-2`.

Bradshaw, C. J. A. and Warkentin, I. G. (2015). “Global estimates of boreal forest carbon stocks and flux”. In: *Global and Planetary Change* 128, pp. 24–30. ISSN: 0921-8181. DOI: `10.1016/j.gloplacha.2015.02.004`.

Broecker, W. S. (2008). “A need to improve reconstructions of the fluctuations in the calcite compensation depth over the course of the Cenozoic”. In: *Paleoceanography* 23.1. ISSN: 1944-9186. DOI: `10.1029/2007PA001456`.

Brovkin, V., Ganopolski, A., Archer, D., and Rahmstorf, S. (2007). “Lowering of glacial atmospheric CO2 in response to changes in oceanic circulation and marine biogeochemistry”. In: *Paleoceanography* 22.4. ISSN: 1944-9186. DOI: `10.1029/2006PA001380`.

Buitenhuis, E. T., Le Quéré, C., Bednaršek, N., and Schiebel, R. (2019). “Large Contribution of Pteropods to Shallow CaCO3 Export”. In: *Global Biogeochemical Cycles* 33.3, pp. 458–468. ISSN: 1944-9224. DOI: `10.1029/2018GB006110`.

Burt, D. J., Fröb, F., and Ilyina, T. (2021). “The Sensitivity of the Marine Carbonate System to Regional Ocean Alkalinity Enhancement”. In: *Frontiers in Climate* 3. ISSN: 2624-9553. URL: `https://www.frontiersin.org/articles/10.3389/fclim.2021.624075`.

Butenschön, M., Lovato, T., Masina, S., Caserini, S., and Grosso, M. (2021). “Alkalinization Scenarios in the Mediterranean Sea for Efficient Removal of Atmospheric CO2 and the Mitigation of Ocean Acidification”. In: *Frontiers in Climate* 3. ISSN: 2624-9553. URL: `https://www.frontiersin.org/articles/10.3389/fclim.2021.614537`.

Caesar, L., Rahmstorf, S., Robinson, A., Feulner, G., and Saba, V. (2018). “Observed fingerprint of a weakening Atlantic Ocean overturning circulation”. In: *Nature* 556.7700, pp. 191–196. ISSN: 1476-4687. DOI: `10.1038/s41586-018-0006-5`.

Caldeira, K. and Rau, G. H. (2000). “Accelerating carbonate dissolution to sequester carbon dioxide in the ocean: Geochemical implications”. In: *Geophysical Research Letters* 27.2, pp. 225–228. ISSN: 1944-8007. DOI: `10.1029/1999GL002364`.

Caldeira, K. and Wickett, M. E. (2005). “Ocean model predictions of chemistry changes from carbon dioxide emissions to the atmosphere and ocean”. In: *Journal of Geophysical Research: Oceans* 110 (C9). ISSN: 2156-2202. DOI: `10.1029/2004JC002671`.

Canadell, J., Monteiro, P., Costa, M., Cotrim da Cunha, L., Cox, P., Eliseev, A., Henson, S., Ishii, M., Jaccard, S., Koven, C., Lohila, A., Patra, P., Piao, S., Rogelj, J., Syampungani, S., et al. (2021). “Global Carbon and other Biogeochemical Cycles and Feedbacks”. In: *Climate Change 2021: The Physical Science Basis. Contribution of Working Group I to the Sixth Assessment Report of the Intergovernmental Panel on Climate Change*. Ed. by V. Masson-Delmotte, P. Zhai, A. Pirani, S. Connors, C. Péan, S. Berger, N. Caud, Y. Chen, L. Goldfarb, M. Gomis, M. Huang, K. Leitzell,

E. Lonnoy, J. Matthews, T. Maycock, et al. Cambridge, United Kingdom and New York, NY, USA: Cambridge University Press, pp. 673–816. DOI: `10.1017/9781009157896.007`.

Cao, M. and Woodward, F. I. (1998). "Dynamic responses of terrestrial ecosystem carbon cycling to global climate change". In: *Nature* 393.6682, pp. 249–252. ISSN: 1476-4687. DOI: `10.1038/30460`.

Cartapanis, O., Galbraith, E. D., Bianchi, D., and Jaccard, S. L. (2018). "Carbon burial in deep-sea sediment and implications for oceanic inventories of carbon and alkalinity over the last glacial cycle". In: *Climate of the Past* 14.11, pp. 1819–1850. ISSN: 1814-9324. DOI: `10.5194/cp-14-1819-2018`.

Carter, B. R., Feely, R. A., Lauvset, S. K., Olsen, A., DeVries, T., and Sonnerup, R. (2021). "Preformed Properties for Marine Organic Matter and Carbonate Mineral Cycling Quantification". In: *Global Biogeochemical Cycles* 35.1, e2020GB006623. ISSN: 1944-9224. DOI: `10.1029/2020GB006623`.

Caserini, S., Storni, N., and Grosso, M. (2022). "The Availability of Limestone and Other Raw Materials for Ocean Alkalinity Enhancement". In: *Global Biogeochemical Cycles* 36.5, e2021GB007246. ISSN: 1944-9224. DOI: `10.1029/2021GB007246`.

Coninck, H. d. and Benson, S. M. (2014). "Carbon Dioxide Capture and Storage: Issues and Prospects". In: *Annual Review of Environment and Resources* 39 (Volume 39, 2014), pp. 243–270. ISSN: 1543-5938, 1545-2050. DOI: `10.1146/annurev-environ-032112-095222`.

Creutzig, F., Ravindranath, N. H., Berndes, G., Bolwig, S., Bright, R., Cherubini, F., Chum, H., Corbera, E., Delucchi, M., Faaij, A., Fargione, J., Haberl, H., Heath, G., Lucon, O., Plevin, R., et al. (2015). "Bioenergy and climate change mitigation: an assessment". In: *GCB Bioenergy* 7.5, pp. 916–944. ISSN: 1757-1707. DOI: `10.1111/gcbb.12205`.

Cusack, M. and Freer, A. (2008). "Biomineralization: Elemental and Organic Influence in Carbonate Systems". In: *Chemical Reviews* 108.11, pp. 4433–4454. ISSN: 0009-2665. DOI: `10.1021/cr078270o`.

Davidson, E. A. and Janssens, I. A. (2006). "Temperature sensitivity of soil carbon decomposition and feedbacks to climate change". In: *Nature* 440.7081, pp. 165–173. ISSN: 1476-4687. DOI: `10.1038/nature04514`.

DeGryze, S., Six, J., Paustian, K., Morris, S. J., Paul, E. A., and Merckx, R. (2004). "Soil organic carbon pool changes following land-use conversions". In: *Global Change Biology* 10.7, pp. 1120–1132. ISSN: 1365-2486. DOI: `10.1111/j.1529-8817.2003.00786.x`. (Visited on 11/11/2024).

DeVries, T. (2022a). "Atmospheric CO2 and Sea Surface Temperature Variability Cannot Explain Recent Decadal Variability of the Ocean CO2 Sink". In: *Geophysical Research Letters* 49.7, e2021GL096018. ISSN: 1944-8007. DOI: `10.1029/2021GL096018`.

– (2022b). "The Ocean Carbon Cycle". In: *Annual Review of Environment and Resources* 47.1, pp. 317–341. ISSN: 1543-5938, 1545-2050. DOI: `10.1146/annurev-environ-120920-111307`.

Dickson, A. G. (1981). “An exact definition of total alkalinity and a procedure for the estimation of alkalinity and total inorganic carbon from titration data”. In: *Deep Sea Research Part A. Oceanographic Research Papers* 28.6, pp. 609–623. ISSN: 0198-0149. DOI: `10.1016/0198-0149(81)90121-7`.

Dickson, A. G. and Millero, F. J. (1987). “A comparison of the equilibrium constants for the dissociation of carbonic acid in seawater media”. In: *Deep Sea Research Part A. Oceanographic Research Papers* 34.10, pp. 1733–1743. ISSN: 0198-0149. DOI: `10.1016/0198-0149(87)90021-5`.

Dickson, R. R. and Brown, J. (1994). “The production of North Atlantic Deep Water: Sources, rates, and pathways”. In: *Journal of Geophysical Research: Oceans* 99 (C6), pp. 12319–12341. ISSN: 2156-2202. DOI: `10.1029/94JC00530`.

Donato, D. C., Kauffman, J. B., Murdiyarso, D., Kurnianto, S., Stidham, M., and Kanninen, M. (2011). “Mangroves among the most carbon-rich forests in the tropics”. In: *Nature Geoscience* 4.5, pp. 293–297. ISSN: 1752-0908. DOI: `10.1038/ngeo1123`.

Dooley, K., Keith, H., Larson, A., Catacora-Vargas, G., Carton, W., Kirstine Lund, C., Ojong, E., Frechette, A., Hugh, S., Ivetic, N., Li Ching, L., Lund, J., Luqman, M., Mackey, B., Monterroso, I., et al. (2023). “The LandGap Report”. In: URL: `https://landgap.org/downloads/2023/Land-Gap-Report_2023-Briefing_FINAL_Jun24.pdf`.

Duarte, C. M., Middelburg, J. J., and Caraco, N. (2005). “Major role of marine vegetation on the oceanic carbon cycle”. In: *Biogeosciences* 2.1, pp. 1–8. ISSN: 1726-4170. DOI: `10.5194/bg-2-1-2005`.

Duarte, C. M., Losada, I. J., Hendriks, I. E., Mazarrasa, I., and Marbà, N. (2013). “The role of coastal plant communities for climate change mitigation and adaptation”. In: *Nature Climate Change* 3.11, pp. 961–968. ISSN: 1758-6798. DOI: `10.1038/nclimate1970`.

Dunne, J. P., Sarmiento, J. L., and Gnanadesikan, A. (2007). “A synthesis of global particle export from the surface ocean and cycling through the ocean interior and on the seafloor”. In: *Global Biogeochemical Cycles* 21.4. ISSN: 1944-9224. DOI: `10.1029/2006GB002907`.

Dutreuil, S., Bopp, L., and Tagliabue, A. (2009). “Impact of enhanced vertical mixing on marine biogeochemistry: lessons for geo-engineering and natural variability”. In: *Biogeosciences* 6.5, pp. 901–912. ISSN: 1726-4170. DOI: `10.5194/bg-6-901-2009`.

Egleston, E. S., Sabine, C. L., and Morel, F. M. M. (2010). “Revelle revisited: Buffer factors that quantify the response of ocean chemistry to changes in DIC and alkalinity”. In: *Global Biogeochemical Cycles* 24.1. ISSN: 1944-9224. DOI: `10.1029/2008GB003407`.

Eisaman, M. D., Geilert, S., Renforth, P., Bastianini, L., Campbell, J., Dale, A. W., Foteinis, S., Grasse, P., Hawrot, O., Löscher, C. R., Rau, G. H., and Rønning, J. (2023). “Assessing the technical aspects of ocean-alkalinity-enhancement approaches”. In: *State of the Planet* 2-oae2023, pp. 1–29. DOI: `10.5194/sp-2-oae2023-3-2023`.

Eisaman, M. D., Parajuly, K., Tuganov, A., Eldershaw, C., Chang, N., and Littau, K. A. (2012). "CO2 extraction from seawater using bipolar membrane electrodialysis". In: *Energy & Environmental Science* 5.6, pp. 7346–7352. ISSN: 1754-5706. DOI: `10.1039/C2EE03393C`.

Elderfield, H. (2002). "Carbonate Mysteries". In: *Science* 296.5573, pp. 1618–1621. DOI: `10.1126/science.1072079`.

Emerson, S. and Hedges, J. (2008). *Chemical Oceanography and the Marine Carbon Cycle*. Cambridge University Press. 696 pp. ISBN: 978-1-139-47161-9.

Fakhraee, M., Planavsky, N. J., and Reinhard, C. T. (2023). "Ocean alkalinity enhancement through restoration of blue carbon ecosystems". In: *Nature Sustainability*, pp. 1–8. ISSN: 2398-9629. DOI: `10.1038/s41893-023-01128-2`.

Falkowski, P., Scholes, R. J., Boyle, E., Canadell, J., Canfield, D., Elser, J., Gruber, N., Hibbard, K., Högberg, P., Linder, S., Mackenzie, F. T., Moore III, B., Pedersen, T., Rosenthal, Y., Seitzinger, S., et al. (2000). "The Global Carbon Cycle: A Test of Our Knowledge of Earth as a System". In: *Science* 290.5490. Publisher: American Association for the Advancement of Science, pp. 291–296. DOI: `10.1126/science.290.5490.291`.

Falkowski, P. G., Barber, R. T., and Smetacek, V. (1998). "Biogeochemical Controls and Feedbacks on Ocean Primary Production". In: *Science* 281.5374, pp. 200–206. DOI: `10.1126/science.281.5374.200`.

Feely, R. A., Sabine, C. L., Takahashi, T., and Wanninkhof, R. (2001). "Uptake and Storage of Carbon Dioxide in the Ocean:" in.

Feely, R. A., Sabine, C. L., Lee, K., Berelson, W., Kleypas, J., Fabry, V. J., and Millero, F. J. (2004). "Impact of Anthropogenic $CO_2$ on the $CaCO_3$ System in the Oceans". In: *Science* 305.5682, pp. 362–366. DOI: `10.1126/science.1097329`.

Feng, E. Y., Koeve, W., Keller, D. P., and Oschlies, A. (2017). "Model-Based Assessment of the CO2 Sequestration Potential of Coastal Ocean Alkalinization". In: *Earth's Future* 5.12, pp. 1252–1266. ISSN: 2328-4277. DOI: `10.1002/2017EF000659`.

Fennel, K., Long, M. C., Algar, C., Carter, B., Keller, D., Laurent, A., Mattern, J. P., Musgrave, R., Oschlies, A., Ostiguy, J., Palter, J. B., and Whitt, D. B. (2023). "Modelling considerations for research on ocean alkalinity enhancement (OAE)". In: *State of the Planet* 2-oae2023, pp. 1–29. DOI: `10.5194/sp-2-oae2023-9-2023`.

Fennel, K., Mattern, J. P., Doney, S. C., Bopp, L., Moore, A. M., Wang, B., and Yu, L. (2022). "Ocean biogeochemical modelling". In: *Nature Reviews Methods Primers* 2.1, pp. 1–21. ISSN: 2662-8449. DOI: `10.1038/s43586-022-00154-2`.

Ferderer, A., Chase, Z., Kennedy, F., Schulz, K. G., and Bach, L. T. (2022). "Assessing the influence of ocean alkalinity enhancement on a coastal phytoplankton community". In: *Biogeosciences* 19.23, pp. 5375–5399. ISSN: 1726-4170. DOI: `10.5194/bg-19-5375-2022`.

Filbee-Dexter, K. and Wernberg, T. (2020). “Substantial blue carbon in overlooked Australian kelp forests”. In: *Scientific Reports* 10.1, p. 12341. ISSN: 2045-2322. DOI: `10.1038/s41598-020-69258-7`.

Fornari, W., Picano, F., Sardina, G., and Brandt, L. (2016). “Reduced particle settling speed in turbulence”. In: *Journal of Fluid Mechanics* 808, pp. 153–167. ISSN: 0022-1120, 1469-7645. DOI: `10.1017/jfm.2016.648`.

Friedlingstein, P., O’Sullivan, M., Jones, M. W., Andrew, R. M., Hauck, J., Landschützer, P., Le Quéré, C., Li, H., Luijkx, I. T., Olsen, A., Peters, G. P., Peters, W., Pongratz, J., Schwingshackl, C., Sitch, S., et al. (2024). “Global Carbon Budget 2024”. In: *Earth System Science Data Discussions*, pp. 1–133. DOI: `10.5194/essd-2024-519`.

Fuhr, M., Geilert, S., Schmidt, M., Liebetrau, V., Vogt, C., Ledwig, B., and Wallmann, K. (2022). “Kinetics of Olivine Weathering in Seawater: An Experimental Study”. In: *Frontiers in Climate* 4. ISSN: 2624-9553. URL: `https://www.frontiersin.org/articles/10.3389/fclim.2022.831587`.

Fuss, S., Johnstone, I., Hoglund, R., and Walsh, N. (2024). “Chapter 4: The Voluntary Carbon Market, The State of Carbon Dioxide Removal - 2nd Edition.” In: ed. by Center For Open Science. DOI: `10.17605/OSF.IO/MG3CY`.

Fuss, S., Lamb, W. F., Callaghan, M. W., Hilaire, J., Creutzig, F., Amann, T., Beringer, T., Garcia, W. d. O., Hartmann, J., Khanna, T., Luderer, G., Nemet, G. F., Rogelj, J., Smith, P., Vicente, J. L. V., et al. (2018). “Negative emissions—Part 2: Costs, potentials and side effects”. In: *Environmental Research Letters* 13.6, p. 063002. ISSN: 1748-9326. DOI: `10.1088/1748-9326/aabf9f`.

Gaillardet, J., Dupré, B., Louvat, P., and Allègre, C. J. (1999). “Global silicate weathering and CO2 consumption rates deduced from the chemistry of large rivers”. In: *Chemical Geology* 159.1, pp. 3–30. ISSN: 0009-2541. DOI: `10.1016/S0009-2541(99)00031-5`.

Gately, J. A., Kim, S. M., Jin, B., Brzezinski, M. A., and Iglesias-Rodriguez, M. D. (2023). “Coccolithophores and diatoms resilient to ocean alkalinity enhancement: A glimpse of hope?” In: *Science Advances* 9.24, eadg6066. DOI: `10.1126/sciadv.adg6066`.

Gattuso, J.-P., Magnan, A. K., Bopp, L., Cheung, W. W. L., Duarte, C. M., Hinkel, J., Mcleod, E., Micheli, F., Oschlies, A., Williamson, P., Billé, R., Chalastani, V. I., Gates, R. D., Irisson, J.-O., Middelburg, J. J., et al. (2018). “Ocean Solutions to Address Climate Change and Its Effects on Marine Ecosystems”. In: *Frontiers in Marine Science* 5. ISSN: 2296-7745. DOI: `10.3389/fmars.2018.00337`.

Gattuso, J.-P., Williamson, P., Duarte, C. M., and Magnan, A. K. (2021). “The Potential for Ocean-Based Climate Action: Negative Emissions Technologies and Beyond”. In: *Frontiers in Climate* 2. ISSN: 2624-9553. DOI: `10.3389/fclim.2020.575716`.

Geerts, L. J. J., Hylén, A., and Meysman, F. J. R. (2025). "Review and syntheses: Ocean alkalinity enhancement and carbon dioxide removal through marine enhanced rock weathering using olivine". In: *Biogeosciences* 22.2, pp. 355–384. ISSN: 1726-4170. DOI: `10.5194/bg-22-355-2025`.

Gehlen, M., Bopp, L., Emprin, N., Aumont, O., Heinze, C., and Ragueneau, O. (2006). "Reconciling surface ocean productivity, export fluxes and sediment composition in a global biogeochemical ocean model". In: *Biogeosciences* 3.4, pp. 521–537. ISSN: 1726-4170. DOI: `10.5194/bg-3-521-2006`.

Gidden, M. J., Roe, S., Ganti, G., Gasser, T., Hasegawa, T., Lamb, W. F., Ochi, Y., Strefler, J., and Vaughan, N. E. (2024). "Chapter 8: Paris-consistent CDR scenarios, The State of Carbon Dioxide Removal - 2nd Edition." In: ed. by S. M. Smith et al. DOI: `10.17605/OSF.IO/8XK7H`. URL: `https://www.stateofcdr.org`.

Giering, S. L. C., Cavan, E. L., Basedow, S. L., Briggs, N., Burd, A. B., Darroch, L. J., Guidi, L., Irisson, J.-O., Iversen, M. H., Kiko, R., Lindsay, D., Marcolin, C. R., McDonnell, A. M. P., Möller, K. O., Passow, U., et al. (2020). "Sinking Organic Particles in the Ocean-Flux Estimates From in situ Optical Devices". In: *Frontiers in Marine Science* 6. ISSN: 2296-7745. DOI: `10.3389/fmars.2019.00834`.

González, M. F. and Ilyina, T. (2016). "Impacts of artificial ocean alkalinization on the carbon cycle and climate in Earth system simulations". In: *Geophysical Research Letters* 43.12, pp. 6493–6502. ISSN: 1944-8007. DOI: `10.1002/2016GL068576`.

Gruber, N. (2011). "Warming up, turning sour, losing breath: ocean biogeochemistry under global change". In: *Philosophical Transactions of the Royal Society A: Mathematical, Physical and Engineering Sciences* 369.1943, pp. 1980–1996. DOI: `10.1098/rsta.2011.0003`.

Gruber, N., Clement, D., Carter, B. R., Feely, R. A., Heuven, S. van, Hoppema, M., Ishii, M., Key, R. M., Kozyr, A., Lauvset, S. K., Lo Monaco, C., Mathis, J. T., Murata, A., Olsen, A., Perez, F. F., et al. (2019). "The oceanic sink for anthropogenic CO $_2$ from 1994 to 2007". In: *Science* 363.6432, pp. 1193–1199. ISSN: 0036-8075, 1095-9203. DOI: `10.1126/science.aau5153`.

Guidi, L., Legendre, L., Reygondeau, G., Uitz, J., Stemmann, L., and Henson, S. A. (2015). "A new look at ocean carbon remineralization for estimating deepwater sequestration". In: *Global Biogeochemical Cycles* 29.7, pp. 1044–1059. ISSN: 1944-9224. DOI: `10.1002/2014GB005063`.

Guo, J. A., Strzepek, R., Willis, A., Ferderer, A., and Bach, L. T. (2022). "Investigating the effect of nickel concentration on phytoplankton growth to assess potential side-effects of ocean alkalinity enhancement". In: *Biogeosciences* 19.15, pp. 3683–3697. ISSN: 1726-4170. DOI: `10.5194/bg-19-3683-2022`.

Guo, L. B. and Gifford, R. M. (2002). "Soil carbon stocks and land use change: a meta analysis". In: *Global Change Biology* 8.4, pp. 345–360. ISSN: 1365-2486. DOI: `10.1046/j.1354-1013.2002.00486.x`.

Güssow, K., Proelss, A., Oschlies, A., Rehdanz, K., and Rickels, W. (2010). "Ocean iron fertilization: Why further research is needed". In: *Marine Policy* 34.5, pp. 911–918. ISSN: 0308-597X. DOI: `10.1016/j.marpol.2010.01.015`.

Hangx, S. J. T. and Spiers, C. J. (2009). "Coastal spreading of olivine to control atmospheric CO2 concentrations: A critical analysis of viability". In: *International Journal of Greenhouse Gas Control* 3.6, pp. 757–767. ISSN: 1750-5836. DOI: `10.1016/j.ijggc.2009.07.001`.

Hartin, C. A., Fine, R. A., Sloyan, B. M., Talley, L. D., Chereskin, T. K., and Happell, J. (2011). "Formation rates of Subantarctic mode water and Antarctic intermediate water within the South Pacific". In: *Deep Sea Research Part I: Oceanographic Research Papers* 58.5, pp. 524–534. ISSN: 0967-0637. DOI: `10.1016/j.dsr.2011.02.010`.

Hartmann, D. L., Ramanathan, V., Berroir, A., and Hunt, G. E. (1986). "Earth Radiation Budget data and climate research". In: *Reviews of Geophysics* 24.2, pp. 439–468. ISSN: 1944-9208. DOI: `10.1029/RG024i002p00439`.

Hartmann, J., Moosdorf, N., Lauerwald, R., Hinderer, M., and West, A. J. (2014). "Global chemical weathering and associated P-release — The role of lithology, temperature and soil properties". In: *Chemical Geology* 363, pp. 145–163. ISSN: 0009-2541. DOI: `10.1016/j.chemgeo.2013.10.025`.

Hartmann, J., Suitner, N., Lim, C., Schneider, J., Marín-Samper, L., Arístegui, J., Renforth, P., Taucher, J., and Riebesell, U. (2023). "Stability of alkalinity in ocean alkalinity enhancement (OAE) approaches – consequences for durability of $CO_2$ storage". In: *Biogeosciences* 20.4, pp. 781–802. ISSN: 1726-4170. DOI: `10.5194/bg-20-781-2023`.

Hartmann, J., West, A. J., Renforth, P., Köhler, P., De La Rocha, C. L., Wolf-Gladrow, D. A., Dürr, H. H., and Scheffran, J. (2013). "Enhanced chemical weathering as a geoengineering strategy to reduce atmospheric carbon dioxide, supply nutrients, and mitigate ocean acidification: ENHANCED WEATHERING". In: *Reviews of Geophysics* 51.2, pp. 113–149. ISSN: 87551209. DOI: `10.1002/rog.20004`.

Hauck, J., Hoppema, M., Bellerby, R. G. J., Völker, C., and Wolf-Gladrow, D. (2010). "Data-based estimation of anthropogenic carbon and acidification in the Weddell Sea on a decadal timescale". In: *Journal of Geophysical Research: Oceans* 115 (C3). ISSN: 2156-2202. DOI: `10.1029/2009JC005479`.

Hauck, J., Gregor, L., Nissen, C., Patara, L., Hague, M., Mongwe, P., Bushinsky, S., Doney, S. C., Gruber, N., Le Quéré, C., Manizza, M., Mazloff, M., Monteiro, P. M. S., and Terhaar, J. (2023). "The Southern Ocean Carbon Cycle 1985–2018: Mean, Seasonal Cycle, Trends, and Storage". In: *Global Biogeochemical Cycles* 37.11, e2023GB007848. ISSN: 1944-9224. DOI: `10.1029/2023GB007848`.

Hauck, J., Köhler, P., Wolf-Gladrow, D., and Völker, C. (2016). "Iron fertilisation and century-scale effects of open ocean dissolution of olivine in a simulated $CO_2$ removal experiment".

In: *Environmental Research Letters* 11.2, p. 024007. ISSN: 1748-9326. DOI: `10.1088/1748-9326/11/2/024007`.

Hayes, C. T., Costa, K. M., Anderson, R. F., Calvo, E., Chase, Z., Demina, L. L., Dutay, J.-C., German, C. R., Heimbürger-Boavida, L.-E., Jaccard, S. L., Jacobel, A., Kohfeld, K. E., Kravchishina, M. D., Lippold, J., Mekik, F., et al. (2021). "Global Ocean Sediment Composition and Burial Flux in the Deep Sea". In: *Global Biogeochemical Cycles* 35.4, e2020GB006769. ISSN: 1944-9224. DOI: `10.1029/2020GB006769`.

He, J. and Tyka, M. D. (2023). "Limits and $CO_2$ equilibration of near-coast alkalinity enhancement". In: *Biogeosciences* 20.1, pp. 27–43. ISSN: 1726-4170. DOI: `10.5194/bg-20-27-2023`.

Held, I. M. and Soden, B. J. (2000). "Water Vapor Feedback and Global Warming1". In: *Annual Review of Environment and Resources* 25 (Volume 25, 2000), pp. 441–475. ISSN: 1543-5938, 1545-2050. DOI: `10.1146/annurev.energy.25.1.441`.

Henson, S. A., Sanders, R., Madsen, E., Morris, P. J., Le Moigne, F., and Quartly, G. D. (2011). "A reduced estimate of the strength of the ocean's biological carbon pump". In: *Geophysical Research Letters* 38.4. ISSN: 1944-8007. DOI: `10.1029/2011GL046735`.

Hinrichs, C., Köhler, P., Völker, C., and Hauck, J. (2023). "Alkalinity biases in CMIP6 Earth system models and implications for simulated $CO_2$ drawdown via artificial alkalinity enhancement". In: *Biogeosciences* 20.18, pp. 3717–3735. ISSN: 1726-4170. DOI: `10.5194/bg-20-3717-2023`.

Ho, D. T. and Bopp, L. (2024). "Marine carbon dioxide removal may be a future climate solution". In: *Dialogues on Climate Change* 1.1, pp. 56–62. ISSN: 2976-8659. DOI: `10.1177/29768659241293223`.

Ho, D. T., Bopp, L., Palter, J. B., Long, M. C., Boyd, P. W., Neukermans, G., and Bach, L. T. (2023). "Monitoring, reporting, and verification for ocean alkalinity enhancement". In: *State of the Planet* 2-oae2023, pp. 1–12. DOI: `10.5194/sp-2-oae2023-12-2023`. URL: `https://sp.copernicus.org/articles/2-oae2023/12/2023/`.

Ho, D. T., Law, C. S., Smith, M. J., Schlosser, P., Harvey, M., and Hill, P. (2006). "Measurements of air-sea gas exchange at high wind speeds in the Southern Ocean: Implications for global parameterizations". In: *Geophysical Research Letters* 33.16. ISSN: 1944-8007. DOI: `10.1029/2006GL026817`.

Hoegh-Guldberg, O., Cai, R., Poloczanska, E. S., Brewer, P. G., Sundby, S., Hilmi, K., Fabry, V. J., and Jung, S. (2014). "The Ocean". In: *Climate Change 2014: Impacts, Adaptation, and Vulnerability. Part B: Regional Aspects*. Ed. by V. R. Barros, C. B. Field, D. J. Dokken, M. D. Mastrandrea, K. J. Mach, T. E. Bilir, M. Chatterjee, K. L. Ebi, Y. O. Estrada, R. C. Genova, B. Girma, E. S. Kissel, A. N. Levy, S. MacCracken, P. R. Mastrandrea, et al. Cambridge, United Kingdom and New York, NY, USA: Cambridge University Press, pp. 1655–1731.

Hoegh-Guldberg, O., Jacob, D., Taylor, M., Bindi, M., Brown, S., Camilloni, I., Diedhiou, A., Djalante, R., Ebi, K. L., Engelbrecht, F., Guiot, J., Hijioka, Y., Mehrotra, S., Payne, A., Seneviratne, S. I., et al. (2018). “Impacts of 1.5°C Global Warming on Natural and Human Systems”. In: *Global Warming of 1.5°C. An IPCC Special Report on the impacts of global warming of 1.5°C above pre-industrial levels and related global greenhouse gas emission pathways, in the context of strengthening the global response to the threat of climate change, sustainable development, and efforts to eradicate poverty*. Ed. by V. Masson-Delmotte, P. Zhai, H.-O. Pörtner, D. Roberts, J. Skea, P. R. Shukla, A. Pirani, W. Moufouma-Okia, C. Péan, R. Pidcock, S. Connors, J. B. R. Matthews, Y. Chen, X. Zhou, M. I. Gomis, et al. Cambridge, UK and New York, NY, USA: Cambridge University Press, pp. 175–312. DOI: `10.1017/9781009157940.005`. URL: `https://doi.org/10.1017/9781009157940.005`.

Holloway, S. and Burnard, K. (2009). “Storage capacity and containment issues for carbon dioxide capture and geological storage on the UK continental shelf”. In: *Proceedings of the Institution of Mechanical Engineers, Part A: Journal of Power and Energy* 223.3, pp. 239–248. ISSN: 0957-6509. DOI: `10.1243/09576509JPE650`.

Iglesias-Rodríguez, M. D., Rickaby, R. E. M., Singh, A., and Gately, J. A. (2023). “Laboratory experiments in ocean alkalinity enhancement research”. In: *State of the Planet* 2-oae2023, pp. 1–18. DOI: `10.5194/sp-2-oae2023-5-2023`.

Ilyina, T., Wolf-Gladrow, D., Munhoven, G., and Heinze, C. (2013). “Assessing the potential of calcium-based artificial ocean alkalinization to mitigate rising atmospheric CO $_2$ and ocean acidification: MODELING MITIGATION POTENTIAL OF AOA”. In: *Geophysical Research Letters* 40.22, pp. 5909–5914. ISSN: 00948276. DOI: `10.1002/2013GL057981`.

Ingrosso, G., Giani, M., Kralj, M., Comici, C., Rivaro, P., Budillon, G., Castagno, P., Zoccarato, L., and Celussi, M. (2022). “Physical and biological controls on anthropogenic CO2 sink of the Ross Sea”. In: *Frontiers in Marine Science* 9. ISSN: 2296-7745. DOI: `10.3389/fmars.2022.954059`.

IPCC (2018). “Annex I: Glossary”. In: *Global Warming of 1.5°C. An IPCC Special Report on the impacts of global warming of 1.5°C above pre-industrial levels and related global greenhouse gas emission pathways, in the context of strengthening the global response to the threat of climate change, sustainable development, and efforts to eradicate poverty*. Ed. by V. Masson-Delmotte, P. Zhai, H.-O. Pörtner, D. Roberts, J. Skea, P. Shukla, A. Pirani, W. Moufouma-Okia, C. Péan, R. Pidcock, S. Connors, J. Matthews, Y. Chen, X. Zhou, M. Gomis, et al. Cambridge, UK and New York, NY, USA: Cambridge University Press, pp. 541–562. DOI: `10.1017/9781009157940.008`.

– (2019). *Climate Change and Land: an IPCC special report on climate change, desertification, land degradation, sustainable land management, food security, and greenhouse gas fluxes in terrestrial ecosystems*. Ed. by P. R. Shukla, J. Skea, E. C. Buendia, V. Masson-Delmotte, H.-O. Pörtner, D. C. Roberts, P. Zhai, R. Slade, S. Connors, R. van Diemen, M. Ferrat, E. Haughey, S. Luz, S. Neogi, M. Pathak, et al. In press.

– (2023). *Climate Change 2023: Synthesis Report. Contribution of Working Groups I, II and III to the Sixth Assessment Report of the Intergovernmental Panel on Climate Change*. Ed. by C. W. Team, H. Lee, and J. Romero. Geneva, Switzerland: IPCC, p. 184. DOI: `10.59327/IPCC/AR6-9789291691647`.

Iudicone, D., Rodgers, K. B., Plancherel, Y., Aumont, O., Ito, T., Key, R. M., Madec, G., and Ishii, M. (2016). "The formation of the ocean's anthropogenic carbon reservoir". In: *Scientific Reports* 6.1, p. 35473. ISSN: 2045-2322. DOI: `10.1038/srep35473`.

Jackson, R. B., Lajtha, K., Crow, S. E., Hugelius, G., Kramer, M. G., and Piñeiro, G. (2017). "The ecology of soil carbon: pools, vulnerabilities, and biotic and abiotic controls". In: *Annual review of ecology, evolution, and systematics* 48.1, pp. 419–445. DOI: `https://doi.org/10.1146/annurev-ecolsys-112414-054234`.

Jackson, R. B., Randerson, J. T., Canadell, J. G., Anderson, R. G., Avissar, R., Baldocchi, D. D., Bonan, G. B., Caldeira, K., Diffenbaugh, N. S., Field, C. B., Hungate, B. A., Jobbágy, E. G., Kueppers, L. M., Nosetto, M. D., and Pataki, D. E. (2008). "Protecting climate with forests". In: *Environmental Research Letters* 3.4, p. 044006. ISSN: 1748-9326. DOI: `10.1088/1748-9326/3/4/044006`.

Jahnke, R. A. (1996). "The global ocean flux of particulate organic carbon: Areal distribution and magnitude". In: *Global Biogeochemical Cycles* 10.1, pp. 71–88. ISSN: 1944-9224. DOI: `10.1029/95GB03525`.

Jansen, H. and Wolf-Gladrow, D. A. (2002). "Carbonate dissolution in copepod guts: a numerical model". In: *Marine Ecology Progress Series* 221, pp. 199–207. URL: `https://www.int-res.com/abstracts/meps/v221/p199-207/`.

Jansen, H., Zeebe, R. E., and Wolf-Gladrow, D. A. (2002). "Modeling the dissolution of settling CaCO3 in the ocean". In: *Global Biogeochemical Cycles* 16.2, pp. 11–1–11–16. ISSN: 1944-9224. DOI: `10.1029/2000GB001279`.

Jeansson, E., Olsen, A., and Jutterström, S. (2017). "Arctic Intermediate Water in the Nordic Seas, 1991–2009". In: *Deep Sea Research Part I: Oceanographic Research Papers* 128, pp. 82–97. ISSN: 0967-0637. DOI: `10.1016/j.dsr.2017.08.013`.

Jeltsch-Thömmes, A., Tran, G., Lienert, S., Keller, D. P., Oschlies, A., and Joos, F. (2024). "Earth system responses to carbon dioxide removal as exemplified by ocean alkalinity enhancement: tradeoffs and lags". In: *Environmental Research Letters* 19.5, p. 054054. ISSN: 1748-9326. DOI: `10.1088/1748-9326/ad4401`.

Jiang, L.-Q., Carter, B. R., Feely, R. A., Lauvset, S. K., and Olsen, A. (2019). "Surface ocean pH and buffer capacity: past, present and future". In: *Scientific Reports* 9.1, p. 18624. ISSN: 2045-2322. DOI: `10.1038/s41598-019-55039-4`.

Johannessen, S. C. and Christian, J. R. (2023). "Why blue carbon cannot truly offset fossil fuel emissions". In: *Communications Earth & Environment* 4.1, pp. 1–4. ISSN: 2662-4435. DOI: `10.1038/s43247-023-01068-x`.

Jones, D. C., Ito, T., Takano, Y., and Hsu, W.-C. (2014). "Spatial and seasonal variability of the air-sea equilibration timescale of carbon dioxide". In: *Global Biogeochemical Cycles* 28.11, pp. 1163–1178. ISSN: 1944-9224. DOI: `10.1002/2014GB004813`.

Joseph, S., Cowie, A. L., Van Zwieten, L., Bolan, N., Budai, A., Buss, W., Cayuela, M. L., Graber, E. R., Ippolito, J. A., Kuzyakov, Y., Luo, Y., Ok, Y. S., Palansooriya, K. N., Shepherd, J., Stephens, S., et al. (2021). "How biochar works, and when it doesn't: A review of mechanisms controlling soil and plant responses to biochar". In: *GCB Bioenergy* 13.11, pp. 1731–1764. ISSN: 1757-1707. DOI: `10.1111/gcbb.12885`.

Jürchott, M., Oschlies, A., and Koeve, W. (2023). "Artificial Upwelling—A Refined Narrative". In: *Geophysical Research Letters* 50.4, e2022GL101870. ISSN: 1944-8007. DOI: `10.1029/2022GL101870`.

Keeling, C. D., Piper, S. C., Bacastow, R. B., Wahlen, M., Whorf, T. P., Heimann, M., and Meijer, H. A. (2005). "Atmospheric CO2 and 13CO2 Exchange with the Terrestrial Biosphere and Oceans from 1978 to 2000: Observations and Carbon Cycle Implications". In: *A History of Atmospheric CO2 and Its Effects on Plants, Animals, and Ecosystems*. Ed. by I. Baldwin, M. Caldwell, G. Heldmaier, R. B. Jackson, O. Lange, H. Mooney, E.-D. Schulze, U. Sommer, J. R. Ehleringer, M. Denise Dearing, and T. E. Cerling. New York, NY: Springer, pp. 83–113. ISBN: 978-0-387-27048-7. DOI: `10.1007/0-387-27048-5_5`.

Keith, M. L., Anderson, G. M., and Eichler, R. (1964). "Carbon and oxygen isotopic composition of mollusk shells from marine and fresh-water environments". In: *Geochimica et Cosmochimica Acta* 28.10, pp. 1757–1786. ISSN: 0016-7037. DOI: `10.1016/0016-7037(64)90021-3`.

Keller, D. P., Feng, E. Y., and Oschlies, A. (2014). "Potential climate engineering effectiveness and side effects during a high carbon dioxide-emission scenario". In: *Nature Communications* 5.1, p. 3304. ISSN: 2041-1723. DOI: `10.1038/ncomms4304`.

Keller, D. P., Lenton, A., Littleton, E. W., Oschlies, A., Scott, V., and Vaughan, N. E. (2018). "The Effects of Carbon Dioxide Removal on the Carbon Cycle". In: *Current Climate Change Reports* 4.3, pp. 250–265. ISSN: 2198-6061. DOI: `10.1007/s40641-018-0104-3`.

Keppler, L., Landschützer, P., Lauvset, S. K., and Gruber, N. (2023). "Recent Trends and Variability in the Oceanic Storage of Dissolved Inorganic Carbon". In: *Global Biogeochemical Cycles* 37.5, e2022GB007677. ISSN: 1944-9224. DOI: `10.1029/2022GB007677`.

Khatiwala, S., Primeau, F., and Hall, T. (2009). "Reconstruction of the history of anthropogenic CO2 concentrations in the ocean". In: *Nature* 462.7271, pp. 346–349. ISSN: 1476-4687. DOI: `10.1038/nature08526`.

Khatiwala, S., Schmittner, A., and Muglia, J. (2019). "Air-sea disequilibrium enhances ocean carbon storage during glacial periods". In: *Science Advances* 5.6, eaaw4981. DOI: `10.1126/sciadv.aaw4981`.

Kheshgi, H. S. (1995). "Sequestering atmospheric carbon dioxide by increasing ocean alkalinity". In: *Energy* 20.9, pp. 915–922. ISSN: 0360-5442. DOI: `10.1016/0360-5442(95)00035-F`.

Knecht, N. S., Benedetti, F., Hofmann Elizondo, U., Bednaršek, N., Chaabane, S., Weerd, C. de, Peijnenburg, K. T. C. A., Schiebel, R., and Vogt, M. (2023). "The Impact of Zooplankton

Calcifiers on the Marine Carbon Cycle". In: *Global Biogeochemical Cycles* 37.6, e2022GB007685. ISSN: 1944-9224. DOI: `10.1029/2022GB007685`.

Köhler, P., Abrams, J. F., Völker, C., Hauck, J., and Wolf-Gladrow, D. A. (2013). "Geoengineering impact of open ocean dissolution of olivine on atmospheric CO $_2$ , surface ocean pH and marine biology". In: *Environmental Research Letters* 8.1, p. 014009. ISSN: 1748-9326. DOI: `10.1088/1748-9326/8/1/014009`.

Köhler, P., Hartmann, J., and Wolf-Gladrow, D. A. (2010). "Geoengineering potential of artificially enhanced silicate weathering of olivine". In: *Proceedings of the National Academy of Sciences* 107.47, pp. 20228–20233. ISSN: 0027-8424, 1091-6490. DOI: `10.1073/pnas.1000545107`.

Krause-Jensen, D. and Duarte, C. M. (2016). "Substantial role of macroalgae in marine carbon sequestration". In: *Nature Geoscience* 9.10, pp. 737–742. ISSN: 1752-0908. DOI: `10.1038/ngeo2790`.

Lacis, A. A., Schmidt, G. A., Rind, D., and Ruedy, R. A. (2010). "Atmospheric CO2: Principal Control Knob Governing Earth's Temperature". In: *Science* 330.6002, pp. 356–359. DOI: `10.1126/science.1190653`.

Lal, R. (2004). "Soil Carbon Sequestration Impacts on Global Climate Change and Food Security". In: *Science* 304.5677, pp. 1623–1627. DOI: `10.1126/science.1097396`.

Lamb, W. F., Minx, J., Vaughan, N., Gasser, T., Smith, H., Roman-Cuesta, R., Grassi, G., Pongratz, J., Smith, S., Schwingshackl, C., Gidden, M., Roe, S., Schenuit, F., and Buck, H. (2024). "Chapter 9: The CDR Gap, The State of Carbon Dioxide Removal - 2nd Edition". In: in collab. with Center For Open Science. Publisher: OSF. DOI: `10.17605/OSF.IO/6V9RF`.

Lambert, F., Tagliabue, A., Shaffer, G., Lamy, F., Winckler, G., Farias, L., Gallardo, L., and De Pol-Holz, R. (2015). "Dust fluxes and iron fertilization in Holocene and Last Glacial Maximum climates". In: *Geophysical Research Letters* 42.14, pp. 6014–6023. ISSN: 1944-8007. DOI: `10.1002/2015GL064250`.

Lannoy, C.-F. de, Eisaman, M. D., Jose, A., Karnitz, S. D., DeVaul, R. W., Hannun, K., and Rivest, J. L. B. (2018). "Indirect ocean capture of atmospheric CO2: Part I. Prototype of a negative emissions technology". In: *International Journal of Greenhouse Gas Control* 70, pp. 243–253. ISSN: 1750-5836. DOI: `10.1016/j.ijggc.2017.10.007`.

Lee, J.-Y., Marotzke, J., Bala, G., Cao, L., Corti, S., Dunne, J., Engelbrecht, F., Fischer, E., Fyfe, J., Jones, C., Maycock, A., Mutemi, J., Ndiaye, O., Panickal, S., and Zhou, T. (2021). "Future Global Climate: Scenario-Based Projections and Near-Term Information". In: *Climate Change 2021: The Physical Science Basis. Contribution of Working Group I to the Sixth Assessment Report of the Intergovernmental Panel on Climate Change*. Ed. by V. Masson-Delmotte, P. Zhai, A. Pirani, S. Connors, C. Péan, S. Berger, N. Caud, Y. Chen, L. Goldfarb, M. Gomis, M. Huang, K. Leitzell, E. Lonnoy, J. Matthews, T. Maycock, et al. Cambridge, United Kingdom and New York, NY, USA: Cambridge University Press, pp. 553–672. DOI: `10.1017/9781009157896.006`.

Lehmann, J. and Joseph, S. (2015). "Biochar for environmental management: an introduction". In: *Biochar for Environmental Management*. 2nd ed. Routledge. ISBN: 978-0-203-76226-4.

Lenton, A., Matear, R. J., Keller, D. P., Scott, V., and Vaughan, N. E. (2018). "Assessing carbon dioxide removal through global and regional ocean alkalinization under high and low emission pathways". In: *Earth System Dynamics* 9.2, pp. 339–357. ISSN: 2190-4987. DOI: `10.5194/esd-9-339-2018`.

Lisiecki, L. E. (2010). "Links between eccentricity forcing and the 100,000-year glacial cycle". In: *Nature Geoscience* 3.5, pp. 349–352. ISSN: 1752-0908. DOI: `10.1038/ngeo828`.

Locatelli, B., Catterall, C. P., Imbach, P., Kumar, C., Lasco, R., Marín-Spiotta, E., Mercer, B., Powers, J. S., Schwartz, N., and Uriarte, M. (2015). "Tropical reforestation and climate change: beyond carbon". In: *Restoration Ecology* 23.4, pp. 337–343. ISSN: 1526-100X. DOI: `10.1111/rec.12209`.

Lovelock, J. E. and Rapley, C. G. (2007). "Ocean pipes could help the Earth to cure itself". In: *Nature* 449.7161, pp. 403–403. ISSN: 1476-4687. DOI: `10.1038/449403a`.

Lüthi, D., Le Floch, M., Bereiter, B., Blunier, T., Barnola, J.-M., Siegenthaler, U., Raynaud, D., Jouzel, J., Fischer, H., Kawamura, K., and Stocker, T. F. (2008). "High-resolution carbon dioxide concentration record 650,000–800,000 years before present". In: *Nature* 453.7193, pp. 379–382. ISSN: 1476-4687. DOI: `10.1038/nature06949`.

Maier-Reimer, E., Mikolajewicz, U., and Winguth, A. (1996). "Future ocean uptake of CO2: interaction between ocean circulation and biology". In: *Climate Dynamics* 12.10, pp. 711–722. ISSN: 1432-0894. DOI: `10.1007/s003820050138`.

Marinov, I., Gnanadesikan, A., Sarmiento, J. L., Toggweiler, J. R., Follows, M., and Mignone, B. K. (2008). "Impact of oceanic circulation on biological carbon storage in the ocean and atmospheric $pCO_2$". In: *Global Biogeochemical Cycles* 22.3. ISSN: 1944-9224. DOI: `10.1029/2007GB002958`.

Martin, J. H. (1990). "Glacial-interglacial CO2 change: The Iron Hypothesis". In: *Paleoceanography* 5.1, pp. 1–13. ISSN: 1944-9186. DOI: `10.1029/PA005i001p00001`.

McCartney, M. S., Bennett, S. L., and Woodgate-Jones, M. E. (1991). "Eastward Flow through the Mid-Atlantic Ridge at 11°N and Its Influence on the Abyss of the Eastern Basin". In: ISSN: 1520-0485. URL: `https://journals.ametsoc.org/view/journals/phoc/21/8/1520-0485_1991_021_1089_efttma_2_0_co_2.xml`.

Mcleod, E., Chmura, G. L., Bouillon, S., Salm, R., Björk, M., Duarte, C. M., Lovelock, C. E., Schlesinger, W. H., and Silliman, B. R. (2011). "A blueprint for blue carbon: toward an improved understanding of the role of vegetated coastal habitats in sequestering CO2". In: *Frontiers in Ecology and the Environment* 9.10, pp. 552–560. ISSN: 1540-9309. DOI: `10.1890/110004`.

Mensa, J. A., Özgökmen, T. M., Poje, A. C., and Imberger, J. (2015). "Material transport in a convective surface mixed layer under weak wind forcing". In: *Ocean Modelling* 96, pp. 226–242. ISSN: 1463-5003. DOI: `10.1016/j.ocemod.2015.10.006`.

Middelburg, J. J., Soetaert, K., and Hagens, M. (2020). "Ocean Alkalinity, Buffering and Biogeochemical Processes". In: *Reviews of Geophysics* 58.3, e2019RG000681. ISSN: 1944-9208. DOI: `10.1029/2019RG000681`.

Milliman, J. D., Troy, P. J., Balch, W. M., Adams, A. K., Li, Y. .-., and Mackenzie, F. T. (1999). "Biologically mediated dissolution of calcium carbonate above the chemical lysocline?" In: *Deep Sea Research Part I: Oceanographic Research Papers* 46.10, pp. 1653–1669. ISSN: 0967-0637. DOI: `10.1016/S0967-0637(99)00034-5`.

Minx, J. C., Lamb, W. F., Callaghan, M. W., Fuss, S., Hilaire, J., Creutzig, F., Amann, T., Beringer, T., Garcia, W. d. O., Hartmann, J., Khanna, T., Lenzi, D., Luderer, G., Nemet, G. F., Rogelj, J., et al. (2018). "Negative emissions—Part 1: Research landscape and synthesis". In: *Environmental Research Letters* 13.6, p. 063001. ISSN: 1748-9326. DOI: `10.1088/1748-9326/aabf9b`.

Mitchell, J. F. B. (1989). "The "Greenhouse" effect and climate change". In: *Reviews of Geophysics* 27.1, pp. 115–139. ISSN: 1944-9208. DOI: `10.1029/RG027i001p00115`.

Mongin, M., Baird, M. E., Lenton, A., Neill, C., and Akl, J. (2021). "Reversing ocean acidification along the Great Barrier Reef using alkalinity injection". In: *Environmental Research Letters* 16.6, p. 064068. ISSN: 1748-9326. DOI: `10.1088/1748-9326/ac002d`.

Mongin, M., Baird, M. E., Tilbrook, B., Matear, R. J., Lenton, A., Herzfeld, M., Wild-Allen, K., Skerratt, J., Margvelashvili, N., Robson, B. J., Duarte, C. M., Gustafsson, M. S. M., Ralph, P. J., and Steven, A. D. L. (2016). "The exposure of the Great Barrier Reef to ocean acidification". In: *Nature Communications* 7.1, p. 10732. ISSN: 2041-1723. DOI: `10.1038/ncomms10732`.

Montserrat, F., Renforth, P., Hartmann, J., Leermakers, M., Knops, P., and Meysman, F. J. R. (2017). "Olivine Dissolution in Seawater: Implications for CO2 Sequestration through Enhanced Weathering in Coastal Environments". In: *Environmental Science & Technology* 51.7, pp. 3960–3972. ISSN: 0013-936X. DOI: `10.1021/acs.est.6b05942`.

Moosdorf, N., Renforth, P., and Hartmann, J. (2014). "Carbon Dioxide Efficiency of Terrestrial Enhanced Weathering". In: *Environmental Science & Technology* 48.9, pp. 4809–4816. ISSN: 0013-936X. DOI: `10.1021/es4052022`.

Moras, C. A., Bach, L. T., Cyronak, T., Joannes-Boyau, R., and Schulz, K. G. (2022). "Ocean alkalinity enhancement – avoiding runaway CaCO $_3$ precipitation during quick and hydrated lime dissolution". In: *Biogeosciences* 19.15, pp. 3537–3557. ISSN: 1726-4189. DOI: `10.5194/bg-19-3537-2022`.

Morée, A. L., Schwinger, J., Ninnemann, U. S., Jeltsch-Thömmes, A., Bethke, I., and Heinze, C. (2021). "Evaluating the biological pump efficiency of the Last Glacial Maximum ocean using". In: *Climate of the Past* 17.2, pp. 753–774. ISSN: 1814-9324. DOI: `10.5194/cp-17-753-2021`.

Morse, J. W. and He, S. (1993). "Influences of *T*, *S* and *P*CO2 on the pseudo-homogeneous precipitation of CaCO3 from seawater: implications for whiting formation". In: *Marine Chemistry* 41.4, pp. 291–297. ISSN: 0304-4203. DOI: `10.1016/0304-4203(93)90261-L`.

Müller, J. D., Gruber, N., Carter, B., Feely, R., Ishii, M., Lange, N., Lauvset, S. K., Murata, A., Olsen, A., Pérez, F. F., Sabine, C., Tanhua, T., Wanninkhof, R., and Zhu, D. (2023). "Decadal Trends in the Oceanic Storage of Anthropogenic Carbon From 1994 to 2014". In: *AGU Advances* 4.4, e2023AV000875. ISSN: 2576-604X. DOI: `10.1029/2023AV000875`.

Nabuurs, G.-J., Mrabet, R., Hatab, A. A., Bustamante, M., Clark, H., Havlík, P., House, J. I., Mbow, C., Ninan, K. N., and Popp, A. (2023). "Agriculture, forestry and other land uses (AFOLU)". In: *Climate Change 2022: Mitigation of Climate Change.* Cambridge University Press, pp. 747–860. URL: `https://library.wur.nl/WebQuery/wurpubs/fulltext/582219`.

Nagwekar, T., Nissen, C., and Hauck, J. (2024). "Ocean Alkalinity Enhancement in Deep Water Formation Regions Under Low and High Emission Pathways". In: *Earth's Future* 12.10, e2023EF004213. ISSN: 2328-4277. DOI: `10.1029/2023EF004213`.

National Academies of Sciences, Engineering, and Medicine, Committee on A Research Strategy for Ocean-based Carbon Dioxide Removal and Sequestration, Ocean Studies Board, and Division on Earth and Life Studies (2021). *A Research Strategy for Ocean-based Carbon Dioxide Removal and Sequestration*. Pages: 26278. Washington, D.C.: National Academies Press. ISBN: 978-0-309-08761-2. DOI: `10.17226/26278`. URL: `https://www.nap.edu/catalog/26278`.

Nissen, C., Lovenduski, N. S., Brooks, C. M., Hoppema, M., Timmermann, R., and Hauck, J. (2024). "Severe 21st-century ocean acidification in Antarctic Marine Protected Areas". In: *Nature Communications* 15.1, p. 259. ISSN: 2041-1723. DOI: `10.1038/s41467-023-44438-x`.

Nissen, C., Timmermann, R., Hoppema, M., Gürses, Ö., and Hauck, J. (2022). "Abruptly attenuated carbon sequestration with Weddell Sea dense waters by 2100". In: *Nature Communications* 13.1, p. 3402. ISSN: 2041-1723. DOI: `10.1038/s41467-022-30671-3`.

Nowicki, M., DeVries, T., and Siegel, D. A. (2022). "Quantifying the Carbon Export and Sequestration Pathways of the Ocean's Biological Carbon Pump". In: *Global Biogeochemical Cycles* 36.3, e2021GB007083. ISSN: 1944-9224. DOI: `10.1029/2021GB007083`.

Oelkers, E. H. (2001). "An experimental study of forsterite dissolution rates as a function of temperature and aqueous Mg and Si concentrations". In: *Chemical Geology* 175.3, pp. 485–494. ISSN: 0009-2541. DOI: `10.1016/S0009-2541(00)00352-1`.

Oelkers, E. H., Declercq, J., Saldi, G. D., Gislason, S. R., and Schott, J. (2018). "Olivine dissolution rates: A critical review". In: *Chemical Geology* 500, pp. 1–19. ISSN: 0009-2541. DOI: `10.1016/j.chemgeo.2018.10.008`.

Olsen, A. A. (2007). "Forsterite Dissolution Kinetics: Applications and Implications for Chemical Weathering". In: URL: `http://hdl.handle.net/10919/28213`.

Orr, J. C., Fabry, V. J., Aumont, O., Bopp, L., Doney, S. C., Feely, R. A., Gnanadesikan, A., Gruber, N., Ishida, A., Joos, F., Key, R. M., Lindsay, K., Maier-Reimer, E., Matear, R., Monfray, P., et al. (2005). "Anthropogenic ocean acidification over the twenty-first century and its impact on calcifying organisms". In: *Nature* 437.7059, pp. 681–686. ISSN: 1476-4687. DOI: `10.1038/nature04095`.

Orsi, A., Johnson, G., and Bullister, J. (1999). "Circulation, mixing, and production of Antarctic Bottom Water". In: *Progress in Oceanography* 43.1, pp. 55–109. ISSN: 00796611. DOI: `10.1016/S0079-6611(99)00004-X`.

Oschlies, A., Koeve, W., Rickels, W., and Rehdanz, K. (2010a). "Side effects and accounting aspects of hypothetical large-scale Southern Ocean iron fertilization". In: *Biogeosciences* 7.12, pp. 4017–4035. ISSN: 1726-4189. DOI: `10.5194/bg-7-4017-2010`.

Oschlies, A., Pahlow, M., Yool, A., and Matear, R. J. (2010b). "Climate engineering by artificial ocean upwelling: Channelling the sorcerer's apprentice". In: *Geophysical Research Letters* 37.4. ISSN: 1944-8007. DOI: `10.1029/2009GL041961`.

Oschlies, A., Bach, L. T., Rickaby, R. E. M., Satterfield, T., Webb, R., and Gattuso, J.-P. (2023). "Climate targets, carbon dioxide removal, and the potential role of ocean alkalinity enhancement". In: *State of the Planet* 2-oae2023, pp. 1–9. DOI: `10.5194/sp-2-oae2023-1-2023`.

Palevsky, H. I. and Doney, S. C. (2018). "How Choice of Depth Horizon Influences the Estimated Spatial Patterns and Global Magnitude of Ocean Carbon Export Flux". In: *Geophysical Research Letters* 45.9, pp. 4171–4179. ISSN: 1944-8007. DOI: `10.1029/2017GL076498`.

Palmiéri, J. and Yool, A. (2024). "Global-Scale Evaluation of Coastal Ocean Alkalinity Enhancement in a Fully Coupled Earth System Model". In: *Earth's Future* 12.3, e2023EF004018. ISSN: 2328-4277. DOI: `10.1029/2023EF004018`.

Pan, Y., Birdsey, R. A., Fang, J., Houghton, R., Kauppi, P. E., Kurz, W. A., Phillips, O. L., Shvidenko, A., Lewis, S. L., Canadell, J. G., Ciais, P., Jackson, R. B., Pacala, S. W., McGuire, A. D., Piao, S., et al. (2011). "A Large and Persistent Carbon Sink in the World's Forests". In: *Science* 333.6045, pp. 988–993. DOI: `10.1126/science.1201609`.

Pardo, P. C., Pérez, F. F., Khatiwala, S., and Ríos, A. F. (2014). "Anthropogenic CO2 estimates in the Southern Ocean: Storage partitioning in the different water masses". In: *Progress in Oceanography* 120, pp. 230–242. ISSN: 0079-6611. DOI: `10.1016/j.pocean.2013.09.005`.

Passow, U. and Carlson, C. A. (2012). "The biological pump in a high $CO_2$ world". In: *Marine Ecology Progress Series* 470, pp. 249–271. ISSN: 0171-8630, 1616-1599. DOI: `10.3354/meps09985`.

Pérez, F. F., Vázquez-Rodríguez, M., Mercier, H., Velo, A., Lherminier, P., and Ríos, A. F. (2010). "Trends of anthropogenic $CO_2$ storage in North Atlantic water masses". In: *Biogeosciences* 7.5, pp. 1789–1807. ISSN: 1726-4170. DOI: `10.5194/bg-7-1789-2010`.

Petit, J. R., Jouzel, J., Raynaud, D., Barkov, N. I., Barnola, J.-M., Basile, I., Bender, M., Chappellaz, J., Davis, M., Delaygue, G., Delmotte, M., Kotlyakov, V. M., Legrand, M., Lipenkov, V. Y., Lorius, C., et al. (1999). “Climate and atmospheric history of the past 420,000 years from the Vostok ice core, Antarctica”. In: *Nature* 399.6735, pp. 429–436. ISSN: 1476-4687. DOI: `10.1038/20859`.

Pierrehumbert, R. T. (2011). “Infrared radiation and planetary temperature”. In: *Physics Today* 64.1, pp. 33–38. ISSN: 0031-9228. DOI: `10.1063/1.3541943`.

Pongratz, J., Smith, S., Schwingshackl, C., Dayathilake, L., Gasser, T., Grassi, G., and Pilli, R. (2024). “Chapter 7: Current levels of CDR, The State of Carbon Dioxide Removal - 2nd Edition.” In: in collab. with Center For Open Science. Publisher: OSF. DOI: `10.17605/OSF.IO/ZXSKB`.

Pörtner, H.-O., Roberts, D., Adams, H., Adelekan, I., Adler, C., Adrian, R., Aldunce, P., Ali, E., Begum, R. A., Friedl, B. B., Kerr, R. B., Biesbroek, R., Birkmann, J., Bowen, K., Caretta, M., et al. (2022). *Climate Change 2022: Impacts, Adaptation and Vulnerability*. Technical Summary. Cambridge, UK and New York, USA: Cambridge University Press, pp. 37–118. ISBN: 9781009325844.

Post, W. M., Emanuel, W. R., Zinke, P. J., and Stangenberger, A. G. (1982). “Soil carbon pools and world life zones”. In: *Nature* 298.5870, pp. 156–159. ISSN: 1476-4687. DOI: `10.1038/298156a0`.

Prentice, I., Farquhar, G., Fasham, M., Goulden, M., Heimann, M., Jaramillo, V., Kheshgi, H., Quéré, C. L., Scholes, R., Wallace, D., Archer, D., Ashmore, M., Aumont, O., Baker, D., Battle, M., et al. (2001). “The carbon cycle and atmospheric carbon dioxide”. In: *Climate change 2001: the scientific basis, Intergovernmental panel on climate change*. URL: `https://hal.science/hal-03333974`.

Rahmstorf, S., Box, J. E., Feulner, G., Mann, M. E., Robinson, A., Rutherford, S., and Schaffernicht, E. J. (2015). “Exceptional twentieth-century slowdown in Atlantic Ocean overturning circulation”. In: *Nature Climate Change* 5.5, pp. 475–480. ISSN: 1758-6798. DOI: `10.1038/nclimate2554`.

Renforth, P. and Henderson, G. (2017). “Assessing ocean alkalinity for carbon sequestration: Ocean Alkalinity for C Sequestration”. In: *Reviews of Geophysics* 55.3, pp. 636–674. ISSN: 87551209. DOI: `10.1002/2016RG000533`.

Riahi, K., Schaeffer, R., Arango, J., Calvin, K., Guivarch, C., Hasegawa, T., Jiang, K., Kriegler, E., Matthews, R., Peters, G. P., Rao, A., Robertson, S., Sebbit, A. M., Steinberger, J., Tavoni, M., et al. (2022). “Mitigation pathways compatible with long-term goals”. In: *Climate Change 2022: Mitigation of Climate Change. Contribution of Working Group III to the Sixth Assessment Report of the Intergovernmental Panel on Climate Change*. Ed. by P. R. Shukla, J. Skea, R. Slade, A. A. Khourdajie, R. van Diemen, D. McCollum, M. Pathak, S. Some, P. Vyas, R. Fradera, M. Belkacemi, A. Hasija, G. Lisboa, S. Luz, and J. Malley. Cambridge, UK and New York, NY, USA: Cambridge University Press. DOI: `10.1017/9781009157926.005`. URL: `https://doi.org/10.1017/9781009157926.005`.

Ridgwell, A., Zondervan, I., Hargreaves, J. C., Bijma, J., and Lenton, T. M. (2007). "Assessing the potential long-term increase of oceanic fossil fuel $CO_2$ uptake due to $CO_2$-calcification feedback". In: *Biogeosciences* 4.4, pp. 481–492. ISSN: 1726-4170. DOI: `10.5194/bg-4-481-2007`.

Ridgwell, A. and Zeebe, R. E. (2005). "The role of the global carbonate cycle in the regulation and evolution of the Earth system". In: *Earth and Planetary Science Letters* 234.3, pp. 299–315. ISSN: 0012-821X. DOI: `10.1016/j.epsl.2005.03.006`.

Riebesell, U., Basso, D., Geilert, S., Dale, A. W., and Kreuzburg, M. (2023). "Mesocosm experiments in ocean alkalinity enhancement research". In: *State of the Planet* 2-oae2023, pp. 1–14. DOI: `10.5194/sp-2-oae2023-6-2023`.

Ringham, M. C., Hirtle, N., Shaw, C., Lu, X., Herndon, J., Carter, B. R., and Eisaman, M. D. (2024). "An assessment of ocean alkalinity enhancement using aqueous hydroxides: kinetics, efficiency, and precipitation thresholds". In: *Biogeosciences* 21.15, pp. 3551–3570. ISSN: 1726-4170. DOI: `10.5194/bg-21-3551-2024`.

Rubino, M., Etheridge, D., Thornton, D., Allison, C., Francey, R., Langenfelds, R., Steele, P., Trudinger, C., Spencer, D., Curran, M., Van Ommen, T., and Smith, A. (2024). "Law Dome Ice Core 2000-Year CO2, CH4, N2O and d13C-CO2". In: DOI: `10.25919/5bfe29ff807fb`.

Saatchi, S. S., Harris, N. L., Brown, S., Lefsky, M., Mitchard, E. T. A., Salas, W., Zutta, B. R., Buermann, W., Lewis, S. L., Hagen, S., Petrova, S., White, L., Silman, M., and Morel, A. (2011). "Benchmark map of forest carbon stocks in tropical regions across three continents". In: *Proceedings of the National Academy of Sciences* 108.24, pp. 9899–9904. DOI: `10.1073/pnas.1019576108`.

Sabine, C. L., Feely, R. A., Gruber, N., Key, R. M., Lee, K., Bullister, J. L., Wanninkhof, R., Wong, C. S., Wallace, D. W. R., Tilbrook, B., Millero, F. J., Peng, T.-H., Kozyr, A., Ono, T., and Rios, A. F. (2004). "The Oceanic Sink for Anthropogenic CO $_2$". In: *Science* 305.5682, pp. 367–371. ISSN: 0036-8075, 1095-9203. DOI: `10.1126/science.1097403`.

Sanz-Pérez, E. S., Murdock, C. R., Didas, S. A., and Jones, C. W. (2016). "Direct Capture of CO2 from Ambient Air". In: *Chemical Reviews* 116.19, pp. 11840–11876. ISSN: 0009-2665. DOI: `10.1021/acs.chemrev.6b00173`.

Sarmiento, J. L. (2013). *Ocean Biogeochemical Dynamics*. Princeton University Press. ISBN: 978-1-4008-4907-9. DOI: `10.1515/9781400849079`.

Scharlemann, J. P., Tanner, E. V., Hiederer, R., and Kapos, V. (2014). "Global soil carbon: understanding and managing the largest terrestrial carbon pool". In: *Carbon management* 5.1, pp. 81–91.

Schenuit, F., Buck, H., Geden, O., Hofbauer, V., Odeh, N., Schell, K., Sugiyama, M., and Zheng, Q. (2024). "Chapter 5: Policy and Governance, The State of Carbon Dioxide Removal - 2nd Edition." In: in collab. with Center For Open Science. Publisher: OSF. DOI: `10.17605/OSF.IO/4EGUH`.

Schuiling, R. D. and Krijgsman, P. (2006). “Enhanced Weathering: An Effective and Cheap Tool to Sequester Co2”. In: *Climatic Change* 74.1, pp. 349–354. ISSN: 1573-1480. DOI: `10.1007/s10584-005-3485-y`.

Schulte, I., Burke, J., Arcusa, S., Mercer, L., and Hondeborg, D. (2024). “Chapter 10: Monitoring, Reporting and Verification, The State of Carbon Dioxide Removal - 2nd Edition”. In: in collab. with Center For Open Science. Publisher: OSF. DOI: `10.17605/OSF.IO/ADHP2`.

Schulz, K. G., Bach, L. T., and Dickson, A. G. (2023). “Seawater carbonate chemistry considerations for ocean alkalinity enhancement research: theory, measurements, and calculations”. In: *State of the Planet* 2-oae2023, pp. 1–14. DOI: `10.5194/sp-2-oae2023-2-2023`.

Schwinger, J., Bourgeois, T., and Rickels, W. (2024). “On the emission-path dependency of the efficiency of ocean alkalinity enhancement”. In: *Environmental Research Letters* 19.7, p. 074067. ISSN: 1748-9326. DOI: `10.1088/1748-9326/ad5a27`.

Shadwick, E. H., Tilbrook, B., and Williams, G. D. (2014). “Carbonate chemistry in the Mertz Polynya (East Antarctica): Biological and physical modification of dense water outflows and the export of anthropogenic CO2”. In: *Journal of Geophysical Research: Oceans* 119.1, pp. 1–14. ISSN: 2169-9291. DOI: `10.1002/2013JC009286`.

Siegel, D. A., DeVries, T., Doney, S. C., and Bell, T. (2021). “Assessing the sequestration time scales of some ocean-based carbon dioxide reduction strategies”. In: *Environmental Research Letters* 16.10, p. 104003. ISSN: 1748-9326. DOI: `10.1088/1748-9326/ac0be0`.

Siegel, D. A., DeVries, T., Cetinić, I., and Bisson, K. M. (2023). “Quantifying the Ocean’s Biological Pump and Its Carbon Cycle Impacts on Global Scales”. In: *Annual Review of Marine Science* 15 (Volume 15, 2023), pp. 329–356. ISSN: 1941-1405, 1941-0611. DOI: `10.1146/annurev-marine-040722-115226`.

Sigman, D. M. and Boyle, E. A. (2000). “Glacial/interglacial variations in atmospheric carbon dioxide”. In: *Nature* 407.6806, pp. 859–869. ISSN: 1476-4687. DOI: `10.1038/35038000`.

Sigman, D. M., Hain, M. P., and Haug, G. H. (2010). “The polar ocean and glacial cycles in atmospheric CO2 concentration”. In: *Nature* 466.7302, pp. 47–55. ISSN: 1476-4687. DOI: `10.1038/nature09149`.

Sloyan, B. M., Talley, L. D., Chereskin, T. K., Fine, R., and Holte, J. (2010). “Antarctic Intermediate Water and Subantarctic Mode Water Formation in the Southeast Pacific: The Role of Turbulent Mixing”. In: *Journal of Physical Oceanography* 40.7, pp. 1558–1574. ISSN: 0022-3670, 1520-0485. DOI: `10.1175/2010JPO4114.1`.

Smetacek, V., Klaas, C., Strass, V. H., Assmy, P., Montresor, M., Cisewski, B., Savoye, N., Webb, A., d’Ovidio, F., Arrieta, J. M., Bathmann, U., Bellerby, R., Berg, G. M., Croot, P., Gonzalez, S., et al. (2012). “Deep carbon export from a Southern Ocean iron-fertilized diatom bloom”. In: *Nature* 487.7407, pp. 313–319. ISSN: 1476-4687. DOI: `10.1038/nature11229`.

Smethie, W. M. and Fine, R. A. (2001). “Rates of North Atlantic Deep Water formation calculated from chlorofluorocarbon inventories”. In: *Deep Sea Research Part I: Oceanographic Research Papers* 48.1, pp. 189–215. ISSN: 0967-0637. DOI: `10.1016/S0967-0637(00)00048-0`.

Smith, K. M., Hamlington, P. E., Niemeyer, K. E., Fox-Kemper, B., and Lovenduski, N. S. (2018). “Effects of Langmuir Turbulence on Upper Ocean Carbonate Chemistry”. In: *Journal of Advances in Modeling Earth Systems* 10.12, pp. 3030–3048. ISSN: 1942-2466. DOI: `10.1029/2018MS001486`.

Smith, P., Bustamante, M., Ahammad, H., Clark, H., Dong, H., Elsiddig, E. A., Haberl, H., Harper, R., House, J., and Jafari, M. (2014). “Agriculture, forestry and other land use (AFOLU)”. In: *Climate change 2014: mitigation of climate change. Contribution of Working Group III to the Fifth Assessment Report of the Intergovernmental Panel on Climate Change*. Cambridge University Press, pp. 811–922. URL: `https://orbit.dtu.dk/files/103008543/ipcc_wg3_ar5_chapter11.pdf`.

Smith, P., Davis, S. J., Creutzig, F., Fuss, S., Minx, J., Gabrielle, B., Kato, E., Jackson, R. B., Cowie, A., Kriegler, E., Vuuren, D. P. van, Rogelj, J., Ciais, P., Milne, J., Canadell, J. G., et al. (2016). “Biophysical and economic limits to negative CO2 emissions”. In: *Nature Climate Change* 6.1, pp. 42–50. ISSN: 1758-6798. DOI: `10.1038/nclimate2870`.

Smith, S., Fuss, S., Buck, H., Schenuit, F., Pongratz, J., Schulte, I., Lamb, W. F., Probst, B., Edwards, M., Nemet, G. F., Cox, E., Smith, S., Johnstone, I., Geden, O., Burke, J., et al. (2024). “The State of Carbon Dioxide Removal - 2nd Edition”. In: in collab. with Center For Open Science. DOI: `10.17605/OSF.IO/F85QJ`.

Sohi, S. P., Krull, E., Lopez-Capel, E., and Bol, R. (2010). “Chapter 2 - A Review of Biochar and Its Use and Function in Soil”. In: *Advances in Agronomy*. Vol. 105. Advances in Agronomy. Academic Press, pp. 47–82. DOI: `10.1016/S0065-2113(10)05002-9`.

Sonntag, S., Ferrer González, M., Ilyina, T., Kracher, D., Nabel, J. E. M. S., Niemeier, U., Pongratz, J., Reick, C. H., and Schmidt, H. (2018). “Quantifying and Comparing Effects of Climate Engineering Methods on the Earth System”. In: *Earth's Future* 6.2, pp. 149–168. ISSN: 2328-4277. DOI: `10.1002/2017EF000620`.

Subhas, A. V., Marx, L., Reynolds, S., Flohr, A., Mawji, E. W., Brown, P. J., and Cael, B. B. (2022). “Microbial ecosystem responses to alkalinity enhancement in the North Atlantic Subtropical Gyre”. In: *Frontiers in Climate* 4. ISSN: 2624-9553. DOI: `10.3389/fclim.2022.784997`.

Suitner, N., Faucher, G., Lim, C., Schneider, J., Moras, C. A., Riebesell, U., and Hartmann, J. (2024). “Ocean alkalinity enhancement approaches and the predictability of runaway precipitation processes: results of an experimental study to determine critical alkalinity ranges for safe and sustainable application scenarios”. In: *Biogeosciences* 21.20, pp. 4587–4604. ISSN: 1726-4170. DOI: `10.5194/bg-21-4587-2024`.

Sundquist, E. T. (1985). “Geological Perspectives on Carbon Dioxide and the Carbon Cycle”. In: *The Carbon Cycle and Atmospheric CO2: Natural Variations Archean to Present*. American Geophysical Union (AGU), pp. 55–59. ISBN: 978-1-118-66432-2. DOI: `10.1029/GM032p0005`.

Tagliabue, A., Twining, B. S., Barrier, N., Maury, O., Berger, M., and Bopp, L. (2023). “Ocean iron fertilization may amplify climate change pressures on marine animal biomass for limited climate benefit”. In: *Global Change Biology* 29.18, pp. 5250–5260. ISSN: 1365-2486. DOI: `10.1111/gcb.16854`.

Takahashi, T., Sutherland, S. C., Sweeney, C., Poisson, A., Metzl, N., Tilbrook, B., Bates, N., Wanninkhof, R., Feely, R. A., Sabine, C., Olafsson, J., and Nojiri, Y. (2002). “Global sea–air $CO_2$ flux based on climatological surface ocean $pCO_2$, and seasonal biological and temperature effects”. In: *Deep Sea Research Part II: Topical Studies in Oceanography*. The Southern Ocean I: Climatic Changes in the Cycle of Carbon in the Southern Ocean 49.9, pp. 1601–1622. ISSN: 0967-0645. DOI: `10.1016/S0967-0645(02)00003-6`.

Talley, L. D. and McCartney, M. S. (1982). “Distribution and Circulation of Labrador Sea Water”. In: ISSN: 1520-0485.

Taylor, J. R., Smith, K. M., and Vreugdenhil, C. A. (2020). “The Influence of Submesoscales and Vertical Mixing on the Export of Sinking Tracers in Large-Eddy Simulations”. In: *Journal of Physical Oceanography*. DOI: `10.1175/JPO-D-19-0267.1`.

Thomas, S., Dargusch, P., Harrison, S., and Herbohn, J. (2010). “Why are there so few afforestation and reforestation Clean Development Mechanism projects?” In: *Land Use Policy* 27.3, pp. 880–887. ISSN: 0264-8377. DOI: `10.1016/j.landusepol.2009.12.002`.

Toggweiler, J. R. (1999). “Variation of atmospheric CO2 by ventilation of the ocean’s deepest water”. In: *Paleoceanography* 14.5, pp. 571–588. ISSN: 1944-9186. DOI: `10.1029/1999PA900033`.

UNFCCC (1998). “Kyoto Protocol To the United Nation Framework Convention on Climate Change (UNFCCC)”. In: URL: `https://unfccc.int/resource/docs/convkp/kpeng.pdf`.

– (2015). “United Nations Framework Convention on Climate Change (UNFCCC): Adoption of the Paris Agreement, 21st Conference of the Parties.” In: URL: `https://unfccc.int/sites/default/files/english_paris_agreement.pdf`.

Urey, H. C. and Korff, S. A. (1952). “The Planets: Their Origin and Development”. In: *Physics Today* 5.8, p. 12. ISSN: 0031-9228. DOI: `10.1063/1.3067687`.

Volk and Hoffert (1985). *Ocean Carbon Pumps: Analysis of Relative Strengths and Efficiencies in Ocean-Driven Atmospheric CO2 Changes - Volk - 1985 - Geophysical Monograph Series - Wiley Online Library*. URL: `https://agupubs.onlinelibrary.wiley.com/doi/abs/10.1029/GM032p0099`.

Walker, J. C. G., Hays, P. B., and Kasting, J. F. (1981). “A negative feedback mechanism for the long-term stabilization of Earth’s surface temperature”. In: *Journal of Geophysical Research: Oceans* 86 (C10), pp. 9776–9782. ISSN: 2156-2202. DOI: `10.1029/JC086iC10p09776`.

Wallace, D. (2001). “Chapter 6.3 Storage and transport of excess $CO_2$ in the oceans:The JGOFS/WOCE global $CO_2$ survey”. In: *International Geophysics*. Ed. by G. Siedler, J. Church, and J. Gould. Vol. 77. Ocean Circulation and Climate. Academic Press, pp. 489–L. DOI: 10.1016/S0074-6142(01)80136-4.

Wang, H., Pilcher, D. J., Kearney, K. A., Cross, J. N., Shugart, O. M., Eisaman, M. D., and Carter, B. R. (2023). “Simulated Impact of Ocean Alkalinity Enhancement on Atmospheric CO $_2$ Removal in the Bering Sea”. In: *Earth's Future* 11.1. ISSN: 2328-4277, 2328-4277. DOI: 10.1029/2022EF002816.

Wanninkhof, R., Park, G.-H., Takahashi, T., Sweeney, C., Feely, R., Nojiri, Y., Gruber, N., Doney, S. C., McKinley, G. A., Lenton, A., Le Quéré, C., Heinze, C., Schwinger, J., Graven, H., and Khatiwala, S. (2013). “Global ocean carbon uptake: magnitude, variability and trends”. In: *Biogeosciences* 10.3, pp. 1983–2000. ISSN: 1726-4170. DOI: 10.5194/bg-10-1983-2013.

Wanninkhof, R. (1992). “Relationship between wind speed and gas exchange over the ocean”. In: *Journal of Geophysical Research: Oceans* 97 (C5), pp. 7373–7382. ISSN: 2156-2202. DOI: 10.1029/92JC00188.

– (2014). “Relationship between wind speed and gas exchange over the ocean revisited”. In: *Limnology and Oceanography: Methods* 12.6, pp. 351–362. ISSN: 1541-5856. DOI: 10.4319/lom.2014.12.351.

West, A. J., Galy, A., and Bickle, M. (2005). “Tectonic and climatic controls on silicate weathering”. In: *Earth and Planetary Science Letters* 235.1, pp. 211–228. ISSN: 0012-821X. DOI: 10.1016/j.epsl.2005.03.020.

White, A. F., Blum, A. E., Bullen, T. D., Vivit, D. V., Schulz, M., and Fitzpatrick, J. (1999). “The effect of temperature on experimental and natural chemical weathering rates of granitoid rocks”. In: *Geochimica et Cosmochimica Acta* 63.19, pp. 3277–3291. ISSN: 0016-7037. DOI: 10.1016/S0016-7037(99)00250-1.

Wolf-Gladrow, D. A., Zeebe, R. E., Klaas, C., Körtzinger, A., and Dickson, A. G. (2007). “Total alkalinity: The explicit conservative expression and its application to biogeochemical processes”. In: *Marine Chemistry*. Special issue: Dedicated to the memory of Professor Roland Wollast 106.1, pp. 287–300. ISSN: 0304-4203. DOI: 10.1016/j.marchem.2007.01.006.

Yamamoto, K., DeVries, T., and Siegel, D. A. (2024). “Metrics for quantifying the efficiency of atmospheric CO2 reduction by marine carbon dioxide removal (mCDR)”. In: *Environmental Research Letters* 19.10, p. 104053. ISSN: 1748-9326. DOI: 10.1088/1748-9326/ad7477.

Yankovsky, E., Zhou, M., Tyka, M., Bachman, S., Ho, D., Karspeck, A., and Long, M. (2024). “Impulse response functions as a framework for quantifying ocean-based carbon dioxide removal”. In: *EGUsphere*, pp. 1–26. DOI: 10.5194/egusphere-2024-2697.

Yool, A., Shepherd, J. G., Bryden, H. L., and Oschlies, A. (2009). “Low efficiency of nutrient translocation for enhancing oceanic uptake of carbon dioxide”. In: *Journal of Geophysical Research: Oceans* 114 (C8). ISSN: 2156-2202. DOI: `10.1029/2008JC004792`.

Zeebe, R. E. and Archer, D. (2005). “Feasibility of ocean fertilization and its impact on future atmospheric CO2 levels”. In: *Geophysical Research Letters* 32.9. ISSN: 1944-8007. DOI: `10.1029/2005GL022449`.

Zeebe, R. E. and Wolf-Gladrow, D. (2001). *CO2 in Seawater: Equilibrium, Kinetics, Isotopes*. Gulf Professional Publishing. 382 pp. ISBN: 978-0-444-50946-8.

Zeebe, R. E. and Westbroek, P. (2003). “A simple model for the CaCO3 saturation state of the ocean: The “Strangelove,” the “Neritan,” and the “Cretan” Ocean”. In: *Geochemistry, Geophysics, Geosystems* 4.12. ISSN: 1525-2027. DOI: `10.1029/2003GC000538`.

Zhou, M., Tyka, M. D., Ho, D. T., Yankovsky, E., Bachman, S., Nicholas, T., Karspeck, A. R., and Long, M. C. (2025). “Mapping the global variation in the efficiency of ocean alkalinity enhancement for carbon dioxide removal”. In: *Nature Climate Change* 15.1, pp. 59–65. ISSN: 1758-6798. DOI: `10.1038/s41558-024-02179-9`.

# DECLARATION

**Versicherung an Eides Statt**

Ich, Tanvi Nagwekar,

versichere an Eides Statt durch meine Unterschrift, dass ich die vorstehende Arbeit selbständig und ohne fremde Hilfe angefertigt und alle Stellen, die ich wörtlich dem Sinne nach aus Veröffentlichungen entnommen habe, als solche kenntlich gemacht habe, mich auch keiner anderen als der angegebenen Literatur oder sonstiger Hilfsmittel bedient habe.

Ich versichere an Eides Statt, dass ich die vorgenannten Angaben nach bestem Wissen und Gewissen gemacht habe und dass die Angaben der Wahrheit entsprechen und ich nichts verschwiegen habe.

Die Strafbarkeit einer falschen eidesstattlichen Versicherung ist mir bekannt, namentlich die Strafandrohung gemäß § 156 StGB bis zu drei Jahren Freiheitsstrafe oder Geldstrafe bei vorsätzlicher Begehung der Tat bzw. gemäß § 161 Abs. 1 StGB bis zu einem Jahr Freiheitsstrafe oder Geldstrafe bei fahrlässiger Begehung.

Ort, Datum

Unterschrift

# CONTRIBUTION TO MULTI-AUTHOR ARTICLES AND MANUSCRIPTS

**Declaration on the contribution of the candidate to a multi-author article/manuscript which is included as a chapter in the submitted doctoral thesis**

**Chapter: "Ocean Alkalinity Enhancement in Deep Water Formation Regions Under Low and High Emission Pathways"**

*Contribution of the candidate in % of the total work load (up to 100% for each of the following categories):*

Experimental concept and design: ca. 70%
Experimental work and/or acquisition of (experimental) data: ca. 100%
Data analysis and interpretation: ca. 70%
Preparation of Figures and Tables: ca. 80%
Drafting of the manuscript: ca. 70%

**Chapter: "Alkalinity Enhancement in the Subduction Regions: Efficiency, Earth System Feedbacks, and Deep Ocean Carbon Sequestration"**

*Contribution of the candidate in % of the total work load (up to 100% for each of the following categories):*

Experimental concept and design: ca. 70%
Experimental work and/or acquisition of (experimental) data: ca. 100%
Data analysis and interpretation: ca. 70%
Preparation of Figures and Tables: ca. 80%
Drafting of the manuscript: ca. 80%

**Chapter: "Effects of Model Resolution on Ocean Alkalinity Enhancement in the Subduction Regions and the Global Ocean"**

*Contribution of the candidate in % of the total work load (up to 100% for each of the following categories):*

Experimental concept and design: ca. 70%
Experimental work and/or acquisition of (experimental) data: ca. 100%
Data analysis and interpretation: ca. 70%
Preparation of Figures and Tables: ca. 90%
Drafting of the manuscript: ca. 90%

Ort, Datum

Unterschrift